Photocatalytic Studies of Doped and Capped ZnO and CeO_2 Nanoparticles

A

Thesis

Submitted for the award of degree of

Doctor of Philosophy

By

MANISH MITTAL

(Regn. No. 950912008)

Under the supervision of

Dr. O. P. Pandey

Senior Professor and Dean (Research and Sponsored Projects)

School of Physics and Materials Science

Thapar University, Patiala-147004

October, 2016

CERTIFICATE

This is to certify that the thesis entitled **"Photocatalytic Studies of doped and capped ZnO and CeO_2 nanoparicles"** which is being submitted by **Manish Mittal** (Regd. No. **950912008**) in fulfillment of the requirement for the degree of ***Doctor of Philosophy*** in *School of Physics and Materials Science, Thapar University, Patiala (Punjab)*, India is an exclusive record of candidate's own research work under my supervision. The thesis in part or in full has not been submitted in any other university or institute for the award of any degree. The thesis is fit to be considered for the award of degree of Doctor of Philosophy.

Dr. O. P. Pandey
Senior Professor and Dean (Research & Sponsored Projects)
School of Physics and Materials Science
Thapar University, Patiala (Punjab) -147004
INDIA

INDEX

Contents		Page No.
Certificate		i
Acknowledgement		vi
List of publications		viii
List of papers presented in conferences (International/National)		viii
List of figures		ix
List of tables		xv
Preface		xvi
Chapter 1	**Introduction**	**1-18**
	Overview	1
1.1	Background	2
1.2	Need of waste water treatment	2
1.3	Technologies for color removal	3
1.4	Photocatalysis for waste water treatment	5
1.5	Semiconductor photocatalysts	6
1.6	Heterogeneous photocatalysis	7
1.6.1	Energy band configuration	9
1.6.2	Modulation of valance band and conduction band	10
1.6.3	Effect of adsorption and pH	11
1.6.4	Source of radiations	12
1.6.5	Charge carrier trapping	12
1.6.6	Photocatalyst size and quantum confinement effect	13
1.7	Synthesis	14
1.7.1	Surface modification of nanoparticles	15
	References	17
Chapter 2	**Literature Review**	**19-44**
	Overview	19
2.1	Introduction	20
2.2	Zinc Oxide (ZnO)	20
2.3	Photocatalysis with ZnO nanomaterials	21

2.4	Cerium Oxide (CeO_2)	30
2.5	Photocatalysis with CeO_2 nanomaterials	30
2.6	Plan of work	37
	References	38
Chapter 3	**Experimental Details**	**45-49**
	Overview	45
3.1	Raw materials	46
3.2	Synthesis of undoped and doped ZnO nanoparticles	46
3.3	Synthesis of undoped and doped CeO_2 nanoparticles	47
3.4	Synthesis of doped ZnO and CeO_2 nanoparticles with varying pH	47
3.5	Characterization Techniques	48
3.6	Apparatus used for photocatalytic study	48
	References	49
Chapter 4	**Result and Discussion (Doped and capped ZnO nanoparticles)**	**50-109**
	Overview	50
4.1	Introduction	51
4.2	PVP capped undoped and Mn doped ZnO nanoparticles	51
4.2.1	XRD studies	51
4.2.2	TEM analysis	53
4.2.3	UV-Visible spectroscopy	53
4.2.4	Photocatalytic studies	55
4.2.5	Reusability	60
4.3	TG capped undoped and Mn doped ZnO nanoparticles	64
4.3.1	XRD studies	64
4.3.2	TEM studies	65
4.3.3	UV-Visible spectroscopy	66
4.3.4	Photoluminescence studies	67
4.3.4.1	Excitation studies	67
4.3.4.2	Emission studies	68
4.3.5	Photocatalytic studies	70
4.3.6	Effect of pH on photocatalysis	73

4.3.7	Effect of H_2O_2 on photocatalysis	76
4.4	TG capped undoped and Cu doped ZnO nanoparticles	81
4.4.1	XRD studies	81
4.4.2	TEM and EDS studies	82
4.4.3	UV-Visible spectroscopy	86
4.4.4	Photoluminescence studies	88
4.4.4.1	Excitation studies	88
4.4.4.2	Emission studies	88
4.4.5	Photocatalytic studies	91
4.4.6	Effect of pH on photocatalytic properties	94
4.4.7	Effect of photocatalyst loading	97
4.5	PVP capped undoped and Cu doped ZnO nanoparticles	98
4.5.1	XRD studies	98
4.5.2	TEM studies	98
4.5.3	UV-Visible spectroscopy	99
4.5.4	Photocatalytic studies	102
4.5.5	Effect of pH on photocatalytic properties	104
	References	106
Chapter 5	**Result and Discussion Doped (Ag and Au) CeO_2 nanoparticles**	**110-142**
	Overview	110
5.1	Introduction	111
5.2	Undoped and doped (Mn and Cu) CeO_2 nanoparticles	111
5.2.1	XRD studies	111
5.2.2	UV-Visible spectroscopy	112
5.2.3	Photocatalytic studies	113
5.3	Ag doped CeO_2 nanoparticles	114
5.3.1	XRD studies	114
5.3.2	TEM and EDS analysis	117
5.3.3	UV-Visible spectroscopy	120
5.3.4	XPS studies	121
5.3.5	Photocatalytic studies	124
5.3.5.1	Effect of pH	127

5.3.5.2	Reusability studies	129
5.3.6	Mechanism	130
5.4	Au doped CeO_2 nanoparticles	133
5.4.1	XRD studies	133
5.4.2	TEM studies	134
5.4.3	UV-Visible spectroscopy	135
5.4.4	Photocatalytic studies	137
5.4.4.1	Effect of pH	139
	References	141
Chapter 6	**Conclusions and Future Scope**	**143-147**
	Overview	143
6.1	Conclusions	144
6.2	Future scope	146

ACKNOWLEDGEMENT

Five years as a Ph. D. student concluded by writing this thesis has been a great learning experience for me, both as a scientist and as a person. I have had the great luck to work and collaborate with a lot of inspiring, competent, and nice people and I am happy to be able to use this space to thank them. The best and worst moments have been shared with many people during my doctoral journey. It has been a great privilege to spend several years in the School of Physics and Materials Science at Thapar University. No matter how much zealous and zestful one's thinking is, yet nobody can do everything all by himself/herself without some help and guidance. It is inhumane if the concerned person's support goes without appreciation and thanks. At the end of my thesis, it gives me pleasure to express my thanks to all those who have contributed in many ways to make this work feasible and has made it an abiding experience for me.

My first and foremost offering of thanks goes to the creator who shaped my dreams into reality, my guide and mentor **Dr. Om Prakash Pandey** for his excellent guidance, care and providing me with an inviting atmosphere for doing research. Perseverance, exuberance and affirmative approach are just some of the traits he imprinted on my personality. He steered me this journey through his invaluable advice, positive criticism, stimulating discussion and consistent encouragement. His meticulous attention towards my proceedings, his devoted time and his ideas has enabled me to make the project a success. His faith in me has always made me more confident. It had been my privilege to work under his guidance.

I would like to express my thanks to the members of doctoral committee: **Dr. Kulvir Singh, Dr. B. N. Chudasama and Dr. Amzad Ali** for their encouragement, guidance, perceptive comments and prolific criticism.

I am thankful to **Dr. Manoj Sharma**, Head, School of Physics and Materials Science, Thapar University for providing kind help and support when required.

I am also very grateful to the faculty of School of Physics and Materials Science, **Dr. D. P. Singh, Dr. S. D. Tiwari, Dr. N. K. Verma, Dr. Loveleen Kaur Brar** for their valuable suggestions during my PhD work. I am thankful to **Dr. Manoj Sharma** (Assistant Professor and Department In-charge, Department of Nanotechnology, Sri Guru Granth Sahib World University, Fatehgarh Sahib, Punjab) for his help and valuable suggestions. I am grateful to him for sharing his time and expertise. His comments and views were very insightful and helpful. I also express my sincere thanks to **SAI Labs**, Thapar University Patiala, and **SAIF**, Punjab University, Chandigarh, for characterizing my samples. I am indeed grateful to **Dr. Rajesh Kumar, Mr. Sandeep and Ms. Richa** of School of Chemistry and Biochemistry for providing me help in difficult hours.

I would also like to acknowledge **Mrs. Parveen, Mrs. Neelam, Mr. Indermani Mishra and Mr. Jant Singh** for their kind help and support during various stages of administrative formalities.

Mrs. Sushila Pandey is highly acknowledged for her unconditional love and kind support. Words are inadequate in expressing my sincere thanks to my dear friends and labmates **Dr. Deepak Kumar,Mr Aayush Gupta, Mr. Piyush Sharma, Mr. Rameez Ahmed, Mr. Suresh Kumar, Dr. Gurbinder Chaudhary, Ms. Parveer Kaur, Dr. Gaurav Singla, Dr. Paramjyot Jha, Dr. Chandni Khurana, Dr. Samiksha Verma, Ms. Navjot Kaur, Ms. Purnima Sharma, and Mrs. Suninder Jeet Kaur,** for their support in every moment of difficulty.

My in-laws family especially my wife, **Mrs. Sunita Rani** deserves special thanks for her patience and moral support during this phase of life. Words are not enough to express my gratitude towards my daughter **Maaheem Mittal**. I am also thankful to my brother **Mr. Pankaj Mittal,** my sister in law **Mrs. Anu Mittal** and my nephew **Manan Mittal** for his moral support whenever I needed.

Last but not the least, I would like to pay high regards to my father **Sh. Pawan Mittal** and my mother, **Smt. Saneh Lata Mittal** for their sincere encouragement and inspiration throughout my research work and lifting me uphill this phase of life. I owe everything to them.

Above all, I would like to thank the Almighty, **God**. He has given me the power to believe in myself and pursue my dreams. I could never have done this without the faith I have in Him.

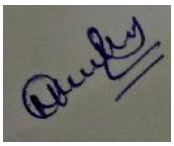

(Manish Mittal)

LIST OF PUBLICATIONS

1. **M. Mittal**, M. Sharma and O.P. Pandey; Fast and quick degradation properties of doped and capped ZnO nanoparticles under UV–Visible light radiations, Solar Energy 125, 51-64 (**2016**).
2. **M. Mittal**, M. Sharma and O.P. Pandey; UV–Visible light induced photocatalytic studies of Cu doped ZnO nanoparticles prepared by co-precipitation method, Solar Energy 110, 386-397 (**2014**).
3. **M. Mittal**, M. Sharma and O.P. Pandey; Photocatalytic studies of crystal violet dye using Mn doped and PVP capped ZnO nanoparticles, Journal of nanoscience and nanotechnology 14 (4), 2725-2733 (**2014**).
4. **M. Mittal** and O.P.Pandey; Photocatalytic studies of Ag doped CeO_2 nanoparticles, Scientific Reports **(Communicated)**.

LIST OF PAPERS PRESENTED IN CONFERENCES (INTERNATIONAL/NATIONAL)

1. **Manish Mittal**, Manoj Sharma and O.P. Pandey, "Photocatalytic studies of crystal violet dye using Mn doped and PVP capped Zno nanoparticles", International Conference on Emerging Trends in Physics for Environmental Monitoring and Management (**ETPEMM-2012**) held on Dec. 17-19, 2012 at Punjabi University, Patiala.
2. **Manish Mittal**, Manoj Sharma and O.P. Pandey, "Enhanced Photo-catalytic activity of Cu doped and TG capped ZnO nanoparticles synthesized by Co-precipitation method", 6th International conference on Nanoscience and nanotechnology (**ICONSAT-2014**) held on Mar. 02-05, 2014 at Panjab University, Chandigarh.
3. **Manish Mittal** and O.P. Pandey, "Synthesis, characterization and photocatalytic properties of silver doped CeO2 nanoparticles", 2nd conference on microscopy in materials science (**AMST-2016**) held on Feb. 25-27, 2016 at Thapar University, Patiala.

LIST OF FIGURES

Page No.

Chapter 1

Figure 1.1 Different wastewater treatment methods currently in use. 4

Figure 1.2 Generation of electron-hole pair in semiconductor materials. 6

Figure 1.3 Catalyzed photoreaction, (a) catalyzed photoreaction (b) sensitized photoreaction. 7

Figure 1.4 Schematic photoexcitation in a solid semiconductor. 7

Figure 1.5 Band-edge positions of semiconductor photocatalysts relative to the energy levels of redox couples in water. 9

Figure1.6 Effect of particle size on the migration of charge carriers to the surface of the photocatalyst. 13

Figure 1.7 Nucleation and growth of NPs during synthesis. 14

Figure 1.8 Particles in a colloid (a) in the absence of double layer (b) presence of electrical double layer to prevent agglomeration. 15

Figure 1.9 Steric stabilization of NPs (a) Entropic effect (b) Osmotic effect. 16

Chapter 3

Figure 3.1 Set up of photochemical reactor for photocatalytic studies. 49

Chapter 4

Figure 4.1 XRD pattern of (a) Undoped (b) Mn (0.5%) doped (c) Mn (1%) doped (d) Mn (1.5%) doped (e) Mn (2%) doped with PVP (1%) capped ZnO NPs. 52

Figure 4.2 Transmission Electron Micrograph (TEM) of (a) Mn (1.0%) and (b) Mn (2.0%) doped with PVP (1.0%) capped ZnO NPs. 53

Figure 4.3 UV-Visible absorption spectra of PVP (1.0%) capped and (a) undoped (b) Mn (0.5%) doped (c) Mn (1%) doped (d) Mn (1.5%) doped (e) (2.0%) doped ZnO NPs. 54

Figure 4.4 Band gap of (a) undoped (b) Mn(0.5%) doped (c) Mn (1%) doped (d) Mn (1.5%) doped (e) Mn (2%) doped and capped ZnO NPs. 55

Figure 4.5 Variation of doping of Mn concentration with %age degradation of CV. 56

Figure 4.6 Absorption spectral changes of crystal violet dye aqueous solution (10mg/L) degraded by (a) UV-Visible radiations 57

	only (b) Undoped (c) Mn (1%) doped and (d) Mn (2%) doped and PVP (1%) capped ZnO NPs.	
Figure 4.7	Photodegradation of crystal violet under different conditions, Curves: (a) Without catalyst under UV-Visible (b) with undoped and capped ZnO (c) With Mn (1%) doped and PVP (1%) capped (d) With Mn (2%) doped and PVP (1%) capped ZnO NPs. (Inset presents the difference in degradation efficiency of Mn (1%) and Mn (2%) doped ZnO NPs.	58
Figure 4.8	Change in color of crystal violet dye with Mn (1%) doped and PVP (1%) capped ZnO NPs in UV-Visible radiations at (a) 0min (b) 30min (c) 60min (d) 90min (e) 120min (f) 150min and (g) 180min.	58
Figure 4.9	Kinetics of crystal violet degradation with UV, undoped ZnO, Mn (1%) doped and PVP (1%) capped ZnO and Mn (2%) doped and PVP (1%) capped ZnO NPs.	59
Figure 4.10	Photochemical experiment to observe photo stability of Mn (1%) doped and PVP (1.0%) capped ZnO NPs. Curve (a) First time used Mn (1.0%) doped with PVP (1.0%) capped ZnO NPs (b) Reused Mn (1.0%) doped with PVP (1.0%) capped ZnO NPs (c) Reused after placing 3h in UV-Visible radiations.	61
Figure 4.11	UV-Visible absorption spectra of Mn (1%) doped and PVP (1%) capped ZnO NPs (a) Without UV (b) With UV treatment.	62
Figure 4.12	(a) PL spectra of undoped and Mn (1%) doped ZnO NPs, (b) PL spectra of Mn (1%) doped PVP (1%) capped ZnO NPs with and without UV treatment for 3h excitation at 325nm.	63
Figure 4.13	XRD pattern of Mn (0.5 – 2.0%) doped and TG (1.0%) capped ZnO NPs.	64
Figure 4.14	TEM images of Mn (1.0%) doped ZnO NPs synthesized at (a) pH-6.7 (b) pH-8.0 (c) pH-10.0 and (d) pH-12.0.	65
Figure 4.15	UV-Visible absorption spectra of (a) Mn (0.5-2.0%) doped ZnO NPs (b) Mn (1.0%) doped ZnO NPs synthesized at different pH values.	66
Figure 4.16	Tauc's plot for (a) Mn (0.5-2.0%) doped ZnO at pH-6.7 and (b) Mn (1.0%) doped ZnO NPs synthesized at different pH values.	67
Figure 4.17	PLE spectra of (a) Undoped and (b) Mn(1.0%) doped ZnO	68

NPs at λ_{em} = 468nm.

Figure 4.18 PL emission spectra of (a) Mn (1.0%) doped ZnO NPs synthesized at pH-8.0, 10.0 and 12.0 at λ_{ex} = 325nm and (b) Variation of Mn doping concentration with PL emission intensities. 69

Figure 4.19 (a) Histogram for percentage degradation of CV dye at different conditions under UV-Visible radiations for 1h. Change in optical absorption spectra of CV dye aqueous solution (10 mg/L) with (b) undoped and (c) Mn (1.0%) doped ZnO NPs. 70

Figure 4.20 (a) Photodegradation of CV under different conditions (b) extent of decomposition of CV with respect to time intervals (c) first order kinetics of CV degradation with and without photocatalyst and (d) second order kinetics of CV dye degradation with Mn (2.0%) doped ZnO NPs synthesized at pH-6.7 under UV–Visible radiations. 72

Figure 4.21 (a) Photodegradation of CV dye (b) Extend of decomposition of CV dye (c) First order kinetics of CV degradation with Mn (1.0%) doped ZnO NPs synthesized at pH- 8.0, 10.0 and 12.0. (d) Second order kinetics of CV degradation with Mn (1%) doped ZnO NPs at pH-12.0 and (e) extend of decomposition of CV dye solution at pH-2.0 and 10.0 with Mn (1.0%) doped ZnO NPs synthesized at pH- 6.7 and 12.0. 75

Figure 4.22 (a) Change in concentration (b) Percentage degradation and (c) first order kinetics of degradation of CV dye under the exposure of UV-Visible light radiations with and without synthesized photocatalyst at different pH values (d) second order kinetics of CV dye with Mn (1.0%) doped ZnO at pH-8.0 in the presence of H_2O_2 and (e) Change in color of CV dye with Mn (1.0%) doped ZnO NPs synthesized at pH-12 in the presence of H_2O_2 under UV-Visible light radiations after 0mins and 30mins. 77

Figure 4.23 Change in concentration and percentage degradation of Sirius red F3B dye using Mn (1.0%) doped ZnO NPs at pH-12.0 in the presence of H_2O_2 under UV-Visible light radiations. 79

Figure 4.24 Schematic illustration of a proposed photocatalytic mechanism of Mn doped ZnO NPs synthesized at pH-12.0. 80

Figure 4.25 (a) XRD pattern and (b) Peak shift of Undoped and Cu (1.0% 81

- 5.0%) doped ZnO NPs.

Figure 4.26 TEM images of Cu (3.0%) doped ZnO NPs synthesized at (a) pH-8.0 (b) 10.0 and (c) pH-12.0. 83

Figure 4.27 Energy dispersive spectra of (a) undoped (b) Cu (1.0%) doped (c) Cu (2.0%) doped (d) Cu (3.0%) doped (e) Cu (4.0%) doped and (f) Cu (5.0%) doped ZnO NPs. 84-85

Figure 4.28 UV-Visible absorption spectra of (a) undoped and Cu (1.0% - 5.0%) doped synthesized at (a) pH-8.0 (b) Cu (3.0%) doped ZnO NPs synthesized at pH-10.0 and 12.0 touc's plot for (c) undoped and Cu (1.0% - 5%) doped ZnO NPs synthesized at pH-8.0 and (d) Cu (3.0%) doped ZnO NPs synthesized at pH 10.0 and 12.0. 87

Figure 4.29 PLE spectra of (a) undoped and Cu (3.0%) doped ZnO NPs at λ_{em} = 468nm and PL spectra of (b) undoped and Cu (3.0%) doped ZnO NPs and (c) Cu (1.0-5.0%) doped ZnO NPs at λ_{ex}= 325nm. 89-90

Figure 4.30 Absorption spectral changes of crystal violet dye aqueous solution (10 mg/L) degraded by (a) Undoped (b) Cu (3.0%) doped ZnO NPs synthesized at pH-8.0. 91

Figure 4.31 (a) Photodegradation of crystal violet under different conditions (b) Extent of decomposition of CV dye with respect to time intervals and (c) Kinetics of CV dye degradation with and without photocatalyst synthesized at pH-8.0 under UV-Visible radiations. 93

Figure 4.32 (a) Photodegradation of CV dye with Cu (3.0%) doped ZnO NPs and (b) Extend of decomposition of CV dye with respect to time intervals with Cu (3.0%) doped ZnO synthesized at pH-8.0, 10.0 and 12.0 (c) Change in color of crystal violetdye with Cu (3.0%) doped ZnO NPs at pH-12.0 in UV-visible radiations at (i) 0 min (ii) 30min (iii) 60min (iv) 90min (v) 120min (vi) 150min. 95

Figure 4.33 Kinetics of crystal violet degradation with Cu (3.0%) doped ZnO NPs synthesized at pH-8.0, 10.0 & 12.0. 96

Figure 4.34 Effect of photocatalyst loading on photodegradation of CV dye with Cu (3.0%) doped ZnO NPs. Concentration of CV dye = 10mg/L. 97

Figure 4.35 X-ray diffraction pattern of PVP capped undoped and Cu (1.0-5.0%) doped ZnO NPs. 99

Figure 4.36	TEM images of undoped and Cu (3.0%) doped ZnO NPs.	100
Figure 4.37	UV-Visible absorption spectra of (a) undoped and Cu (1.0% - 5.0%) doped synthesized at (a) pH-8.0 (b) Cu (3.0%) doped ZnO NPs synthesized at pH-10.0 and 12.0.	101
Figure 4.38	Touc's plot for (a) undoped and Cu (1.0% - 5%) doped ZnO NPs synthesized at pH-8.0 and (b) Cu (3.0%) doped ZnO NPs synthesized at pH 10.0 and 12.0.	101
Figure 4.39	(a) Change in concentration (b) Histogram to study the percentage degradation of CV dye and (c) Kinetics of crystal violet degradation with and without photocatalyst synthesized at pH-8.0 under different conditions.	103
Figure 4.40	(a) Change in concentration (b) Histogram to study the percentage degradation of CV dye and (c) Kinetics of crystal violet degradation under Cu (3.0%) doped ZnO NPs synthesized at different pH value.	104

Chapter 5

Figure 5.1	XRD pattern for undoped and doped CeO_2 NPs.	112
Figure 5.2	UV-Visible absorption spectra for undoped and doped CeO_2 NPs.	112
Figure 5.3	Calibration curve of RhB dye.	113
Figure 5.4	(a) Change in concentration and (b) Percentage degradation of RhB dye with undoped and Mn and Cu doped CeO2 NPs.	113
Figure 5.5	(a) XRD pattern and (b) Peak shift of CS0-CS212 NPs.	115
Figure 5.6	Williamson-hall plot for CS0-CS212 NPs.	116
Figure 5.7	TEM images of (a) CS0 (b) CS2 NPs.	118
Figure 5.8	EDS of CS0-CS212 samples.	118-119
Figure 5.9	(a,b) UV-Visible absorption spectra and (c,d) Tauc's plot for CS0-CS3 NPs.	120
Figure 5.10	(a,b) survey before and after doping of ceria (c,d) Ce3d of CS0 and CS2 NPs (e) Ce^{3+} centration on the surface of CS0-CS3 (inset : concentration of oxygen vacancies of CS0-CS3) (f,g) O1s of CS0 and CS2 and (h) Ag(3d) spectrum in CS2 NPs.	122
Figure 5.11	Variations in Ce^{3+} of undoped and Ag doped CeO_2 extracted from XPS data with respect to etching time by using Ar ion beam.	124

Figure 5.12	(a) Change in concentration and (b) percentage degradation of RhB under various conditions.	125
Figure 5.13	Kinetic studies of the photocatalytic degradation of RhB dye under various conditions.	127
Figure 5.14	(a) Percentage degradation of RhB using CS210 and CS212 photocatalysts (inset: Change in color of RhB with CS212) and (b) percentage degradation using CS2 and CS212 photocatalysts with the variation of pH of dye solution.	128
Figure 5.15	Kinetic studies of the photocatalytic degradation of RhB dye with CS210 and CS212 NPs.	129
Figure 5.16	Cyclic runs of RhB degradation using CS212 photocatalyst.	129
Figure 5.17	Photoluminescence emission spectra of CS0-CS3 samples.	130
Figure 5.18	Schematic diagram of the degradation mechanism for RhB dye (red spheres) with CS0 and CS212 NPs under UV-Visible irradiations.	132
Figure 5.19	XRD pattern of CA0-CA412 NPs.	133
Figure 5.20	Peak shift of CA0-CA412 NPs.	134
Figure 5.21	TEM images of (a) CA0 (b) CA4 NPs.	135
Figure 5.22	UV-Visible absorption spectra of (a) CA0-CA4 and (b) CA410 and CA412 NPs.	135
Figure 5.23	Tauc's plot for band gap determination of CA0-CA412 NPs.	136
Figure 5.24	Percentage degradation of RhB under various conditions.	137
Figure 5.25	Kinetic studies of the photocatalytic degradation of RhB dye under various conditions.	138
Figure 5.26	(a) Percentage degradation and (b) Kinetic studies of the photocatalytic degradation of RhB dye with CA410 and CA412 NPs.	139

LIST OF TABLES

Page No.

Chapter 2

Table 2.1 Summery of photocatalytic studies of ZnO by various research groups and their main findings. 23

Table 2.2 Summery of photocatalytic studies of CeO_2 by various research groups and their main findings. 32

Chapter 4

Table 4.1 Reaction rate constant of crystal violet without catalyst, undoped, Mn (1% and 2%) doped with PVP (1%) capped ZnO NPs. 58

Table 4.2 Reaction rate constant of crystal violet without catalyst, undoped, Mn (0.5%, 1.0%, 1.5% and 2.0%) doped and TG (1.0%) capped ZnO NPs synthesized at pH-8.0, 10.0 and 12.0. 78

Table 4.3 Elemental composition of undoped and Cu doped ZnO NPs. 86

Table 4.4 Reaction rate constant of crystal violet without catalyst, undoped, Cu (1.0%, 2.0%, 3.0%, 4.0% and 5.0%) doped and TG (1.0%) capped ZnO NPs at pH-8.0. 94

Table 4.5 Reaction rate constant of crystal violet without catalyst, undoped, Cu (1.0%, 2.0%, 3.0%, 4.0% and 5.0%) doped and TG (1.0%) capped ZnO NPs at pH-8.0. 105

Chapter 5

Table 5.1 Lattice parameter, d-spacing and crystallite size of as synthesized samples**.** 117

Table 5.2 Elemental composition of undoped and Ag doped CeO_2NPs. 119

Table 5.3 Ce^{3+} concentration of various as synthesized undoped and doped samples. 123

Table5.4 Reaction rate constant of RhB dye with and without photocatalyst at different pH. 126

Table 5.5 Reaction rate constant of RhB dye with and without photocatalyst at different pH. 138

PREFACE

The present work deals with the synthesis, characterization and photocatalytic studies of undoped and doped ZnO and CeO_2 nanoparticles (NPs). The entire work is divided into six chapters.

Chapter 1 includes the background of nanomaterials and their unique properties. It describes the need of waste water treatment and different types of techniques involved in this treatment process. Role of semiconductor photocatalyst and mechanism behind the degradation of organic pollutants are discussed in detail. Various parameters like techniques used for modulation of valance band and conduction band, effect of adsorption and pH, source of radiations, charge carrier trapping, photocatalyst size and quantum confinement effect, which affect the efficiency of photocatalyst, are described in this section. Further, the synthesis of nanoparticles, methods to prevent their agglomeration and to stabilize them by various methods has been discussed in detail.

In Chapter 2 details of literature pertaining to ZnO and CeO_2 nanoparticles and their unique properties has been described. Various synthesis routes for fabrication of undoped and doped ZnO and CeO_2 nanomaterials have been given. The photocatalytic properties of these nanomaterials have been described. Various parameters which affect the photocatalytic efficiency of these nanomaterials like types of irradiations, irradiation time, dopant, effect of doping concentrations, capping, morphology, pH nature of dye solution, photocatalyst dosage, variation in dye concentrations, have been discussed in this chapter. Also, the effect of photodegradation efficiency of these nanomaterials with alteration in photoluminescence intensity with capping and doping has been illustrated.

Chapter 3 describes the details of the chemicals used and synthesis procedure adopted to prepare undoped and doped ZnO and CeO_2 nanoparticles. Procedure followed to synthesize NPs at different pH is also discussed. Various characterization techniques used to characterize NPs has been described. The set-up of photochemical reactor and the procedure for photocatalysis of organic dyes has been discussed. At the end of the chapter brief introduction about the pollutants selected for photocatalytic study is provided.

Chapter 4explains the study of doped ZnO nanoparticles (NPs) synthesized by co-precipitation method. Various techniques viz. X-ray diffraction (XRD), transmission electron microscopy (TEM), energy dispersive spectroscopy (EDS), UV-Visible spectroscopy, photoluminescence (PL) emission and excitation spectroscopy has been employed to characterize as synthesized doped and capped NPs. Photocatalytic efficiency of synthesized NPs has been studied by evaluating the degradation of crystal violet (CV) dye under UV-Visible irradiations. Further the effect of pH has also been studied in detail. Here it is important to mention that the pH of NPs has been adjusted during synthesis only.

Chapter 5 describes the study of doped CeO_2 (ceria) nanoparticles (NPs) synthesized by co-precipitation method. Various techniques has been employed to characterize as synthesized doped and capped NPs. Photocatalytic efficiency of synthesized NPs has been studied by evaluating the degradation of rhodamine B (RhB) dye under UV-Visible irradiations. Further the effect of pH has also been studied in detail.

Chapter 6 summarizes the results obtained from various experiments discussed in previous chapters. Effect of morphology, capping agent, dopant and doping concentration, irradiation time and pH of the synthesized NPs (pH adjusted during synthesis) has been summarized. Results obtained from doped and capped ZnO NPs has been concluded. The results obtained from the doped CeO_2 NPs have been also summarized. Based on the results obtained from the present work, some suggestions have been provided at the end of the chapter to carry out more work in this field.

CHAPTER 1

INTRODUCTION

Overview

The present chapter describe about background of nanomaterials and their unique properties. It describes the need of waste water treatment and different types of techniques involved for this treatment process. Role of semiconductor photocatalyst and mechanism behind the degradation of organic pollutants are discussed in detail. Various parameters like techniques used for modulation of valance band and conduction band, effect of adsorption and pH, source of radiations, charge carrier trapping, photocatalyst size and quantum confinement effect, which affect the efficiency of photocatalyst, are described in this section. Further, the synthesis of nanoparticles, methods to prevent their agglomeration and to stabilize them by various methods has been discussed in detail.

1.1 Background

The potential of science and technology on nanoscale has been recognized all over the world for their impact on industrial output. A semiconductor nanocrystal is an emerging area of nanoscience and their unique properties have attracted great attention by researchers during last two decades. Nanoscience is the science that relates to objects with at least one dimension between one and one hundred nanometers in length [1]. Nanotechnology is the application of nanomaterically organized materials owning attractive properties compared to conventional materials at significantly reduced dimensions. Nanotechnology is gaining its application beyond research stage to its commercial use after more than twenty years of basic and applied research [2-4].Main objective of nanotechnology is to control the size of particles in such a way where sharp transitions in basic properties as compared to bulk are observed. Nanoscale materials show behavior which is intermediate between macroscopic and an atomic or molecular system from which they are composed of. Compared to bulk materials, nanomaterials possess enhanced performance properties when they use in similar applications. Due to their reduced dimension and increased surface area, these materials possess new physical and chemical properties which are distinctively different from their bulk counterparts. Nanoparticles are supposed to have nearly half of their atoms contained in top two monolayers, which make optical properties highly sensitive to surface morphology. Control over the structure and movement of electrons and holes has been of special importance for low dimensional optonics and photocatalysis. In semiconductor nanomaterials, when the dimension of material is comparable or smaller than the Bohr radius of exciton the absorption edge is blue-shifted from the bulk bandgap. In transition metalnanoparticles, the increase in the surface-to-volume ratio makes them useful as photocatalyst with high surface reactivity and selectivity.

1.2 Need of waste water treatment

With increasing diversity in industrial products environmental problems related to industrial effluents are becoming more and more complex. The residual dyes originates from different sources like textile industries, pharmaceutical industries, bleaching industries, dyeing, paper and pulp industries etc. introduces a variety of organic pollutants into natural resources of water. Water contamination due to hazardous water soluble organic chemicals and dyes pose a severe threat to environment and excess azo dyes effluents are usually resistant to biodegradation. These organic chemicals and dyes are stable and contain large degree of organics which cause severe ecological problems by depleting the dissolved oxygen of water

and release toxic compounds that are harmful for aquatic life. Increase in population and industrialization has also increase the demand of water for household, industry utilization purpose and for general ecosystems. In developing countries, freshwater scarcity is already in reality. The United Nations has predicted that two-thirds of world's population will live in water-scarce regions by 2025 [4]. Also to fulfill the increased demand of food due to increase in global population, lots of pesticides and herbicides are used in agriculture to increase the production which further affect the quantity and quality of fresh and clean water. The environment regulations are becoming stringent with time to keep the environment friendly for all living beings. Thus, it is the necessity of the day to develop effluents treatment methods to remove harmful chemicals and undesirable color from water. An ideal treatment process for water purification should have a capability to remove all toxic organic components and mineralize it completely without leaving behind any harmful by-products. Scientists and researchers are trying to develop new or improving the existing water purification process to overcome the water pollution problems.

1.3 Technologies for color removal

As the wastewater containing dyes are resistant to aerobic digestion, recalcitrant organic molecules and is very stable to light. It is very difficult to efficiently decolorize the synthetic dye containing wastewater because of their high cost and disposal problems at large scale in various types of industries. There are various methods of treatments to purify contaminated water like biological, thermal, mechanical, chemical or physical treatments or their combinations. Figure 1.1 illustrates the different wastewater treatment methods which are currently in use. Each of these water treatment methods has their own drawbacks. Air stripping process (ASP) and Granular activated carbon (GAC) adsorption are the part of phase transfer process. In air stripping process volatile organic pollutants for aqueous medium is merely transfer from water phase to air phase. It do not destroy the pollutants completely. Also GAC adsorption is used to remove the organic pollutants from wastewater and the spent carbon must be either regenerated or incinerated which convert adsorbed pollutants to innocuous by-products. Biological treatments are also an alternative to other treatments for decolorization and degradation of azo dyes. But they required very large land area and have less flexibility in design and operation. Further biological treatment is incapable of obtaining satisfactory color elimination and also due to their xenobiotic nature azo dyes are not totally degraded [6]. Chlorination, ozonation and advanced oxidation process (AOP) are the parts of chemical process. Chlorination is water disinfection process but it may

form trihalomethane toxic disinfection by-product. So, it is not very much suitable for water purification treatment. Ozonation is supposed to be better alternative to chlorination process as it avoids the formation of disinfection by-products. Disadvantage of ozonation is its short life and its stability is affected by the presence of pH, salts and temperature. Careful monitoring of pH is necessary because ozone decomposition is fast in alkaline medium. Cost is also one of the major drawbacks because continuous ozonation is required due to short half-life [6]. However, it has recently discovered that ozone can generate cancer causing agent. Thus all these processes have their own limitations. Recently developed new technology called Advanced Oxidation Process (AOP) has been considered to be better for waste treatment process as compared to traditional methods. In AOP, short-lived oxygen containing intermediates has been generated such as hydroxyl radical ($OH^{\cdot}$) and superoxide anion free radical ($O_2^{\cdot -}$). These are highly reactive and strong oxidizing agents.

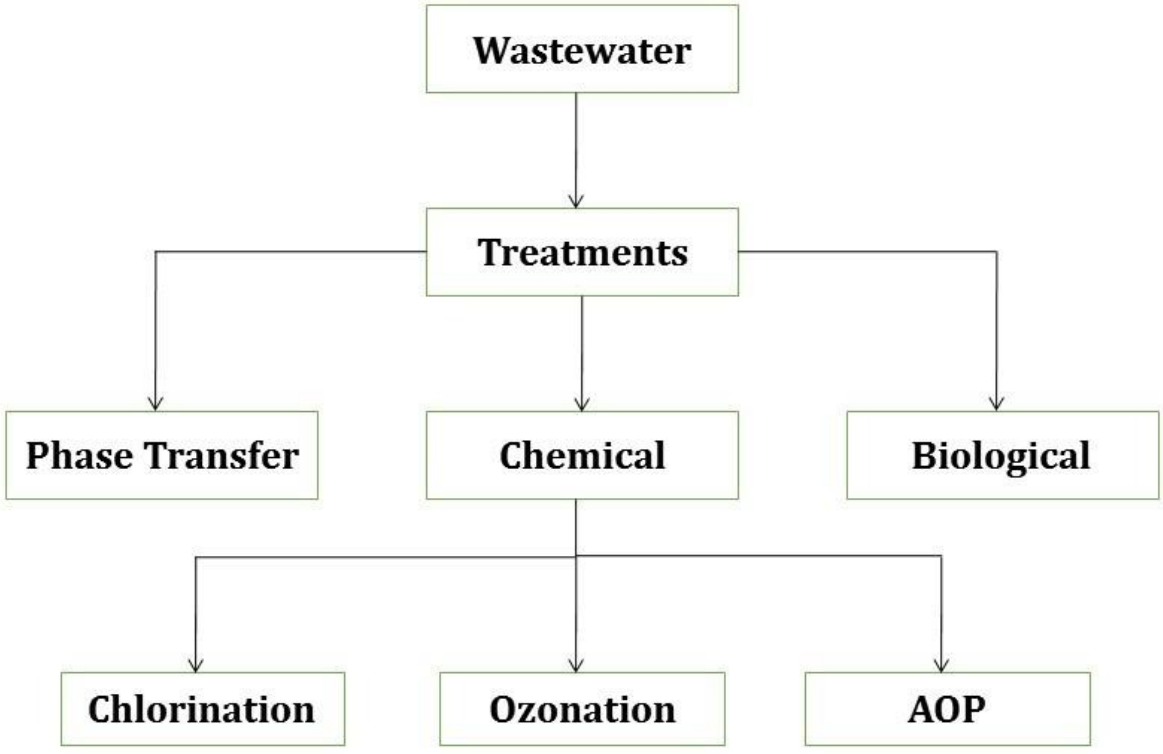

Figure 1.1: Different waste water treatment methods currently in use.

Some of other oxidants such as H_2O_2 or O_3have been also used along with ultra-violet (UV) light radiations to produce highly reactive species to oxidize substances like organic molecules and pesticides. Large number of organic molecules and pesticides can be easily oxidize using AOP which are difficult to treat in other traditional methods discussed above.

1.4 Photocatalysis for waste water treatment

In order to decontamination of waste water it is necessary to adopt more effective reactive systems than the conventional purification processes. Among all AOP processes heterogeneous photocatalysts has high efficiency in degrading wide range of organic contaminants into mineral acids, CO_2 and water [7]. Photocatalysis is defined as a chemical reaction induced by photo-absorption of a solid material which remains chemically unchanged during and after the reaction. In other words the solid acts catalytically without any change in structure or composition under photo-irradiations. Photocatalysis is different from other AOPs because it require light radiations and reusable catalyst without any need of other strong oxidants to generate oxidizing agents like $OH^{\cdot}$ to proceed degradation of complex organic compounds. The hydroxyl radicals can destroy any organic contaminant present in water they can destroy even those pollutants which are characterized by high chemical stability and difficult to mineralized. In photocatalysis solar light is also use for degradation process. The advantages of photocatalysis over other conventional treatment methods are as follows:

1. Almost all organic pollutants in wastewater can be minimized.
2. This process is environmental friendly because the byproducts obtained after degradation of organic pollutants like CO_2, mineral acids etc.are not harmful.
3. External strong and expensive oxidants are not required to generate oxidizing agents for degradation process.
4. Ambient operating conditions, complete degradation of organic pollutants and their intermediate compounds, low operating cost, stability, non-toxicity, insoluble under most conditions, reusable and chemically inert in nature [7].
5. UV, UV-Visible and Visible radiations are used for photocatalyst activation so as to generate strong oxidizing agents for initiation of redox reactions in aqueous medium [8].

A photocatalytic degradation reaction is mainly based on the irradiation of semiconductor particles by light radiations which have energy equal to more than the band gap energy(energy gap between upper level of valance band and bottom of conduction band) of the semiconductor. Upon irradiation of the semiconductor by a suitable light, holes and electrons will generate within the semiconductor. These so generated positive holes and electrons on reaction with H_2O generates strong oxidizing agents like hydroxyl radical ($OH^{\cdot}$), superoxide anion radical ($O_2^{-\cdot}$) to oxidize the adsorbed organic and inorganic compounds.

In the past few decades, semiconductor photocatalysis considered as 'green approach' has received great attention due to its intriguing advantages in water purification, air purification and self-cleaning surfaces.

1.5 Semiconductor photocatalysts

Semiconductor photocatalysis has been considered as a green approach and is particularly used for photocatalytic process because of its favorable combination of electronic structure, non-selectivity, low temperature and non-energy intensive approach for complete mineralization of complex organic and inorganic water pollutants. In semiconductors, the valance band (VB) is an electron filled band and conduction band (CB) is completely vacant. The energy gap between the upper level of VB and lower level of the CB is called forbidden gap or bandgap (E_g). An electron is excited from VB to CB by photo-irradiations of energy equal to or greater than bandgap energy. The bandgap is different for different semiconductors so the excitation energy for electron from VB to CB is different for different for semiconducting materials. However the CB is partially filled therefore the electron can move freely through the lattice of the semiconductor. On the other side, the resulting vacancy created due to excitation of electron can move freely in the VB which is partially filled now. The process of excitation of electron and thus creation of electron and hole is shown in Figure 1.2.

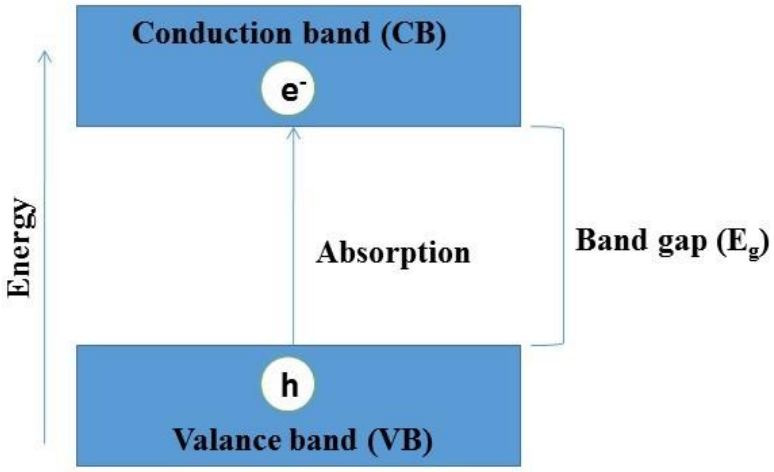

Figure 1.2: Generation of electron-hole pair in semiconductor materials.

The process of photocatalysis is mainly divided into two categories depending upon initial excitation. In the first case photoexcitation takes place in an adsorbate (dye molecule). The nanoclusters act as a mediator for charge transfer. This process is referred as catalysed

photoreaction. Figure 1.3(a) shows the mechanism of catalysed photoreaction. In second case, charge-separation in semiconductor nanoparticles occur when light excite their bandgaps. Photogenerated electrons and holes pairs are capable of oxidizing/reducing adsorbed substrate. This process is referred as sensitized photoreaction. Figure 1.3(b) shows sensitized photoreaction mechanism [9].

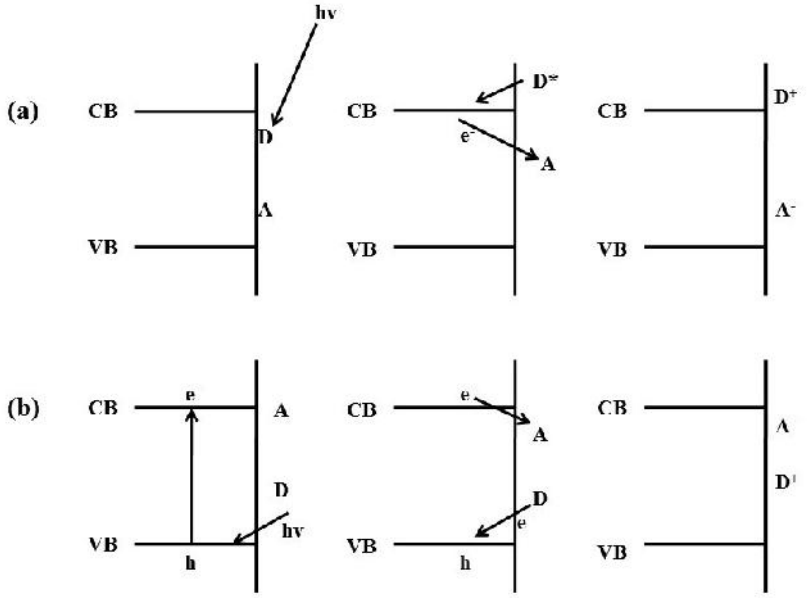

Figure1.3: Catalyzed photoreaction, (a) catalyzed photoreaction (b) sensitized photoreaction [9].

1.6 Heterogeneous photocatalysis

Unlike metals, semiconductors possess a void energy region where no energy levels are

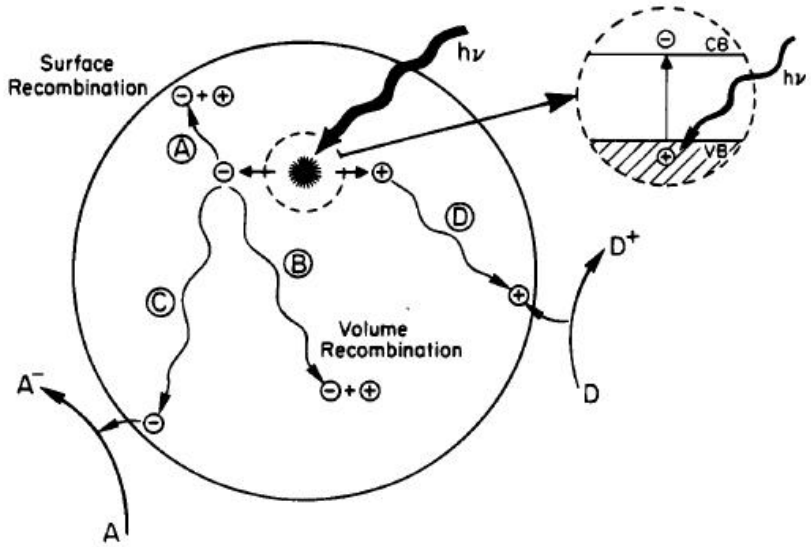

Figure 1.4: Schematic photoexcitation in a solid semiconductor [9].

available to promote recombination of an electron and hole produced by photo-activation in the solid. The void region extends from the top of the filled VB to the bottom of the vacant CB is called the bandgap. Once excitation occurs across the bandgap there is a sufficient lifetime for the created electron-hole pair to undergo charge transfer to adsorbed species on the semiconductor surface. If the semiconductor remains intact and the charge transfer to the adsorbed species is continuous and exothermic in nature, the process is termed heterogeneous photocatalysis. The generation of electron-hole pairs is an initial process for heterogeneous photocatalysis of organic and inorganic compounds by semiconductor particles. The enlarge section of Figure 1.4 represent the excitation of electron from VB to CB initiated by light absorption having energy equal to greater than bandgap energy of the semiconductor material. The concentration electron-hole pairs in semiconductor particle depend upon the intensity of incident radiations and their recombinations.

Upon excitation, the fate of the separated electron and hole can follow several pathways. Figure 1.4represents some of the de-excitation pathways for the electrons and holes in semiconductor. The photo-excited electron transfer to adsorbed organic or inorganic species results from migration of electrons and holes to the semiconductor surface. The electron transfer process is more efficient if the species are pre-adsorbed on semiconductor surface [10]. While at the surface, semiconductor can donate electrons to reduce an electron acceptor which is usually oxygen in an aerated solution (pathway C). On the other hand hole can migrate to the surface where an electron from a donor species can combine with the surface hole oxidizing the donor species (pathway D).The probability and rate of the charge transfer processes for electrons and holes depends upon the respective positions of the band edges for the CB and VB and the redox potential levels of the adsorbate species. Also, electron and hole recombination is in competition with charge transfer to adsorbed species. Recombination of the separated electron and hole occurs in the volume (pathway B) or on the surface of the semiconductor particle (pathway A)with the release of heat. The photogenerated charge carriers, which migrate towards the surface of the photocatalyst, participate in various redox reactions with adsorbed species such as water, oxygen and other organic and inorganic species. Various redox reactions participated by photogenerated charge carriers due to excitation of photocatalyst are as follows:

Photocatalyst + hν $\rightarrow e^{-}_{CB} + h^{+}_{VB}$ …….. 1.1

$OH^{-}_{surface} + h^{+} \rightarrow OH^{\cdot}$ …….. 1.2

$H_2O + h^{+} \rightarrow OH^{\cdot} + H^{+}$ …….. 1.3

$O_2 + e^- \rightarrow O_2^-$ …….. 1.4

$O_2^- + e^- + 2H^+ \rightarrow H_2O_2$ …….. 1.5

$2O_2^- + 2H^+ \rightarrow O_2 + H_2O_2$ …….. 1.6

$H_2O_2 + e^- \rightarrow OH^- + OH^\cdot$ …….. 1.7

The resulting OH^- and O_2^- species are strong oxidizing agents and they help in mineralization of organic and inorganic pollutants in waste water [11].The recombinations of electron-hole pair generated should be very small for effective degradation of adsorbed organic or inorganic compounds on the surface of photocatalyst. There are various factors which affect the efficiency of photocatalytic process and are discussed below.

1.6.1 Energy band configuration

Nanomaterials have emerged as pioneering photocatalysts. Nanomaterials can provide abundant surface states, diverse morphologies and large surface area.

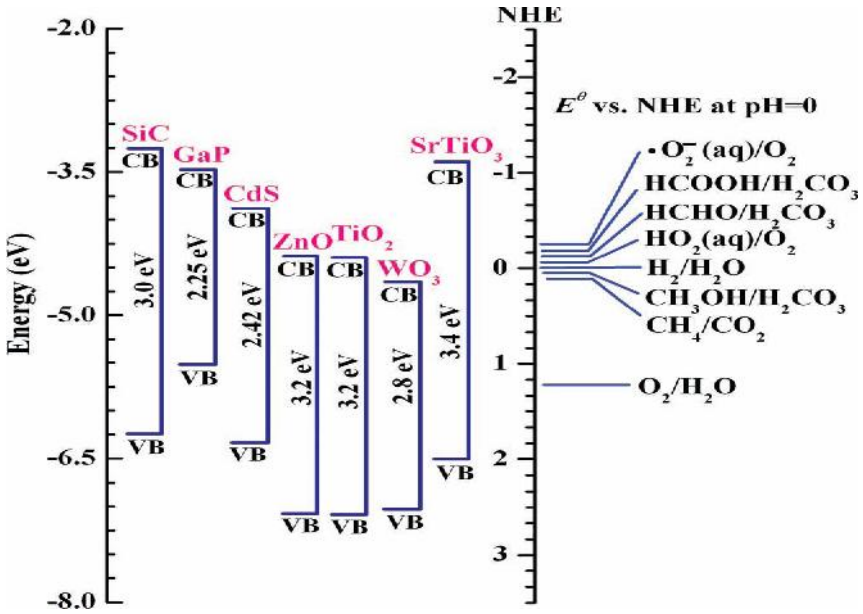

Figure 1.5: Band-edge positions of semiconductor photocatalysts relative to the energy levels of redox couples in water [12].

Most important property for effective photocatalysis is its energy band configuration. It determines the absorption of incident photons, photoexcitation of electron-hole pairs, migration of charge carriers and the redox capabilities of the photogenerated charge carriers [12]. For thermal requirement, the potential level of acceptor species must be below (more positive) the semiconductor CB potential to accept the electron donated by the semiconductor and that of donor species needs to be above (more negative) the VB potential of the

semiconductor to donate an electron to the vacant hole [9]. The band edges of various semiconductor photocatalysts are presented in Figure 1.5.Band edge positions of semiconductor photocatalysts shown in Figure 1.5 are at pH=0. Here it should be noted that the band edge positions of the various semiconductors also influenced by pH of an electrolyte solution as compared to redox potentials of the adsorbate.

1.6.2 Modulation of valance band and conduction band

Since the energy band configuration directly affects the photocatalytic efficiency of a semiconductor photocatalyst and the direct and narrow band gap semiconductors are more likely to exhibit high absorbance of low energy photons. But the disadvantage of these types of semiconductor is the high recombination probability of photo-excited electron-hole pairs and the band edge positions are incompatible with electrochemical potential that is necessary to commence photocatalytic reactions. In most of metal oxide semiconductors, the VB maxima are significantly positive with respect to water and CB minima are slightly negative than reduction potential of water. Also the inter-particle electronic coupling of semiconductor materials is effective for reconstruction of energy band and bandgap narrowing [13]. Therefore in order to modulate VB band edge positions in precise manner, three techniques are proved to be most effective. These involve doping with 3d-transition elements, cations with d^{10} or $d^{10}s^2$ configurations and non-metal element.

Earlier sensitizing of metal oxide semiconductor to visible light by doping with 3d-transition elements attracted considerable attention [14-16].Theoretical studies based on ab-initio band structure calculations showed that the increase in dopant atomic number shifts the localized 3d levels to lower energy. Thus, the split 3d states can mix with the CB or VB, and can insert a new band into the original bandgap [17].However, doping with 3d-transition elements can have two critical disadvantages which restrict its applicability. Firstly, foreign elements introduce considerable bulk defects and thus increase the recombination probability of photogenerated electron-hole pairs. Secondly, the localized d-states in the electronic structure suppress the migration of charge carriers. Doping of cations with d^{10} or $d^{10}s^2$ electronic configurations such as Ag^+, Pb^{2+} and Bi^{3+} in metal oxides can introduce occupied d or s-states into the VB [18-20]. Hybridization of these d/s states with oxygen 2p states contributes to an up-shift of the top of the VB and therefore to a narrowing of the bandgap. The other strategy used to raise the VB maximum of metal oxide semiconductor is to introduce different anions on the O sites by doped with N, C, B and S [21-24]. However, very small enhancement in light absorption has thus far been obtained. With N-doping, the light-absorption edge remains

almost the same as in the undoped material and doping with C, B and S narrows the bandgap by less than 0.3 eV. Because the level of the CB is closely related to the capability of reducing H_2O and O_2 and therefore the CB modulation also receive attention. When the CB is at a suitable level, photoexcited electrons in the CB can reduce H^+ to produce H_2 or combine with O_2 to form oxidative $\bullet O_2^-$ radical for water splitting and the elimination of organic contaminants. It should be noted that the level of the CB determines whether these reactions can proceed and how efficient these processes are. Therefore, adjustment of the CB should be performed carefully. The substitution of alkali metal or alkaline earth metal elements lower in the periodic table is known to be effective in lowering the minimum of the CB [25-26]. Doping is done to achieve modulation in band gap of the photocatalyst. The dopants form their own energy band in energy gap of host photocatalyst and thus reduce the effective band gap. Narrow band gap semiconductors are more likely to exhibit high absorbance of low energy photons. Thus the doping increases the photocatalytic activity by scavenging electrons that reduce the recombination and favors the formation of $OH^{\cdot}$ which could enhance the photocatalytic process.

The mechanism of photocatalytic activity on ceria is a subject under exploration. The expected reasons revolve around their high oxygen storage capacity (OSC) which is due to the multivalent nature of cerium and the high mobility of the oxygen vacancies at the surface of the materials. The shift between Ce (III) and Ce (IV) states leads to a high oxygen mobility in ceria lattice, which in turn can lead to its enhanced photocatalytic activity. The formation of oxygen vacancies results due to decrease in oxygen contents in cerium oxide. The oxygen vacancies increase with rise in Ce^{3+} fraction in ceria lattice in order to maintain electroneutrality. Oxygen vacancies reduce the electron-hole recombinations and thus help to enhance the photocatalytic activity of the photocatalyst.

1.6.3 Effect of adsorption and pH

Photocatalytic degradation of organic compounds varies with adsorption of organic compounds over photocatalyst surface. Also adsorption affects the mechanism involved in degradation process. Adsorption directly linked with the surface charge of organic compound and photocatalyst surface. Adsorption varies with concentration of organic compounds, pH of dye and the photocatalyst and loading of photocatalyst. Initially with increase in dye (organic compound) concentration, the degradation increases. But increasing the concentration of dye molecule beyond the optimum limits the degradation starts decreasing. Because as the dye concentration increases the number of photons approaching the photocatalyst surface

decreases due to decrease in exposed area of photocatalyst. Which further reduce the generation of electron-hole pairs and hence reduces the formation of strong oxidizing agents required for degradation of dye molecule. Adsorption can also be modulated by varying the pH of dye or photocatalyst. It will facilitate more or less number of dye molecules to get adsorbed on the surface of photocatalyst depending upon the surface charge of both the dye and the photocatalyst. Also, the loading of photocatalyst affect the degradation of organic compounds. The degradation increase upto a certain loading of photocatalyst because of increase in photocatalyst particles for adsorption of dye molecules. But further increase in photocatalyst shows the reverse effect because of increase in turbidity which reduces the penetration of light radiation in the slurry and hence the photoexcitation of charge carriers in the semiconductor materials, the primary step for photocatalytic degradation of organic compounds.

1.6.4 Source of radiations

Radiation sources play a key role in the performance of photocatalytic reaction. The choice of particular lamp is made on the basis of the photoexcitation energy requirement of particular photocatalyst. Since the photocatalyst is solid particles and suspended in solution, so during the design of photocatalytic reactor the opacity, distribution, scattering effect and depth of penetration of radiation are to be taken into account in selection of lamp. The proper shape with proper radiation spectra of lamp is also required to be considered in the photocatalytic reactor design.

1.6.5 Charge carrier trapping

It is necessary to retard photoexcited electron-hole pair recombination for better charge transfer process to photocatalyst surface so that photocatalytic reaction can occur efficiently. Charge carrier trapping suppresses recombinations and thus increase the life time of photoexcited electron-hole pairs to above a fraction of nanosecond. During synthesis an ideal crystal lattice of a semiconductor can never be produced, however, surface and bulk irregularities naturally occur during preparation process. These irregularities associated with surface electron states have different energy from the bands present in the bulk semiconductor. The electron states serve as charge carrier trap states and thus suppress the probability of electron-hole recombination. Thus the competition between the recombination and charge carrier trapping followed by the competition between recombination of trapped carriers and interfacial charge transfer determine the overall efficiency of interfacial charge transfer [27].

1.6.6Photocatalyst size and quantum confinement effect

Crystal structure, particle size and crystallinity strongly affect the separation and migration of photogenerated carriers to the surface of the photocatalyst. As shown in Figure 1.6 the photoexcited charge carriers have to travel longer distance to reach at surface active sites.

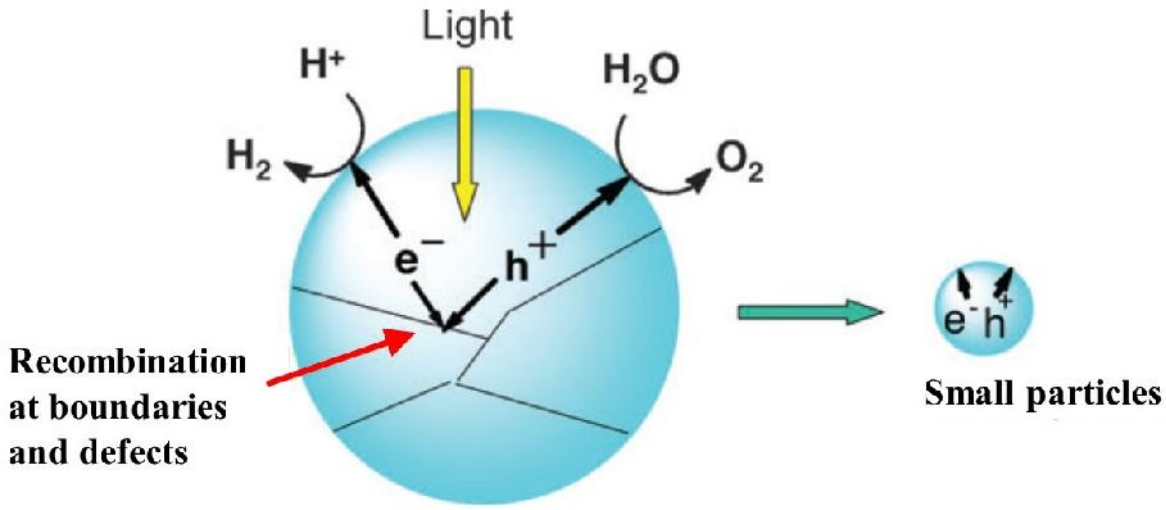

Figure 1.6: Effect of particle size on the migration of charge carriers to the surface of the photocatalyst [28].

As a result, they recombine at boundaries and defects before they reach to the active site at the surface to participate in redox reactions. However, this effect can be minimized by making the particle size to be very small. By reducing the particle size, the distance that photogenerated charge carriers have to travel to migrate towards reaction sites become short and this decrease in recombination probability. Thus by reducing the particle size, large number of charge carriers are available at the surface active sites and photocatalysis of organic compounds could be made easily and rapidly. Semiconductors exhibit size dependent structural, optical and photocatalytic properties when their size becomes smaller than Bohr exciton radius. When the radius the particle approaches to Bohr radius, the exciton in the particle experience a spatial confinement and can exist in the particle when it is in the state of higher energy which leads to an increase in energy gap of semiconductor. At this stage the energy bands splits into discrete energy levels. This phenomenon is called quantum confinement effect [29]. Mathematically the increase in bandgap energy (ΔE_g) varies with particle radius (R), reduced effective mass (μ) and dielectric constant (ε) by the relation as [30]

$$\Delta E_g = h^2/ 8\mu R^2 - 1.8e^2/ \varepsilon R \qquad .....(1.8)$$

Where h is Planck's constant ($h = 6.626 \times 10^{-34}$ Js)

$$\mu = m_e^{-1} + m_h^{-1}$$

Quantum confinement effect affects the radiative and non-radiative electronic transitions of nanoparticles (NPs). Thus in NPs the fractions of atom present at the surface are very large as compared to their bulk counterpart which is highly recommended for photocatalysis. The increase in surface-to-volume ratio causes enhanced reactivity and selectivity. Thus with decrease in particle size, greater number of photogenerated electron-hole pairs migrate to the surface active sites of the photocatalyst thus reduces the volume recombination which dominantly occur in bulk semiconductor particles. Thus the particle size plays a crucial role for photocatalysis of various organic and inorganic compounds.

1.7 Synthesis

During last decade, there has been an explosive growth of nanoscience and technology because of the availability of new methods of synthesizing nanomaterials, as well as tools for characterization and manipulation. Controlling various parameters like size, shape and structure of nanoparticles is technologically important because they have strong correlation with optical, electrical, magnetic and photocatalytic properties [31].

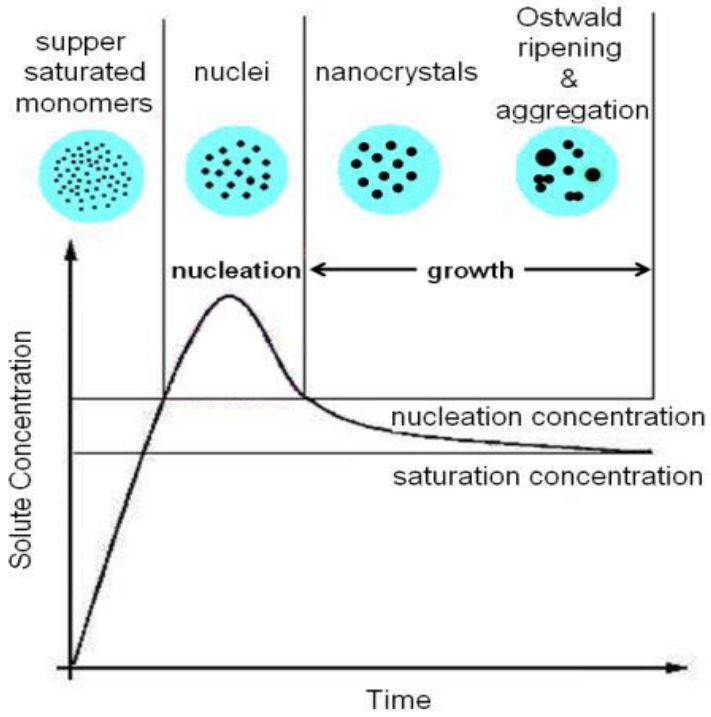

Figure 1.7: Nucleation and growth of NPs during synthesis [32].

The conventional approach for the synthesis of nanoparticles involves chemical or physical attrition from bulk into objects of desired sizes and shapes and is referred as the “top-down”

approach. Inverse to the “top-down” approach involving the assembly of materials from molecular levels to form micro or macro-sized shapes and structures, often referred as “bottom-up” approach or “self-assembly” [31]. Wet chemical synthesis involving colloids is the most energy efficient “bottom up” technique for the synthesis of semiconductor nanoparticles. The chemical synthesis has the advantages of producing size-controlled, un-agglomerated nanoparticles. During synthesis of nanoparticles by chemical precipitation technique, initially formed products are termed as seed. Further, growth in the size of seeds due to agglomeration form nanocrystallites in a thermodynamically controlled manner. If this growth is not controlled then due to Vander Waals interactions and Ostwald ripening between the particles, they will result in agglomeration and will finally settle down. Figure 1.7 shows the nucleation and growth mechanism during synthesis of nanoparticles. The agglomeration of NPs is highly undesirable for their potential use in photocatalysis.

1.7.1 Surface modification of nanoparticles

Particles in the nanometer range have a strong tendency to agglomerate due to Vander Waals interactions. Therefore it is important to develop synthetic methods by which the particles can be stabilized, that is, where repulsive forces between the particles can be provided to balance this attraction Figure 1.8(a).

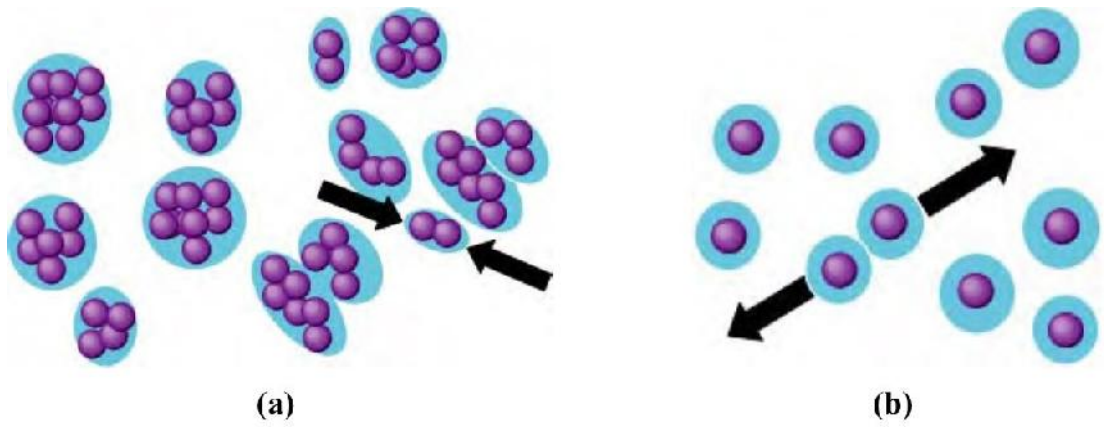

Figure 1.8: Particles in a colloid (a) in the absence of double layer and (b) presence of electrical double layer to prevent agglomeration [31].

Generally two types of stabilization are used to prevent agglomeration namely, electrostatic stabilization and steric stabilization by adsorbed molecules or steric hindrance. Electrostatic stabilization involves the creation of an electrical double layer arising from ions adsorbed on the surface and associated counter ions that surround the particle. If the electric potential

associated with the double layer is sufficiently high, the coulombic repulsion between the particles prevents their agglomeration Figure 1.8(b). The steric stabilization of colloidal particles can be achieved by the adsorption of large molecules such as polymers on the surface of the particles. The stabilization of dispersed particles by an adsorption of polymer layer over them is termed as steric stabilization.

Actually the coil dimensions of polymers are usually larger as compared to the range over which the attraction forces between colloidal particles are larger. Two types of effects namely volume restriction contribution and osmotic diffusion describe this type of stabilization. First effect describes the fact that the adsorbed molecule restricted in motion decrease the configurationally entropic contribution to the free energy (Figure 1.9(a)). Second, when two particles containing an adsorbed polymer layer approach each other, the polymer layers overlaps that results some compression. This causes an increase of local segment density of the polymer chains in overlap region. This increase in local segment density results strong repulsion which result in increase in osmotic pressure in this region. This phenomenon is known as osmotic repulsion (Figure 1.9(b)).

The capping reduces the agglomeration of semiconductor photocatalyst during synthesis and thus helps in controlling the size of synthesized NPs. As nanosized mono dispersed NPs have high surface to volume ratio and thus are more active for photocatalytic processes.

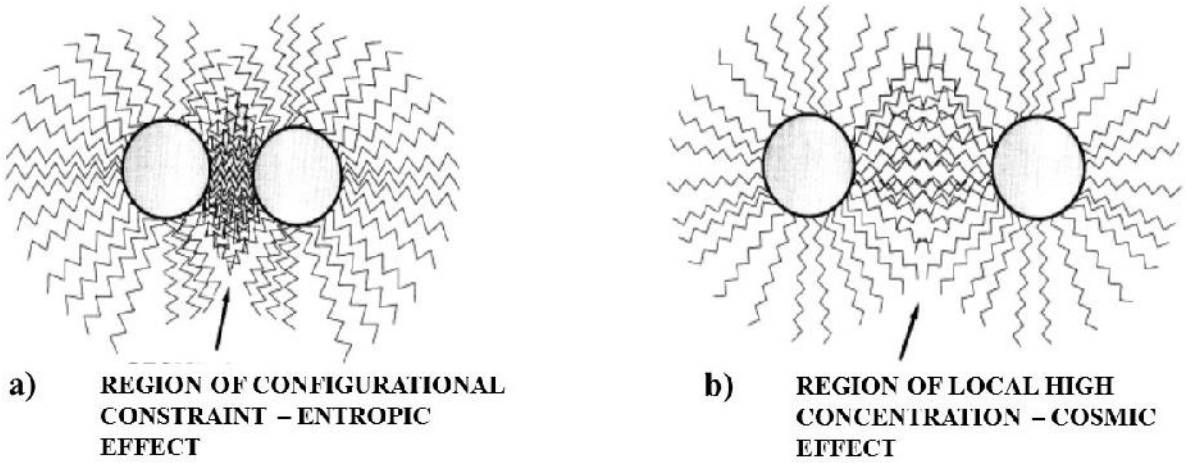

Figure 1.9: Steric stabilization of NPs (a) Entropic effect and (b) Osmotic effect.

References

[1] G. Cao, Nanostructures & Nanomaterials: Synthesis, Properties & Applications; Imperial College Press, (2004).

[2] C. N. Rao, A. Muller, A. K. Cheetham, The Chemistry of Nanomaterials: Synthesis, Properties and Applications, Wiley-VCH, Weinheim, **1** (2004).

[3] A. P. Alivisatos, T. D. Harris, P. J. Carroll, M. L. Stiegerwald, L. E. Brus, Electron-vibration coupling in semiconductor clusters studied by resonance Raman spectroscopy, J Chem. Phys., **90** (1989) 3463.

[4] T. J. Bukowski, and J. H. Simmons, Quatum Dot Research: Current State and Future Prospects, Critical Review in Solid state and Materials Sciences, **27** (2002) 119-142.

[5] J. Ganoulis, Risk Analysis of Water Pollution 2nd Edition. WILEY-VCH. **Chapter 1**(2009) 1-29.

[6] T. Robinson, G. McMullan, R. Marchant, P. Nigam, Remediation of dyes in textiles effluent: a critical review on current treatment technologies with a proposed alternative, Bioresource Technology, **77** (2001) 247-255.

[7] M. N Chong, B. Jin, C. W. K. Chow, C. Saint, Recent developments in photocatalytic water treatment technology: A review. Water Research, **44** (2010) 2997-3027.

[8] C. Minero, G. Mariella, V. Maurino, D. Vione and E. Pelizzetti, Photocatalytic Transformation of Organic Compounds in the Presence of Inorganic Ions. 2. Competitive Reactions of Phenol and Alcohols on a Titanium Dioxide-Fluoride System, Langmuir, **16** (2000) 8964-8972.

[9] A. L. Linsebigler, G. Lu and Jr. J. T. Yates, Photocatalysis on TiO2 Surfaces: Principles, Mechanisms and Selected Results, Chemical Reviews, **95** (1995) 735-758.

[10] R.W. Matthews, Kinetics of Photocatalytic Oxidation of Organic Solutes over Titanium Dioxide, J. Catal., **111** (1988) 264-272.

[11] C. A. K. Gouvea, F. Wypych, S. G. Moraes, N. Duran, N. Nagata, P. P. Zamor, Semiconductor-assisted photocatalytic degradation of reactive dyes in aqueous solution, Chemosphere, **40** (2000) 433-440.

[12] H. Tong, S. Ouyang, Y. Bi, N. Umezawa, M. Oshikiri, and J. Ye, Nano-photocatalytic Materials: Possibilities and Challenges, Adv. Mater., **24** (2012) 229–251.

[13] H. Tong, N. Umezawa, J. H. Ye, Visible light photoactivity from a bonding assembly of titanium oxide nanocrystals, Chem. Commun., **47** (2011)4219-4221.

[14] H. Yamashita, Y. Ichihashi, M. Takeuchi, S. Kishiguchi, M. Anpo, Characterization of metal ion-implanted titanium oxide photocatalysts operating under visible light irradiation, J. Synchrotron Radiat.,**6** (1999) 451-452.

[15] J. M. Herrmann, J. Disdier, P. Pichat, Effect of chromium doping on the electrical and catalytic properties of powder titania under UV and visible illumination, Chem. Phys. Lett., **108** (1984) 618-622.

[16] E. Borgarello, J. Kiwi, E. Pelizzetti, M. Visca, M. Gratzel, Sustainable water cleavage by visible light, J. Am. Chem. Soc., **103** (1981) 6324-6329.

[17] T. Nishikawa, Y. Shinohara, T. Nakajima, M. Fujita, S. Mishima, Prospect of Activating a photocatalyst by Sunlight - A Quantum Chemical Study of Isomorphically Substituted Titania, Chem. Lett.,**28** (1999) 1133-1134.

[18] S. X. Ouyang, N. Kikugawa, Z. G. Zou, J. H. Ye, Effective decolorizations and mineralizations of organic dyes over a silver germanium oxide photocatalyst under indoor-illumination irradiation Appl. Catal. A-Gen., **366** (2009) 309-314.

[19] S. X. Ouyang, H. T. Zhang, D. F. Li, T. Yu, J. H. Ye, Z. G. Zou, Electronic Structure and Photocatalytic Characterization of a Noval Photocatalyst $AgAlO_2$, J. Phys. Chem. B, **110** (2006) 11677-11682.

[20] T. Kako, J. H. Ye, Comparison of photocatalytic activities of two kinds of lead magnesium niobate for decomposition of organic compounds under visible-light irradiation. J. Mater. Res., **22** (2007) 2590-2597.

[21] R. Asahi, T. Morikawa, T. Ohwaki, K. Aoki, Y. Taga, Visible-Light Photocatalysis in Nitrogen-Doped Titanium Oxides, Science, **293** (2001) 269-271.

[22] S. Sakthivel, H. Kisch, Angew. Daylight Photocatalysis by Carbon-Modified Titanium Dioxide, Chem. Int. Ed., **42** (2003) 4908-4911.

[23] W. Zhao, W. H. Ma, C. C. Chen, J. C. Zhao, Z. G. Shuai, Efficient Degradation of Toxic Organic Pollutants with $Ni_2O_3/TiO_{2-x}B_x$ under Visible Irradiation, J. Am. Chem. Soc., **126** (2004) 4782-4783.

[24] X. B. Chen, C. Burda, The Electronic Origin of the Visible-Light Absorption Properties of C-, N- and S-Doped TiO_2 Nanomaterials, J. Am. Chem. Soc., **130** (2008) 5018-5019.

[25] J. Yin, Z. G. Zou, J. H. Ye, A Noval Series of the New Visible-Light-Driven Photocatalysts $MCo_{1/3}Nb_{2/3}O_3$ (M= Ca, Sr and Ba) with Special Electronic Structures, J. Phys. Chem. B, **107** (2003) 4936-4941.

[26] W. F. Zhang, J. W. Tang, J. H. Ye, Structural, photocatalytic, and photophysical properties of perovskite $MSnO_3$ (M= Ca, Sr, and Ba) photocatalysts, J. Mater. Res., **22** (2007) 1859-1871.

[27] M. R. Hoffmann, S. T. Martin, W. Choi and D. Bahnemann, Environmental applications of semiconductor photocatalysis, Chemical Review, **95** (1995) 69-96.

[28] A. Kudo and Y. Miseki, Heterogeneous photocatalyst materials for water splitting, Chemical Society Review, **28** (2009) 253-278.

[29] S. V. Gaponenko, P. L. Knight, A. Miller, Optical Properties of Semiconductor Nanocrystals, Cambridge University Press (2005).

[30] R. M. Mohamed, D. L. Mckinney, W. M. Sigmund, Enhanced nanocatalysts, Materials Science and Engineering R, **73** (2012) 1-13.

[31] J. Dutta and H. Hofmann, Self-organization of colloidal nanoparticles, in: H. S. Nalwa (Ed.), Encyclopedia of Nanoscience and Nanotechnology, American Scientific Publisher, California, CA, **9** (2004) 617-640.

[32] J. deMello and A. demello, Microscale reactors: nanoscale products. Lab Chip, **4** (2004) 11N-15N.

CHAPTER 2

LITERATURE REVIEW

Overview

The present chapter describesthe details of literature pertaining to ZnO and CeO_2 nanoparticles and their unique properties. Various synthesis routes have been used for fabrication of undoped and doped ZnO and CeO_2 nanomaterials have been given. It provides the photocatalytic properties of these nanomaterials. Various parameters which affect the photocatalytic efficiency of these nanomaterials like types of irradiations, irradiation time, dopant, effect of doping concentrations, capping, morphology, pH nature of dye solution, photocatalyst dosage, variation in dye concentrations, have been discussed in this chapter. Also, the effect of photodegradation efficiency of these nanomaterials with alteration in photoluminescence intensity with capping and doping has been illustrated.

2.1 Introduction

2.2 Zinc Oxide (ZnO)

Zinc Oxide (ZnO) crystallizes commonly in a wurtzite structure (space group $P6_3mc$, a=3.25 Å, c=5.20 Å) having a direct bandgap of 3.37 eV with large excitonic binding energy (60 meV), which is even larger than the thermal energy at room temperature (RT) [1-2]. The specific physicochemical and optoelectronic properties of ZnO stimulates and its feasible application in various disciplines such as photocatalysis, light emitting diodes, solar cells, gas sensors, luminescent materials, pigments, UV shielding materials, surface acoustic wave filters, actuators, spin electronics, short-wavelength optoelectronic devices, varistors, antifungal, and piezodielectric nanogenerators is well known [3-5]. The admirable attributes of ZnO such as inexpensiveness, high redox potential, non-toxicity, high photosensitivity, large bandgap offering an excellent driving force to induce redox reactions, mechanical-thermal stability, versatility in synthesis with hierarchical morphology, ease of crystallization, anisotropic growth and natural abundance manifests its scope in the photocatalysis has been well studied. The refractive index of ZnO is 2.0 hence ZnO scarcely scatters light, thereby making it colorless and boost the transparency. The emission properties of ZnO have made possible to set up an original catalytic system able to 'sense and shoot'the environmental contaminants and thus motivating further exploration on the properties of ZnO [8].

The presence of intrinsic impurities in ZnO, the electron mobility (200 – 300 $cm^2V^{-1}s^{-1}$) and electron lifetime (> 10 s) of ZnO is very high which reduces the electrical resistance and promotes the electron transfer efficiency [9-10]. Therefore, high concentration of photogenerated charge carriers transfer to the surface contributes to an efficient photocatalysis. The position of VB (+3.06 V) of ZnO is such that the hydroxyl radical generated in it has high oxidation potential and the electron derived from the ZnO CB is believed to be more negative (at pH 0 *vs.* NHE). The ZnO absorbs a large fraction of UV spectrum and more light quanta thus exhibiting a better performance for pollutant treatment under the light illumination [11]. The surface band of ZnO is upward bent in air which indicate that its built in electric field direction is from inner to outer facilitating the hole migration to particle surface, while electrons diffuse to the bulk of particle [12]. The presence of various types of defects like oxygen vacancies, zinc interstitials, oxygen interstitials, and generation of hydrogen peroxide, superoxide and hydroxyl radicals on the ZnO surface are reported to be responsible for photocatalytic activity [2, 13-15].

2.3 Photocatalysis with ZnO nanomaterials

Guo et al. [16] synthesized wurtzite ZnO nanocrystals using the polymer PVP for surface passivation.They studied the effect of molar ratio of Zn(II)/PVP on the luminescence properties and found that molar ratio of Zn(II)/PVP = 5:3 showed the most intense near band-edge luminescence with only a weak green luminescence, whereas the green luminescence was significantly enhanced in the ZnO nanoparticle sample with no PVP modification. This result has led to believe that the green emission is due to the surface traps, e.g., oxygen vacancy and the UV emission band may be ascribed to surface shallow traps or dark excitons. Mclaren et al. [17] varied the olaic acid (OA) and zinc acetate ratio to synthesize ZnO NPs and found that an increase in the solvent/OA molar ratio (decreasing OA concentration) led to an increase in average NPs size. They showed that the exposure of a greater proportion of polar faces leads to greater photocatalytic activity. The OH^- ions preferentially adsorb onto this face because of its positive charge. This leads to a greater rate of production of $OH\cdot$ radicals and thus the degradation of the dye, during the photocatalysis.

Hong et al. [18] prepared ZnO nanoparticles with an average diameter of 20 nm and grafted Polystyrene (PSt) in it. The photocatalytic degradation of methyl orange (MeOr) using ZnO nanoparticles were observed for 5 h at MeOr concentration of 20 ppm and a catalyst concentration of 1.5 g/L, a pH of 7.0 at 30 °C. The photodegradation of MeOr followed pseudo first-order reaction and bare ZnO nanoparticles showed high photocatalytic activity in photodegradation of MeOr under UV irradiation. The photocatalytic activity of ZnO nanoparticles for some other azo dyes was also very high. Surface modification of ZnO nanoparticles by polystyrene improved the compatibility of the inorganic nanoparticles but reduced the photocatalytic activity of the modified ZnO NPs. Salehi et al. [19] have investigated the dye adsorption properties of novel biocompatible composite Chitosan–zinc oxide nanoparticle (CS/n-ZnO). Equilibrium and kinetic studies were done for the adsorption of Direct Blue 78 (DB78) and Acid Black 26 (AB26) from aqueous solutions onto CS/n-ZnO. They showed that zinc oxide nanoparticles were immobilized onto Chitosan and CS/n-ZnO could be effectively used as a biocompatible composite adsorbent for the removal of anionic dyes. The adsorption kinetics studies of dyes performed were based on pseudo-first order, pseudo-second order and intraparticle diffusion rate mechanism. The results indicated that the adsorption kinetics of dyes on CS/n-ZnO followed the pseudo-second order kinetics and CS/n-ZnO being a biocompatible and eco-friendly adsorbent with relatively large adsorption

capacity which might be a suitable alternative for elimination of dyes from colored aqueous solutions.

Eskizeybek et al. [20] have synthesized polyaniline (PANI) homopolymer and PANI/ZnO nanocomposite in aqueous diethylene glycol solution medium via chemical oxidative polymerization of aniline and their photocatalytic activities were investigated by the degradation of methylene blue (MB) and malachite green (MG) dyes in aqueous medium under UV and natural light irradiations. They showed that the little amount of PANI/ZnO nanocomposite photocatalyst degrades both of dye solutions with 99% efficiency after 5h of natural sunlight irradiations.

Further, Baruah et al., [2] have synthesized ZnO NPs by hydrolysis and microwave method and showed an enhanced photocatalytic activity with the increase in electronic defects in the crystallites. Defects were introduced by fast nucleation and growth by rapid heating using microwave irradiation and subsequent quenching during the precipitation reaction. By introducing defects, they observed a red shift in the optical absorption from the ultraviolet region to the visible region by to the creation of intermediate defect states that inhibit the electron hole recombination process. The nature of the photodegradation process was elucidate by recording the electronic transitions resulting from the de-excitation of the electrons to their stable states. Photodegradation studies showed that defect engineered ZnO nanoparticles obtained through fast crystallization during growth lead to a faster initial degradation rate of methylene blue as compared to the conventionally synthesized nanoparticles.

In addition to these, various research groups have explored the photocatalytic properties of undoped and various elements doped ZnO nanomaterials to enhance their photocatalytic efficiency. Work done by various research groups in this field, their route of synthesis and outcomes have been summarized in Table 2.1.

Table 2.1: Summery of photocatalytic studies of ZnO by various research groups and their main findings.

Auther's Name (Year) [Ref.]	**System**	**Method of synthesis**	• **Organic compound degraded** • **Parameter studied**	**Outcomes**
Pauporte et al. (2007) [21]	Mesoporous films of ZnO	electrochemical deposition	• Methylene blue and Congo red dye. • Concentration of Eosin Y as a structure directing agent.	• Maximum degradation of methylene blue and congo red dye was achieved at 40µM concentration of eosin Y. • Photodegradation was preferentially occurred at large pores of the film and pore diameters less than 8nm have not contributed to large extent to photodegradation.
Daneshvar et al. (2007) [22]	ZnO nanocrystals	Co-precipitation	• An insecticide diazinon. • Illumination time of UV, pH of the dye, insecticide concentration and photocatalyst amount.	• Optimal amount of photocatalyst and insecticide concentration was 150 ppm and 20 ppm respectively for maximum degradation under UV irradiations.
Wu et al. (2008) [23]	ZnO nanoparticles from Fluka	As received	• Reactive red 198. • Influence of ZnO dosage, pH, addition of NaCl,1-butnol, UV/ZnO, UV/US/ZnO and US/ZnO (US-Ultrasound, UV-ultra violet).	• The percentage of RR198 removal was increased with ZnO dosage. • The degradation rate constant of US, UV/US, UV/ZnO and UV/US/ZnO systems was increased with pH and the order follows UV/US/ZnO> UV/ZnO>US/ZnO>US/UV>US. • Addition of NaCl increased decolorization of RR198in UV/ZnO and UV/US/ZnO systems. • Addition of 1-butanol inhibited decolorization of RR198 in UV/ZnO and UV/US/ZnO systems.
Tsuzuki et al. (2009)	Mn doped ZnO	Sol-gel	• Rhodamine B.	• Photodegradation of rhodamine B dye was

[24]	nanoparticles		• Varied the doping concentration upto 5 at.%.	significantly decreased with Mn doping as compared to undoped ZnO under sunlight.
Mekasuwandumrong et al. (2010) [25]	ZnO nanoparticles	Flame pyrolysis	• Methylene blue. • Flame height and high temperature residence during synthesis of photocatalyst.	• Improved crystalline quality and photocatalytic activity were obtained at high flame height and temperature. • Post treatment annealing of ZnO at high temperature obtained larger particle size and exhibited reduction in photocatalytic activity due decrease in surface availability.
Slama et al. (2010) [26]	Vanadium doped ZnO nanoparticles	Sol-gel	• Methylene blue.	• Vanadium doped ZnO NPs showed improved photocatalytic degradation of methylene blue dye due generation of deep levels in ZnO NPs.
Wahab et al. (2011) [27]	ZnO nanoparticles	Reflux	• Methyl orange. • Made comparison with commercial Degussa P-25.	• Synthesized ZnO NPs had higher photocatalytic activity under UV radiations as compared to commercial Degussa P-25.
Abdollahi et al. (2011) [28]	Mn doped ZnO nanoparticles	Precipitation	• Cresol. • Compare the photocatalytic degradation of cresol with commercial ZnO NPs.	• Mn (1.0%) doped ZnO NPs had shown better photocatalytic efficiency as compared undoped and commercial ZnO NPs due to smaller particle size, high surface area and lower agglomeration. • Smaller band gap of Mn doped ZnO NPs than undoped ZnO was attributed to better photocatalytic efficiency in visible light in 6hours.
Mahmood et al. (2011) [29]	Mn doped ZnO nanoparticles	Microwave assisted route	• Methylene blue. • Compared the photocatalytic properties with	• Microwave assisted Mn doped ZnO NPs generated higher defects to induce midgap states for electrons to excite from valance band to conduction band.

			conventional undoped and Mn doped ZnO NPs.	• Microwave assisted Mn doped ZnO NPs had higher reaction rate constant for the degradation of methylene blue dye as compared to conventional undoped and Mn doped ZnO NPs.
Khatamian et al. (2012) [30]	ZnO, ZnO/HZSM-5, ZnO/zeolite HY and ZnO/Clinoptilolite nanocomposite	poly acryl amide pyrolysis	• 4-nitrophenol. • Compared the photocatalytic activity of various nanocomposites.	• Among all the nanocomposite catalysts, ZnO/HZSM-5 showed higher percentage of adsorption and complete mineralization of 4-nitrophenol in 75mnutes under visible light radiations.
Eskizeybek et al. (2012) [31]	Polyaniline (PANI) homopolymer and PANI/ZnO nanocomposite	Chemical Polymerization	• Methylene blue and malachite green dyes. • UV and natural sunlight radiations.	• Addition of the ZnO nanoparticles to the PANI homopolymer enhanced the photocatalytic efficiency under natural sunlight irradiation and a little amount of PANI/ZnO nanocomposite photocatalyst (0.4 g/L) had degraded both of the dye solutions with 99% efficiency after 5 h of irradiation under natural sunlight.
Jia et al. (2012) [32]	Nanocrystalline ZnO superstructures	Thermal decomposition of zinc oxalate	• Methyl orange. • Heat treatment temperature and irradiation time.	• The optimum preparation condition for catalyst with higher photocatalytic activity was at 450 °C for 6h. • The dye molecules and radicals adsorbed effectively on porous surface that resulted in the promotion of the photocatalytic process and more active site on the surface of porous structure may had accelerated the photocatalytic reaction.

Faisal et al. (2012) [33]	ZnO nanoparticles	Hydrothermal treatment	• Methylene blue. • Compared the photocatalytic activity of ZnO NPs with TiO_2-UV100.	• Methylene Blue was efficiently degraded about 91.0% in just 85 minutes and showed better degradation as compared to TiO_2-UV100.
Etacheri et al. (2012) [34]	Magnesium doped ZnO nanoparticles	Co-precipitation	• Methylene blue. • Undoped and variable composition of Mg doped samples was synthesized at different calcined temperature.	• Undoped and 0.02, 0.05, 0.1 and 0.2-Mg doped ZnO NPs were synthesized at 400°C, 600°C and 700°C. • All Mg doped samples exhibited smaller crystallite size, enhanced textural properties and wide band gap as compared to undoped ZnO. • Mg doped samples exhibited near band edge PL emission and enhanced sunlight-induced photocatalytic activities as compared to undoped ZnO. • 0.1-Mg doped ZnO calcined at 600°C had shown highest photocatalytic activity attributed to better electron-hole separation, wider bandgap and superior textural properties.
Djaja et al. (2013) [35]	Ce doped ZnO nanoparticles	Co-precipitation	• Methyl orange. • Varied the concentration of Ce upto 19 at.%.	• Ce dopant had strong effect on structural and optical properties. • Reduction in the band gap due to formation of new states attributed to doping level and presence of an oxygen vacancy. • Photocatalytic activity was increased with increased in Ce ion content and then decreased beyond the optimal value of doping. • 9 at.% of Ce ion doping shown highest photocatalytic degradation of methyl orange

				dye.
Milenova et al. (2013) [36]	Cu doped ZnO nanoparticles	Precipitation	• Reactive Black5. • Studied variation in doping concentration of Cu.	• Cu doped (0.24-1.07 at.%) ZnO NPs were synthesized and photocatalytic efficiency was evaluated by degradation of Reactive Black5 dye. • Decrease in Cu content in ZnO lead to enhancement in photocatalytic activities due to segregation of doping element on the surface of ZnO particles. • Pure ZnO exhibited best photocatalytic properties.
Voicu et al. (2013) [37]	Mn doped ZnO nanoparticles	Hydrolysis	• Methylene blue. • Doping of Mn was varied upto 5%.	• Mn (1, 2.5 and 5%) ZnO NPs were synthesized and evaluated them for photodegradation of methylene blue dye. • Luminescence intensity was decreased with increased in Mn doping concentration. • Photocatalytic activity was increased with increased Mn percentage and 5% of Mn doping had shown highest photodegradation efficiency.
Xu et al. (2014) [38]	ZnO nanostructure	Sol-gel	• RhodamineB. • Various ZnO nanostructures were evaluated for degradation of dye.	• ZnO nanorods, ZnO film and ZnO leaf-like nanostructures were evaluated for degradation of rhodamine B dye. • ZnO with leaf-like structure had shown better photocatalytic activity than others because ZnO leaf-like structure had larger surface area than their counterparts.
Umar et al. (2015) [39]	ZnO nanourchins	Hydrothermal	• Acridine orange dye. • UV light irradiations.	• Synthesized ZnO nanourchins exhibited crystalline nature with hexagonal wurtzite phase. • 98.5% acridine orange dye was degraded within 80minutes of UV light irradiations.

Hosseini et al. (2015) [40]	Ag doped ZnO nanoparticles	Solid state milling	• Methyl violet. • Variation in Ag doping concentration.	• Ag doping had shown red shift in absorption band edge and thus reduced the energy gap. • Ag 2% had shown the highest photodegradation of methyl violet due presence of optimal oxygen vacancies.
Mardani et al. (2015) [41]	Fe and Cu doped ZnO nanoparticles	Hydrolysis and oxidation	• Methylene blue. • Studied the effect of metal doping on methylene degradation.	• Undoped, Fe and Cu doped ZnO NPs wereprepared and evaluated their photocatalytic efficiency with photodegradation of methylene blue dye under visible light radiations. • Presented that Fe and Cu doped ZnO NPs has shown better photodegradation as compared to undoped. • Fe doped ZnO NPs had degraded methylene blue dye more efficiently as compared to Cu doped ZnO NPs due to their smaller particle size.
Elangovan et al. (2015) [42]	Na doped ZnO nanocrystals	Wet chemical method	• Methylene blue. • Effect of Na doping, catalyst dosage and UV irradiation time.	• Undoped, 2, 3 and 5% Na doped ZnO nanocrystals were synthesized to the photocatalytic degradation of methylene blue dye under UV light irradiations. • Degradation wasincreased with increased in Na doping concentration and 5% Na doping had shown the maximum degradation in 5 hours under UV illuminations. • 0.1g/50ml of 5% of Na doped ZnO nanocrystals were found to be optimum to achieve maximum degradation.
Manna et al. (2015) [43]	Hybrid Au/ZnO nanoparticles	Microwave	• Rhodamine-6G. • Varied Zn^{2+} concentration.	• Zn^{2+} concentration was varied from 0.005 to 0.1M in ZnO to achieve maximum degradation efficiency and maximium degradation of rhodamine-6G was obtained after 120minutes

				under UV illuminations. • Optimized 0.1M of Zn^{2+} in ZnO, Au NPs were attached to evaluate photocatalytic studies of Au/ZnO NPs. • Hybrid Au/ZnO NPs exhibited enhance photocatalytic properties under UV illumination after 60minutes.
Pandiyarajan et al. (2015) [44]	Sm doped ZnO nanostructures	Wet chemical	• Acid blue 113. • 0.05-1.5mmol% of Sm concentration was varied.	• Sm1.0 mmol% of Sm was optimal for more than 80% degradation of acid blue 113 dye under UV-A radiations for 80minutes.
Mishra et al. (2015) [45]	ZnO tetrapods	Flame transport	• Methylene blue.	• ZnO tetrapods with different types of arm shape exhibited significantly high photocatalytic activity against methylene blue under UV radiations.
Dong et al. (2016) [46]	1D-ZnO nanostructures	Electrospinnig	• Rhodamine blue. • Deposition of Au NPs on ZnO NPs.	• Out of various 1D- ZnO nanostructures, ZnO nanobelts had shown maximum degradation of rhodamine B dye under 180minutes of UV light radiations. • ZnO-Au composite had further improved the photocatalytic efficiency due to formation of ohmic contact.

2.4 Cerium Oxide (CeO_2)

Ceria (CeO_2) is a rare earth metal oxide and it is most abundant in earth's crust. It has exceptional technological importance due to its versatile properties like mechanical strength, electronic conductivity, oxygen ion conductivity and oxygen storage capacity.Due to these exceptional properties, it is a basic component materials for solid oxide fuel cell, sensors, abrasive pastes and catalysis. Ceria containing materials have been extensively investigated in the field of metallurgy, smart glass materials, electrochemistry, optics and ceramics [47-54]. After europium, cerium is the most reactive earth metal which easily oxidized at room temperature. Most of rare earth metals exist in trivalent state, cerium exist in +3 and +4 state and flip-flop between these two in redox reaction [55-56]. Ceria has a fluorite structure with Fm3m space group from room temperature to the melting point. The fluorite structure consists of face centered cubic (fcc) unit cell of anions and cations occupying octahedral sites. The color of ceria is pale yellow and is due to charge transfer of Ce(IV) - O(II) [57]. Ceria can accommodate high oxygen deficiency by the substitution of lower valence elements that leads to high oxygen ion conductivities. Defects such as oxygen vacancies dominate the chemical and electronic properties of ceria. Oxygen vacancies play a significant role in reactivity of ceria for photocatalytic oxidation of organic contaminants [58-59]. Enhanced activity is mainly attributed to oxygen storage capacity which is closely linked with the fact that how easily cerium can change its oxidation states. The formation of oxygen vacancies in ceria is mainly due to increase in Ce^{3+} concentration in order to maintain electroneutrality [60]. Ceria nanoparticles with large surface to volume ratio act catalytically because with decrease in particle size, ceria NPs demonstrate more oxygen vacancies, along with some new properties like enhanced electron conductivity, pressure induced lattice relaxation and blue shift in UV absorption spectra [61-64]. These all properties have a major contribution towards the photodegradation applications. Thus ceria has been used as a photocatalyst by various research groups. Before this various methods has been employed to synthesize ceria NPs and other nanostructures like hydrolysis [65], precipitation [66], thermal deposition [49], flame or combustion synthesis [67], hydrothermal or solvothermal [68], sol-gel [69], sonochemical [70], electrochemical [71] and so on.

2.5 Photocatalysis with CeO_2 nanomaterials

Bamwenda et al. [72] in 2000 demonstrated that ceria can be used as a potential photocatalyst for decomposition of water to produce oxygen in aqueous suspension. O_2 yield strongly depended upon duration of irradiation, ceria concentration and pH of suspension under

illumination time more than 10h and of wavelength less than 420nm. They showed that, ceria is a promising material that can be used in photocatalytic reactions with an appropriate design. Further Coronado et al. [73] in 2002 presented that CeO_2 sample upon irradiation in vacuum produces superoxide radicals that were helpful for oxidation of toluene where photodegradation rate for CeO_2/TiO_2 was slightly lower than TiO_2 sample. Although the photo-oxidation rate was lower than TiO_2 but complete mineralization of toluene was obtained with CeO_2 sample. Similar type of toluene degradation was studied by Alonso et al. [74] and suggested that hydroxyl and superoxide radicals were main species resulting from hole and electron trapping as active species for photo-oxidation of toluene. Qiu et al. [75] synthesized CeO_2 nanophotocatalyst by precipitation method and shown that CeO_2 NPs have better UV absorption property than commercial ceria microparticles. They found that the CeO_2 NPs exhibited photocatalytic activity for decomposition of methyl orange under UV light irradiation.

In addition to these, various research groups have explored the photocatalytic properties of undoped and various elements doped CeO_2 nanomaterials to enhance their photocatalytic efficiency. Work done by various research groups in this field, their route of synthesis and outcomes have been summarized in Table 2.2.

Table 2.2: Summery of photocatalytic studies of CeO_2 by various research groups and their main findings.

Auther's Name (Year) [Ref.]	**System**	**Method of synthesis**	• **Organic compound degraded** • **Parameter studied**	**Outcomes**
Mao et al.(2008) [76]	N doped CeO_2 nanoparticles	Wet-chemical	• Methylene blue. • N doping concentration.	• 1.6 to 8.7% of N doped ceria samples were synthesized by wet chemical route and methylene blue dye was selected to study the photodegradation efficiency of as synthesized NPs. • Approximate 4% of N doping was observed to be optimal for best decomposition rate where the degradation was nearly 20% under visible light in more than 300minutes.
Ameta et al. (2009) [77]	$CeFeO_3$	Co-precipitation	• Gentian Violet. • Concentration of gentian violet, pH, and light intensity.	• Maximum degradation of gentian violet was achieved at 0.1g of catalyst loading at pH 6.0 of dye solution. • Degradation of gentian violet increased with increased in light intensity and degradation was maximum at mW/cm^2.
Ji et al. (2009) [78]	CeO_2 nanoparticles	Precipitation	• Acid orange 7. • Photodegradation rate of ceria was compared with commercial Degussa P25.	• Acid orange7 was decolorized and partially mineralized after 10h under visible light radiations. • Ceria NPs had shown better degradation after 10h than commercial Degussa P25. • At lower pH of dye solution, photocatalysis had increased due to increase in adsorption of dye molecules on ceria NPs. • CeO_2 could serve as an excellent electron transfer mediator to transfer electron from photo-excited dye molecule to produce oxidizing agents for degradation of dye.
Cai et al. (2010) [79]	Fe doped CeO_2	Hydrothermal	• Acid orange7. • Fe doping and effect of H_2O_2.	• Lower doping of Fe improved Ce^{3+} concentration as well as enhanced photocatalytic performance. • Further increase in Fe doping concentration reduced the photocatalytic efficiency. • Fe doped CeO_2 with Fe: Ce :: 1:100 had showed maximum degradation in the presence of H_2O_2 in visible region than CeO_2:H_2O_2 system.
Bhati et al. (2010) [80]	Nanosized $CeCrO_3$	Microwave	• Fast green dye. • Effect of catalyst	• Maximum degradation of dye was achieved at 0.05g of photocatalyst with 10^{-5} of dye at 7.5pH value. Further change in

			dosage, pH, light intensity and concentration of dye.	optimal parameters had reduced the degradation of dye. • The maximum degradation of dye was achieved at 70mW/cm^2.
Pouretedal et al. (2010), [81]	CeO_2 nanoparticles	Precipitation	• Methylene blue. • CeO_2 calcined temperature, pH of dye and photocatalyst dosage.	• 1.0g/L of CeO_2 NPs synthesized at 600ºC had shown the maximum degradation of methylene blue dye. • The optimized pH of dye to obtain maximum degradation was 11.
Pradhan et al. (2010) [82]	Mesoporous and nano structures Iron-cerium mixed oxides	Precipitation	• Phenol, Methylene blue and Congo red. • Iron content was varied for efficient photocatalysis.	• 50 Fe catalyst with 50-50 content of both Fe and Ce acted as an efficient photocatalyst for all tested dyes. • 13% phenol, 93% methylene blue and almost complete mineralization of congo red dye was obtained after 4h under direct illumination to sun light. • The percentage of total carbon removed was 9%, 77% and 85% for phenol, methylene blue and congo red respectively.
Zholobak et al. (2011) [83]	CeO_2 nanoparticles		• Methyl orange. • Compare the degradation efficiency with TiO_2 and ZnO.	• Nanoceria possessed lower photocatalytic efficiency as compared to TiO_2 and ZnO NPs. • Photocatalytic activity of ceria was decreased with decrease in ceria particle size.
Sifontes et al. (2013) [84]	CeO_2 nanoparticles	Thermal treatment	• Congo red. • Variation in synthesis temperature, catalyst amount and dye concentration.	• Rate of congo red degradation was increased with irradiation time. • 62, 71 and 91% of congo red dye was degraded with ceria NPs calcined at 350, 650 and 960°C respectively after 24hours of UV radiations. • Increased in calcination temperature had led to increase the rate of photodegradation efficiency of ceria NPs.
Channei et al. (2013) [85]	Fe doped CeO_2 nanoparticles	Flame spray pyrolysis	• Formic and oxalic acid. • Fe doping concentration was varied to achieve maximum degradation.	• Fe doped CeO_2 NPs had shown better photocatalytic degradation of formic and oxalic acid. • 2.0mol% was optimal to achieve maximum degradation.
Jamahidi et	CeO_2 nanoparticles	Sonochemical	• Methyl orange.	• CeO_2 NPs had degraded methyl orange effectively under UV

al. (2013) [86]				irradiations in 60 minutes.
Khan et al. (2013) [87]	CeO_2 nanoparticles	Hydrothermal	• Acridine orange.	• Photocatalytic efficiency of ceria NPs was evaluated by photodegradation of acridine orange dye and 50% of degradation was achieved after 170 minutes. • Reduction in particle size enhanced the active surface area which resulted in photodegradation.
Ma et al. (2014) [88]	Ag/CeO_2Nanosphere	Hydrothermal	• Formaldehyde. • Catalysis of formaldehyde was performed above 110°C.	• Ag/CeO_2 nanosphere catalysts exhibited much higher activity than Ag/CeO_2 particles and pure CeO_2 particles. • The specific reaction rate of Ag/CeO_2 nanosphere was almost 3.6times higher than Ag/CeO_2 particles.
Channei et al. (2014) [89]	Fe doped CeO_2 nanoparticles	Homogeneous precipitation	• Methyl orange. • Fe doping concentration was varied from 0.5 to 5.0 mol%.	• Fe doped CeO_2 NPs had shown better photodegradation efficiency as compared to undoped and other doped CeO_2 samples. • 1.5mol% was optimal to achieve maximum degradation (approximately 50%) of dye in 120minutes. • PL emission intensity gradually decreased with increased Fe doping. • Presence of Fe^{3+} observed from XPS contributed to Fe^{3+}/ Fe^{2+} and Fe^{4+}/ Fe^{3+} additional levels in CeO_2 had decreased the bandgap energy and also reduced the recombination rate of electron-hole pairs. • Lesser recombination increased the life-time electron hole pair separation thus resulted in better degradation of methyl orange dye.
Ansari et al. (2014) [90]	EAB modified CeO_2 nanostructure	CeO_2 nanostructures were purchased from Sigma-Aldrich.	• 4-nitrophenol and methylene blue.	• Pure CeO_2 nanostructure and electrochemically active biofilm (EAB) modified CeO_2 nanostructures was synthesized and had shown that modified CeO_2 exhibit red shift with enhanced PL intensity due to increased defects. • Approximate 80% and more than 80% 4-nitrophenol and methylene blue dye was degraded in 5h under visible light readiations. • Modified CeO_2 had shown better degradation efficiency as

				compared to pure CeO_2 nanostructures.
Liyanage at al. (2014) [91]	Y-doped CeO_2 nanorods	Hydrothermal	• Indigo carmine and rhodamine B dye. • Doping of Y doping and temperature.	• Increase in doping concentration resulted in increase in amount of oxygen vacancies. • The doped nanorods had shown higher photocatalytic activity compared to ceria at lower level of doping due to low band gap energy and presence of oxygen vacancies. • Doping with 50% of Y resulted in lower photocatalytic activity as compared to pure ceria at room temperature due to fast electron-hole pair recombinations. • Maximum of 60% indigo carmine and 40% of rhodamine B dye was degraded with Y doped ceria at Ce:Y ::0.89:0.11 composition at room temperature under 100minutes of UV-Visible light illumination. • Ce:Y :: 0.44:0.56 composition had shown maximum (approximate 50%) degradation of inigo carmine at 100°C.
Lei et al. (2015) [92]	CeO_2 nanoroda and nanocrystals and Au loading	Hydrothermal	• Methyl orange. • Loading of Au nanoparticles.	• Loading of Au NPs onto CeO_2 nanorods to form Au/CeO_2 plasmonic nanocomposites had enhanced methyl orange photodegradation. • 11.6 wt% Au/CeO_2 had shown 1.3 times photoreactivity under UV light as compared to visible light.
Mandal et al. (2015) [93]	Sm^{3+} doped CeO_2 nanopowder	Microwave	• Acid orange 7. • Calcination temperature of photocatalyst and pH of dye.	• Sm^{3+} doped ceria calcined at 500°C had shown better photodegradation activity as compared to samples synthesized at 600 and 800 °C. • pH of dye solution was adjusted from 2.9 to 9.1 and found that photodegradation of acid orange 7 was maximum in acidic solution. • At pH 2.9 the decolorization efficiency was 99.5% which reduces to 95% at pH 9.1 after 10h under visible light illuminations. This was attributed to basic nature of acid orange 7 dye, which could easily adsorbed on catalyst surface in acidic medium.
Sharma et al. (2015) [94]	Eu doped CeO_2 nanoparticles	Chemical precipitation	• Methyl orange. • Eu doping concentration.	• Eu doped (upto 30 mol%) CeO_2 NPs were synthesized and their photocatalytic activity was evaluated by degradation of methyl orange dye under UV radiations.

				• Eu 30mol% doped ceria NPs had shown maximum (~80%) of methyl orange degradation in 90min under UV radiation.
Li et al. (2015) [95]	CeO_2 nanocrystals	Hydrothermal	• Rhodamine B. • Degradation efficiency of synthesized samples was compared with commercial TiO_2 P25.	• CeO_2 NPs had shown better degradation of rhodamine B dye than ceria nanorods and commercial TiO_2 P25. • ~83% rhodamine B dye was degraded in 240minutes under visible light illuminations.
Younis et al. (2016) [96]	In doped Ceria nanoparticles	Hydrothermal	• Methyl orange and methylene blue. • In doping concentration, temperature.	• 5.0, 10.0 and 15.0at% in doped ceria NPs were synthesized by hydrothermal route and to explore their photocatalytic efficiency, methyl orange and methylene blue dye degradation was evaluated under UV radiations. • In with 10at% had shown better photocatalytic efficiency as compared to other doped and undoped ceria NPs. • More than 90% and nearly 60% of methyl orange and methylene blue dye was degraded under UV radiations after 100 minutes of illuminations respectively. • Rate of reaction was increased on rising the temperature to 100°C due to enhanced oxygen mobility. • In 10at% doped Ceria sample had shown maximum degradation efficiency due to lower band gap and higher concentration of oxygen vacancies on surface.

2.6 Plan of work

Although tremendous efforts have been made by various research groups to enhance the photocatalytic behavior of ZnO nanomaterials by doping with various metal ions, yet some more systematic study is required to explore this field. For example: (a) Some of the groups have shown that Mn doping has decreased the photocatalytic efficiency of ZnO NPs. On the other side some other groups have shown that Mn doping in ZnO has increased the photocatalytic behavior. Optimal doping concentration of Mn has been reported to be different for maximum degradation of organic compound. Therefore more systematic studies are required to obtain optimal doping concentration of Mn for maximum degradation. (b) Similarly it can be seen from the literature survey that Cu doping in ZnO has decrease the photodegradation efficiency, which further need more study to explore the effect of Cu doping in ZnO for better degradation efficiency. (c) Number of groups have studied the effect of pH of dye solution and found different pH values for maximum degradation of dyes. However, no photocatalyst/system has been proposed which could degrade the organic compounds at all pH values i.e. in all acidic and basic medium of the pollutants.

Except ZnO, although CeO_2 nanomaterials is not a semiconductor material, but still have similar bandgap as that of ZnO, can be used as a photocatalyst. As literature review suggested that ceria nanomaterials have shown photocatalytic activity with various metals and non-metals but majority of them have not shown complete degradation of dyes. Therefore still some other metals needed to be considered to explore photocatalytic property of this nanomaterial. Various groups have shown the degradation of various organic compounds under different light radiations. The percentage degradation of dyes has been very small and the irradiation time is very large. Again there is no photocatalyst /system where the maximum degradation and pollutants with at all pH (acidic, neutral and basic region) can be degraded.

Thus considering the above limitations or gaps, the main objectives behind the present work were as below:

1 To synthesize Mn and Cu doped and undoped ZnO nanomaterials by chemical precipitation route.
2 To study effect of capping agent like PVP and TG and photocatalytic properties.
3 To synthesize Ag and Au doped and undoped CeO_2 nanomaterials.

4 To study effect of dopant on photodegradation properties of CeO_2 nanomaterials by conversion of Ce^{4+} to Ce^{3+}.

5 To study their photocatalytic properties using UV-visible, PLE and PL spectroscopy.

6 To study morphological studies for structural and size measurement using XRD, SEM, TEM etc.

References

[1] S. S. Warule, N. S. Chaudhari, B. B. Kale and M. A. More, Novel sonochemical assisted hydrothermal approach towards the controllable synthesis of ZnO nanorods, nanocups and nanoneedles and their photocatalytic study, CrystEngComm, 11 (2009) 2776-2783.

[2] S. Baruah, S. S. Sinha, B. Ghosh, S. K. Pal, A. K. Raychaudhuri and J. Dutta, Photoreactivity of ZnO nanoparticles in visible light: Effect of surface states on electron transfer reaction, Journal of Applied Physics, 105 (2009) 074308.

[3] S. C. Pillai, J. M. Kelly, R. Ramesh and D. E. McCormack, Advances in the synthesis of ZnO nanomaterials for varistor devices, Journal of Materials Chemistry C, 1 (2013) 3268- 3281.

[4] A. B. Djurisic, A. M. C. Ng, X. Y. Chen, ZnO nanostructures for optoelectronics: Material properties and device applications, Progress in Quantum Electronics, 34 (2010) 191-259.

[5] Y. Tu, L. Zhou, Y. Z. Jin, C. Gao, Z. Z. Ye, Y. F. Yang and Q. L. Wang, Transparent and flexible thin films of ZnO-polystyrene nanocomposite for UV-shielding applications, Journal of Materials Chemistry,20 (2010) 1594-1599.

[6] Z. L. Wang and J. Song, Piezoelectric nanogenerators based on zinc oxide nanowire arrays, Science, 312 (2006) 242-246.

[7] L. S. Mende and J. L. M. Driscoll, ZnO-nanostructures, defects and devices, Materials Today, 10(5) (2007) 40-48.

[8] P. V. Kamat, R. Huehn and R. Nicolaescu, A " Sense and shoot" approach for photocatalytic degradation of organic contaminants in water, Journal of Physical Chemistry B, 106 (2002) 788-794.

[9] D. C. Look, D. C. Reynolds, J. R. Sizelove, R. L. Jones, C. W. Litton, G. Cantwell and W. C. Harsch, Elctrical properties of bulk ZnO, Solid State Communications,105 (1998) 399-401.

[10] A. K. Chandiran, M. A. Jalebi, M. K. Nazeeruddin and M. Gratzel, Analysis of electron transfer properties of ZnO and TiO_2 photoanodes for dye-sensitized solar cells, ACS Nano, 8 (2014) 2261-2268.

[11] N. Daneshvar, D. Salari and A. R. Khataee, Photocatalytic degradation of azo dye acid 14 in water on ZnO as an alternative catalyst to TiO_2, J. Photochemistry and Photobiology A: Chemistry, 162 (2004) 317-322.

[12] J. Liqiang, W. Dejun, W. Baiqi, L. Shudan, X. Baifu, F. Honggang and S. Jiazhong, Effects of noble metal modification on surface oxygen composition, charge separation

and photocatalytic activity of ZnO nanoparticles, Journal of Molecular Catalysis A: Chemical, 244 (2006) 193-200.
[13] Y. Lv, C. Pan, X. Ma, R. Zong, X. Bai and Y. Zhu, Production of visible activity and UV performance enhancement of ZnO photocatalyst via vacuum deoxidation, Applied Catalysis B: Environmental, 138-139 (2013) 26-32.
[14] D. Chen, Z. Wang, T. Ren, H. Ding, W. Yao, R. Zong and Y. Zhu, Influence of defects on the photocatalytic activity of ZnO, Journal of Physical Chemistry C, 118 (2014) 15300-15307.
[15] Z. Pei, L. Ding, J. Hu, S. Weng, Z. Zheng, M. Huang and P. Liu, Defects and its dominance in ZnO films: A new insight into the role of defects over photocatalytic activity, Applied Catalysis B: Environmental, 142-143 (2013) 736-743.
[16] L. Guo, S. Yang, C. Yang, P. Yu, J. Wang, W. Ge, and G. K. L. Wong Synthesis and Characterization of Poly(vinylpyrrolidone)-Modified Zinc Oxide Nanoparticles, Chem. Mater. 12 (2000) 2268-2274.
[17] A. Mclaren, T. V. Solis, G. Li, S. C. Tsang, Shape and Size Effects of ZnO Nanocrystals on Photocatalytic Activity, Journal American Chemical. Society, 131 (2009) 12540–12541.
[18] R. Y. Hong, J. H. Li, L. L. Chen, D. Q. Liu, H. Z. Li, Y. Zheng, J. Ding, Synthesis, surface modification and photocatalytic property of ZnO nanoparticles, Powder Technology, 189 (2009) 426–432.
[19] R. Salehi, M. Arami, N. M. Mahmoodi, H. Bahrami, S. Khorramfar, Novel biocompatible composite (Chitosan–zinc oxide nanoparticle): Preparation, characterization and dye adsorption properties, Colloids and Surfaces B: Biointerfaces 80 (2010) 86–93.
[20] V. Eskizeybek, F. Sari, H. Gulce, A. Gulce, A. Avci, Preparation of the new polyaniline/ZnO nanocomposite and its photocatalytic activity for degradation of methylene blue and malachite green dyes under UV and natural sun lights irradiations. Applied Catalysis B: Environmental, 119-120 (2012) 197-206.
[21] T. Pauporte and J. Rathousky, Electrodeposited Mesoporous ZnO Thin Films as Efficient Photocatalysts for the Degradation of Dye Pollutants, Journal of Physical Chemistry C, 111 (2007) 7639-7644.
[22] N. Daneshvar, S. Aber, M. S. Seyed Dorraji, A. R. Khataee, M. H. Rasoulifard Photocatalytic degradation of the insecticide diazinon in the presence of prepared nanocrystalline ZnO powders under irradiation of UV-C light. Separation and Purification Technology, 58 (2007) 91–98.
[23] C. H. Wu, Effects of sonication on decolorization of C. I. reactive red 198 in UV/ZnO system, Journal of Hazardous Materials, 153 (2008) 1254-1261.
[24] T. Tsuzuki, Z. Smith, A. Parker, R. He, X. Wang, Photocatalytic Activity of Manganese-Doped ZnO Nanocrystalline Powders, Journal of the Australian Ceramic Society, 45(1) (2009) 58-62.
[25] O. Mekasuwandumrong, P. Pawinrat, P. Praserthdam, J. Panpranot, Effects of synthesis conditions and annealing post-treatment on the photocatalytic activities of ZnO nanoparticles in the degradation of methylene blue dye, Chemical Engineering Journal, 164 (2010) 77–84.
[26] R. Slama, F. Ghribi, A. Houas, C. Barthon, L. E. Mir, Photocatalytic and optical properties of vanadium doped zinc oxide nanoparticles, J. Nanoelectronics and Materials, 3 (2010) 133-142.

[27] R. Wahab, I. H. Hwang, Y. S. Kim, J. Musarrat, M. A. Siddiqui, H. K. Seo, S. K. Tripathy, H. S. Shin, Non-hydrolytic synthesis and photo-catalytic studies of ZnO nanoparticles, Chemical Engineering Journal, 175 (2011) 450–457.
[28] Y. Abdollahi, A. H. Abdullah, Z. Zainal, N. A. Yusof, Synthesis and Characterization of Manganese Doped ZnO Nanoparticles, International Journal of Basic & Applied Sciences IJBAS-IJENS Vol: 11 No: 04 (2011).
[29] M. A. Mahmood, S. Baruah, J. Dutta, Enhanced visible light photocatalysis by manganese doping or rapid crystallization with ZnO nanoparticles, Materials Chemistry and Physics 130 (2011) 531– 535.
[30] M. Khatamian, B. Divband, A. Jodaei, Degradation of 4-nitrophenol (4-NP) using ZnO nanoparticles supported on zeolites and modeling of experimental results by artificial neural networks, Materials Chemistry and Physics, 134 (2012) 31– 37.
[31] V. Eskizeybek, F. Sarı, H. Gülce, A. Gülce, A. Avcı, Preparation of the new polyaniline/ZnO nanocomposite and its photocatalytic activity for degradation of methylene blue and malachite green dyes under UV and natural sun lights irradiations, Applied Catalysis B: Environmental, 119–120 (2012) 197–206.
[32] Z. Jia, D. Ren, L. Xu, R. Zhu, Preparation, characterization and photocatalytic activity of porous zinc oxide superstructure, Materials Science in Semiconductor Processing, 15 (2012) 270–276.
[33] M. Faisal, S. B. Khan, M. M. Rahman, A. Jamala, M. M. Abdullah, Fabrication of ZnO nanoparticles based sensitive methanol sensor and efficient photocatalyst, Applied Surface Science, 258 (2012) 7515– 7522.
[34] V. Etacheri, R. Roshan, V. Kumar, Mg doped ZnO nanoparticles for efficient sunlight driven photocatalysis, ACS Applied Materials & Interfaces, 4 (2012) 2717-2725.
[35] N. F. Djaja, R. Saleh , Characteristics and Photocatalytics Activities of Ce-Doped ZnO Nanoparticles, Materials Sciences and Applications, 4 (2013) 145-152**.**
[36] K. Milenova, I. Stambolova, V. Blaskov, A. Eliyas, S. Vassilev, M. Shipochka, The effect of introducing copper dopant on the photocatalytic activity of ZnO nanoparticles, Journal of Chemical Technology and Metallurgy, 48 (2013) 259-264.
[37] G. Voicu, O. Oprea, B. S. Vasile, E. Andronescu, Photoluminescence and photocatalytic activity of Mn doped ZnO nanoparticles, Digest Journal of Nanomaterials and Biostructures, 8 (2013) 667-675.
[38] L. Xu, G. Zheng, J. Wang, M. Lai, J. Miao, F. Xian, F. Gu, T. Sun, Leaf-like ZnO nanostructure and its excellent photocatalytic activity, Materials Letters, 122 (2014) 1-4.
[39] A. Umar, M.S. Akhtar, A. Al-Hajry, M.S. Al-Assiri, G.N. Dar, M. Saif Islam, Enhanced photocatalytic degradation of harmful dye and phenyl hydrazine chemical sensing using ZnO nanourchins, Chemical Engineering Journal, 262 (2015) 588-596.
[40] S. M. Hosseini, I. A. Sarsari, P. Kameli, H. Salamati, Effect of Ag doping on structural, optical and photocatalytic properties of ZnO nanoparticles, Journal of Alloys and Compounds, 640 (2015) 408-415.
[41] H. R. Mardani, M. Forouzani, M. Ziari, P. Biparva, Visible light photodegradation of methylene blue over Fe or Cu promoted ZnO nanoparticles, Spectrochimica Acta Part A: Molecular and Biomolecular Spectroscopy, 141 (2015) 27-33.
[42] S. V. Elangovan, V. Chandramohan, N. Sivakumar, T.S. Senthil, Synthesis and characterization of sodium doped ZnO nanocrystals and its application to photocatalysis, 85 (2015) 901–907.

[43] J. Manna, T. P. Vinod, K. Flomin, R. Jelinek, Photocatalytic hybrid Au/ZnO nanoparticles assembled through a one-pot method, Journal of Colloid and Interface Science, 460 (2015) 113-118.

[44] T. Pandiyarajan, R. V. Mangalaraja, B. Karthikeyan, P. sathishkumar, H. D. Mansilla, D. Contreras, J. Ruiz, UV-A light –induced photodegradation of Acid Blue 113 in the Presence of Sm-doped ZnO nanostructures, Applied Physics A : Materials Science & Processing, 119 (2015) 487-495.

[45] Y. K. Mishra, G. Modi, V. Cretu, V. Postica, O. Lupan, T. Reimer, I. Paulowicz, V. Hrkac, W. Benecke, L. Kienle, R. Adelung, Direct growth of freestanding ZnO terrapod networks for multifunctional applications in photocatalysis, UV photodetection and gas sensing, ACS Applied Materials & Interfaces, 7 (26) **(**2015**)** 14303–14316.

[46] X. Dong, P, Yang, Y. Liu, C. Jia, D. Wang, J. Wang, L. Chen, Q. Che, Morphology evolution of one-dimensional ZnO nanostructures towards enhanced photocatalysis performance, Ceramics International, 42 (2016) 518-526.

[47] M. K. Devaraju, S. Yin, T. Sato, Morphology control of cerium oxide particles synthesized via a supercritical solvothermal method, ACS Applied Materials & Interfaces, 1 (11) (2009) 2694.

[48] B. Djuricic, S.Pickering, Nanostructured cerium oxide: preparation and properties of weakly-agglomerated powders, Journal of the European Ceramamic Society, 19 (1999) 1925-1934.

[49] M. Kamruddin, P. K. Ajikumar, R. Nithya, A. K. Tyagi, B. Raj, Synthesis of nanocrystalline ceria by thermal decomposition and soft-chemistry methods, Scripta Materialia, 50 (2004) 417-422.

[50] M. D. H. Alonso, A. N. Hungria, A. M. Arias, J. M. Coronado, J. C. Conesa, J. soria, M. F. Garcia, Confinement effects in quasi-stoichiometric CeO_2 nanoparticles, Physical Chemistry Chemical Physics, 6 (2004) 3524-3529.

[51] M. S. Tsai, Formation of nanocrystalline cerium oxide and crystal growth, Journal of Crystal Growth, 274 (2005) 632.

[52] P. Marecot, L. Pirault, G. Mabilon, M. Prigent and J. Barbier, Influence of the redox properties of ceria on the preparation of three-way automotive platinum-rhodium/alumina- ceria catalysts, Applied Catalysis B: Environmental, 5 (1994) 57

[53] H.C. Lin, Application and market of cerium oxide, Hydrometallurgy (China), 24 (2005) 9-11.

[54] Q. Fu, H. Saltsburg, M. F. Stephanopoulos, Active nanometallic Au and Pt species on ceria-based water-gas shift catalysts, Science, 301 (2003) 935-938.

[55] G. S. Herman, Characterization of surface defects on epitaxial CeO_2 (001) films, Surface Science 437 (1-2) (1999) 207-214.

[56] J. C. Conesa, Computer Modeling of Surfaces and Defects on Cerium Dioxide, Surface Science 339 (3) (1995) 337-352.

[57] M. Mogensen, N. M. Sammes, G. A. Tompsett, Physical, chemical and electrochemical properties of pure and doped ceria, Solid State Ionics, 129 (2000) 63–94.

[58] C. J. Zhang, A. Michaelides, D. A. King, S. J. Jenkins, Oxygen vacancy clusters on ceria: decisive role of cerium f electrons, Physical Review B, 79 (2009) 075433.
[59] C. T. Campbell, C. H. F. Peden, Oxygen vacancies and catalysis on ceria surfaces, Science, 309 (2005) 713–714.
[60] N. J. Lawrence, J. R. Brewer, L. Wang, T. Wu, J. W. Kingsbury, M. M. Ihrig, G. Wang, Y. Soo, W. Mei, C. L. Cheung, Defect engineering in cubic cerium oxide nanostructures for catalytic oxidation, Nano Letters,11(2011) 2666–2671.
[61] S. Deshpande, S. Patil, S. V. N. T. Kuchibhatla, S. Seal, Size dependency variation in lattice parameter and valency states in nanocrystalline cerium oxide, Applied Physics Letters, 87 (2005) 133113.
[62] Y. M. Chiang, E. B. Lavik, I. Kosacki, H. L. Tuller, Defect and transport properties of nanocrystalline CeO_2_x, Applied Physics Letters, 69 (1996) 185–187.
[63] X. D. Zhou, W. Huebner, Size-induced lattice relaxation in CeO_2 nanoparticles, Applied Physics Letters, 79 (2001) 3512–3514.
[64] S. Tsunekawa, T. Fukuda, A. Kasuya, Blue shift in ultraviolet absorption spectra of monodisperse CeO_{2-x} nanoparticles, Journal of Applied Physics, 87 (2000) 1318–1321.
[65] M. Hirano, M. Inagaki, Preparation of monodispersed cerium(IV) oxide particles by thermal hydrolysis: influence of the presence of urea and Gd doping on their morphology and growth, Journal Materials Chemistry, 10 (2000) 437–477.
[66] F. Zhang, Q. Jin, S. W. Chan, Ceria nanoparticles: size, size distribution, and shape, Journal of Applied Physics, 95 (2004) 4319–4326.
[67] L. Madler, W. J. Stark, S. E. Pratsinis, Flame-made ceria nanoparticles, Journal of Materials Research, 17 (2002) 1356–1362.
[68] C. W. Sun, L. Q. Chen, Controlled synthesis of shuttle-shaped ceria and its catalytic properties for CO oxidation, European Journal of Inorganic Chemistry, 2009, 3883–3887.
[69] C. L. Robert, J. W. Long, E. M. Lucas, K. A. Pettigrew, R. M. Stround, M. S. Doescher, D. R. Rolison, Sol–gel derived ceria nanoarchitectures: synthesis, characterization, and electrical properties, Chemistry of Materials, 18 (2006) 50–58.
[70] L. Yin, Y. Wang, G. Pang, Y. Koltypin, A. Gedanken, Sonochemical synthesis of cerium oxide nanoparticles- effect of additives and quantum size effect, Journal of Colloid and Interface Science, 246 (2002) 78–84.
[71] Y. Zhou, R. J. Phillips, J. A. Switzer, Electrochemical synthesis and sintering of nanocrystalline cerium(IV) oxide powders, Journal of American Ceramic Society, 78 (1995) 981–985.
[72] G. R. Bamwenda, H. Arakawa, Cerium dioxide as a photocatalyst for water decomposition to O_2 in the presence of Ce_{aq}^{4+} and Fe_{aq}^{3+} species, Journal of Molecular Catalysis A: Chemical, 161 (2000) 105-113.
[73] J. M. Coronado, A. J. Maira, A. M. Arias, J. C. Conesa, J. Soria, EPR study of the radicals formed upon UV irradiation of ceria-based photocatalysts, Journal of Photochemistry and Photobiology A: Chemistry, 150 (2002) 213-221.
[74] M. D. H. Alonso, A. B. Hungria, A. M. Arias, M. F. Garcia, J. M. Coronado, J. C. Conesa, J. Soria, EPR study of the photoassisted formation of radicals on CeO_2 nanoparticles employed for toluene photooxidation, Applied Catalysis B. Environmental, 50 (2004) 167-175.
[75] K. Qui, Y. Wang, P. Zhang, W. Zhang, Preparation of CeO_2 nanophotocatalyst using precipitation method, Materials Science Forum, 544-545 (2007) 119-122.

[76] C. Mao, Y. Zhao, X. Qiu, J. Zhu, C. Burda, Synthesis, characterization and computational study of nitrogen-doped CeO_2 nanoparticles with visible-light activity, Physical Chemistry Chemical Physics, 10 (2008) 5633-5638.
[77] J. Ameta, A. Kumar, R. Ameta, V. K. Sharma, S. C. Ameta, Synthesis and characterization of $CeFeO_3$ photocatalyst used in photocatalytic bleaching of gentian violet, Journal of the Iranian Chemical Society, 2 (2009) 293-299.
[78] P. Ji, J. Zhang, F. Chen, M. Anpo, Study of adsorption and degradation of acid orange 7 on the surface of CeO_2 under visible light irradiation, Applied Catalysis B: Environmental, 85 (2009) 148-154.
[79] W. Cai, F. Chen, X. Shen, L. Chen, J. Zhang, Enhanced catalytic degradation of AO7 in the CeO_2-H_2O_2 system with Fe3+ doping, Applied Catalysis B: Environmental, 101 (2010) 160-168.
[80] I. Bhati, P. B. Punjabi, S. Ameta, Photocatalytic degradation of fast green using nanoseized $CeCrO_3$, Macedonian journal of chemistry and chemical Engineering, 29 (2010) 195-202.
[81] H. R. Pouretedeal, A. Kadekhodaie, Synthetic CeO_2 NPs catalysis of methylene blue photodegradation: nKinetics and Mechanism, Chinese Journal of Catalysis, 31 (2010) 1328-1334.
[82] G. K. Pradhan, K. M. Parida, Fabrication of iron-cerium mixed oxide: an efficient photocatalyst for dye degradation, International Journal of Engineering, Science and Technology, 2 (2010) 53-65.
[83] N. M. Zholobak, V. K. Ivanov, A. B. Shcherbakov, O. S. Polezhaeva, A. Y. Baranchikov, Y. D. Tretyakov, UV- shielding property, photocatalytic activity and photocytotoxicity of ceria colloid solutions, Journal of Photochemistry and Photobiology B: Biology, 102 (2011) 32-38.
[84] A. B. Sifontes, M. Rosales, F. J. Mendez, O. Oviedo, T. Zoltan, Effect of calcination temperature on structural properties and photocatalytic activity of ceria nanoparticles synthesized employing chitosan as template, Journal of Nanomaterials, 2013 (2013) 9.
[85] D. Channei, B. Inceesungvorn, N. Wetchakun, S. Phanichphant, A. Nakaruk, P. Koshy, C. C. Sorrell, Photocatalytic activity under visible light of Fe doped CeO_2 nanoparticles synthesized by flame spray pyrolysis, Ceramics International, 39 (2013) 3129-3134.
[86] P. Jamahidi, M. S. Niasari, D. Ghanbari, H. R. Shams, Synthesis, Characterizations, Photoluminescence and Photocatalytic properties of CeO_2 nanoparticles by the sonochemical method, Journal of Cluster Science, 24(4) (2013) 1151-1162.
[87] S. B. Khan, M. Faisal, M. M. Rahman, K. Akhtar, A. M. Asiri, A. Khan, K. A. Alamry, Effect of particle size on the photocatalytic activity and sensing properties of CeO_2 nanoparticles, International Journal of Electrochemical Science, 8 (2013) 7284-7297.
[88] L. Ma, D. Wang, J. Li, B. Bai, L. Fu, Y. Li, Ag/CeO_2 nanosphere: Efficient catalysts for formaldehyde oxidation, Applied Catalysis B: Environmental, 148-149 (2014) 36-43.
[89] D. Channei, B. Inceesungvorn, N. Wetchakun, S. Ukritnukun, A. Nattestad, J. Chen, S. Phanichphant, Photocatalytic degradation of methyl orange by CeO_2 and Fe doped CeO_2 films under visible light irradiation, Scientific Report, 4 (2014) 5757.
[90] S. A. Ansari, M. M. Khan, M. O. Ansari, S. Kalathil, J. Lee, M. H. Cho, Band gap engineering of CeO_2 nanostructure using an electrochemically active biofilm for visible light applications, RSC Advances, 4 (2014) 16782-16791.

[91] A. D. Liyanage, S. D. Perera, K. Tan, Y. Chabal, K. J. B. Jr, Synthesis, characterization and photocatalytic activity of Y-doped CeO_2 nanorods, ACS Catalysis, 4 (2014) 577-584.
[92] W. Lei, T. Zhang, L. Gu, P. Liu, J. A. Rodriguez, G. Liu, M. Liu, Surface structure sensitivity of CeO_2 nanocrystals in photocatalysis and enhancing the reactivity with nanogold, ACS Catalysis, 5 (2015) 4385-4393.
[93] B. Mandal, A. Mondal, Solar light sensitive samarium-doped ceria photocatalysts: microwave synthesis, characterization and photodegradation of Acid Orange 7 at atmospheric conditions and in the absence of any oxidizing agents, RSC Advances, 5 (2015) 43081-43091.
[94] A. Sharma, M. Varshney, J. Park, T. K. Ha, K. H. Chae, H. J. Shin, Bifunctional $Ce_{1-x}Eu_xO_2$ ($0 \leq x \leq 0.3$) nanoparticles for photoluminescence and photocatalyst applications: An X-ray absorption spectroscopy study, Physical Chemistry Chemical Physics, 17 (2015) 30065-30075.
[95] L. Li, H. Wang, L. Zou, X. Wang, Controllable synthesis, photocatalytic and electrocatalytic properties of CeO_2 nanocrystals, RSC Advances, 5 (2015) 41506-41512.
[96] A. Younis, D. Chu, Y. V. Kaneti, S. Li, Tuning the surface oxygen concentration of {111} surrounded ceria nanocrystals for enhanced photocatalytic activities, Nanoscale, 8 (2016) 378-387.

CHAPTER 3

EXPERIMENTAL DETAILS

Overview

This chapter describes the details of the chemical used and synthesis procedure adopted to prepare undoped and doped ZnO and CeO_2 nanoparticles. Procedure followed to synthesize NPs at different pH is also discussed. Various characterization techniques used to characterize NPs has been described. The set-up of photochemical reactor and the procedure for photocatalysis of organic dyes has been discussed. At the end of the chapter brief introduction about the pollutants selected for photocatalytic study is provided.

3.1 Raw materials

For the synthesis of various doped and undoped samples, raw materials used were zinc acetate dehydrate $Zn(CH_3COO)_2.2H_2O$ (99.99% Sigma Aldrich), manganese acetate tetrahydrate $Mn(CH_3COO)_2.4H_2O$ (99.99% Sigma Aldrich), copper acetate monohydrate $Cu(CH_3COO)_2.H_2O$ (99.99% Sigma Aldrich), sodium hydroxide NaOH (≥98.0%, Sigma Aldrich), cerium nitrate hexahydrate $Ce(NO_3)_3.6H_2O$ (99.99%, Sigma Aldrich), silver nitrate $AgNO_3$ (≥98.0%, Sigma Aldrich), gold chloride $AuCl_3$ (99.0%, sigma Aldrich), hydrogen peroxide H_2O_2 (Merck), polyvinylpyrrolidone PVP (sigma Aldrich) and Thioglycerol TG (sigma Aldrich). All the chemicals were used in as received condition.

3.2 Synthesis of undoped and doped ZnO nanoparticles

For the synthesis of undoped ZnO, 40mL homogeneous solutions of 0.5M zinc acetate, (1.0 at. % (atomic %)) Thioglycerol (TG) / polyvinylpyrrolidone (PVP) and 0.5M sodium hydroxide were prepared in distilled water separately by stirring them for half an hour. Then TG / PVP solution was added to 40mL solution of 0.5M zinc acetate in aqueous medium. After half an hour of stirring 0.5M sodium hydroxide was added drop wise to the above solution with constant stirring. Soon after the addition of sodium hydroxide the precipitation phenomenon occurs and the concentration of precipitates increases as the addition was increased. The stirring was allowed for another half an hour. For the synthesis of Mn (0.5, 1.0, 1.5 and 2.0%) / Cu (1.0, 2.0, 3.0, 4.0 and 5.0%) doped and TG / PVP capped ZnO NPs, 40mL homogeneous solution of 0.5M zinc acetate and 40mL solution of 0.5M sodium hydroxide was prepared. 40mL homogeneous solution of 0.5M dopant and TG / PVP solution each were prepared in distilled water separately with constant stirring for half an hour. Firstly required amount of dopant solution was added drop wise to 40mL zinc acetate solution then after half an hour TG / PVP solution was added to same solution. After stirring of about half an hour sodium hydroxide solution was added drop wise. The stirring was allowed for another half an hour. The capping agent was used to avoid agglomeration. The precipitated particles were centrifuged at 10,000 rpm for 5min and then filtered using Whatman-40 filter paper. The particles were washed several times to remove the last traces of adhered impurities. All the wet powders were dried at 70°C in vacuum oven for 24h. Finally, the powders were calcined at 300°C for 3h to produce the nano sized doped and capped ZnO powder.

3.3 Synthesis of undoped and doped CeO_2 nanoparticles

For the synthesis of undoped CeO_2, 30mL homogeneous solution of 0.3M cerium nitrate hexahydrate, (1.0 at.%) TG and 0.3M sodium hydroxide were prepared in distilled water separately by stirring them for half an hour. For the synthesis of undoped and capped CeO_2 NPs, TG solution was added to the 30mL solution of 0.3M cerium nitrate hexahydrate in aqueous medium. After half an hour 0.3M sodium hydroxide was added dropwise to the above solution. Soon after the addition of sodium hydroxide the precipitation phenomenon occurs and purple precipitates appears within few minutes. The concentration of precipitates increases as the addition was increased and finally purple colored precipitates turned into light yellow suspensions. The stirring was allowed for another half an hour. For synthesis of Ag (1.0, 2.0 and 3.0%) / Au (0.1, 0.2, 0.3, 0.4 and 0.5%) doped and TG (1.0%) capped CeO_2 NPs, required amount of dopant was dissolved in distilled water and then pipette the particular amount of solution to 30mL homogeneous solution of 0.3M cerium (III) nitrate hexahydrate prior to the addition of TG solution. The capping agent was used for avoiding agglomeration. Different solutions containing TG (1.0%) capped undoped and Ag/Au doped CeO_2 NPs were then centrifuged at 10,000 rpm for 5min. The precipitated particles were filtered using Whatman-40 filter paper. The particles were washed several times with distilled water to remove the last traces of adhered impurities. The wet powders were dried at 70°C in vacuum oven for 24h. Finally, the powders were calcined at 250°C for 2.5h to produce the nano sized doped and capped CeO_2 powder.

3.4 Synthesis of Doped ZnO and CeO_2 nanoparticles with varying pH

Mn/Cu doped ZnO NPs and Ag/Au doped CeO_2 were synthesized by similar method as discussed in above sections. With optimal doping concentration doped ZnO and CeO_2 NPs were synthesized at varing pH. pH of solution was adjusted with the addition of NaOH till the pH of solution reaches to 8.0, 10.0 and 12.0. The reaction mixture was further stirred for 30minutes at room temperature. Then the solutions were centrifuged and washed several times to removes last traces of unreacted species. The white precipitates for doped ZnO and yellow precipitates for doped ceria were dried at 70°C for 24 hr. and then calcined at 300°C and 250°C for doped ZnO and CeO_2 respectively. Finally the powder so obtained was crushed to obtain fine powder for characterizations and photocatalysis applications.

3.5 Characterization Techniques

The as synthesized samples were characterized by X-ray diffraction (XRD) technique using Panalytical Xpert Pro MPD diffractometer with Cu (Kα) radiations. Transmission electron microscope (TEM) images were recorded using Hitachi (H-7500) operating at 80kV and high resolution transmission electron microscope (HR-TEM) images were recorded using Tecnai G2 F30 operating at 300kV. Elemental analysis of the samples was recorded with energy dispersive spectroscopy (EDS) using oxford INCA model attached to JEOL JSM-6510LV. Photoluminescence (PL) excitation and emission spectra of powdered sample has been recorded with Edinburgh Instruments FS920 spectrometer equipped with 450W Xenon Arc Lamp and a cooled single photon counting photomultiplier (Hamamatsu R2658P) and PL emission spectra was also recorded with a fluorescence spectrophotometer (Varien-Cary Eclipse). X-ray photoelectron spectroscopy (XPS) was performed using thermo scientific K-Alpha spectrometer with a monochromatized Al Kα X-ray source. The pass energy, step size and spot size were 30eV, 0.1eV and 40mm respectively. Etching of the sample was carried out in situ with a beam of Ar ions having an acceleration voltage of 1KV. High-resolution XPS (HR-XPS) data were corrected for charging by shifting peaks with respect to C peaks located at 284.8eV. Peak deconvolution was performed using the Avantage software without applying any restrictions to the spectral location and full width at half maximum (FWHM) values.

3.6 Apparatus used for photocatalytic study

A photo reactor was designed and fabricated in our laboratory for photo degradation studies. It contains three jackets. A mercury lamp having broad emission spectrum in far UV and visible region was placed axially in the innermost jacket of cylindrical vessel. The middle jacket was surrounded by circulating water intended to control the temperature during the reaction. Solution dye and prepared photocatalyst was placed in the outermost jacket and whole apparatus was then placed on the magnetic stirrer which can work on variable temperature and revolution per minute (rpm). Here all experiments were performed at room temperature and at 1500 rpm. The photocatalytic reaction was carried out with 0.25g nanopowder suspended in 100mL of dye solution. The concentration of the dye used for photocatalytic degradation was 10mg/L. At different time intervals the slurry (dye and photocatalyst nanopowder) was sampled and centrifuged at 10,000 rpm and then supernatants were analyzed by the UV–Visible

spectrophotometer to study the photocatalytic degradation dye. Three dyes viz. crystal violet (CV, λ_{max}= 590nm), Sirius red F3B (SRF3B, λ_{max}= 529nm) and rhodamine B (RhB, λ_{max}= 554nm) has been used to study the photocatalytic efficiency of as synthesized undoped and doped NPs photocatalysts.

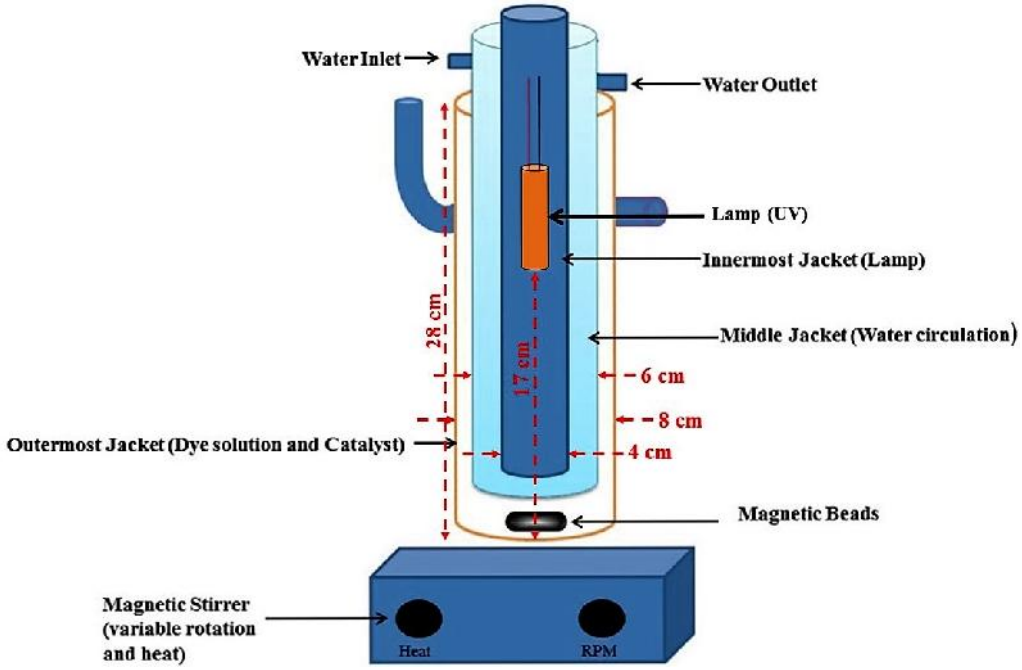

Figure3.1: Set up of photochemical reactor for photocatalytic studies.

CV, RhB and SRF3B dyes are triarylmethane, xanthenes and poly azo dyes with molecular formula $C_{25}N_3H_{30}Cl$, $C_{28}H_{31}ClN_2O_3$ and $C_{45}H_{26}N_{10}Na_6O_{21}S_6$ respectively. These dyes have wide range of applications in medical and non-medical areas. These dyes are also toxic in nature. The exposure of these toxic dyes have adverse effect on mankind and aquatic life and may lead to cancer [1] and tumor growth [2].These dyes are mitotic poison as well as clastogen in vitro [3] and genetically active [4].

References

[1] P. Drinkwater, Gentian violet- is it safe? Australian and New Zealand Journal of Obstetrics and Gynaecology, 30 (1990) 65-66.

[2] G. S. Elloit, R. W. Mason, I. R. Edwards, Journal of Toxicology Clinical Toxicology, 25 (1) (1990) 45-59.

[3] W. Au, S. Pathak, C. J. Collie, T. C. Hsu, Cytogenetic toxicity of gentian violet and crystal violet on mammalian cells in vitro. Mutation Research/Genetic Toxicology, 58 (1978) 269-276.

[4] IARC monographs on the carcinogenic risks to humans, 16 (1978) 221.

CHAPTER 4

RESULTS AND DISCUSSION

Doped and capped ZnO nanoparticles

Overview

The present chapter describes the study of doped ZnO nanoparticles (NPs) synthesized by co-precipitation method. Various techniques viz. X-ray diffraction (XRD), transmission electron microscopy (TEM), energy dispersive spectroscopy (EDS), UV-Visible spectroscopy, photoluminescence (PL) emission and excitation spectroscopy has been employed to characterize as synthesized doped and capped NPs. Photocatalytic efficiency of synthesized NPs has been studied by evaluating the degradation of crystal violet (CV) dye under UV-Visible irradiations. Further the effect of pH has also been studied in detail. Here it is important to mention that the pH of NPs has been adjusted during synthesis only.

4.1 Introduction

In recent years, advanced oxidation processes (AOPs) have attracted the scientists and the industries for its ability to convert the pollutants into the harmless substances directly in the wastewater. Till now, many kinds of semiconductors have been studied as photocatalysts including TiO_2, ZnO, CdS, ZnS, WO_3 etc. [1–5]. TiO_2 is the most widely used effective photocatalyst for its high efficiency, photochemical stability, non-toxic nature and low cost. As a contrast, ZnO, a kind of semiconductor that has the similar band gap as TiO_2, is not thoroughly investigated. However, the biggest advantage of ZnO in comparison with TiO_2 is that it absorbs over a larger fraction of UV spectrum and the corresponding threshold of ZnO is 425 nm [6]. ZnO nanopowders have been reported, sometimes, to be more efficient than TiO_2 and its efficiency has been reported to be particularly noticeable in the advanced oxidation of pulp mill bleaching wastewater [7, 8] the photo oxidation of 2-phenylphenol and photocatalysed oxidation of phenol [9]. Need for even higher photocatalytic efficiency has led to attempts of doping. The prime objective of doping the photocatalyst is to create crystal defects which improve the optical absorption in the visible region. Mn doped ZnO shows magnetic behavior and better degradation in visible region as Mn doping creates defect states which act as the intermediate steps for the electrons in their photo excitations from valence to the conduction band [10-12]. Also, silver is one of the metal that influences the photocatalytic activity of ZnO particles by trapping the photoinduced charge carriers and inhibiting the charge recombination process [13]. As silver is very expensive metal so doping with copper (Cu) in ZnO is an alternative to modify absorption and emission in visible region. Cu can enter into the ZnO lattice substitutionally as deep acceptors in combination with neighboring oxygen (O) vacancy [14]. However, optical and structural properties have strong influence on the photocatalytic properties of doped ZnO NPs. Thus to modify these properties capping agents has been used to reduce agglomeration and growth of NPs. Nanosize doped and capped ZnO NPs has been synthesized to enhance photocatalytic efficiency of as synthesized NPs. In this chapter, effect of doping and capping has been studied simultaneously to increase the photocatalytic efficiency. PVP /TG capped and Mn / Cu doped ZnO NPs have been successfully synthesized by co-precipitation route. The detail of the synthesis for doped and capped ZnO NPs has been provided in chapter 3. The as synthesized NPs have been used as a photocatalyst for the degradation of crystal violet (CV)

and Sirius red F3B (SRF3B) dyes. Apart from this, the effect of pH has also been studied to achieve maximum degradation of dyes in smaller time.

4.2 PVP capped undoped and Mn doped ZnO nanoparticles

4.2.1 XRD studies

Figure 4.1(a-e) shows XRD data for undoped ZnO and Mn (0.5-2.0%) doped and PVP (1%) capped ZnO NPs. It reveals a highly crystallized wurtzite structure (ICDD No. 36-1451) and there is no new peak in Figure 1(b-e) for Mn phase has been observed. The average crystallite size is estimated by Debye-Scherrer formula

$$D = 0.89\lambda/\beta\cos\theta \qquad \ldots\ldots(4.1)$$

where D is crystallite size (in nm), λ is the wavelength (in nm), β is the full width at half maximum (FWHM—in radian) and θ is Bragg diffraction angle (in degree) The average crystallite size is 26.4nm for undoped, 24.4nm for Mn (0.5%), 18.0nm for Mn (1.0%), 20.2nm for Mn (1.5%) doped and 21.2nm for Mn (2.0%) doped and PVP (1.0%) capped ZnO NPs.

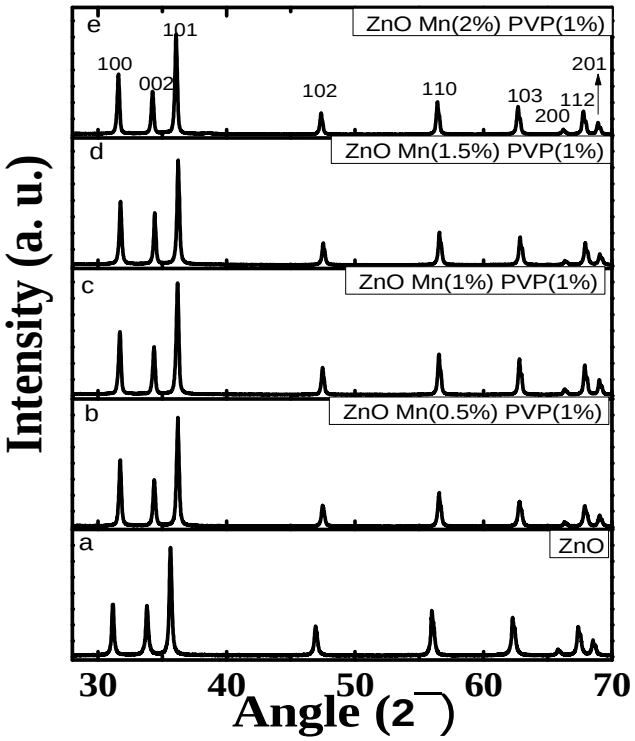

Figure 4.1: XRD pattern of (a) Undoped (b) Mn (0.5%) doped (c) Mn (1%) doped (d) Mn (1.5%) doped (e) Mn (2%) doped with PVP (1%) capped ZnO NPs.

4.2.2 TEM analysis

TEM micrograph of Mn (1% & 2%) doped and PVP (1%) capped ZnO NPs is shown in Figure 4.2(a & b) respectively. It is clear from micrograph that as synthesized doped and capped ZnO NPs exhibit spherical and hexagonal morphology. The particles are agglomerated with particle size 15–20nm and 22-25nm for Mn (1%) and Mn (2%) respectively which is close to the estimated size obtained from XRD.

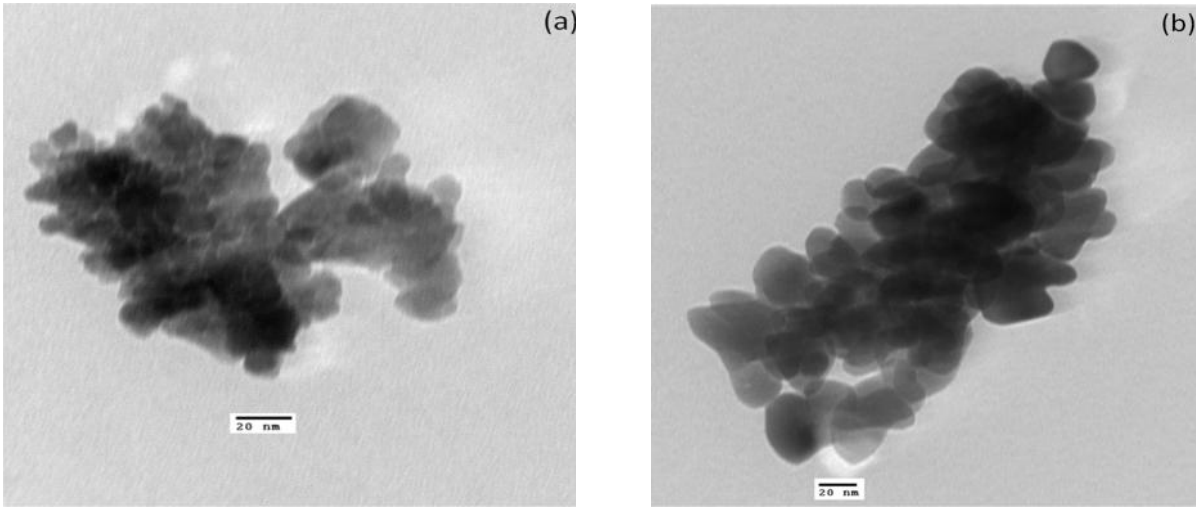

Figure 4.2: Transmission Electron Micrograph (TEM) of (a) Mn (1.0%) and (b) Mn (2.0%) doped with PVP (1.0%) capped ZnO NPs.

4.2.3 UV-Visible spectroscopy

Optical absorption spectroscopy of prepared undoped and Mn (0.5-2.0%) doped and PVP (1%) capped ZnO NPs is performed by UV-Visible absorption spectroscopy at room temperature. Figure 4.3 shows UV-Visible absorption spectra of undoped, Mn (0.5 -2.0%) doped and PVP capped ZnO NPs. It shows absorption peak at 372nm, 373nm, 368nm, 371nm and 370nm for undoped, Mn (0.5%), Mn (1.0%), Mn (1.5%) and Mn (2%) doped ZnO NPs respectively which is close to bulk counterpart having absorption peak at ~375nm. [10-12]. The weak absorption starts from 600nm which becomes strong near 370nm, which means that all samples can absorb some portion of visible light along with UV radiations. Further band gap has been calculated by using Tauc's formula which shows relationship between absorption coefficient (α) and incident photon energy (hν) and can be written as [15,16]

$$\alpha h\nu = A(h\nu - E_g)^n \qquad \ldots\ldots(4.2)$$

where A is contant, α is the absorption coefficient and n depends on the type of transition having values 1/2, 2, 3/2 and 3 corresponding to the allowed direct, allowed indirect, forbidden direct and forbidden indirect respectively [17]. The exact value of the band gap has been determined by extrapolating the straight line portion of the $(\alpha h\nu)^{1/n}$ versus hν graph. Figure 4.4 shows the graphs between $(\alpha h\nu)^2$ and hν for undoped and Mn (0.5-2.0%) doped ZnO NPs. The exact band gap values has been found to be 3.27eV, 3.13eV, 2.94eV, 2.80eV and 3.24eV for undoped, Mn (0.5%) doped, Mn (1.0%) doped, Mn (1.5%) doped and Mn (2%) doped ZnO NPs respectively. The band gap of undoped ZnO is 3.24eV. This little less value as compared to bulk ZnO is due to defects in synthesized NPs [18]. The band gap of doped ZnO NPs decreases with increase in Mn doping concentration from 0.5- 1.5% doping. After this when Mn doping concentration is increased, band gap increases to 3.24 eV which is close to undoped ZnO NPs as d-electron of Mn (t_{2g} level) can easily overlap with ZnO's valance band (VB) because t_{2g} of Mn is very close to valance band of ZnO [19]. This overlap increases the width of ZnO valance band and results in decrease in effective band gap. So the photocatalyst's valance band electrons can be excited by visible light radiations.

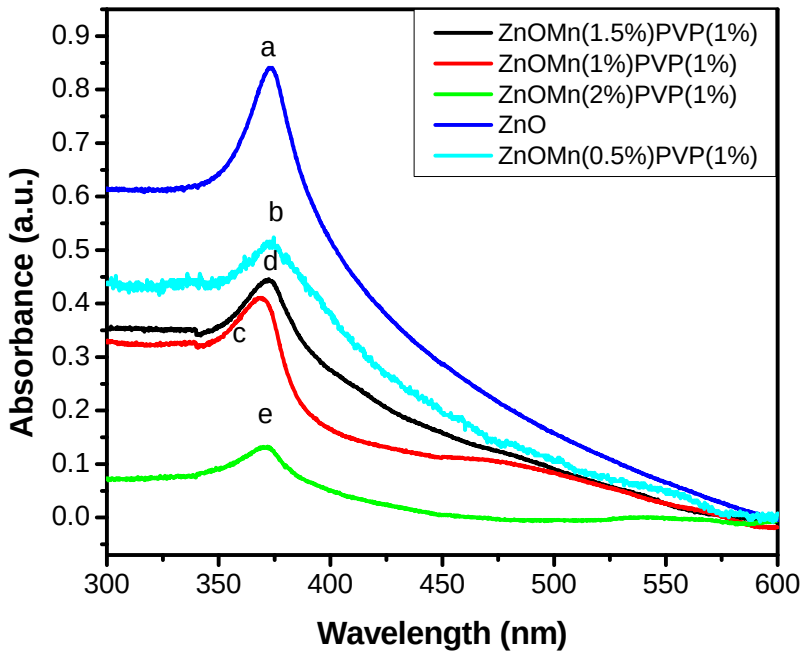

Figure 4.3: UV-Visible absorption spectra of PVP (1.0%) capped and (a) undoped (b) Mn (0.5%) doped (c) Mn (1%) doped (d) Mn (1.5%) doped (e) (2.0%) doped ZnO NPs.

However, the band gap (3.24eV) of Mn (2%) doped ZnO NPs again increases in comparison to other doped NPs. It becomes comparable to undoped NPs which may be due to increase in dopant concentration from optimum level as similar behavior has been observed in vanadium doped ZnO NPs [20]. This may be due to structural parameters, carrier concentrations and the defects such as oxygen vacancies, which may leads to Burstein Moss shift [21].

.

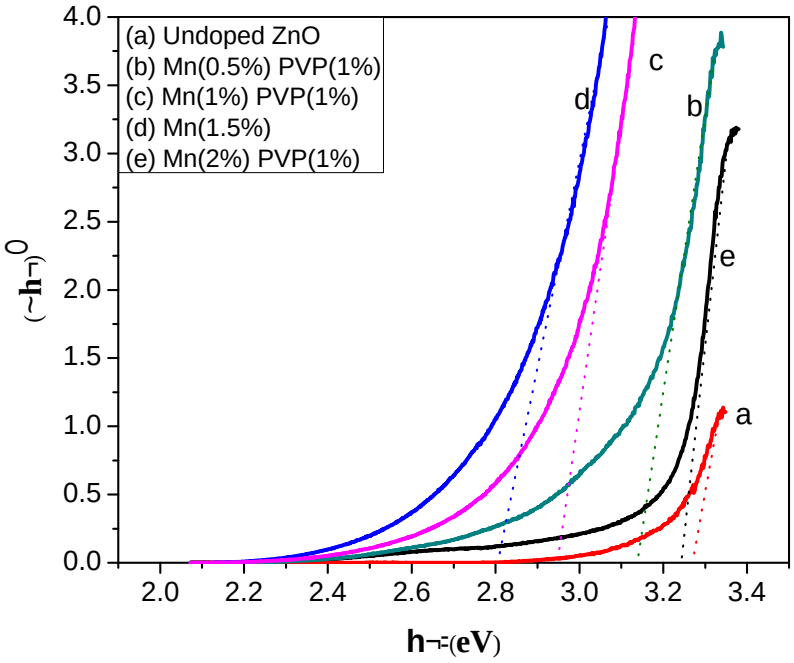

Figure 4.4: Band gap of (a) undoped (b) Mn(0.5%) doped (c) Mn (1%) doped (d) Mn (1.5%) doped (e) Mn (2%) doped and capped ZnO NPs.

4.2.4 Photocatalytic studies

Figure 4.5 shows the histogram between variations of doping concentration with percentage degradation of crystal violet (CV) for 1h only. It shows that 21.48%, 48.23%, 50.41, 60.43%, 57.12 and 58.73% of crystal violet has been degraded in 1h using UV-Visible radiations without catalyst, undoped, Mn (0.5, 1, 1.5 and 2%) doped ZnO NPs respectively. Thus maximum degradation has been achieved by Mn (1%) doped ZnO NPs. For complete degradation studies the photocatalytic activity of as synthesized undoped, Mn (1%) doped and Mn (2%) doped ZnO NPs were evaluated by degradation of crystal violet dye

molecules under UV-Visible irradiations because of their better catalytic activity in 1h. This dye was used as a test contaminant as its degradation can be easily monitored by optical absorption spectroscopy.

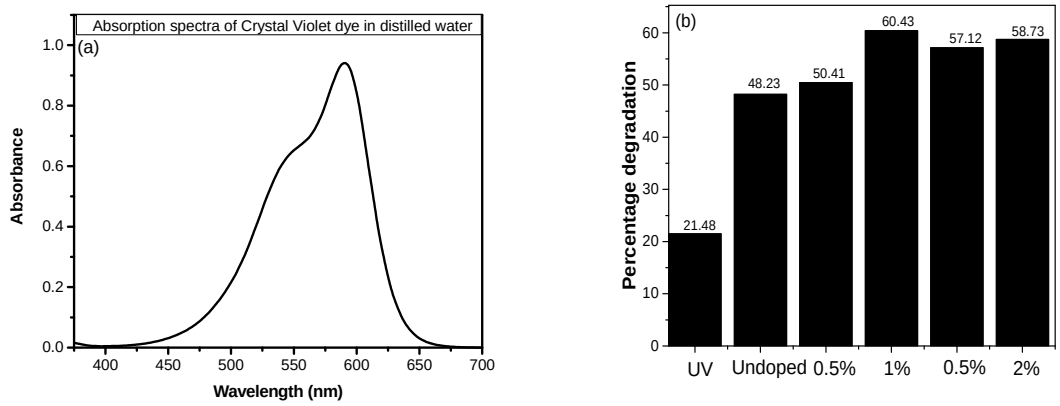

Figure 4.5: (a) Calibration curve of crystal violet dye (b) Variation of doping of Mn concentration with percentage degradation of CV.

Figure 4.6 (a-d) shows the absorption spectra of CV dye solution without catalyst, undoped ZnO, Mn (1%) doped and Mn (2%) doped with PVP (1%) capped ZnO NPs which have been taken at different intervals after exposing the solution with UV-Visible light. The intensity of absorption spectra decreases as the exposing time increases from 0 to 3h. The intensity of main peak decreases or even disappears due to degradation of CV dye.

Figure 4.7 shows a decrease in concentration of CV over time under different conditions (C is the concentration of CV determined at λ_{max} of absorption and C_0 is initial concentration). Curve (a) indicates CV dye degrades 29% only when exposed to UV- Visible irradiations for 3h without catalyst. However, curves (b, c & d) indicate 79.5%, 98.1% and 97.5% of CV dye has been degraded with undoped, Mn (1%) doped and Mn (2%) doped ZnO NPs respectively. Inset of Figure 4.7 also demonstrate that Mn (1%) doped NPs shows better degradation efficiencies as compared to Mn (2%) doped ZnO NPs. From this it can be concluded that photocatalyst is necessary factor in photocatalytic process. Although CV has been degraded sufficiently with undoped ZnO but doped and capped ZnO has shown faster degradation. Therefore doping of ZnO is necessary to degrade CV completely which increases its degradation rate. Also CV dye has been degraded to almost 100% using Mn (1%) doped PVP (1%) capped ZnO NPs. The degradation of crystal violet for Mn (2%) doped ZnO NPs is lower than that of Mn (1%) doped ZnO NPs. This observation can be explained on the basis that Mn (1%) doped ZnO has better incorporation of Mn dopant

and smaller particle size (confirmed from XRD studies shown above) as compared to other synthesized NPs.

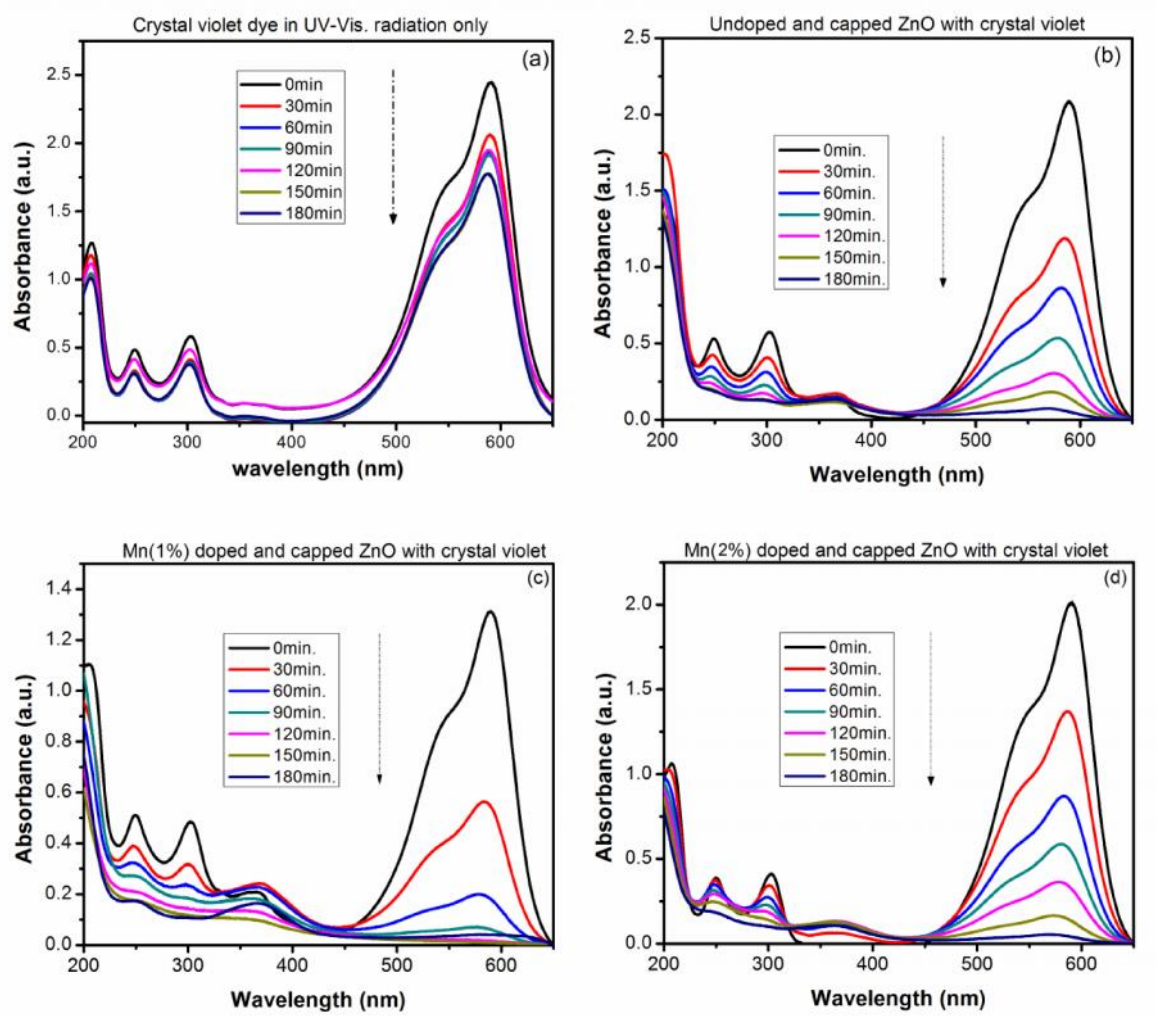

Figure 4.6: Absorption spectral changes of crystal violet dye aqueous solution (10mg/L) degraded by (a) UV-Visible radiations only (b) Undoped (c) Mn (1%) doped and (d) Mn (2%) doped and PVP (1%) capped ZnO NPs.

Therefore, surface to volume ratio for Mn (1%) doped and PVP (1%) capped ZnO NPs is higher and activity of photocatalyst depends on the adsorption amount of dye molecules on the surface of the photocatalyst and also doping induced surface defects in nanoparticles which contribute strongly to higher photocatalytic activity. This has been discussed later in PL studies.

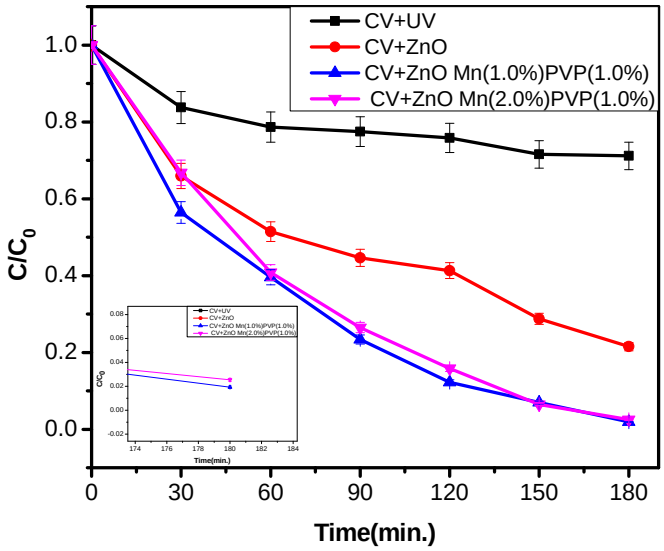

Figure 4.7: Photo degradation of crystal violet under different conditions, Curves: (a) without catalyst under UV-Visible (b) with undoped and capped ZnO (c) With Mn (1%) doped and PVP (1%) capped (d) With Mn (2%) doped and PVP (1%) capped ZnO NPs. (Inset presents the difference in degradation efficiency of Mn (1%) and Mn (2%) doped ZnO NPs.

Figure 4.8 shows the change in color of CV dye when exposed to UV-Visible radiations for 0- 3h with Mn (1%) doped ZnO NPs. The color of CV dye has been changed from violet to colorless after 3h. This change in color shows that dye has been almost degraded 100% using Mn (1%) doped ZnO NPs.

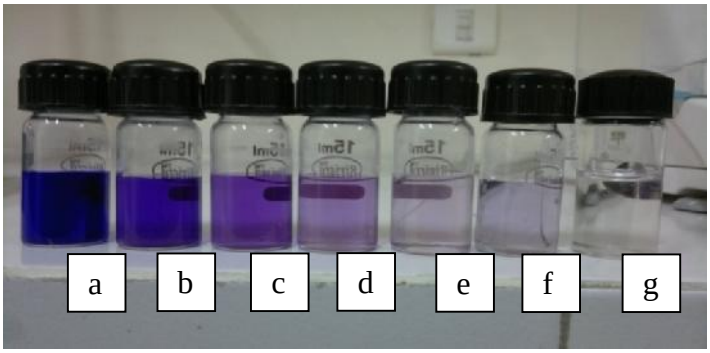

Figure 4.8: Change in color of crystal violet dye with Mn (1%) doped and PVP (1%) capped ZnO NPs in UV-Visible radiations at (a) 0min (b) 30min (c) 60min (d) 90min (e) 120min (f) 150min and (g) 180min.

The photocatalytic decomposition of CV on the surface of ZnO NPs also follows a pseudo first-order kinetic law, and can be expressed as,

$$-\ln C/C_0 = kt \qquad \ldots\ldots(4.3)$$

where C and C_0 are the reactant concentration at time t = t and t = 0, respectively. k and t are the pseudo-first-order rate constant (reaction rate constant) and time, respectively [22]. The relationship between $-\ln (C/C_0)$ and irradiation time (Reaction time) are shown in Figure 4.9. It is obvious that there exists a linear relationship between $-\ln (C/C_0)$ and irradiation time. The pseudo-first-order rate constant k and linear regression coefficient (R) for degradation of crystal violet without catalyst, undoped ZnO, Mn (1%) doped and Mn (2%) doped ZnO NPs are summarized in Table 4.1. It shows that photoreaction rates are highest for Mn (1%) doped NPs followed by Mn (2%) doped NPs and undoped ZnO NPs. Reaction rate is least for UV-Visible radiations without any catalyst.

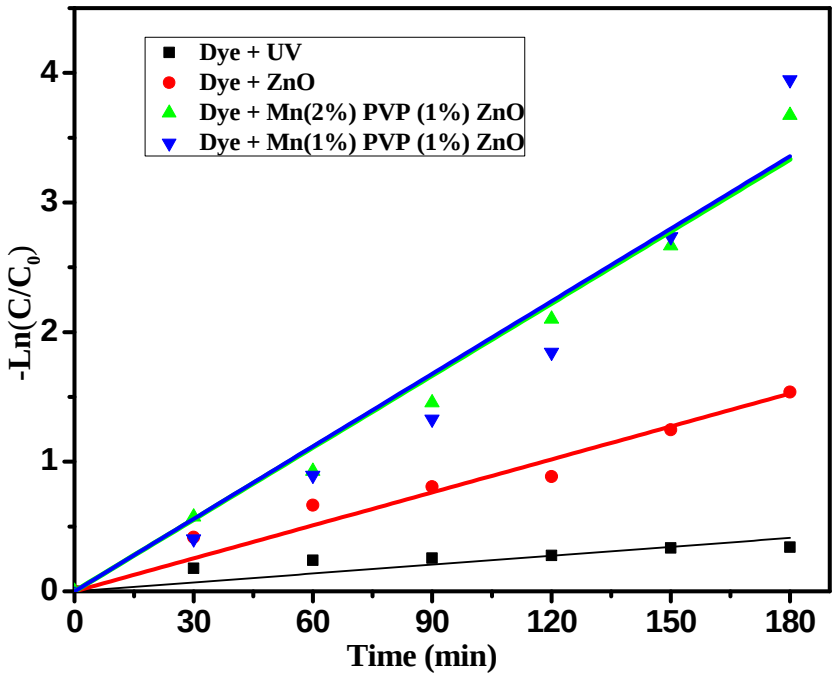

Figure 4.9: Kinetics of crystal violet degradation with UV, undoped ZnO, Mn (1%) doped and PVP (1%) capped ZnO and Mn (2%) doped and PVP (1%) capped ZnO NPs.

The enhanced photo catalytic activity as discussed above may be due to the surface charge modification and passivation of surface electronic states of ZnO by PVP capping. The above study indicates that after 3h of irradiation, the absorption peaks almost disappears. This process indicates that most of the conjugated structures of dye disappear after the photo catalytic process. Since Mn (1%) doped ZnO NPs has smaller band gap as

shown by UV-Visible absorption spectra so it can be excited better in UV-Visible region.

Table 4.1: Reaction rate constant of crystal violet without catalyst, undoped, Mn (1% and 2%) doped with PVP (1%) capped ZnO NPs.

Experiment	Concentration of crystal violet dye(mg/L)	Catalyst concentration (g/100mL)	K (min^{-1}) (Rate constant)	R^2	K (min^{-1}) (Rate constant)
1	10	Without catalyst 0.25	0.00163	0.82307	----
2	10	ZnO (Undoped) 0.25	0.00772	0.96773	0.0023 [23]
3	10	ZnO Mn(2%) PVP (1%) 0.25	0.0195	0.9808	------
4	10	ZnO Mn(1%) PVP (1%) 0.25	0.02078	0.95272	0.0025 [23]

4.2.5 Reusability

The reusability of photocatalyst has been investigated in order to establish stability of catalyst and degree of photo degradation of CV. Mn (1%) doped sample has been taken to check the reusability because of its high degree of degradation as compare to others. The reaction mixture (retrieved catalyst + slurry) was filtered and washed with double distilled water and then dried at 70^0 C for 24h in an oven. Finally, the powder was calcined at 300^0C for 3h. The recovered photocatalyst has been again used to degrade CV using same concentration used above. Figure 4.10 shows the photo stability of Mn (1%) doped ZnO NPs. Curve (a) shows the degradation of CV with actual sample whereas the curve (b) shows the reusability of the same sample. It has been found that the reused catalyst degrade almost 100% of CV after 3h whereas 98.1% of CV was degraded with first time used doped and capped sample. This means the photocatalytic properties of the as prepared catalyst has been slightly increased after when it has been exposed to UV-Visible irradiations. However, it has been reported by many researchers that the photocatalytic activity of the catalyst reduces after reusing the same catalyst [24, 25]. But in our case photocatalytic activity increases on reusing the same sample. To check this

different observation, the prepared sample was first exposed to UV-Visible radiations only for 3h and then again used for degradation that study for the CV dye of same concentration. Curve (c) shows the similar results as of curve (b). This shows photocatalytic properties of prepared sample has been slightly improved after exposures to UV-Visible radiations. Earlier it is reported that ZnO NPs with UV treatment displays a low water contact angle which indicates more hydrophilic ZnO surface. This is attributed to surface modification which leads to the transition from hydrophobic (low energy state) to hydrophilic (high surface energy) state, resulting in uniform distribution of ZnO nanoparticles on the substrate [26].

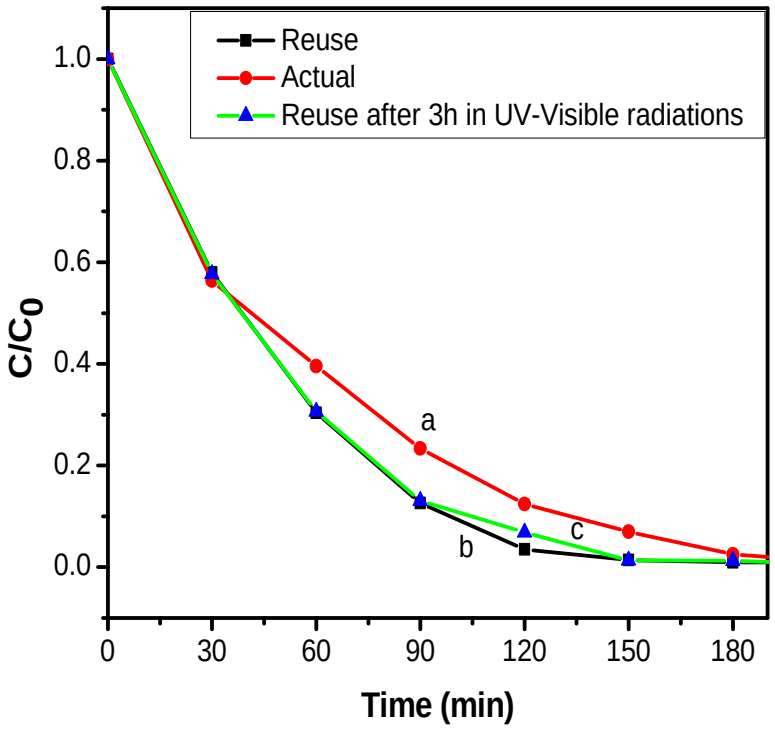

Figure 4.10: Photochemical experiment to observe photo stability of Mn (1%) doped and PVP (1%) capped ZnO NPs. Curve (a) First time used Mn (1.0%) doped with PVP (1.0%) capped ZnO NPs (b) Reused Mn (1.0%) doped with PVP (1.0%) capped ZnO NPs (c) Reused after placing 3h in UV-Visible radiations.

In our case also UV treatment results in enhanced optical and catalytic properties. These results are observed by UV-Visible spectra. Figure 4.11 shows the UV-Visible spectra of Mn (1%) doped ZnO NPs before and after UV treatment for 3h. The absorbance of sample after 3h UV treatment is higher as compare to without UV treated sample.

Figure 4.12 (a) shows the typical room temperature photoluminescence spectra of as prepared undoped and Mn (1%) doped NPs whereas Figure 4.12(b) shows PL spectra of Mn (1%) doped and PVP (1%) capped ZnO NPs without and with UV treatment for 3h when excited at 325nm wavelength. Figure 4.12 (a) clearly shows shifting of emission peak from UV (380nm, band edge emission) for undoped to broad peak in green region (400-528nm, defect/dopant related emission) for Mn (1%) doped ZnO NPs which is due to the presence of energy states of dopant Mn between conduction band and valance band of host ZnO NPs.

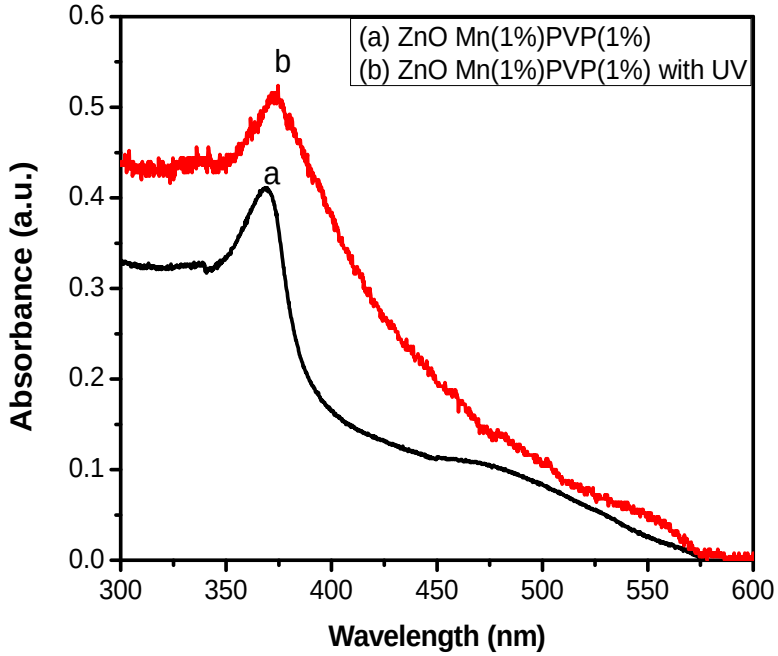

Figure 4.11: UV-Visible absorption spectra of Mn (1%) doped and PVP (1%) capped ZnO NPs (a) Without UV (b) With UV treatment.

In Figure 4.12(b), broad visible emission peaks including violet emission at ~ 423nm (~2.93eV), blue emission at ~ 447nm (~2.78eV), blue-green emission at ~ 484nm (~ 2.56eV) and green emission at ~ 528nm (~ 2.35eV) have been observed. Visible emission in ZnO consist of blue, violet, green and yellow emission peaks that can be attributed to different intrinsic defects such as oxygen vacancies (V_o), Zinc vacancies (V_{zn}), oxygen interstitials (O_i), zinc interstitials (Zn_i) and oxygen antisites (O_{zn}) [25]. The violet emission at ~ 423nm (~ 2.93eV) is attributed to an electron transition from a shallow donor level to neutral Zn_i to top level of valance band [26]. The blue emission centered around ~447nm (~ 2.78eV) is attributed to singly ionized V_{zn}^- [26, 27]. A blue green emission centered at

around ~ 484nm (~ 2.56eV) is due to a radiative transition of an electron from the shallow donor level of Zn_i to an accepter level of neutral V_{zn} [28]. The green emission centered at ~528nm (~2.35eV) is attributed to radiative transition from conduction band to the edge of acceptor levels of O_{zn} caused by oxygen antisites [27, 29]. The UV peak is usually considered as the characteristic emission of ZnO and attributed to the band edge emission. But there are many reports that showed the band edge emission of ZnO was absent in their luminescence spectra [30, 31]. Generally the UV emission in ZnO disappears in two cases. Firstly, if the excitation energy is considerably lower than its band gap energy [30] and second, if the intensity of visible emission is much higher due to increased defect density [32, 33]. Since in our case the defects are strongly present so they increase the intensity in visible region. Also defects and dopants (Mn in our case) in crystals create energy states within the band gap which act as intermediate steps for electrons in their transitions between the valence and conduction bands as a result of photo excitation. Hence UV emission is absent and maximum emission is in visible region.

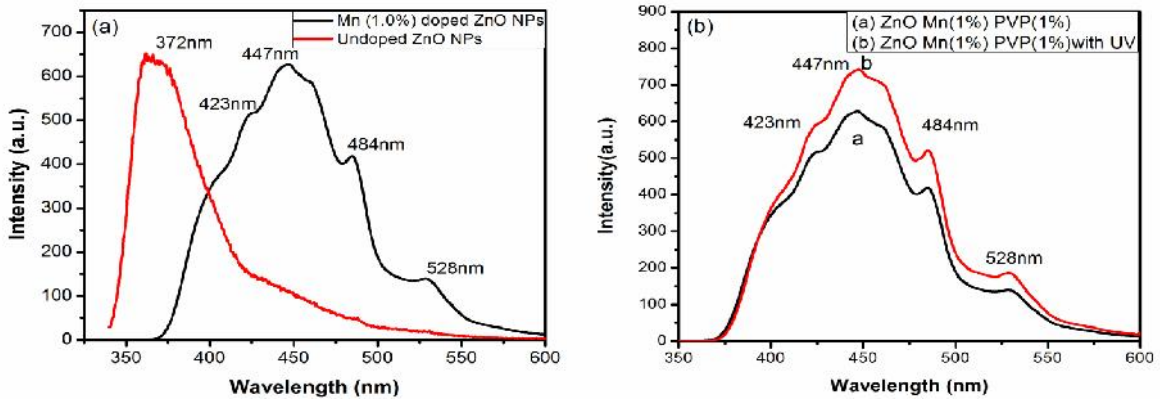

Figure 4.12: (a) PL spectra of undoped and Mn (1%) doped ZnO NPs, (b) PL spectra of Mn(1%) doped PVP(1%) capped ZnO NPs with and without UV treatment for 3h excitation at 325nm.

Further both PL curves (with and without UV treatment) shows emission peaks at almost same wavelength. However, the intensity of Mn (1%) doped and PVP (1%) capped ZnO NPs after 3h UV treatment (curve (b)) is higher as compared to Mn (1%) doped and PVP (1%) capped ZnO NPs without UV treatment. The increase in intensity is due to passivation of surface defect after UV radiation. As the UV treatment increase the surface energy and causes some decrease in particle size [25], so the surface to volume ratio of UV treated

sample increases. Also the transition from hydrophobic to hydrophilic nature of the treated sample has increased the degradation of CV dye.

4.3 TG capped undoped and Mn doped ZnO nanoparticles

4.3.1 XRD studies

The XRD pattern of TG (1.0%) capped undoped and Mn (0.5-2.0%) doped ZnO NPs synthesized at natural pH is shown in Figure 4.13. The diffraction peaks corresponding to (1 0 0), (0 0 2), (1 0 1), (1 0 2), (1 1 0), (1 0 3), (2 0 0), (1 1 2) and (2 0 1) planes reveals a highly crystalline hexagonal wurtzite structure (JCPDS No. 36-1451). There is no extra peak corresponding to Mn, oxides of Mn or Mn related secondary and impurity phases in Figure 4.13 confirming that manganese has been incorporated to ZnO lattice rather than interstitial ones. The average crystallite size is estimated by Debye- Scherer formula is 38nm for undoped, 16 nm for Mn (0.5%), 13 nm for Mn (1.0%), 28 nm for Mn (1.5%) and 20 nm for Mn (2.0%) doped and TG (1.0%) capped ZnO NPs.

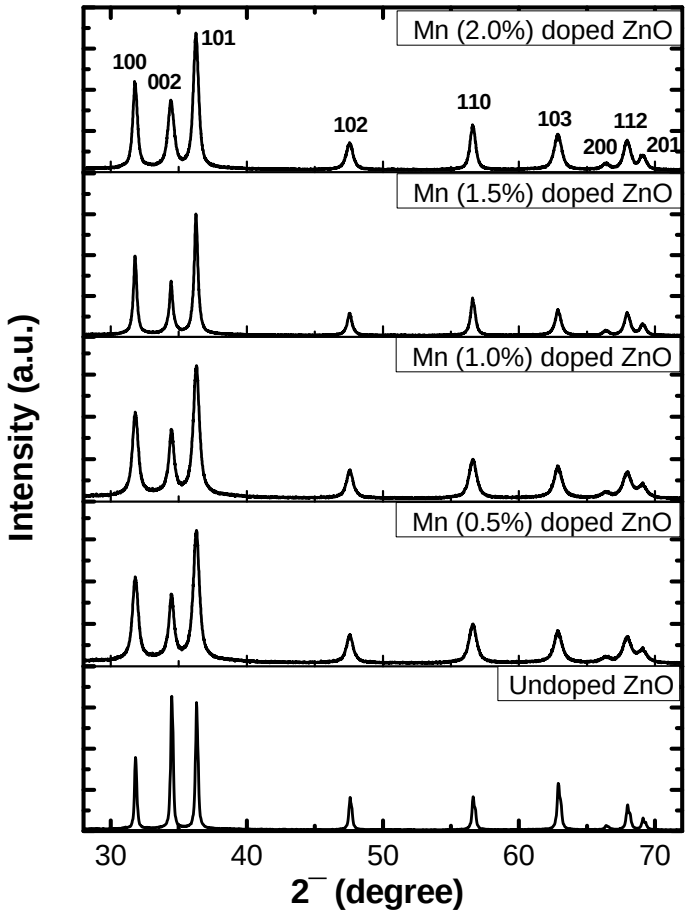

Figure 4.13: XRD pattern of Mn (0.5–2.0%) doped and TG (1.0%) capped ZnO NPs.

4.3.2 TEM studies

TEM micrographs of Mn (1.0%) doped and TG (1.0%) capped ZnO NPs synthesized at various pH values are shown in figure 4.14(a-d). It is clear from micrographs that Mn (1.0%) doped ZnO NPs at different pH have spherical morphology. Figure 4.14(a) shows Mn (1.0%) doped ZnO NPs synthesized at pH-6.7 have agglomerated spherical shape particles with average particle size of 12-18nm. Mn (1.0%) doped ZnO NPs synthesized at pH-8.0, 10.0 and 12.0 as shown in Figure 4.14(b, c and d) also have agglomerated spherical particles with average particle size lying between 10-15nm.

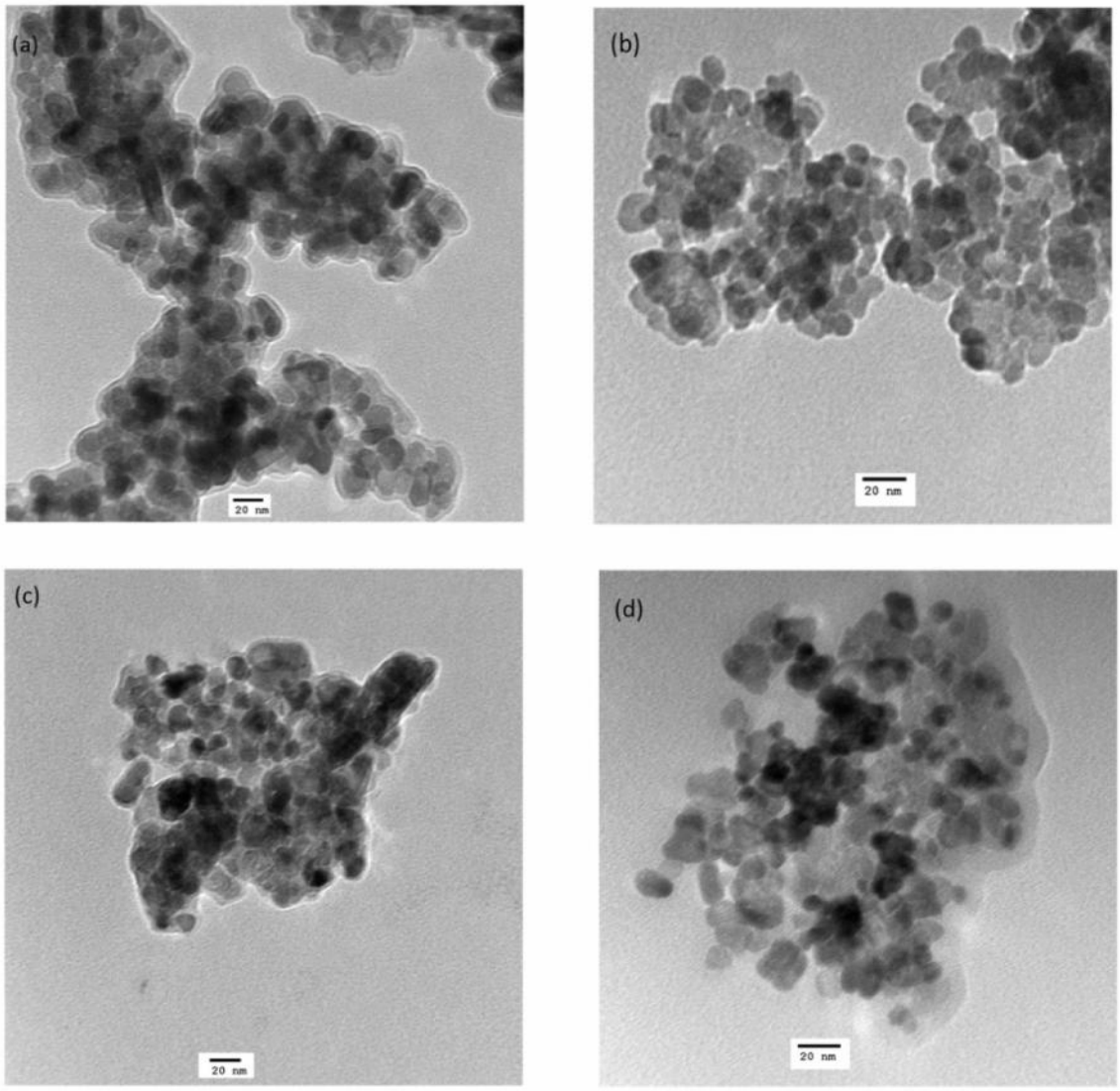

Figure 4.14: TEM images of Mn (1.0%) doped ZnO NPs synthesized at (a) pH-6.7 (b) pH-8.0 (c) pH-10.0 and (d) pH-12.0.

4.3.3 UV-Visible spectroscopy

Optical absorption spectroscopy of prepared undoped and Mn (0.5-2.0%) doped ZnO NPs is performed by UV-Visible absorption spectroscopy at room temperature. Figure 4.15(a) shows the absorption spectra of undoped and Mn (0.5-2.0%) doped ZnO NPs at natural pH i.e. at pH-6.7 and Figure 4.15(b) shows the absorption spectra of Mn (1.0%) doped ZnO NPs at various pH values i.e. at pH- 6.7 (natural pH), 8.0, 10.0 and 12.0. It can be seen from Figure 4.15(a, b) that there is strong excitonic absorption peak for all as prepared samples. Figure 4.15(a) shows the absorption peaks at 364nm, 358nm, 365nm, 364nm and 364nm for undoped, Mn (0.5%), Mn (1.0%), Mn (1.5%) and Mn (2.0%) doped ZnO NPs respectively. Figure 4.15(b) shows the absorption peak at 365nm, 367nm, 354nm and 371nm for Mn (1.0%) doped ZnO NPs at pH-6.7, 8.0, 10.0 and 12.0 respectively. These peaks in all samples are blue shifted in comparison to bulk ZnO having absorption peak at ~375nm [10]. All these blue shifted peaks attributed to large exciton binding energy and good optical quality of synthesized doped ZnO NPs. The weak absorption in all synthesized samples starts from 650nm and becomes strong around 360nm. The band gap has been calculated by using Tauc's formula. Figure 4.16(a & b) show the graphs between $(\alpha h\nu)^2$ and hν for undoped and Mn (0.5-2.0%) doped ZnO NPs at natural pH and Mn (1.0%) doped ZnO NPs synthesized at pH-6.7 (natural), 8.0, 10.0 and 12.0. The band gap values obtained are 3.20eV, 3.24eV, 3.00eV, 2.77eV and 3.13eV for undoped, Mn (0.5%), Mn (1.0%), Mn (1.5%) and Mn (2.0%) doped ZnO NPs synthesized at pH-6.7 and 3.28eV, 3.15eV and 3.05eV for Mn (1.0%) doped ZnO NPs synthesized at pH- 8.0, 10.0 and 12.0 respectively.

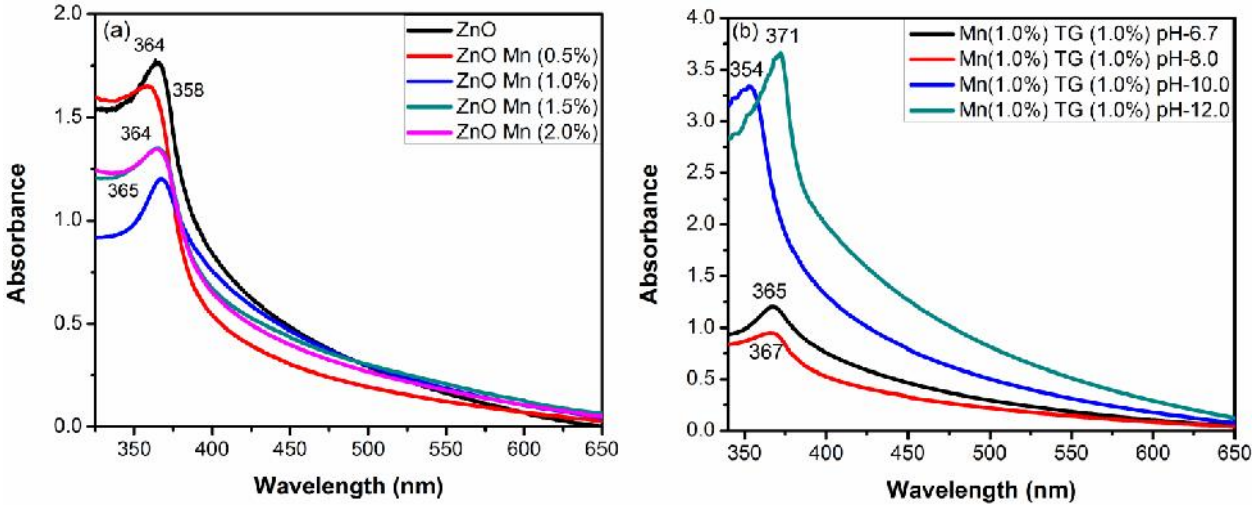

Figure 4.15:.UV-Visible absorption spectra of (a) Mn (0.5-2.0%) doped ZnO NPs (b) Mn (1.0%) doped ZnO NPs synthesized at different pH values.

The band gap of doped ZnO NPs decreases as the doping concentration increases from 0.5% to 1.5%. This decrease in band gap of doped ZnO NPs is because the d-electron of Mn (t_{2g} levels) can easily overlap with ZnO valence band and this results in decrease in effective band gap [19]. So, the photocatalyst's valence band gap can now be excited by visible light radiations. However, when Mn doping concentration increases to 2.0%, the band gap increases in comparison to other doped ZnO NPs and reaches to 3.13eV which may be attributed to increase in doping concentration from optimum level as similar behavior has been observed in vanadium doped ZnO NPs [20]. This may be due to carrier concentration, structural parameter and defects due to oxygen vacancy which leads to Burstein Moss Shift [21]. Also, the band gap values calculated for doped NPs synthesized at pH-10.0 and 12.0 are significantly lesser than undoped ZnO NPs and thus may act as a better photocatalyst in UV-Visible light radiations (discussed later).

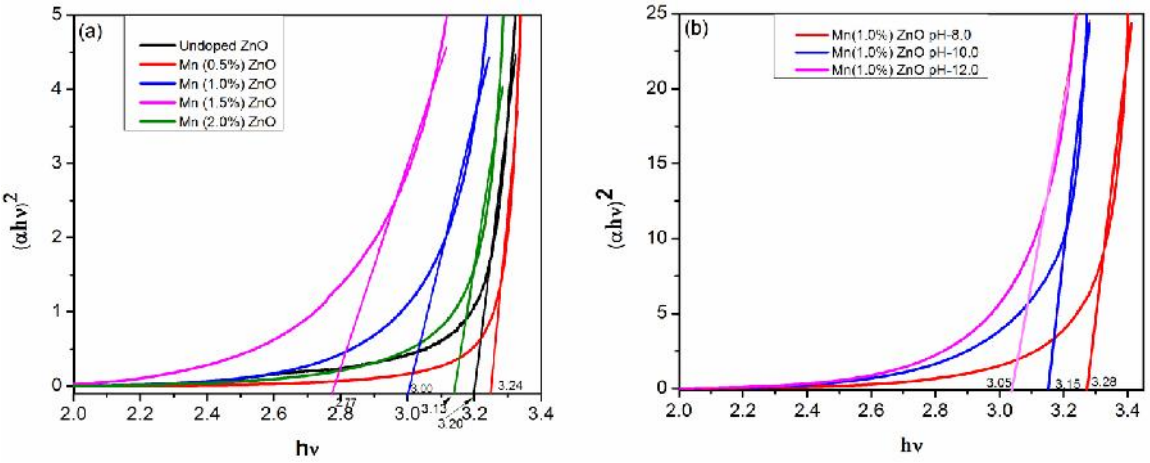

Figure 4.16: Tauc's plot for (a) Mn (0.5-2.0%) doped ZnO at pH-6.7 and (b) Mn (1.0%) doped ZnO NPs synthesized at different pH values.

4.3.4 Photoluminescence studies

4.3.4.1 Excitation studies

Room temperature photoluminescence excitation spectra of undoped and Mn (1%) doped ZnO NPs monitored at 468nm emission are shown in Figure 4.17. It has been found that undoped ZnO NPs shows broad excitation peak at 307nm with small peak at 407nm. In comparison to undoped ZnO NPs, Mn (1.0%) doped ZnO NPs shows sharp excitation peaks in UV region lying at 302nm, 323nm and 378nm and one broad absorption peak in visible region at 439nm. The broad absorption in between 370-450 nm comprises of three absorptions, assigned to $6A_{1g}(S) \rightarrow 4A_{1g}(G)$, 4 $E_g(G)$ and $6A_{1g}(S) \rightarrow 4\ T_{2g}(G)$ transition [19].

The broad absorption peak in visible region appear due to the energy levels created by Mn atom in the host ZnO NPs. The relative absorption intensities of Mn doped and undoped ZnO ($I_{Mn\ doped/undoped}$) are very high for the peaks considered around 307 nm and 439 nm.Thus PLE spectra show that energy levels have been created by impurity (Mn) atoms in the host ZnO samples therefore doped sample has better absorption in visible region as compared to undoped ZnO NPs.

4.3.4.2 Emission studies

Photoluminescence emission spectra of undoped and Mn (1.0%) doped ZnO NPs in powdered form which are synthesized at various pH values at 325nm excitation is shown in Figure 4.18. Inset of Fig 4.18(a) shows magnified view of undoped ZnO NPs having strong emission peaks both in UV and Visible region. The UV emission mainly originates from near-band-edge (NBE) transitions in band gap of ZnO while the visible emission belongs to defect states such as impurities and oxygen vacancies in ZnO.

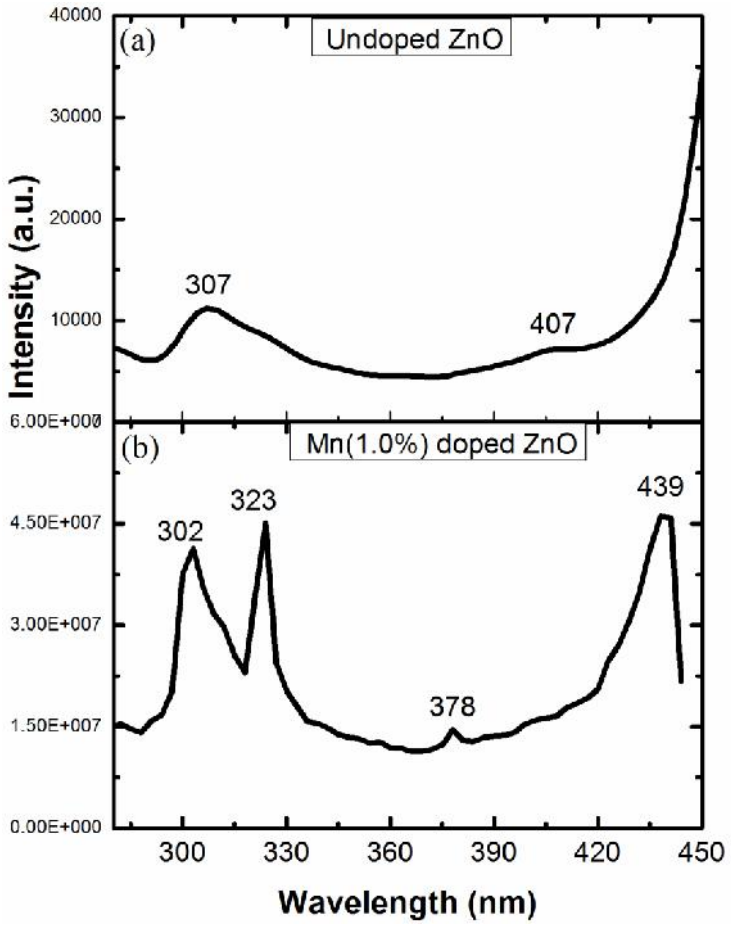

Figure 4.17: PLE spectra of (a) Undoped and (b) Mn (1.0%) doped ZnO NPs at λ_{em} = 468nm.

On the other side Mn (1.0%) doped ZnO NPs synthesized at different pH shows very weak emission in UV region (380 nm) and strong emission in visible region (469 nm) along with small peaks at 532 and 612 nm. Emission intensity in UV region w.r.t. visible region in Mn doped NPs is very less as compared to undoped ZnO NPs. Thus incorporation of Mn ions into ZnO lattice leads to partial quenching of the band edge emission of ZnO. Mn doped II-VI nanomaterials generally emits fixed 590nm emission due to well-known d-d transitions [$6A_{1g}(S) \rightarrow 4\ T_{1g}(G)$] of Mn which lie in wide band gap of semiconductors [17,34]. In case of Mn doped ZnO NPs this well-known 590nm emission is absent. This has already been discussed in UV Visible absorption studies and earlier reports that d- states of Mn (t_{2g} levels) can easily overlap with ZnO valence band (V.B) and this results in quenching of 590nm emission and results in decrease in effective band gap [19]. So overlap of one state (t_{2g}) of Mn with host V.B and presence of upper d state $6A_{1g}(S)$ in band gap helps to dissociate electron and hole wave function and decrease recombination. This is clear from PL studies that with doping both band edge (380nm) of host ZnO decreases and d-d transitions (590nm) of dopant Mn are absent. Weak blue emission lying at 469nm can be due to the recombination of one d state $6A_{1g}(S)$ of Mn and defect states of ZnO host [35].

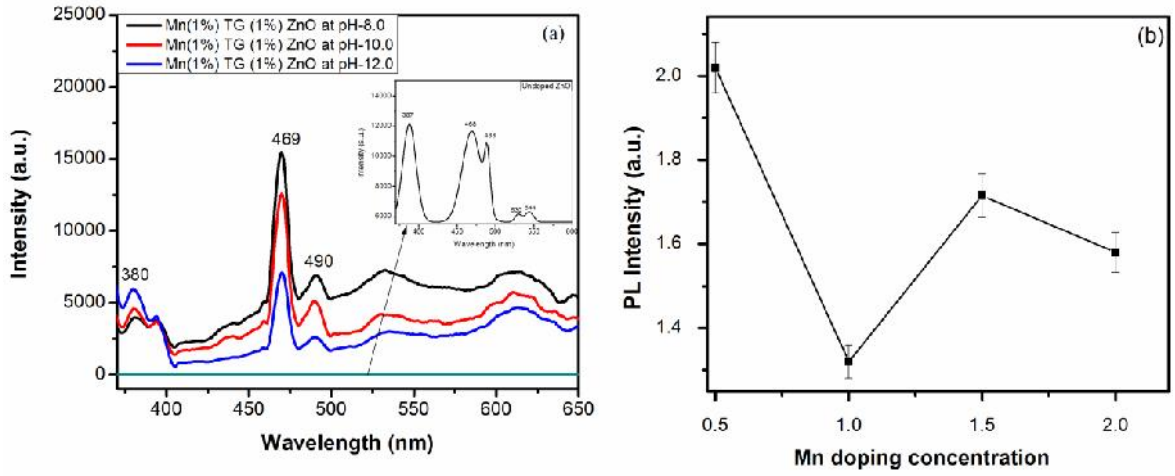

Figure 4.18: PL emission spectra of (a) Mn (1.0%) doped ZnO NPs synthesized at pH-8.0, 10.0 and 12.0 at λ_{ex} = 325 nm and (b) Variation of Mn doping concentration with PL emission intensities.

Figure 4.18(b) shows that Mn (1.0%) doped NPs PL emission intensity is minimum which suggests that at this optimum doping concentration electron hole recombination is minimum. From Figure 4.18(a) it can be observed that emission peak intensity of optimum doped NPs

further decreased with increase in pH value from 8.0 to 12.0. This might be due to further reduction of recombination rate of electron and holes because Mn ions act as electron scavenger and increased pH helps to decrease recombination which is discussed in photocatalytic studies later.

4.3.5 Photocatalytic studies

Figure 4.19(a) shows the histogram representing the variations of doping concentration with percentage degradation of CV for 1h only. It shows that under UV-Visible radiations 10.48%, 20.25%, 38.21, 66.10%, 42.26% and 52.35% of crystal violet has been degraded in 1 h without using any photocatalyst, using undoped NPs, Mn (0.5, 1.0, 1.5 and 2.0%) doped ZnO NPs as a different photocatalyst respectively.

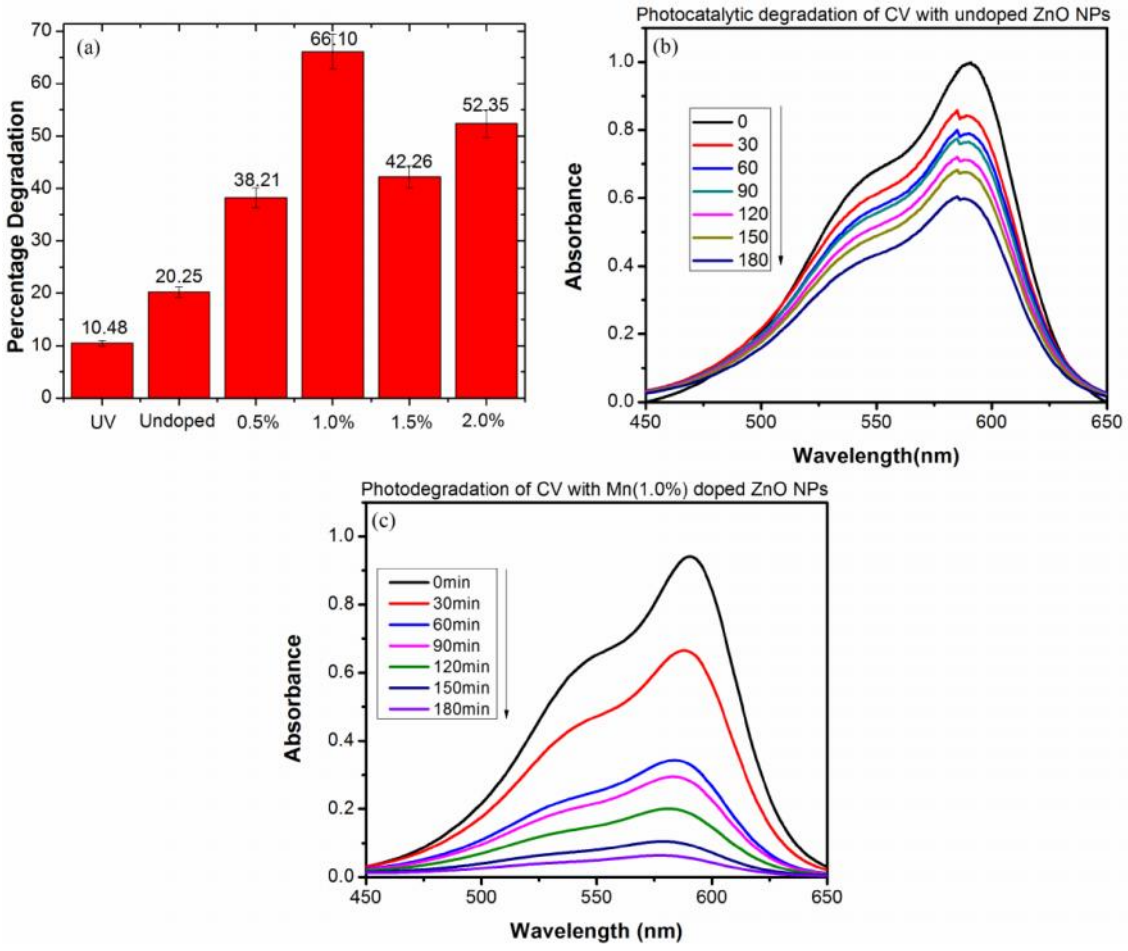

Figure 4.19: (a) Histogram for percentage degradation of CV dye at different conditions under UV-Visible radiations for 1h. Change in optical absorption spectra of CV dye aqueous solution (10 mg/L) with (b) undoped and (c) Mn (1.0%) doped ZnO NPs.

Thus maximum degradation has been achieved by Mn (1.0%) doped ZnO NPs. For complete degradation studies, the photocatalytic activity of as synthesized undoped, Mn (1%) doped and Mn (2%) doped ZnO NPs were evaluated by degradation of CV dye molecules under UV-Visible irradiations because of their better photocatalytic activity in 1h. This dye was used as a test contaminant owing to its absorption peaks in visible range and its degradation can be easily monitored by optical absorption spectroscopy. The changes in optical absorption spectra of CV dye with undoped and Mn (1.0%) doped ZnO NPs synthesized at pH- 6.7 is shown in Figure 4.19(b, c). The spectra have been taken after 30min. intervals after exposing the solution under UV-Visible light. The intensity of absorption spectra decreases as the exposing time increases from 0 to 3h. The intensity of main peak lying at 589nm decreases due to degradation of CV dye.

Figure 4.20(a) shows the change in concentration of CV dye as a function of irradiation time for the dye derivatives in absence and presence of undoped, Mn (1.0%) and Mn (2.0%) doped ZnO NPs. Here 'C' is the concentration of CV determined at λ_{max} of absorption and 'C_0' is initial concentration. Figure 4.20(b) shows the percentage degradation of CV dye under different conditions. It shows that 22% of CV dye dissolved in water disappears in 3h of UV-Visible radiations in the absence of any photocatalyst. This smaller degradation of CV dye might be due to the interaction between $OH^{\cdot}$ radical generated from water molecules and CV dye. 40% of CV dye has been degraded with undoped ZnO NPs. Photocatalytic activity of undoped ZnO NPs are due to defect states caused by donor and acceptor states such as oxygen vacancies, interstitial zinc atom and zinc vacancies and interstitial oxygen respectively. Interfacial electron transfer takes place between donor state and CV dye. As CV dye is cationic in nature so it acquire electron from donor excited state and get decomposed. Figure 4.20(b) shows 92.6% and 69.7% of CV dye degraded with Mn(1.0%) and Mn (2%) doped ZnO NPs synthesized at pH- 6.7 when exposed to UV-Visible light radiations for 3h. Thus photocatalyst is necessary for photocatalytic reaction. Mn doped ZnO samples have shown better degradation as compare to undoped ZnO NPs. As discussed earlier in excitation and emission spectroscopy studies Mn doping in ZnO NPs modify the energy band of ZnO, through the creation of localized Mn dopant energy levels within the bandgap. Under UV-visible light illumination, the photogenerated electrons could easily transfer from the VB of ZnO to the localized Mn energy levels, along with the d-d transitions between the Mn dopant energy levels. The excited electrons were readily trapped in these Mn dopant sites, while the

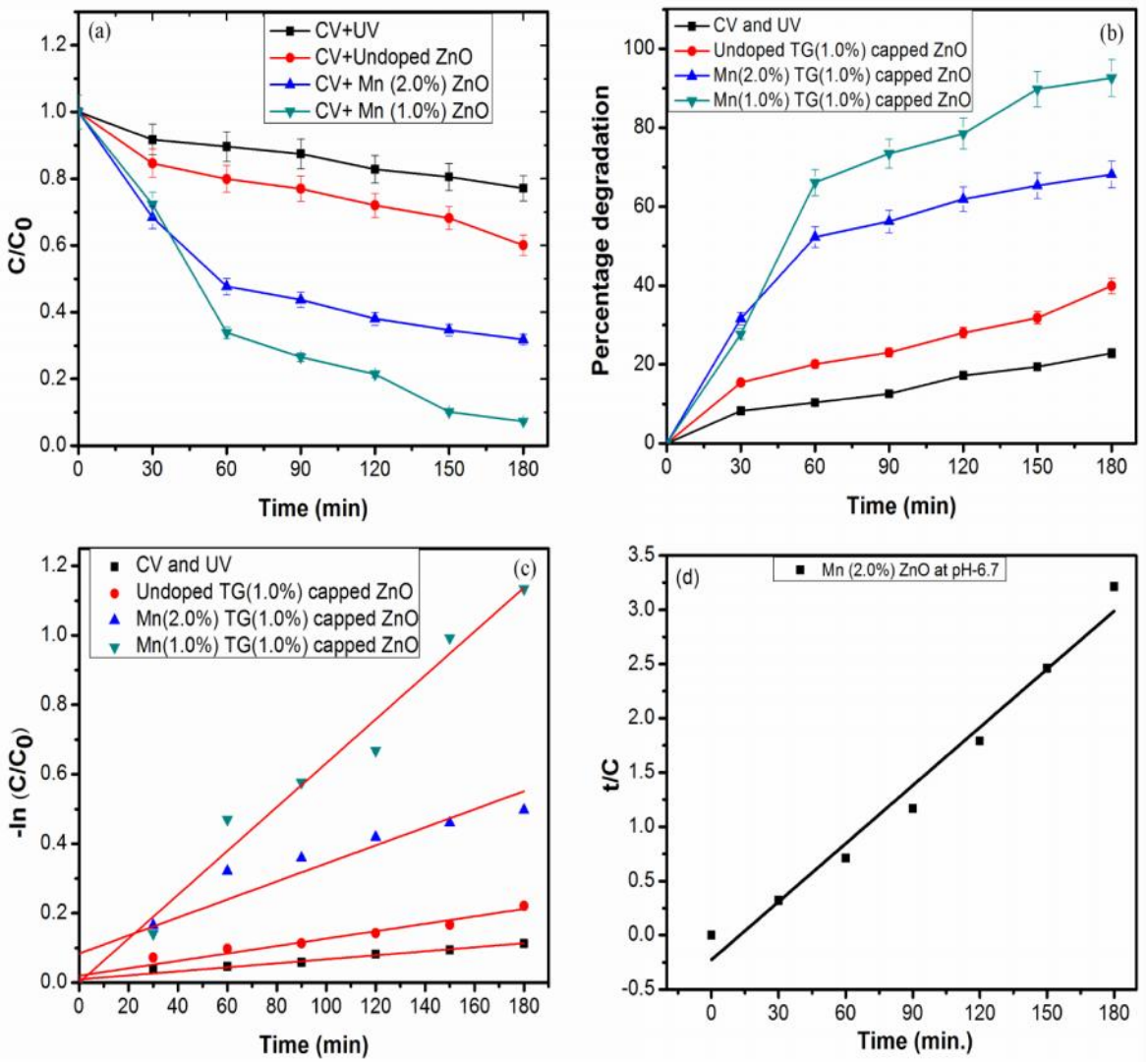

Figure 4.20: (a) Photodegradation of CV under different conditions (b) extent of decomposition of CV with respect to time intervals (c) first order kinetics of CV degradation with and without photocatalyst and (d) second order kinetics of CV dye degradation with Mn (2.0%) doped ZnO NPs synthesized at pH-6.7 under UV–Visible radiations.

photogenerated holes were left in the valence band of ZnO and migrated to the surface of doped NPs, yielding active hydroxyl radical species to decompose the CV dye. As discussed above in excitation and emission studies there is considerable shift in excitation and emission spectra by addition of Mn dopant ions in host ZnO NPs. Therefore, the incorporation of Mn dopant ions in ZnO NPs act as effective trapping sites. The photogenerated electrons and holes can be efficiently separated and the recombination of these charge carriers has been greatly inhibited which results in the improved photocatalytic activities [36]. Mn (1.0%) doped ZnO NPs has shown better photocatalytic activity than Mn (2.0%) doped ZnO sample.

It may be due to smaller particle size (confirmed from XRD) as compared to Mn (2.0%) doped ZnO photocatalyst. The surface to volume ratio for Mn (1.0%) doped ZnO NPs is higher and activity of photocatalyst depends upon the adsorption amount of dye molecules on the surface of the photocatalyst. Also the effective band gap of Mn (1.0%) doped ZnO sample is smaller than Mn (2.0%) doped ZnO NPs (discussed earlier). This also increases the photocatalytic efficiency of Mn (1.0%) doped ZnO sample under exposure of UV-Visible light radiations. The photocatalytic decomposition of CV dye on the surface of ZnO NPs follows a pseudo first and second-order kinetic law, which can be expressed by following equations as,

$$-\ln (C/C_0) = K_1 t \quad \ldots\ldots(4.4)$$

$$t/C = 1/K_2 C_0^{\,2} + t/ C_0 \quad \ldots\ldots(4.5)$$

Where C and C_0 are the reactant concentration at time t = t and t = 0, respectively. K_1, K_2 and t are the pseudo-first and second-order rate constants (reaction rate constant) and time, respectively [22, 37]. The relationship between $-\ln (C/C_0)$ and irradiation time (Reaction time) for first order and t/C and irradiation time for second order are shown in Figure 4.20(c, d) respectively. Rate constants (K_1 and K_2) and regression coefficient (R) for degradation of CV dye with and without catalysts are summarized in Table 4.2. It shows that Mn (2.0%) doped ZnO NPs follows second order kinetics. Also the photoreaction rate is highest for Mn (1.0%) doped ZnO NPs and is least for CV dye under UV-Visible radiations only. This shows that Mn (1.0%) doped ZnO NPs shows highest photocatalytic performance among all synthesized photocatalysts.

4.3.6 Effect of pH on photocatalysis

Since the waste water from textile industries have wide range of pH values and it is very difficult to study the pH of waste water from industries at each time and adjust the photocatalytic reaction. To optimize the type of photocatalyst according to waste water pH, many groups have studied the effect of pH by varying the pH of dye solution with addition of acids and bases [38, 39] till now no one has synthesized Mn doped ZnO NPs at variable pH and studied their effect on photodegradation of dyes, so attempts have been made to optimize doping and pH of Mn doped ZnO NPs during synthesis of NPs to achieve maximum degradation of dye under UV-Visible light radiations. At this point it is important to mention that pH of photocatalytic reaction is constant (neutral) in all experiments with samples having different pH during synthesis of NPs. But they show considerable effect of photocatalytic

reaction. As Mn (1.0%) doped ZnO NPs synthesized at pH-6.7 (natural) exhibit higher percentage of photodegradation of CV dye, therefore this category of sample has been selected for further study by varying the pH so that both doping and pH effect can be studied simultaneously. Mn (1.0%) doped ZnO NPs have been synthesized at pH 8.0, 10.0 and 12.0 to study the effect of pH on photocatalytic degradation studies. Figure 4.21(a) shows the decrease in concentration of CV dye when exposed to UV-Visible radiations in the presence of Mn (1.0%) doped ZnO NPs prepared at pH-8.0, 10.0 and 12.0. Percentage degradation of CV dye under similar conditions is shown in Figure 4.21(b). It indicates that 95% and 98.3% CV dye has been degraded with Mn (1.0%) doped ZnO NPs at pH-8.0 and 10.0 respectively in 3h of UV-Visible exposure of radiations. However, 99.8% of CV dye has been degraded with Mn (1.0%) doped ZnO NPs synthesized at pH-12 after 2.5h of exposure of UV-Visible radiations.

Thus higher degree of CV dye degradation has been obtained at higher pH value at lower irradiation time. The linear relationship between $-\ln(C/C_0)$ and irradiation time for first order and t/C and irradiation time for second order is shown in Figure 4.21(c, d) respectively. The pseudo-first-order rate constant (K) and regression coefficient (R) for degradation of CV dye with Mn (1.0%) doped ZnO NPs at different pH valued are summarized in Table 4.2. The zero point charge of ZnO (pH_{zpc}) has been reported to be 9.0 [40] and the surface functional groups of ZnO are $ZnOH_2^+$, ZnOH and ZnO^- at pH < pH_{zpc} , pH_{zpc} and pH > pH_{zpc} respectively. As zero point charge (pH_{zpc}) of ZnO is 9.0, so at pH-10.0 (pH > pH_{zpc}) ZnO surface is anionic in nature which is further more anionic at pH-12.0 and CV dye is cationic in nature, so there is weak interaction, normal interaction and strong interactions between CV dye and Mn (1.0%) doped NPs synthesized at pH 8.0, 10.0 and 12.0 respectively. Therefore, greater dye molecule will adsorb on photocatalyst surface at pH-12.0 than at pH-8.0 and 10.0. Also higher photodegradation efficiency at higher pH is due to the main reaction presented by hydroxyl radical attack, which can be highly favored by the high concentration of adsorbed hydroxyl groups at high pH values [41]. Further to check the photodegradation efficiency of as synthesized Mn (1.0%) doped ZnO NPs at pH-12.0, the CV dye solution has been prepared at pH-2.0 (acidic medium) and 10.0 (basic medium) with the addition of HNO_3 and NaOH. The CV solution at pH-2.0 and 10.0 has been degraded with Mn (1.0%) doped ZnO NPs synthesized at pH-6.7 and 12.0. Figure 4.21(e) shows the percentage degradation of CV dye solution at different pH values under UV-Visible light in the presence of Mn (1.0%) doped ZnO NPs synthesized at pH-6.7 and 12.0. It shows that the 31.6% and 77% CV dye solution

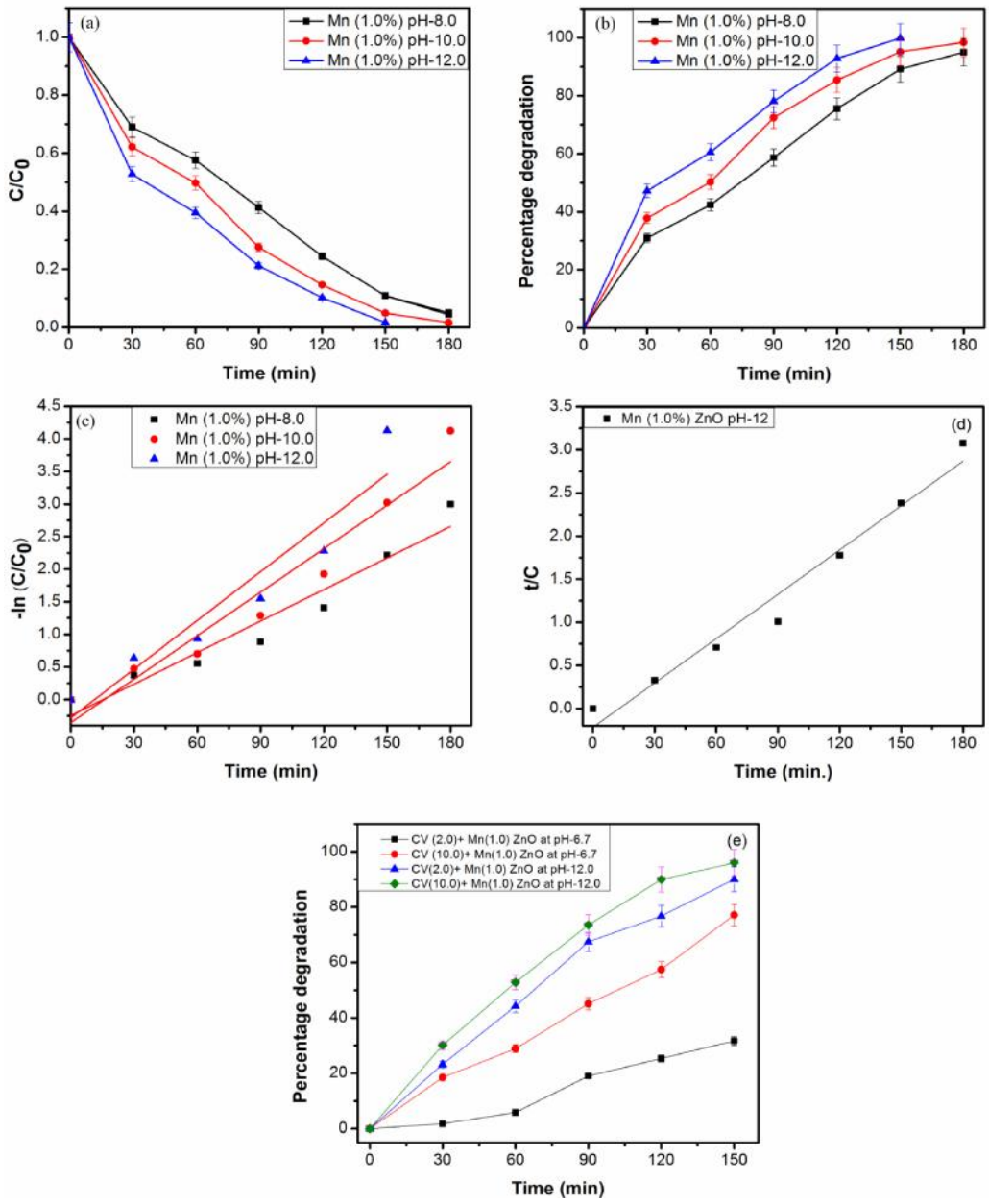

Figure 4.21: (a) Photodegradation of CV dye (b) Extend of decomposition of CV dye (c) First order kinetics of CV degradation with Mn (1.0%) doped ZnO NPs synthesized at pH- 8.0, 10.0 and 12.0. (d) Second order kinetics of CV degradation with Mn (1%) doped ZnO NPs at pH-12.0 and (e) extend of decomposition of CV dye solution at pH-2.0 and 10.0 with Mn (1.0%) doped ZnO NPs synthesized at pH- 6.7 and 12.0.

at pH-2.0 and 10.0 has been degraded with Mn (1.0%) doped ZnO NPs synthesized at pH-6.7 and 90.4% and 96.0% CV dye has been degraded with Mn (1.0%) doped ZnO NPs synthesized at pH-12.0 in 150 minutes of UV-Visible light radiations. Thus Mn doped ZnO sample synthesized at pH-12.0 has efficiently degraded the CV dye in acidic, neutral and

basic medium. These results confirm the utility of these NPs for degradation of waste water effluents from industries.

4.3.7 Effect of H_2O_2 on photocatalysis

As discussed above, doping and pH has dominant effect on photocatalysis of CV dye**.** In order to further enhance the degradation rate, the effect of H_2O_2 has been investigated so that effect of doping, pH and H_2O_2 could be studied simultaneously. The minimum amount of H_2O_2 (1.0%) has been added to 100mL slurry solution (dye and ZnO nanopowder). Figure 4.22(a) shows decrease in concentration of CV dye when exposed to UV-Visible light in the presence of H_2O_2 along with and without Mn (1.0%) doped ZnO NPs synthesized at different pH values. Percentage degradation of CV dye under similar conditions is shown in Figure 4.22(b). It shows that more than 82% of CV dye has been degraded in 2h with H_2O_2 only under UV-Visible radiations. More than 90% and almost 100% CV dye has been degraded in 1.5h in the presence of Mn (1.0%) doped ZnO NPs synthesized at pH-8.0 and 10.0 respectively. However, very quick degradation has been observed with Mn (1.0%) doped ZnO NPs synthesized at pH-12 along with H_2O_2. It has been found that 99% dye has been degraded in 20min. and 100% CV dye has been degraded 30 min. respectively. The linear relationship between $-\ln(C/C_0)$ and irradiation time shows the first order and for t/C and irradiation time shows the second order reaction which is shown in Figure 4.22(c, d). The pseudo-first and second-order rate constants and regression coefficients (R) for degradation of CV dye in the presence of H_2O_2 without and with Mn (1.0%) doped ZnO NPs at different pH valued are summarized in Table 4.2. The photoreaction rate is higher for Mn (1.0%) doped ZnO NPs synthesized at pH-12.0 as compared to others. Change in color of CV dye using Mn (1.0%) doped ZnO NPs synthesized at pH-12.0 in the presence of H_2O_2 for 0min and 30min under UV-Visible light radiations is shown in Figure 4.22(e). It shows that color of CV dye has been changed from violet to colorless after 30mins. This change in color shows that dye has been degraded. The degradation of CV dye with H_2O_2 only is due to direct photocatalysis of H_2O_2 by UV-Visible light radiations that can generate free radicals. Also H_2O_2 is suggested to be better electron acceptor than oxygen. As hydroxyl radicals are strong oxidizing agents and hence play significant role in degradation of dyes.

Further to check the photocatalytic activity of Mn (1.0%) doped ZnO NPs at pH-12.0 in the presence of H_2O_2, anionic industrial polyazo Sirius red F3B (SRF3B) dye has been degraded. Change in concentration and percentage degradation of SRF3B dye has been shown in Figure

4.24. It indicates very fast and quick degradation of SRF3B dye under UV-Visible light radiations.

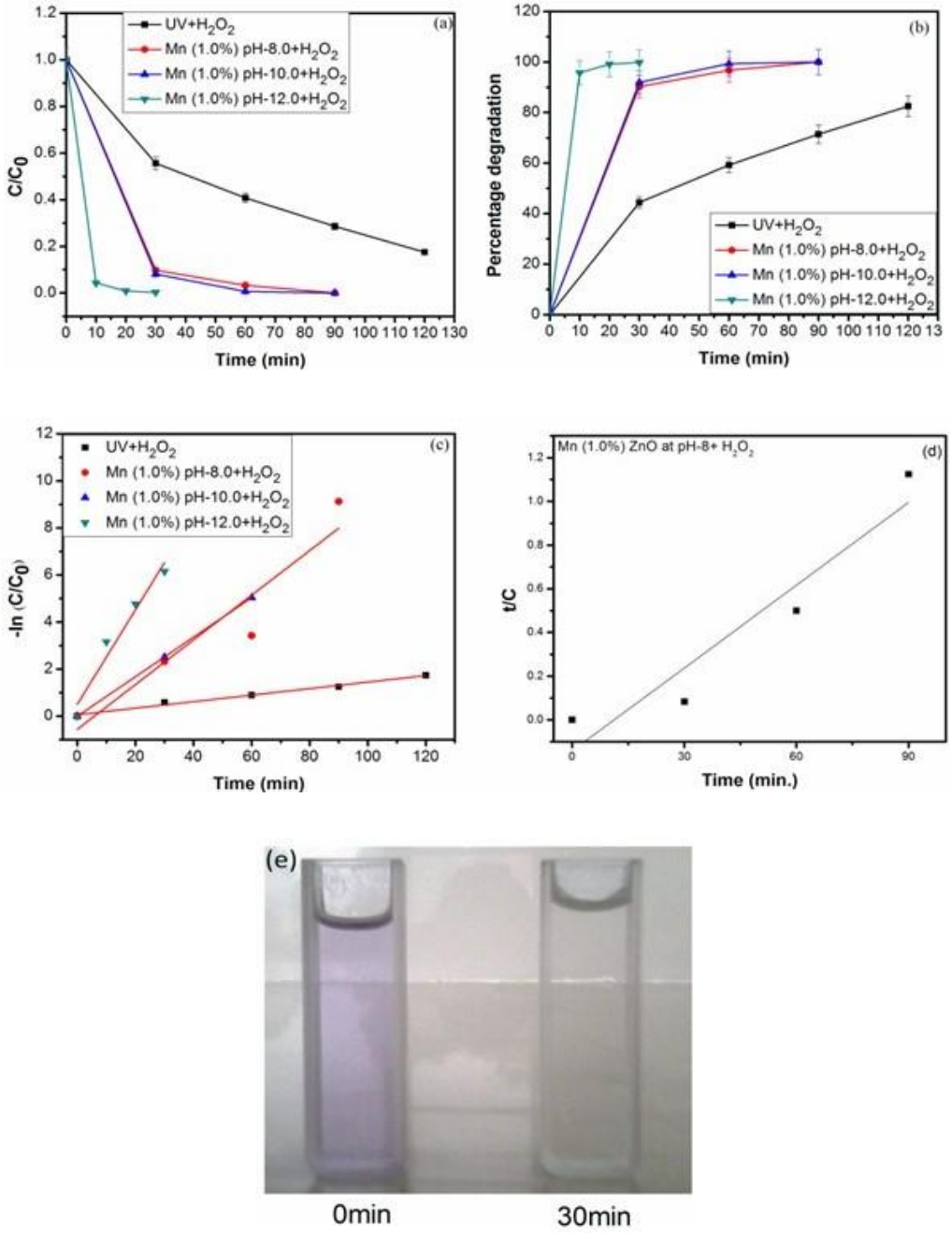

Figure 4.22: (a)Change in concentration (b) Percentage degradation and (c) first order kinetics of degradation of CV dye under the exposure of UV-Visible light radiations with and without synthesized photocatalyst at different pH values (d) second order kinetics of CV dye with Mn (1.0%) doped ZnO at pH-8.0 in the presence of H_2O_2 and (e) Change in color of CV dye with Mn (1.0%) doped ZnO NPs synthesized at pH-12 in the presence of H_2O_2 under UV-Visible light radiations after 0mins and 30mins.

100% degradation of SRF3B dye has been achieved within 15mins under exposure of UV-Visible light radiations. Thus highly efficient photocatalyst has been synthesized for degradation of both cationic and anionic dyes in industrial effluents to reduce water pollution and to save aquatic life.

Table 4.2: Reaction rate constant of crystal violet without catalyst, undoped, Mn (0.5%, 1.0%, 1.5% and 2.0%) doped and TG (1.0%) capped ZnO NPs synthesized at pH-8.0, 10.0 and 12.0.

S. No.	Concent-ration of CV (mg/L)	Catalyst type	pH of photoc-atalyst	Pseudo-first order		Pseudo-second order	
				Rate of reaction (K_1) min^{-1}	R^2	Rate of reaction (K_2) min^{-1}	R^2
1	10	No catalyst	-----	0.00057	0.9669	-----	-----
2	10	Undoped ZnO	6.7	0.00107	0.9477	-----	-----
3	10	Mn (1.0%) ZnO	6.7	0.00631	0.9756	0.00027	0.5171
4	10	Mn (2.0%) ZnO	6.7	0.0026	0.8788	0.0016	0.9779
5	10	Mn (1.0%) ZnO	8.0	0.01613	0.9297	-----	-----
6	10	Mn (1.0%) ZnO	10.0	0.02125	0.9330	-----	-----
7	10	Mn (1.0%) ZnO	12.0	0.02494	0.8852	0.0186	0.9728
8	10	No Catalyst H_2O_2	-----	0.01385	0.9854	-----	-----
9	10	Mn (1.0%) ZnO H_2O_2	8.0	0.09493	0.8485	0.0015	0.90651
10	10	Mn (1.0%) ZnO H_2O_2	10.0	0.09955	0.9761	-----	-----
11	10	Mn (1.0%) ZnO H_2O_2	12.0	0.20064	0.9377	-----	-----

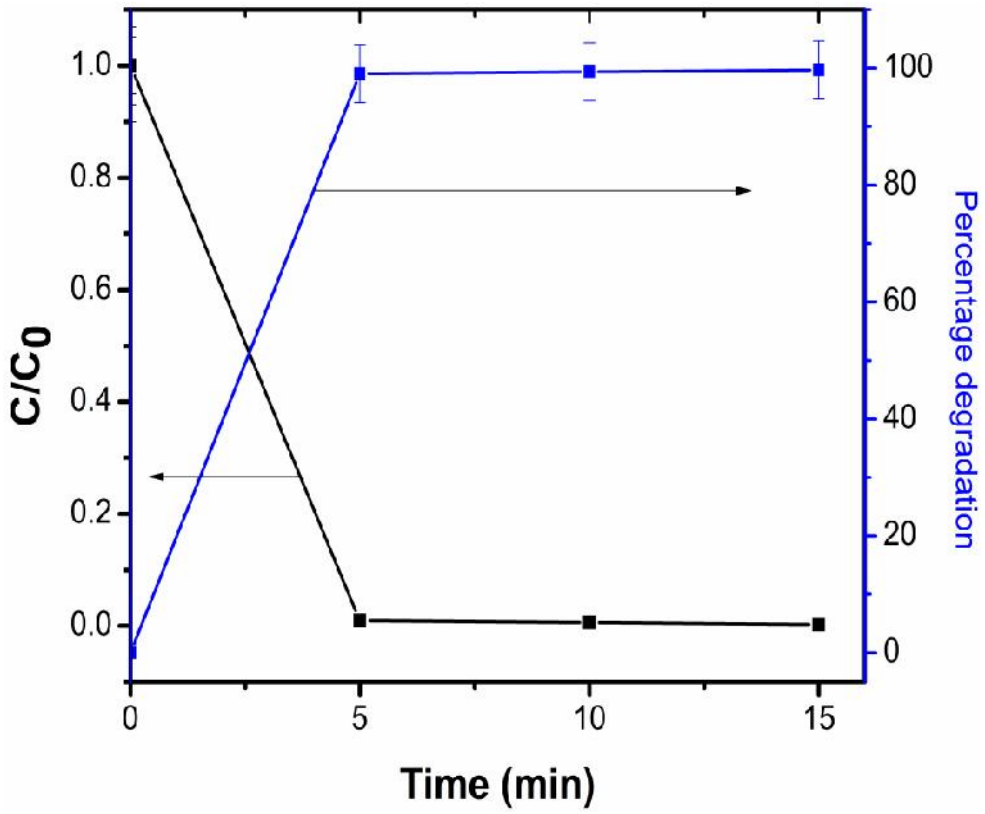

Figure 4.23: Change in concentration and percentage degradation of Sirius red F3B dye using Mn (1.0%) doped ZnO NPs at pH-12.0 in the presence of H_2O_2 under UV-Visible light radiations.

The possible mechanism of photocatalysis is shown in Figure 4.24. It shows when a photocatalyst is irradiated with light source of photon energy greater than its band gap energy then it promotes an electron from valance band to conduction band and generates an electron-hole pair. Also, the overlapping of one state (t_{2g}) of Mn with host V.B and presence of upper d state $6A_{1g}(S)$ in band gap helps to dissociate electron and hole wavefunction and decrease recombination. These electrons and holes so produced migrate to the surface of the photocatalyst and start oxidation and reduction reactions with the dye adsorbed on the surface of the photocatalyst. Here pH of as synthesized NPs performs a vital role. At higher pH value there is strong interactions between the dye and the photocatalyst surface and thus allow enough amount of dye to get adsorbed on the surface of the photocatalyst. Doping of Mn ions act as scavengers as it reacts with superoxide species and prevents the electron-hole recombination.

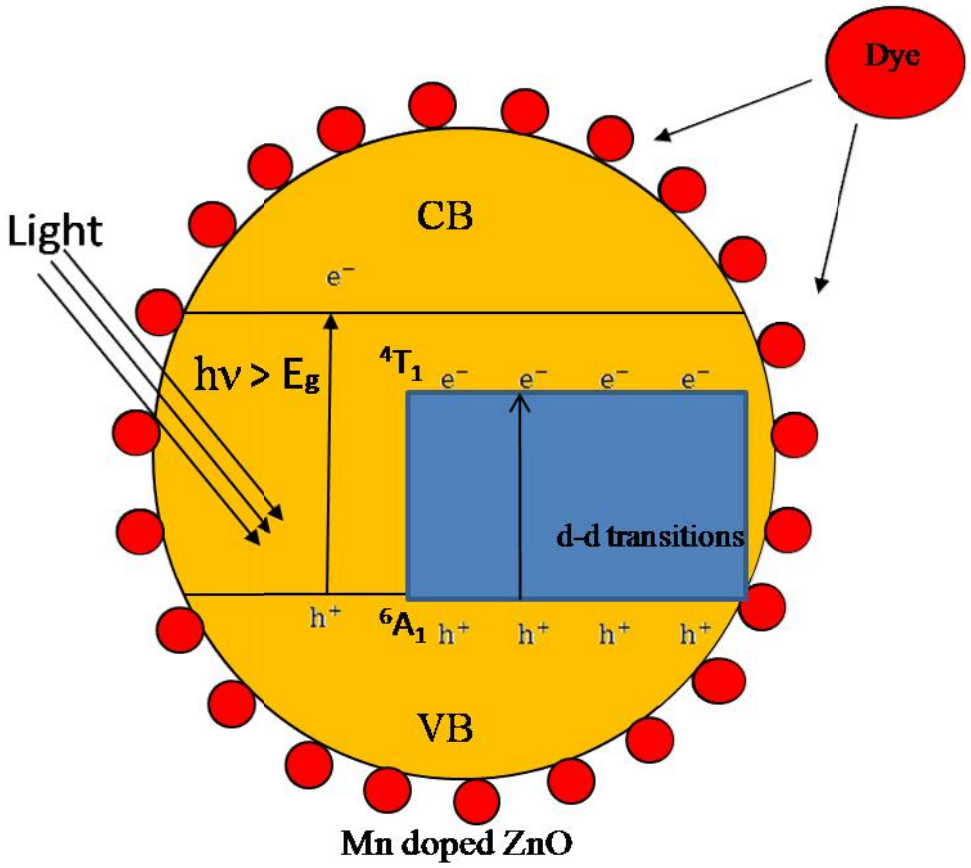

Figure 4.24: Schematic illustration of a proposed photocatalytic mechanism of Mn doped ZnO NPs synthesized at pH-12.0.

Thus the electron in the conduction band and hole in the valance band generated superoxide anion radical and hydroxyl free radical by following reactions:

$e^-_{cb} + O_2 \longrightarrow {}^{\cdot}O_2^-$ ……(4.6)

$h^+_{VB} + OH^- \longrightarrow {}^{\cdot}OH$ ……(4.7)

Thus generated strong oxidizing agents efficiently degrade the dye. Further, the addition of H_2O_2 to optimal doped sample at pH-12.0 produces strong oxidizing hydroxyl radical as:

$H_2O_2 + e^-_{cb} \longrightarrow {}^{\cdot}OH + OH^-$ ……(4.8)

$H_2O_2 + {}^{\cdot}O_2^- \longrightarrow {}^{\cdot}OH + OH^- + O_2$ ……(4.9)

$H_2O_2 + h\nu \longrightarrow 2{}^{\cdot}OH$ ……(4.10)

So in Mn (1.0%) doped ZnO NPs, Mn reduces electron–hole recombination which help H_2O_2

to generate higher amount of hydroxyl radicals. Also pH plays significant role for producing strong oxidizing agents. Therefore this two way process generate strong oxidizing agents causes faster degradation of CV dye in the presence of photocatalysts synthesized at different pH values. Thus doping, pH and presence of H_2O_2 appears to be promising factors for quick degradation of CV dye.

4.4 TG capped undoped and Cu doped ZnO nanoparticles

4.4.1 XRD studies

The XRD diffraction peaks of undoped and Cu (1.0 -5.0%) doped ZnO NPs synthesized at pH-8.0 is shown in Figure 4.25(a).

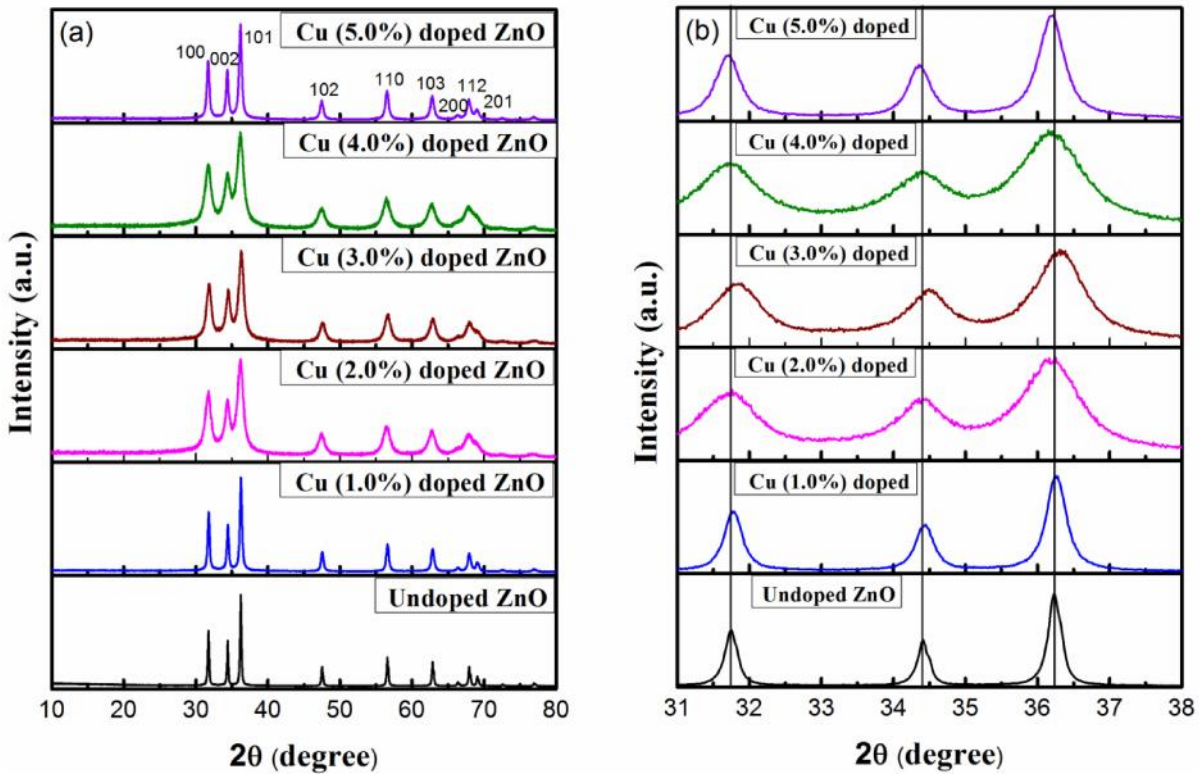

Figure 4.25: (a) XRD pattern and (b) Peak shift of Undoped and Cu (1.0% - 5.0%) doped ZnO NPs.

The diffraction peaks corresponding to (1 0 0), (0 0 2), (1 0 1), (1 0 2), (1 1 0), (1 0 3), (2 0 0), (1 1 2) and (2 0 1) planes reveal a highly crystalline hexagonal wurtzite structure (ICDD No. 36-1451) and there is no extra peak corresponding to Cu, oxides of Cu or Cu related secondary and impurity phases in Figure 4.25(a) which confirm that Cu has been

incorporated to ZnO lattice site rather than interstitial ones. The average crystallite size is estimated by Debye-Scherer formula. The average calculated crystallite size is 38nm for undoped, 32nm for Cu (1.0%), 14nm for Cu (2.0%), 12nm for Cu (3.0%) doped, 12nm for Cu (4.0%) doped and 23nm for Cu (5.0%) doped ZnO NPs. To check the occupancy of Cu into the lattice of ZnO, we have selected most dominant (1 0 0), (0 0 2) and (1 0 1) peaks of undoped and Cu doped NPs from Figure 4.25(b). A careful comparison of diffraction peaks in the range of $2\theta = 31.0^{o}$ - 38.0° (Figure 4.25(b)) shows that the peak position of Cu (3.0%) doped ZnO NPs is shifted towards larger 2θ value as compared to undoped ZnO NPs. This shift is attributed to the shrinkage of ZnO crystal lattice due to the substitution by smaller Cu^{2+} (0.057 nm) on Zn^{2+} (0.06nm) site [41].

The substitution of Cu dopant would affect the concentration of interstitial Zn, oxygen vacancies and Zn vacancies [43]. A very small shift in diffraction peak position to the higher angle for Cu (3.0%) NPs are observed and the broadening of diffraction peaks are noticed with increase in Cu doping concentration from Cu (1.0-4.0%). This small change in diffraction peaks position and broadening indicates that Cu has been incorporated in the ZnO lattice with no change in crystal lattice.

4.4.2 TEM and EDS studies

TEM micrographs of Cu (3.0%) doped ZnO NPs synthesized at various pH are shown in Figure 4.26(a, b & c). It is clear from micrographs that Cu (3.0%) doped ZnO NPs synthesized at different pH shows spherical and hexagonal morphology. In Figure 4.26(a), Cu (3.0%) doped ZnO NPs synthesized at pH-8.0 shows agglomerated spherical particles with average particle size of 15-25nm. Cu (3.0%) doped ZnO synthesized at pH-10.0 and 12.0 shows hexagonal and spherical morphology with average particle size lying between 20-35nm and 22-38nm respectively (Figure 4.26(b & c)). Figure 4.27(a-f) shows Energy dispersive spectroscopy (EDS) of undoped and Cu (1.0% -5.0%) doped ZnO NPs. It clearly shows that the intensity of Cu increases with increasing Cu incorporation in ZnO lattice. Table 4.3 summarizes the elemental compositional data derived from Figure 4.27(a-f). The measurements confirmed the presence of the main constituents Zn, O and Cu in undoped and Cu doped samples respectively.

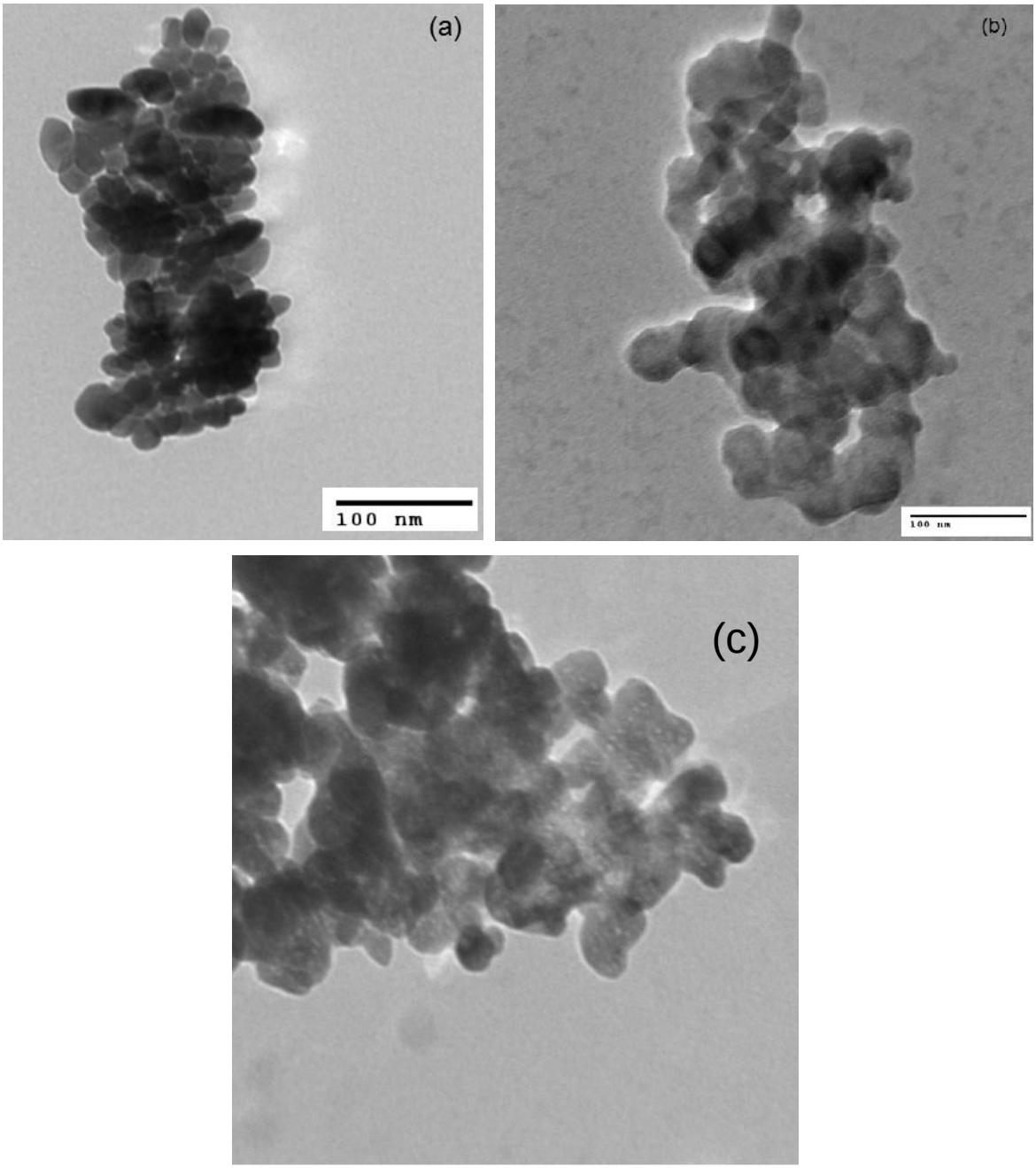

Figure 4.26: TEM images of Cu (3.0%) doped ZnO NPs synthesized at (a) pH-8.0 (b) 10.0 and (c) pH-12.0.

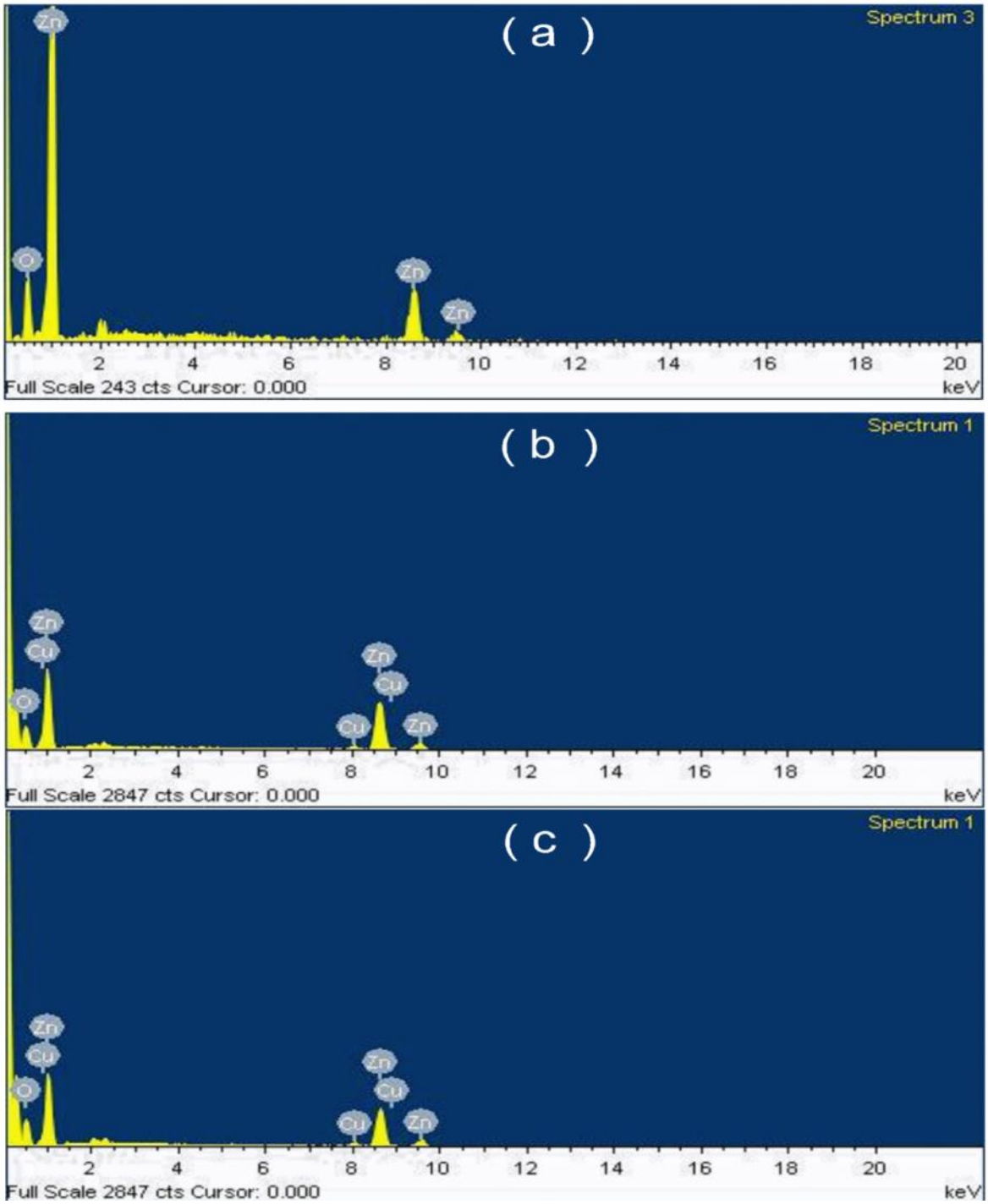
(a)
Spectrum 3
Zn
O
Zn
Zn
2 4 6 8 10 12 14 16 18 20
Full Scale 243 cts Cursor: 0.000
keV
(b)
Spectrum 1
Zn
Cu
O
Zn
Cu
Cu
Zn
2 4 6 8 10 12 14 16 18 20
Full Scale 2847 cts Cursor: 0.000
keV
(c)
Spectrum 1
Zn
Cu
O
Zn
Cu
Cu
Zn
2 4 6 8 10 12 14 16 18 20
Full Scale 2847 cts Cursor: 0.000
keV

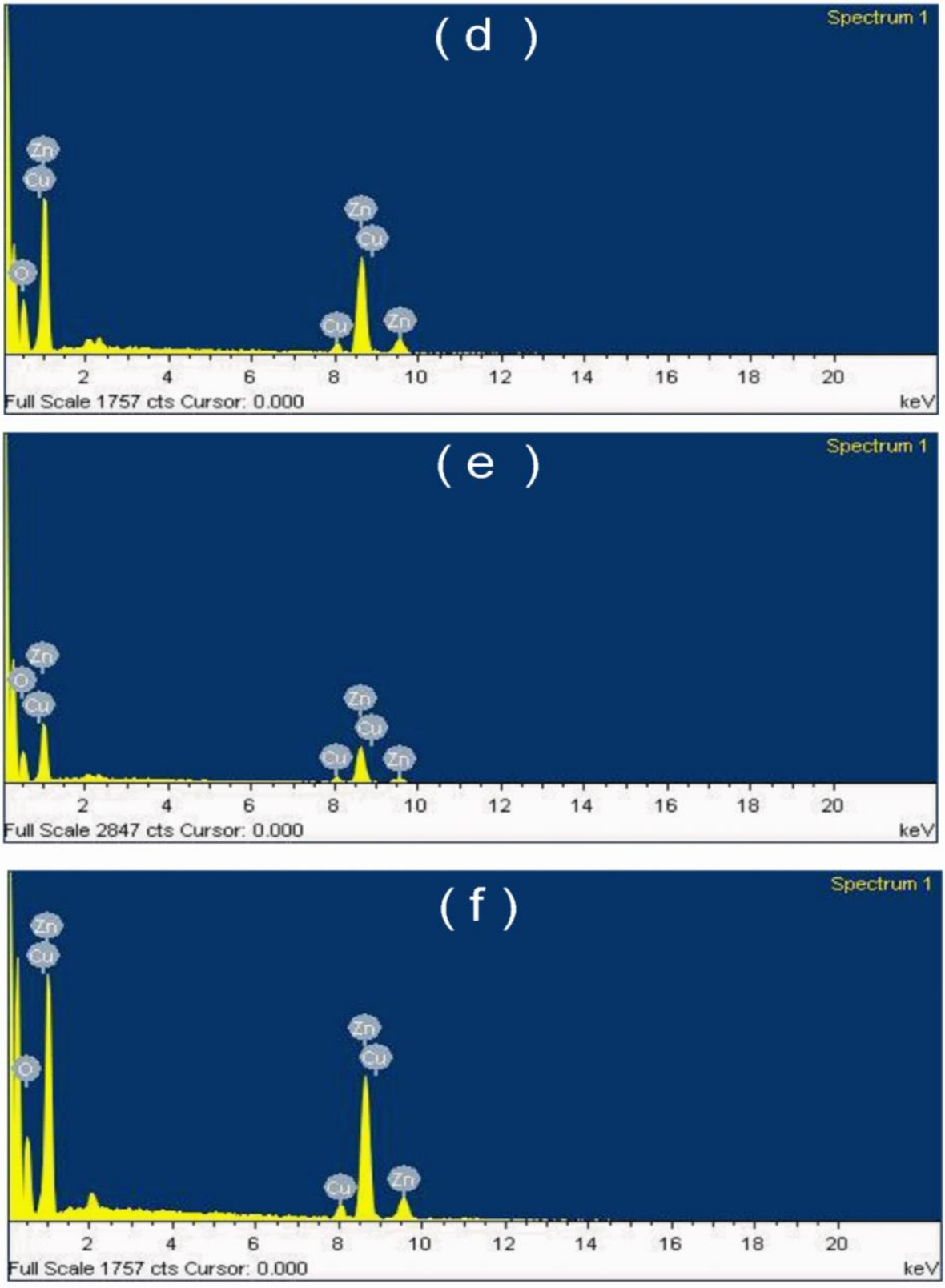

Figure 4.27: Energy dispersive spectra of (a) undoped (b) Cu (1.0%) doped (c) Cu (2.0%) doped (d) Cu (3.0%) doped (e) Cu (4.0%) doped and (f) Cu (5.0%) doped ZnO NPs.

Table 4.3: Elemental composition of undoped and Cu doped ZnO NPs.

S.No.	Sample	Elements	Weight%	Atomic%
1	ZnO	O Zn	21.05 78.95	52.14 47.86
2	ZnO:Cu(1.0%)	O Zn Cu	19.67 78.09 2.24	50.00 48.57 1.43
3	ZnO:Cu(2.0%)	O Zn Cu	19.69 76.08 4.23	50.00 47.29 2.71
4	ZnO:Cu(3.0%)	O Zn Cu	19.69 76.02 4.29	50.00 47.26 2.74
5	ZnO:Cu(4.0%)	O Zn Cu	19.69 75.14 5.17	50.00 46.70 3.30
6	ZnO:Cu(5.0%)	O Zn Cu	19.70 73.55 6.75	50.00 45.69 4.31

4.4.3 UV-Visible spectroscopy

Optical absorption spectroscopy of prepared undoped and Cu (1.0-5.0%) doped ZnO NPs is performed by UV-Visible absorption spectroscopy at room temperature. Figure 4.28(a) shows UV-Visible absorption spectra of as prepared samples synthesized at pH-8.0 and Figure 4.28(b) shows absorption spectra of Cu (3.0%) doped ZnO NPs synthesized at pH-10.0 and 12.0. It can be seen in Figure 4.28(a & b) that there is strong excitonic absorption peak in all samples. Fig 4(a) shows absorption peak at 364nm, 356nm, 352nm, 356nm, 356nm and 350nm for undoped, Cu (1.0%), Cu (2.0%), Cu (3.0%), Cu (4.0%) and Cu (5.0%) doped ZnO NPs respectively. Figure 4.28(b) shows absorption peak at 360nm for both Cu (3.0%) doped ZnO NPs synthesized at pH-10.0 and 12.0. These peaks are attributed to large exciton binding energy and good optical quality of synthesized NPs. Also peaks in all samples are blue shifted in comparison to bulk ZnO having absorption peak at ~375nm [10]. The weak absorption starts from 650nm which becomes strong around 350nm. From Figure 4.28(a & b), it can be observed that all Cu doped NPs shows better absorption of visible light as compared to undoped NPs.

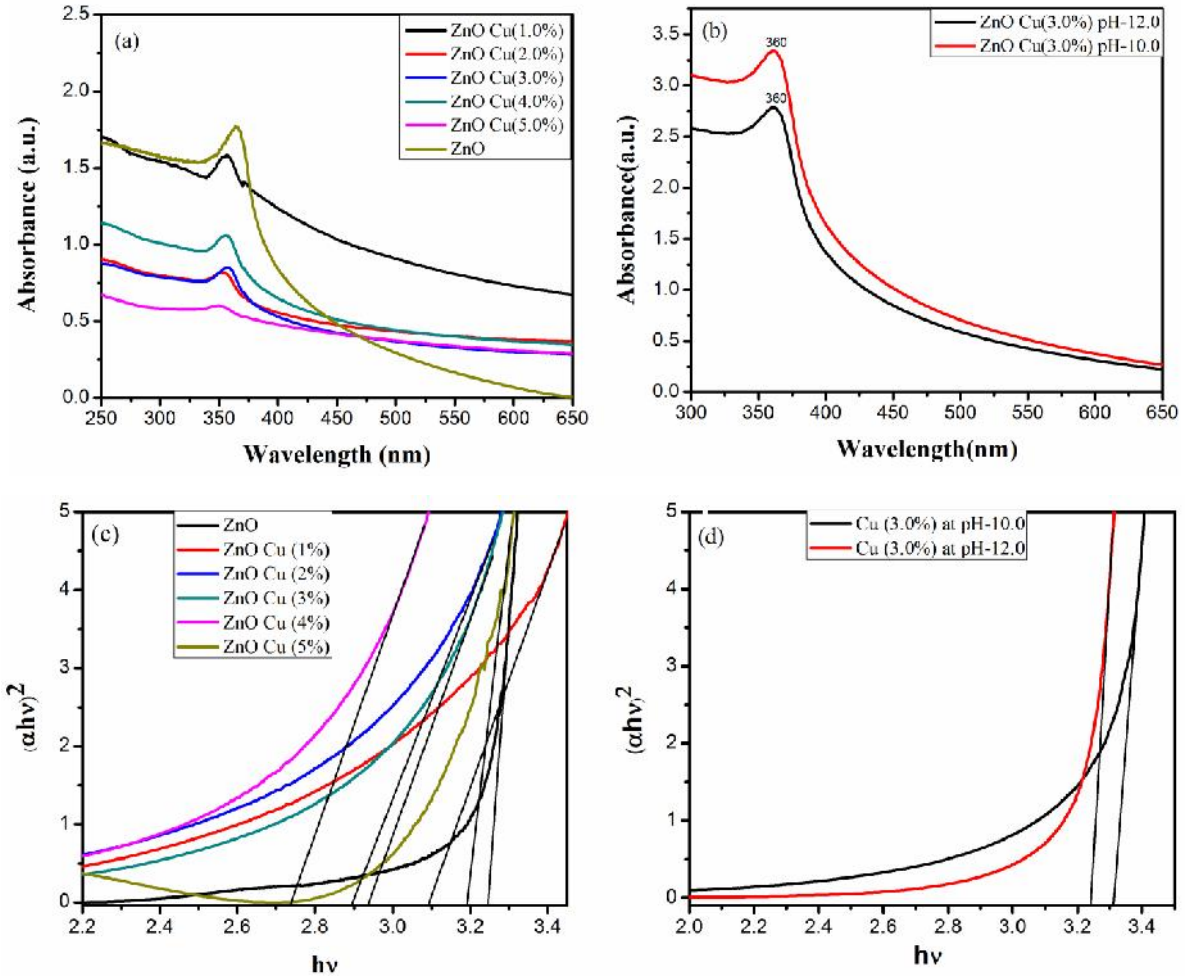

Figure 4.28: UV-Visible absorption spectra of (a) undoped and Cu (1.0% - 5.0%) doped synthesized at (a) pH-8.0 (b) Cu (3.0%) doped ZnO NPs synthesized at pH-10.0 and 12.0 touc's plot for (c) undoped and Cu (1.0% - 5%) doped ZnO NPs synthesized at pH-8.0 and (d) Cu (3.0%) doped ZnO NPs synthesized at pH 10.0 and 12.0.

Further band gap has been calculated by using Tauc's formula. Figure 4.28(c & d) shows the graphs between $(\alpha h\nu)^2$ and hν for undoped and Cu (1.0% –5.0%) doped ZnO NPs. The exact band gap values has been found to be 3.24 eV, 3.09 eV, 2.89 eV, 2.93 eV, 2.73 eV and 3.19 eV for undoped, Cu (1.0%), Cu (2.0%) , Cu (3.0%) , Cu (4.0%) and Cu (5.0%) doped ZnO NPs synthesized at pH-8.0. The calculated band gaps for NPs synthesized at pH 10.0 and 12.0 are 3.24eV and 3.31eV respectively. It can be seen that all Cu doped ZnO samples at pH-8.0 have an optical energy band gap lower than that of undoped ZnO. The band gap value of undoped ZnO is 3.24 eV. It has been observed that band gap of doped ZnO NPs decreases as the Cu doping concentration increases from 1.0 to 4.0%. After this when Cu doping concentration increases to 5.0%, the band gap again increases to 3.19 eV, which is

slightly less compared to undoped ZnO NPs. This decrease in band gap for Cu (1.0 - 4.0%) doped NPs correspond to p - d spin exchange interactions between the band electrons and the localized d electrons of doped Cu metal [44]. Moreover, decrease in band gap is attributed to the merging of an impurity band into conduction band [45]. Thus the red shift in Cu doped samples confirms the uniform incorporation of Cu in ZnO lattice.

4.4.4 Photoluminescence studies

4.4.4.1 Excitation studies

Photoluminescence excitation spectra (PLE) of undoped and Cu (3.0%) ZnO NPs monitored at 468nm emission is shown in Figure 4.29(a). It has been found that undoped ZnO NPs (Figure 4.29(a) Inset) shows absorption at 307nm and very weak absorption at 407nm. In comparison to undoped NPs, Cu (3.0%) doped sample shows small absorption peaks in UV region at 300nm, 325nm and 375nm and strong absorption peaks in visible region at 398nm, 404nm, 417nm and 425nm. These high intensity absorption peaks in visible region are due to the presence of energy levels created by impurity (Cu) atoms in host ZnO NPs. The relative absorption intensities of Cu doped and undoped ZnO ($I_{Cu\ doped}$ /$_{undoped}$) are 3.5 in UV region and 48 in visible region for peaks considered around 307nm and 418nm respectively. Thus PLE spectra indicates that Cu doped samples have large absorption in visible region than undoped ZnO NPs.

4.4.4.2 Emission studies

To reveal the effect of Cu doping, PL measurement of undoped and Cu (1.0-5.0%) doped ZnO NPs has been carried out at room temperature. Figure 4.29(b) shows the PL spectra of undoped and Cu (3.0%) doped ZnO NPs synthesized at pH-8.0. Inset of Figure 4.29(b) shows the magnified view of PL spectra of undoped ZnO NPs. It shows emission peaks in UV and visible region located at 387nm and at 468nm, 487nm, 529nm and 543nm respectively. The UV emission originates from the near-band-edge (NBE) transition in band gap of ZnO, which is due to exciton transition from localized levels below conduction band to the valance band [46], while the visible emission belongs to defect states (such as impurities and oxygen vacancies) in ZnO [47]. The major peak for Cu doped ZnO NPs at 465nm is also present in undoped NPs which according to literature reports is attributed to intrinsic defects of oxygen and zinc interstitials [48]. But in our case this peak is 15.5 times enhanced in comparison to undoped NPs. This shows Cu ions have contributed significantly in enhancing this emission

peak in visible region. The relative intensity of various peaks {from Figure 4.29(b)} for doped and undoped ZnO NPs are as follows:

$I_{doped/undoped}$ is 8.0, 6.3, 15.5 and 6.0 for peaks around 390, 415, 465 and 529nm respectively. From Figure 4.29(c) it has been found that the luminescence intensity is maximum for Cu (3.0%) doped NPs because of better doping of Cu at 3.0 at.% as confirmed by XRD and EDS analysis discussed earlier.

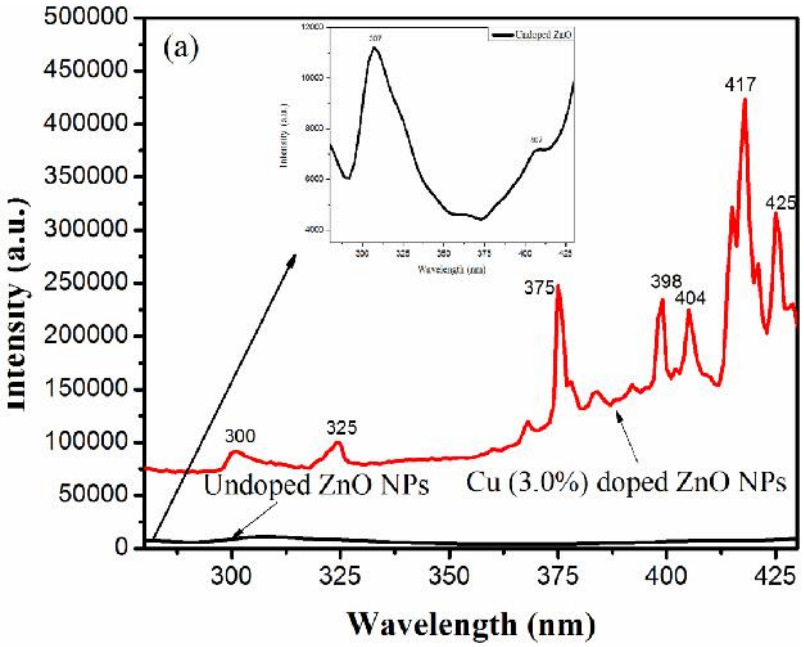

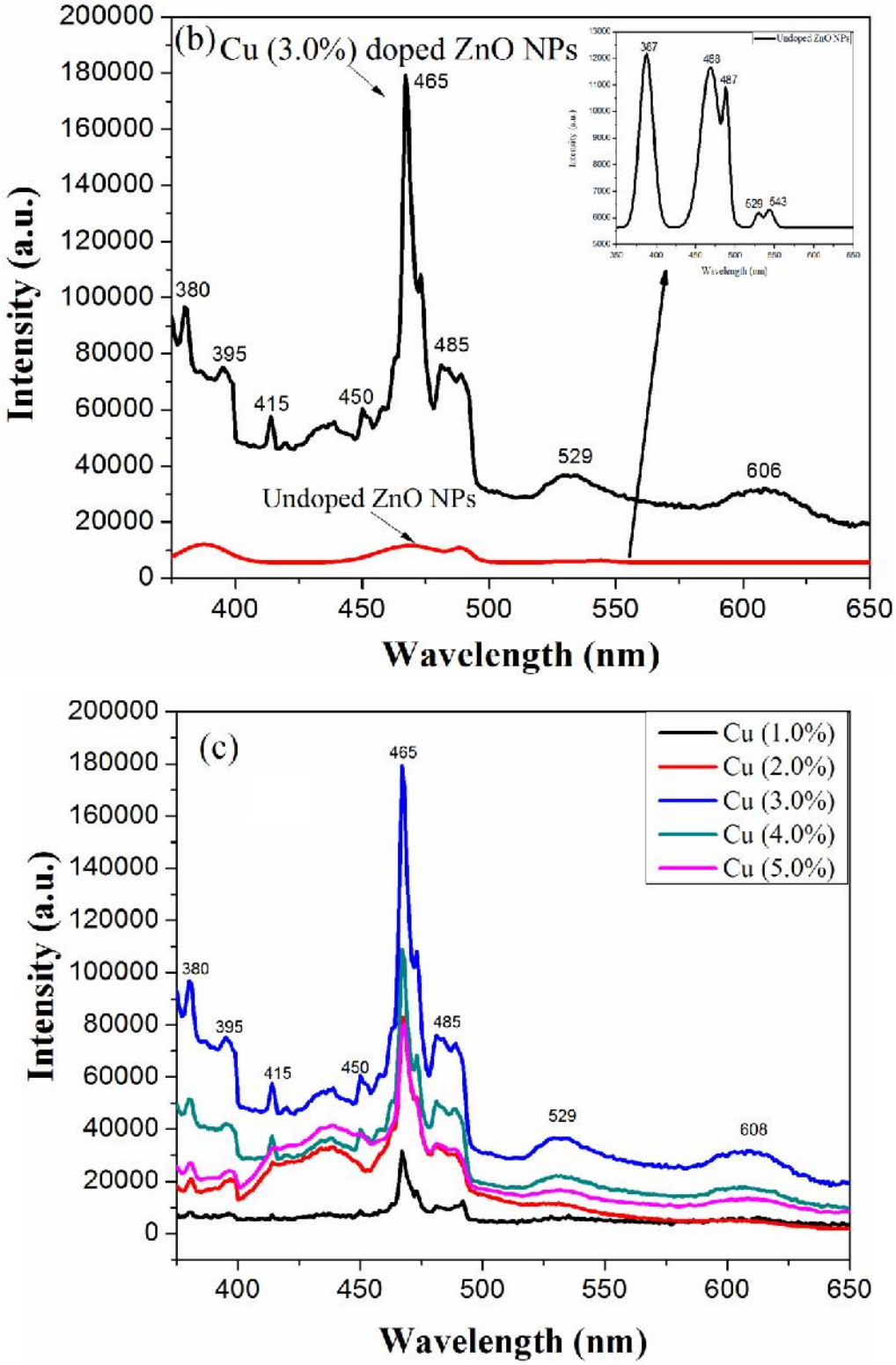

Figure 4.29: PLE spectra of (a) undoped and Cu (3.0%) doped ZnO NPs at λ_{em} = 468nm and PL spectra of (b) undoped and Cu (3.0%) doped ZnO NPs and (c) Cu (1.0-5.0%) doped ZnO NPs at λ_{ex}= 325nm.

4.4.5 Photocatalytic Studies

The photocatalytic degradation of CV dye in the presence of undoped and doped ZnO NPs synthesized at pH-8.0 were investigated under UV-Visible irradiation. This dye was used as a test contaminant owing to its absorption peaks in the visible range and thus its degradation can be easily monitored by optical absorption spectroscopy. The change in optical absorption spectra of CV dye with undoped and Cu (3.0%) doped ZnO synthesized at pH-8.0 under UV-Visible irradiations for different time intervals is shown in Figure 4.30. These spectra have been taken at different intervals after exposing the solution under UV-Visible light. The intensity of absorption spectra decreases as the exposing time increases from 0 to 3.5h. The intensity of main peak decreases due to degradation of CV dye.

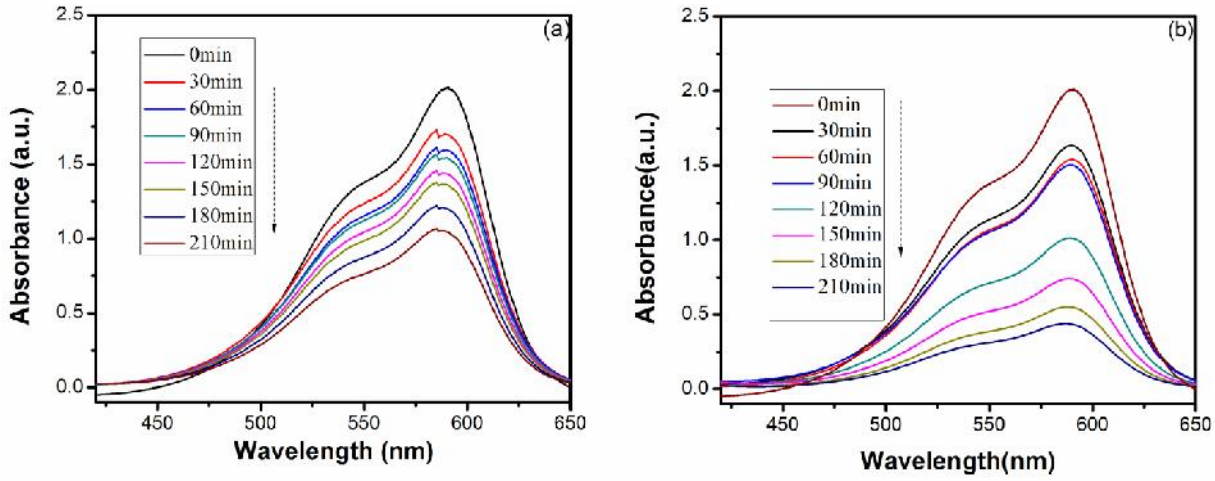

Figure 4.30: Absorption spectral changes of crystal violet dye aqueous solution (10 mg/L) degraded by (a) Undoped (b) Cu (3.0%) doped ZnO NPs synthesized at pH-8.0.

Figure 4.31(a) shows the change in concentration of CV dye as a function of irradiation time for the dye derivative in absence and presence of undoped and Cu (1.0-5.0%) doped ZnO NPs (C is the concentration of CV determined at λ_{max} of absorption and C_0 is initial concentration). Figure 4.31(b) shows percentage decrease in concentration of CV dye over time under different conditions. It shows that only 25.2% of CV dye dissolved in water disappears after 3.5h of UV-Visible radiations without any photocatalyst. This smaller degradation of CV dye might be due to the interaction between $OH^{\cdot}$ radical generated from water and CV dye. 48.19% of CV dye degraded with undoped ZnO NPs. Photocatalytic activity of undoped ZnO NPs is due to defect states caused by donor and acceptor states such as oxygen vacancies, interstitial zinc atom and zinc vacancies and interstitial oxygen

respectively. Interfacial electron transfer take place between donor states and CV dye. CV dye as a cationic dye acquire electron from excited donor states and get decomposed. Figure 4.31(b) shows 51.5%, 60.7%, 78.7%, 75.7% and 59.4% of CV dye degraded with Cu (1.0%), Cu (2.0%), Cu (3.0%), Cu (4.0%) and Cu (5.0%) doped ZnO NPs synthesized at pH-8.0 when exposed to UV-Visible radiations for 3.5h. From this it can be concluded that degradation of CV dye increases from 51.5% to 78.7% for Cu (1.0%) to Cu (3.0%), afterwards it reduces for higher Cu doping concentration. This is because ZnO act as a source of electrons and holes. The dopant Cu atoms and donor states (oxygen vacancy/ defects) act like a sink to electron and hole pairs which decreases the electron-hole pair recombination that results higher production of $OH^{\bullet}$ radicals [49]. This results in greater decomposition of CV dye using Cu doped ZnO NPs. Here Cu (3.0%) doped ZnO shows higher degree of degradation of CV dye over other doped ZnO NPs because higher concentration of Cu doping also shows negative effect. It creates a cyclic process without generating active $OH^{\cdot}$ radicals [50]. Since Cu (3.0%) has smaller particle size (confirmed from XRD studies shown above) as compared to other Cu doped ZnO NPs at pH-8.0. Therefore, surface to volume ratio for Cu (3.0%) doped ZnO NPs is higher as compared to other doped ZnO NPs and activity of photocatalyst depends on the adsorption amount of dye molecules on the surface of the photocatalyst. Also, Cu (3.0%) doped sample shows better PL emission intensity in visible region as compared to other doped and undoped samples which attribute better degradation of CV dye. The photocatalytic decomposition of CV dye on the surface of ZnO NPs also follows a pseudo first-order kinetic law, and can be expressed as,

$$-\ln(C/C_0) = Kt \qquad \ldots\ldots(4.11)$$

where C and C_0 are the reactant concentration at time t = t and t = 0, respectively. K and t are the pseudo-first-order rate constant (reaction rate constant) and time, respectively [22]. The relationship between $-\ln (C/C_0)$ and irradiation time (Reaction time) are shown in Figure 4.31(c).

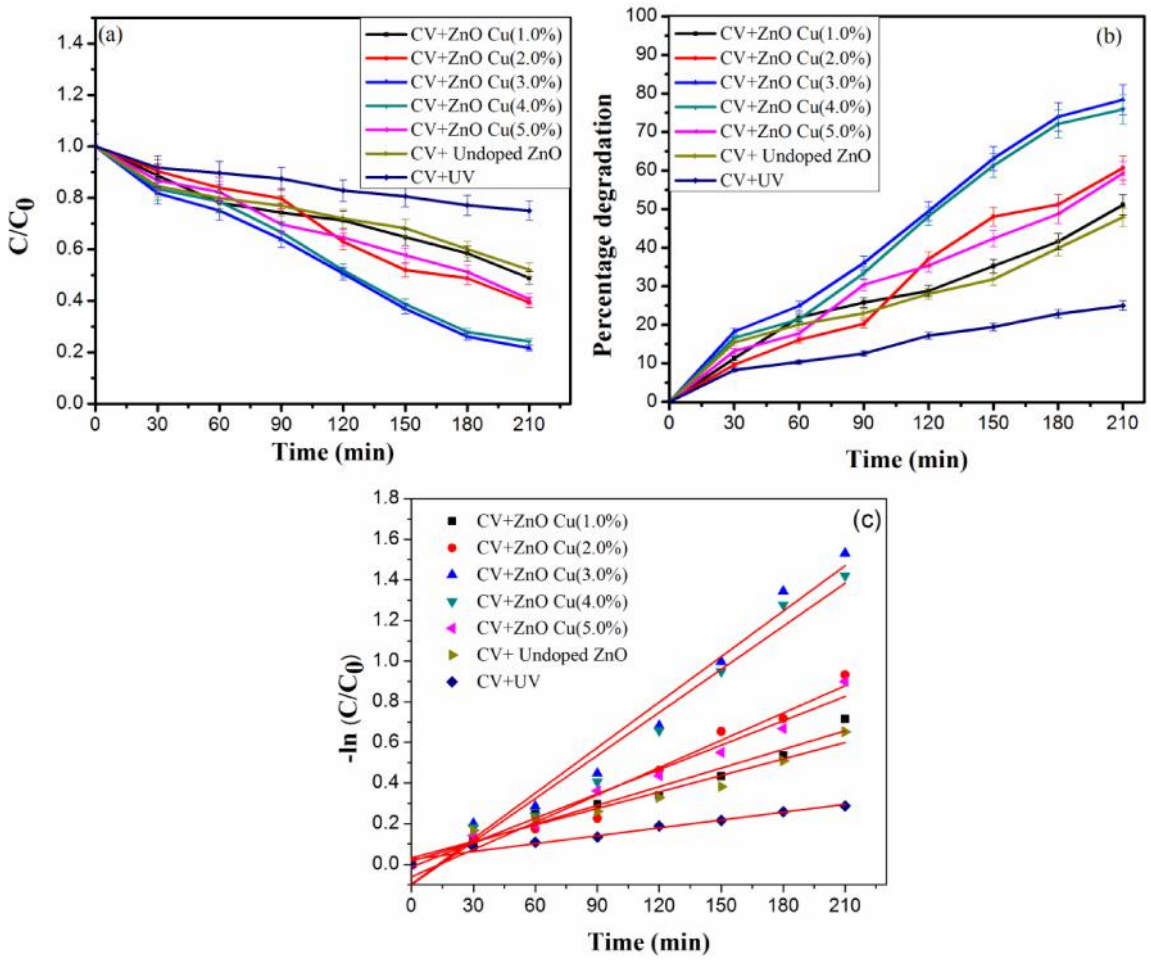

Figure 4.31:(a) Photodegradation of crystal violet under different conditions (b) Extent of decomposition of CV dye with respect to time intervals and (c) Kinetics of CV dye degradation with and without photocatalyst synthesized at pH-8.0 under UV-Visible radiations.

It is obvious that there exists a linear relationship between –ln (C/C_0) and irradiation time. The pseudo-first-order rate constant (K) and linear regression coefficient (R) for degradation of CV dye without catalyst, undoped ZnO, Cu (1.0 – 5.0%) doped ZnO NPs are summarized in Table 4.4. It shows that photoreaction rates are highest for Cu (3.0%) doped ZnO NPs at pH-8.0 and is least for without any catalyst under UV-Visible radiations. The higher value of first order rate constant demonstrates higher photocatalytic performance. Thus Cu (3.0%) doped ZnO NPs at pH-8.0 shows highest photocatalytic performance among all synthesized photocatalysts.

Table 4.4: Reaction rate constant of crystal violet without catalyst, undoped, Cu (1.0%, 2.0%, 3.0%, 4.0% and 5.0%) doped and TG (1.0%) capped ZnO NPs at pH-8.0.

Experiment	Concentration of crystal violet dye (mg/L)	Catalyst concentration (0.25g/100 mL)	pH	K, min^{-1} (rate constant)	R^2
1	10	Without catalyst	8.0	0.00129	0.97501
2	10	Undoped ZnO	8.0	0.00271	0.95297
3	10	Cu (1.0%) doped ZnO	8.0	0.00306	0.96669
4	10	Cu (2.0%) doped ZnO	8.0	0.00448	0.96336
5	10	Cu (3.0%) doped ZnO	8.0	0.00746	0.96625
6	10	Cu (4.0%) doped ZnO	8.0	0.00706	0.96458
7	10	Cu (5.0%) doped ZnO	8.0	0.004	0.97789
8	10	Cu (3.0%) doped ZnO	10.0	0.01712	0.98822
9	10	Cu (3.0%) doped ZnO	12.0	0.03943	0.98066

4.4.6 Effect of pH on photocatalytic properties

Owing to amphoteric behavior of most semiconductors, the pH also affect the photocatalytic process of various pollutants and thus is an important parameter in the reaction taking place on semiconductor surface. Earlier it has been reported that by that variation in pH of dye solution effects the degradation efficiency of photocatalyst synthesized at constant pH [51,39]. But in our case photocatalytic degradation has been studied by varying the pH of as synthesized Cu doped ZnO NPs instead of varying the pH of dye solution during every experiment. As at pH-8.0, Cu (3.0%) doped ZnO NPs exhibit higher percentage of photodegradation of CV dye, therefore this category of sample has been selected for further study by varying the pH so that both doping and pH effects can be studied simultaneously. Cu doped ZnO NPs synthesized at pH-8.0, 10.0 and 12.0 has been prepared to study the effect of pH on photocatalytic degradation studies. Figure 4.32(a) indicates the decrease in concentration of CV dye when exposed under UV-Visible radiations in the presence of Cu (3.0%) doped samples synthesized at pH- 8.0, 10.0 & 12.0. Percentage degradation of CV dye using Cu (3.0%) doped ZnO NPs at various pH are shown in Figure 4.32(b). From this figure it is clear that 78.7% and 96.5% CV dye has been degraded with Cu (3.0%) doped ZnO NPs at pH-8.0 and 10.0 respectively after 3.5h of UV-Visible exposure of radiations. However, almost 100% CV dye has been degraded with Cu (3.0%) doped ZnO NPs synthesized at pH-12.0 and that too only after 2.5h of UV-Visible irradiation. Thus higher degree of CV dye degradation has been obtained at much lower irradiation time. Figure

4.32(c) shows the change in color of CV dye when exposed to UV-Visible radiations from 0-2.5h with Cu (3.0%) doped ZnO NPs synthesized at pH-12.0. The color of CV changes from violet to colorless after 2.5h. This change in color of CV shows that dye has been degraded to 100%.

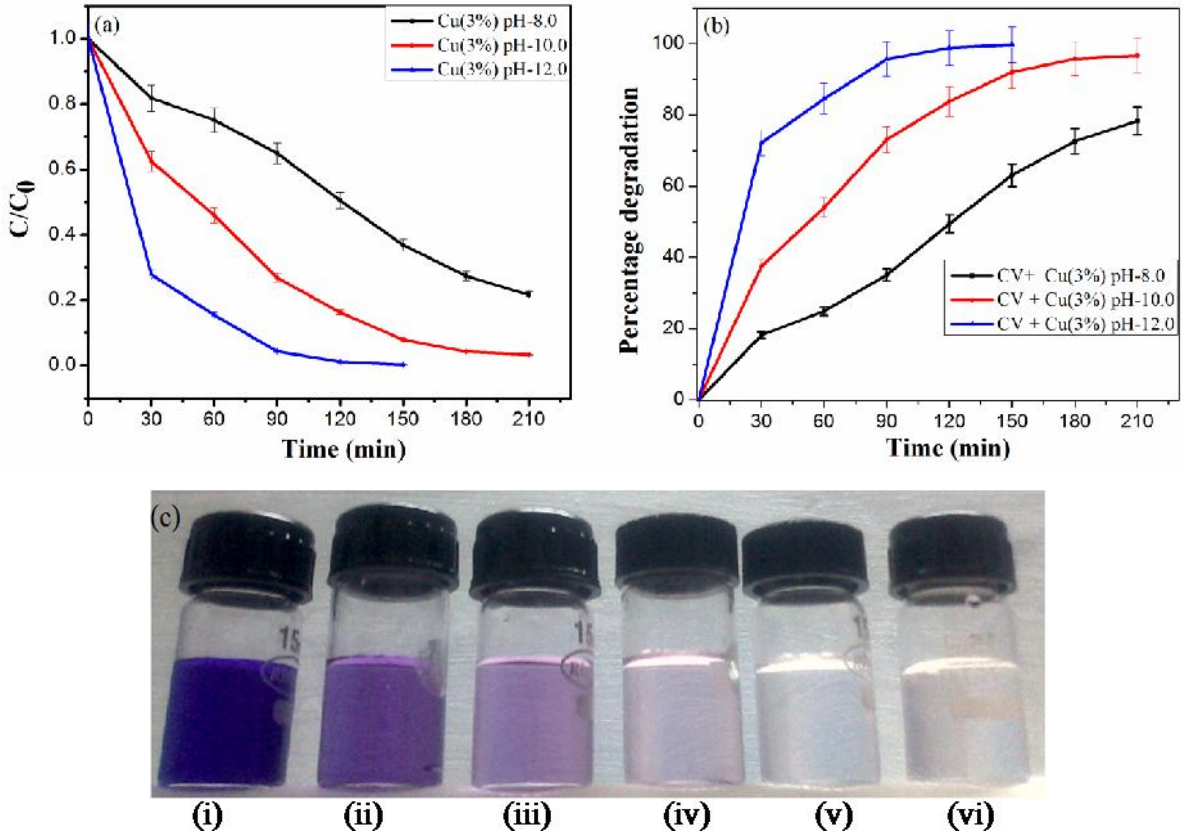

Figure 4.32: (a) Photodegradation of CV dye with Cu (3.0%) doped ZnO NPs and (b) Extend of decomposition of CV dye with respect to time intervals with Cu (3.0%) doped ZnO synthesized at pH-8.0, 10.0 and 12.0 (c) Change in color of crystal violet dye with Cu (3.0%) doped ZnO NPs at pH-12.0 in UV-visible radiations at (i) 0min (ii) 30min (iii) 60min (iv) 90min (v) 120min (vi) 150min.

Also, linear relationship between $-\ln(C/C_0)$ and irradiation time is shown in Figure 4.33. The pseudo-first-order rate constant (K) and linear regression coefficient (R) for degradation of CV dye using Cu (3.0%) doped ZnO NPs at different pH are summarized in Table 4.4. It shows that photoreaction rates are highest for Cu (3.0%) doped NPs at pH-12.0 compared to Cu (3.0%) doped NPs synthesized at pH-8.0, 10.0 and 12.0. These observations can be explained on the basis that the zero point charge of ZnO (pH_{zpc}) has been reported to be 9.0 [40]. Therefore the surface functional groups of ZnO are $ZnOH_2^+$, ZnOH and ZnO^- at pH <

pH_{zpc}, pH_{zpc} and pH > pH_{zpc}, respectively. On the other side CV dye is cationic in nature and to adsorb greater dye molecule on photocatalyst surface. Therefore, it is necessary to make photocatalyst surface to be anionic in nature. Now, as zero point charge (pH_{zpc}) of ZnO is 9.0, so at pH-10.0 (pH > pH_{zpc}) ZnO surface is anionic in nature which is further more anionic at pH-12.0. Thus, there is weak interaction, normal interaction and strong interactions between CV dye and Cu (3.0%) doped NPs at pH 8.0, 10.0 and 12.0 respectively. Therefore, greater dye molecule will adsorb on photocatalyst surface at pH-12.0 as compared to at pH-8.0 and 10.0. The other possible reason for higher photodegradation efficiency of as prepared catalyst at higher pH is due to the main reaction presented by hydroxyl radical attack, which can be highly favored by the high concentration of adsorbed hydroxyl groups at higher pH values [41]. Also in our case as the shape of Cu (3.0%) doped NPs at pH- 10.0 and 12.0 is hexagonal and spherical respectively (confirmed from TEM analysis). Since the surface area of spherical particle is higher as compared to hexagonal ones, surface to volume ratio of Cu (3.0%) doped ZnO NPs synthesized at pH-12.0 is more as compared to similar doped ZnO NPs synthesized at pH-10.0. Therefore surface area of Cu (3.0%) doped NPs synthesized at pH-12.0 is more exposed for CV dye to get adsorbed and degraded. Thus along with pH, morphology of Cu (3.0%) doped and capped ZnO NPs at pH-12.0 plays a significant role in degrading CV dye so efficiently.

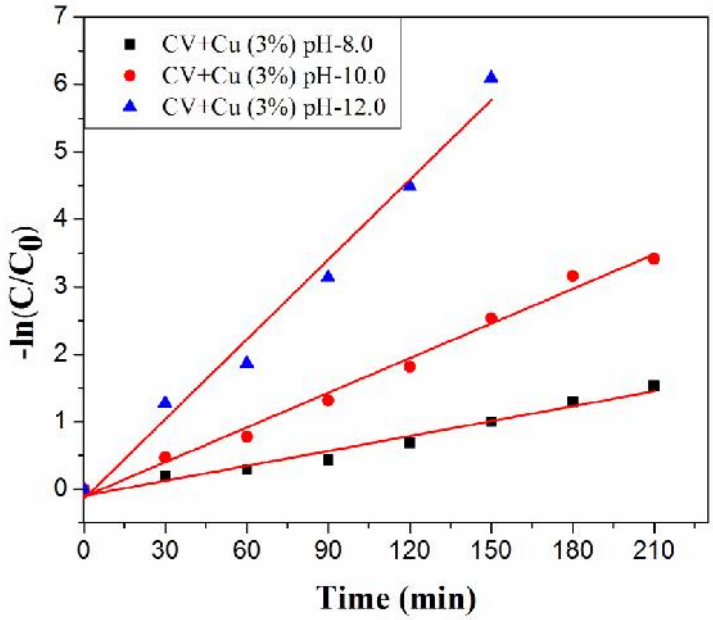

Figure 4.33: Kinetics of crystal violet degradation with Cu (3.0%) doped ZnO NPs synthesized at pH-8.0, 10.0 & 12.0.

4.4.7 Effect of photocatalyst loading

Photocatalytic activity of Cu doped ZnO NPs at various pH has been assessed according to the photodegradation of CV dye. As discussed above Cu (3.0%) doped ZnO NPs at pH-12.0 shows maximum degradation (~ 100%) at smaller time as compared to other undoped and doped photocatalysts. The variation of photocatalyst concentration (2.5g/L to 3.5g/L) has been taken into consideration to avoid unnecessary amount of photocatalyst by keeping the same CV dye concentration (10 mg/L). The percentage of photodegradation of CV dye as a function of irradiation time at different photocatalyst concentration is shown in Figure 4.34. The maximum percentage of photodegradation has been obtained at 3.0g/L of photocatalyst. This is because the number of adsorbed dye molecules increases with increase in photocatalyst particles and also number of active sites increases with increase in photocatalyst dosage which further enhance $OH^{\bullet}$ radical production [52]. When the amount of photocatalyst increases above optimum level then the degradation percentage reduces. This might be due to increase in turbidity of the slurry (photocatalyst and dye) that reduces the penetration of UV-Visible light irradiations through the solution known as light screening effect [53]. Therefore, dye adsorbed photocatalyst surface becomes unavailable for photons absorption and thus the photocatalytic degradation reaction reduces at higher concentration of photocatalyst.

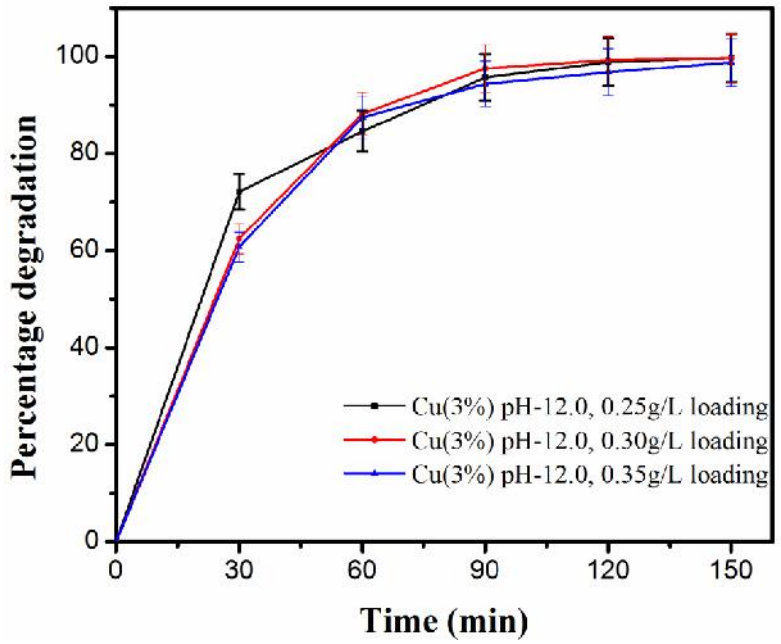

Figure 4.34: Effect of photocatalyst loading on photodegradation of CV dye with Cu (3.0%) doped ZnO NPs. Concentration of CV dye = 10mg/L.

From above discussion on photocatalytic studies it has been observed that optimal Cu doping has increased photocatalytic degradation efficiency in comparison to undoped samples. It has been reported earlier that on changing the pH of dye solution, NPs tend to agglomerate at acidic conditions and so the surface area availability for adsorption of dye and photon absorption reduces [52]. So, here the pH of as synthesized Cu doped ZnO NPs has been varied to avoid any agglomeration of NPs that occurred during adjusting the pH of dye solution done by earlier researchers [54]. Photocatalytic efficiency has been improved by changing the pH of as synthesised optimum Cu doped ZnO NPs from 8.0 to 12.0. Spherical morphology, maximum adsorption of CV dye and optimal doping are three main reasons for better photocatalytic activity of Cu (3%) doped ZnO NPs synthesised at pH-12.0. With this system there is no need to study the pH of wastewater containing various toxic dyes as optimized Cu doped ZnO NPs synthesised at higher pH are sufficient to degrade dyes having different pH.

4.5 PVP capped undoped and Cu doped ZnO nanoparticles

4.5.1 XRD studies

The XRD diffraction peaks of PVP capped undoped and Cu (1.0 -5.0%) doped ZnO NPs synthesized at pH-8.0 is shown in Figure 4.35(a). The diffraction peaks corresponding to (1 0 0), (0 0 2), (1 0 1), (1 0 2), (1 1 0), (1 0 3), (2 0 0), (1 1 2) and (2 0 1) planes reveal a highly crystalline hexagonal wurtzite structure (ICDD No. 36-1451) and there is no extra peak corresponding to Cu, oxides of Cu or Cu related secondary and impurity phases in Figure 4.35 which confirm that Cu has been incorporated to ZnO lattice site rather than interstitial ones. The average crystallite size is estimated by Debye-Scherer formula. The average calculated crystallite size is 38nm for undoped, 32nm for Cu (1.0%), 26nm for Cu (2.0%), 22nm for Cu (3.0%) doped, 20nm for Cu (4.0%) doped and 19nm for Cu (5.0%) doped ZnO NPs respectively.

4.5.2 TEM studies

TEM micrographs of undoped and Cu (3.0%) doped ZnO NPs are shown in Figure 4.36 (a & b). It is clear from micrographs that undoped and Cu (3.0%) doped ZnO NPs shows spherical and faceted morphology. In Figure 4.36(a), undoped ZnO NPs shows agglomerated spherical particles with average particle size of 25-45nm. Figure 4.36(b) shows Cu (3.0%) doped ZnO shows average particle size lying between 18-25nm.

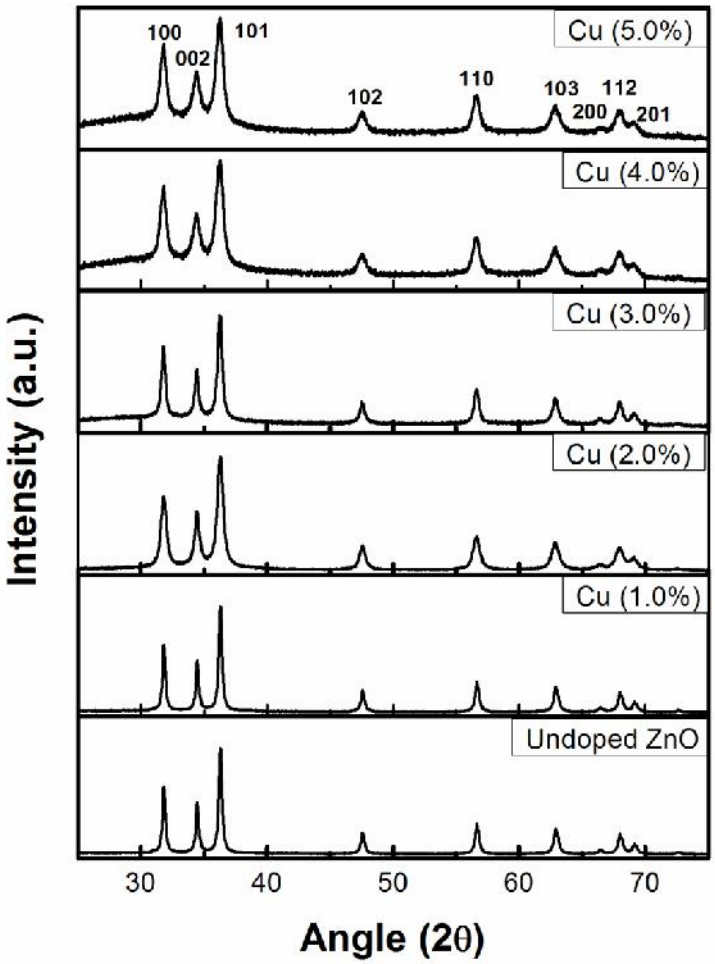

Figure 4.35: X-ray diffraction pattern of PVP capped undoped and Cu (1.0-5.0%) doped ZnO NPs.

4.5.3 UV-Visible spectroscopy

Optical absorption spectroscopy of prepared undoped and Cu (1.0-5.0%) doped ZnO NPs is performed by UV-Visible absorption spectroscopy at room temperature. Figure 4.28(a) shows UV-Visible absorption spectra of as prepared samples synthesized at pH-8.0 and Figure 4.28(b) shows absorption spectra of Cu (3.0%) doped ZnO NPs synthesized at pH-10.0 & 12.0. It can be seen in Figure 4.28(a & b) that there is strong excitonic absorption peak in all samples. Figure 4.37(a) shows absorption peak at 371nm, 371nm, 374nm,

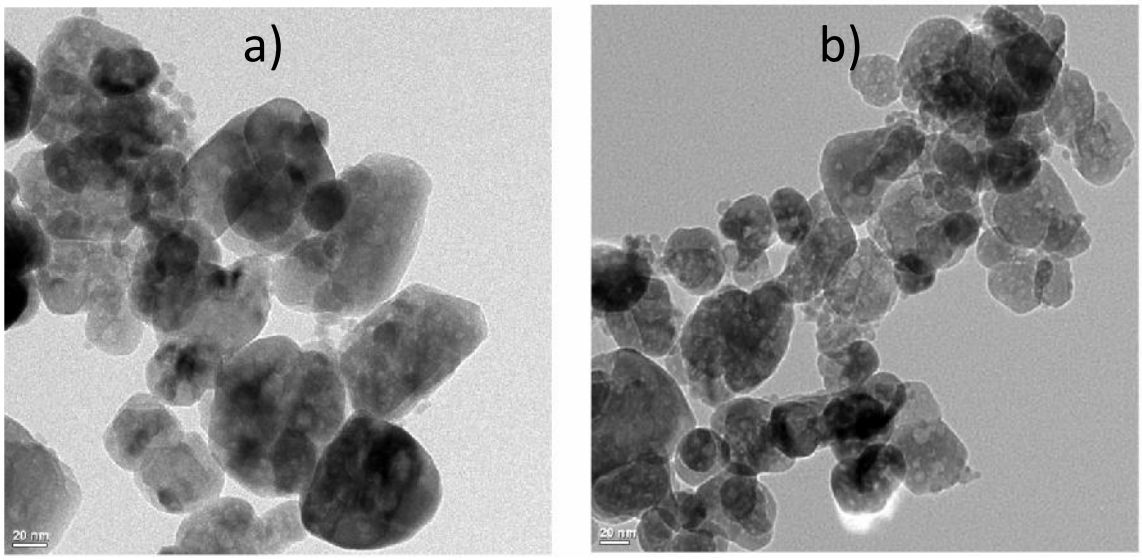

Figure 4.36: TEM images of undoped and Cu (3.0%) doped ZnO NPs.

371nm, 373nm and 364nm for undoped, Cu (1.0%), Cu (2.0%), Cu (3.0%), Cu (4.0%) and Cu (5.0%) doped ZnO NPs respectively. Figure 4.37(b) shows absorption peak at 366nm and 358nm Cu (3.0%) doped ZnO NPs synthesized at pH-10.0 and 12.0. These peaks are attributed to large exciton binding energy and good optical quality of synthesized NPs. The weak absorption starts from 650nm which becomes strong around 350nm. From Figure 4.37(a & b), it can be observed that all Cu doped NPs shows better absorption of visible light as compared to undoped NPs.

Further band gap has been calculated by using Tauc's formula. Figure 4.38(a & b) shows the graphs between $(\alpha h\nu)^2$ and $h\nu$ for undoped and Cu (1.0% –5.0%) doped ZnO NPs. The band gap values has been found to be 3.23 eV, 2.64 eV, 2.82 eV, 2.98 eV, 3.04 eV and 3.08 eV for undoped, Cu (1.0%), Cu (2.0%) , Cu (3.0%) , Cu (4.0%) and Cu (5.0%) doped ZnO NPs synthesized at pH-8.0. The calculated band gaps for NPs synthesized at pH 10.0 and 12.0 are 3.3eV and 3.16eV respectively. It can be seen that all Cu doped ZnO samples synthesized at pH-8.0 have an optical energy band gap lower than that of undoped ZnO.

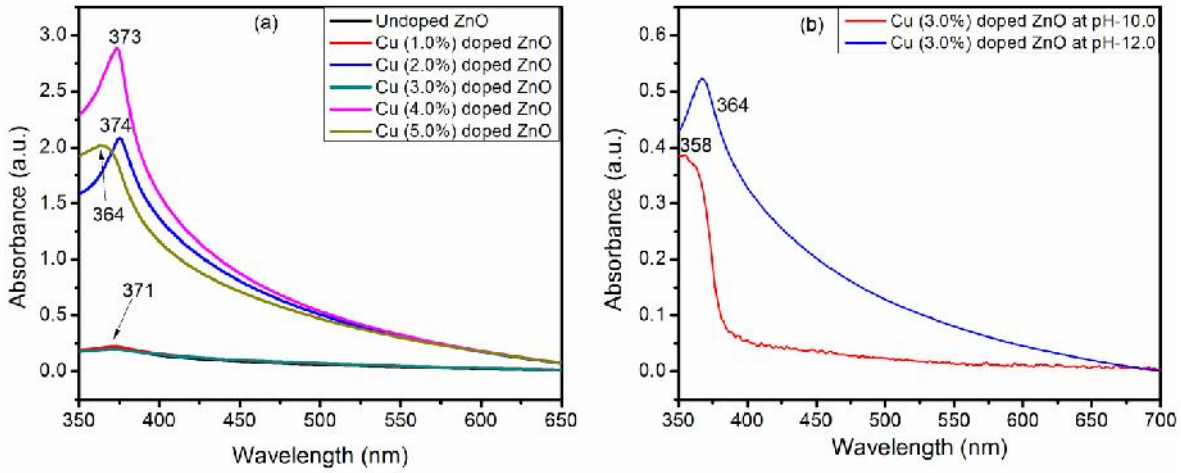

Figure 4.37: UV-Visible absorption spectra of (a) undoped and Cu (1.0% - 5.0%) doped synthesized at (a) pH-8.0 (b) Cu (3.0%) doped ZnO NPs synthesized at pH-10.0 and 12.0.

The band gap value of undoped ZnO is 3.23 eV. It has been observed that band gap of doped ZnO NPs decreases as the Cu doping concentration increases from 1.0 – 3.0%. After this when Cu doping concentration increases to from 4.0 to 5.0%, the band gap again increases from 3.04 to 3.08 eV, which is still less compared to undoped ZnO NPs. This decrease in band gap for Cu doped NPs correspond to p - d spin exchange interactions between the band electrons and the localized d electrons of doped Cu metal [44]. Moreover, decrease in band gap is attributed to the merging of an impurity band into conduction band [45]. Thus the red shift in Cu doped samples confirms the uniform incorporation of Cu in ZnO lattice.

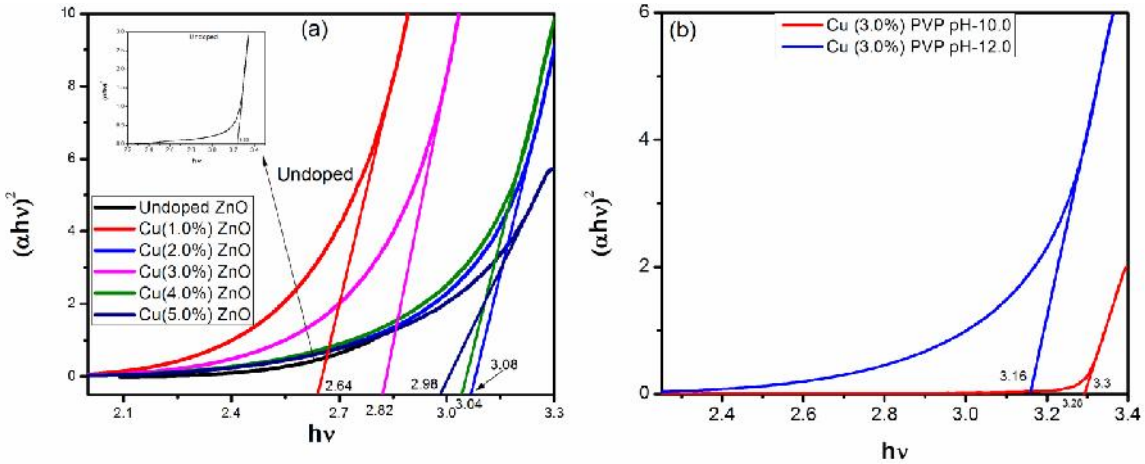

Figure 4.38: Touc's plot for (a) undoped and Cu (1.0% - 5%) doped ZnO NPs synthesized at pH-8.0 and (b) Cu (3.0%) doped ZnO NPs synthesized at pH 10.0 and 12.0.

4.5.4 Photocatalytic Studies

The photocatalytic degradation of CV dye in the presence of undoped and doped ZnO NPs synthesized at pH-8.0 was investigated under UV-Visible irradiation. This dye was used as a test contaminant owing to its absorption peaks in the visible range and thus its degradation can be easily monitored by optical absorption spectroscopy. Figure 4.39(a) shows the change in concentration of CV dye as a function of irradiation time for the dye derivative in absence and presence of undoped and Cu (1.0-5.0%) doped ZnO NPs (C is the concentration of CV determined at λ_{max} of absorption and C_0 is initial concentration). Figure 4.39(b) shows histogram for percentage decrease in concentration of CV dye over time under different conditions. It shows only 25% of CV dye dissolved in water disappears after 3.5h of UV-Visible radiations without any photocatalyst. This smaller degradation of CV dye might be due to the interaction between $OH^{\cdot}$ radical generates from water and CV dye. 48% of CV dye degraded with undoped ZnO NPs. Photocatalytic activity of undoped ZnO NPs is due to defect states caused by donor and acceptor states such as oxygen vacancies, interstitial zinc atom, zinc vacancies and interstitial oxygen respectively. Interfacial electron transfer takes place between donor states and CV dye. CV dye as a cationic dye acquire electron from excited donor states and get decomposed. Figure 4.31(b) shows 57%, 64%, 94%, 85% and 59% of CV dye degraded with Cu (1.0%), Cu (2.0%), Cu (3.0%), Cu (4.0%) and Cu (5.0%) doped ZnO NPs synthesized at pH-8.0 when exposed to UV-Visible radiations for 3.5h. From this it can be concluded that degradation of CV dye increases from 57% to 94% for Cu (1.0%) to Cu (3.0%), afterwards it reduces for higher Cu doping concentration. This is because ZnO act as a source of electrons and holes. The dopant Cu atoms and donor states (oxygen vacancy/ defects) act like a sink to electron and hole pairs which decreases the electron-hole pair recombination that results higher production of $OH^{\bullet}$ radicals [49]. This results in greater decomposition of CV dye using Cu doped ZnO NPs. Here Cu (3.0%) doped ZnO shows higher degree of degradation of CV dye over other doped ZnO NPs because higher concentration of Cu doping also shows negative effect. It creates a cyclic process without generating active $OH^{\cdot}$ radicals [50]. Since Cu (3.0%) has smaller particle size (confirmed from XRD studies shown above) as compared to other Cu doped ZnO NPs at pH-8.0. Also, linear relationship between $-\ln(C/C_0)$ and irradiation time is shown in Figure 4.39 (c). The pseudo-first-order rate constant (K) and linear regression coefficient (R) obtained from Figure 4.39 (c) for degradation of CV dye with and without photocatalyst at different

conditions are summarized in Table 4.5. It shows that photoreaction rates are highest for Cu (3.0%) doped ZnO NPs at pH-8.0 and is least for without any photocatalyst under UV-Visible radiations. The higher value of first order rate constant demonstrates higher photocatalytic performance. Thus Cu (3.0%) doped ZnO NPs at pH-8.0 shows highest photocatalytic performance among all the synthesized photocatalysts.

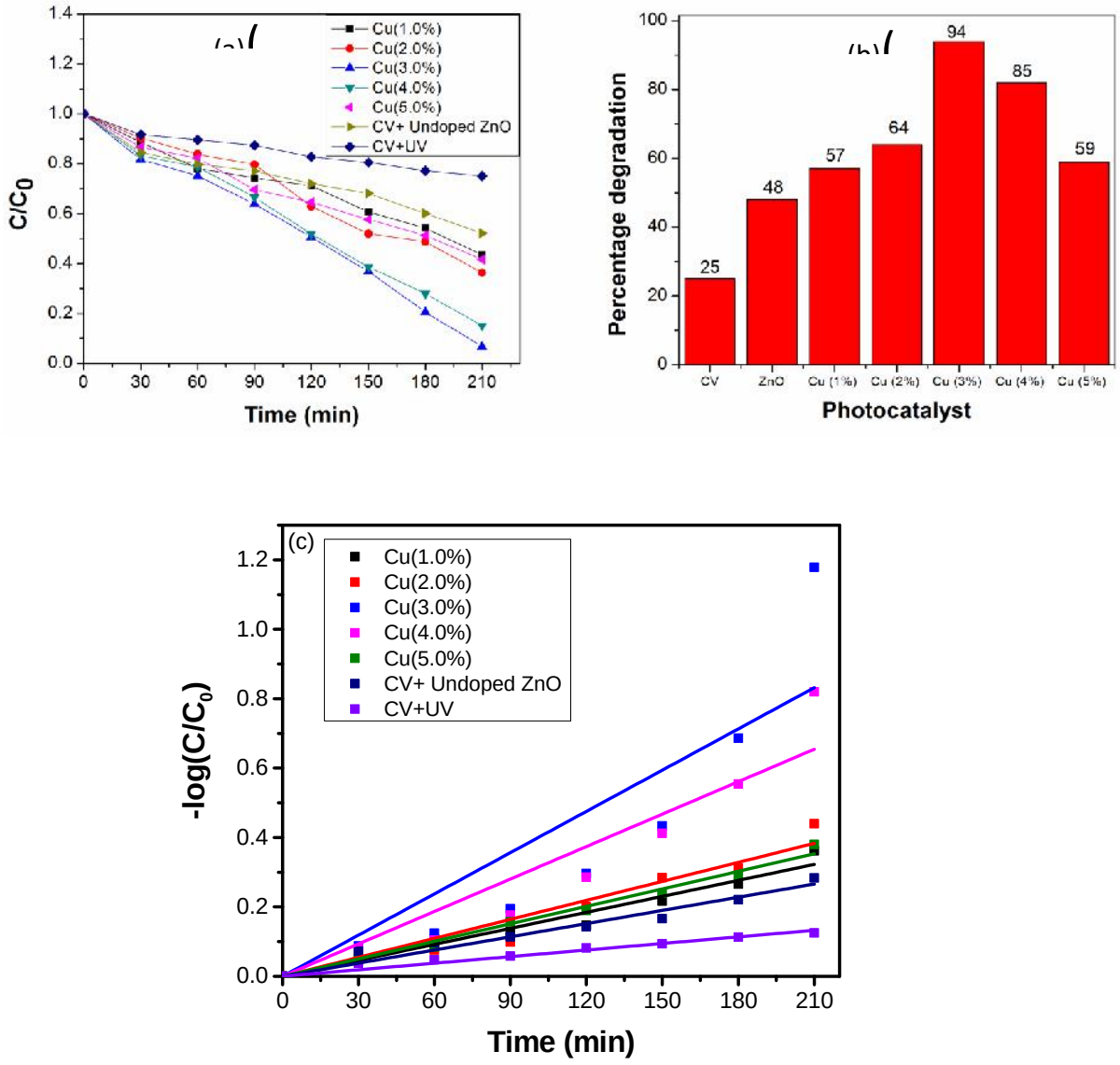

Figure 4.39: (a) Change in concentration (b) Histogram to study the percentage degradation of CV dye and (c) Kinetics of crystal violet degradation with and without photocatalyst synthesized at pH-8.0 under different conditions.

4.5.5 Effect of pH on photocatalytic properties

As discussed in section 4.4.6, the pH also affect the photocatalytic process of various pollutants and thus is an important parameter in the reaction taking place on semiconductor surface.

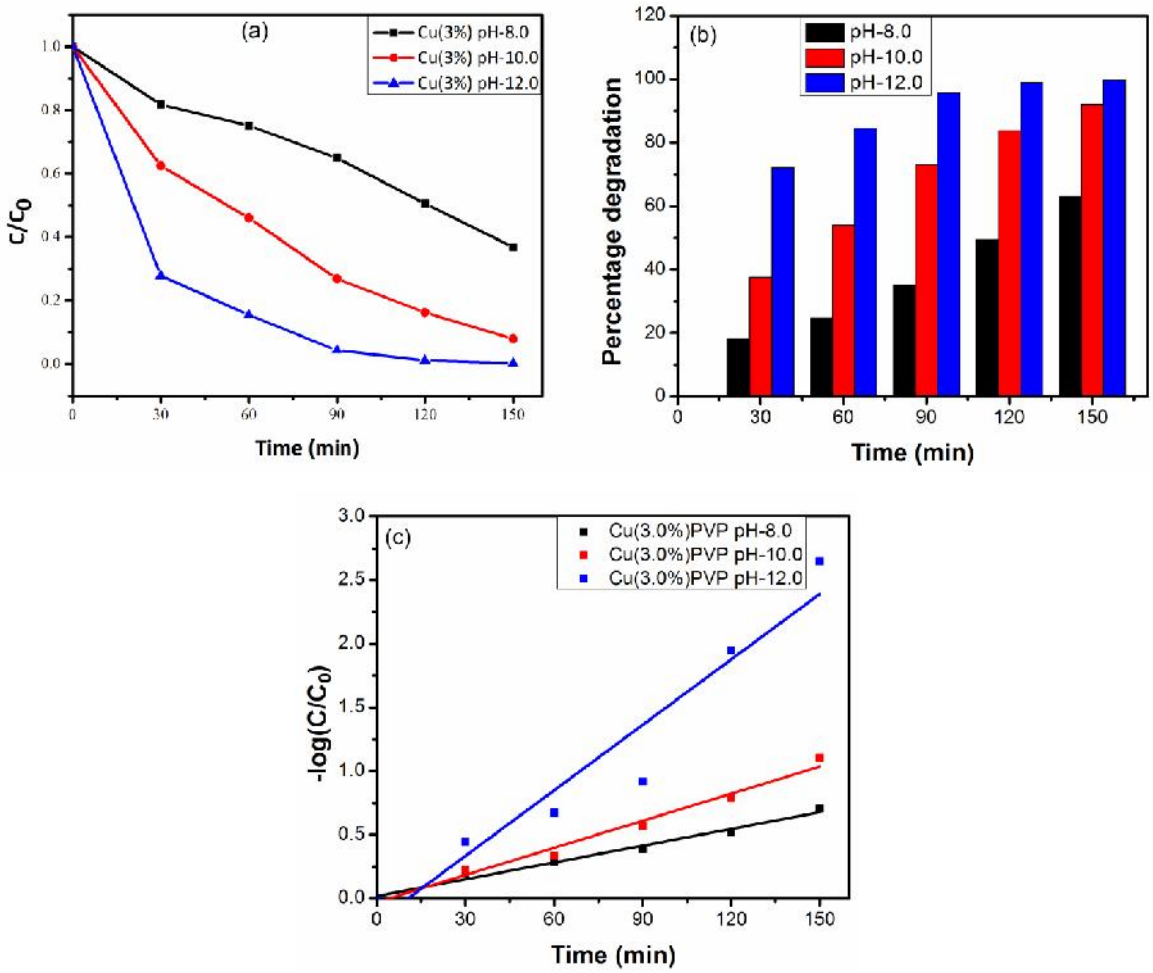

Figure 4.40: (a) Change in concentration (b) Histogram to study the percentage degradation of CV dye and (c) Kinetics of crystal violet degradation under Cu (3.0%) doped ZnO NPs synthesized at different pH value.

Therefore to study the effect of pH on doping and capping agent, optimal doped ZnO NPs has been synthesized at higher pH value. The pH of the photocatalysts has been adjusted during the synthesis. Figure 4.40(a) indicates the decrease in concentration of CV dye when exposed under UV-Visible radiations in the presence of Cu (3.0%) doped samples synthesized at pH-8.0, 10.0 & 12.0. Histogram for comparing the percentage degradation of CV dye using Cu (3.0%) doped ZnO NPs at various pH are shown in Figure 4.32(b). From this Figure it is clear that 63.1% and 92.2% CV dye has been degraded with Cu (3.0%) doped ZnO NPs at pH-8.0

and 10.0 respectively after 2.5h of UV-Visible exposure. However, almost 100% CV dye has been degraded with Cu (3.0%) doped ZnO NPs synthesized at pH-12.0 and that to only after 2.5h of UV-Visible irradiation. Thus higher degree of CV dye degradation has been obtained at much lower irradiation time. The linear relationship between $-\ln(C/C_0)$ and irradiation time as shown in Figure 4.40(c) is obtained. The pseudo-first-order rate constant (K) and linear regression coefficient (R) for degradation of CV.

Table 4.5: Reaction rate constant of crystal violet without catalyst, undoped, Cu (1.0%, 2.0%, 3.0%, 4.0% and 5.0%) doped and TG (1.0%) capped ZnO NPs at pH-8.0.

Experiment	Concentration of crystal violet dye (mg/L)	Catalyst concentration (0.25g/100 mL)	pH	K (rate constant) min^{-1}	R^2
1	10	Without catalyst	8.0	0.00129	0.97501
2	10	Undoped ZnO	8.0	0.00118	0.9596
3	10	Cu (1.0%) doped ZnO	8.0	0.00157	0.9637
4	10	Cu (2.0%) doped ZnO	8.0	0.00204	0.9578
5	10	Cu (3.0%) doped ZnO	8.0	0.00363	0.9551
6	10	Cu (4.0%) doped ZnO	8.0	0.00299	0.9547
7	10	Cu (5.0%) doped ZnO	8.0	0.00171	0.9857
8	10	Cu (3.0%) doped ZnO	10.0	0.00709	0.98412
9	10	Cu (3.0%) doped ZnO	12.0	0.01714	0.95066

dye using Cu (3.0%) doped ZnO NPs at different pH are also summarized in Table 4.5. It shows that photoreaction rates are highest for Cu (3.0%) doped NPs at pH-12.0 among Cu (3.0%) doped NPs synthesized at pH-8.0, 10.0 and 12.0. The cause of better degradation efficiency of as synthesized optimal doped ZnO photocatalysts at higher pH value is already discussed in section 4.4.6. Thus pH is an essential factor need to study, to enhance the photodegradation efficiency of as synthesized NPs for their application in various textile industries. Although, both Mn and Cu doped ZnO NPs have degraded dye significantly but on comparing, it can be stated that Cu doped ZnO NPs synthesized at higher pH values has shown slightly better degradation efficiency as compared to Mn doped ZnO NPs. Cu doped ZnO NPs capped with TG and PVP has degraded almost 100% CV dye in 150min whereas, Mn doped TG capped ZnO NPs synthesized at pH 12 has degraded 96% dye in 150 mins.

References

[1] H. F. Lin, S. C. Liao, S. W. Hung, The dc thermal plasma synthesis of ZnO nanoparticles for visible light photocatalyst, J.Photochem. Photobiol. A: Chem.,174, 82–87 **(2005).**

[2] M. Sharma, T. Jain, S. Singh and O.P.Pandey, Photocatalytic degradation of organic dyes under UV-Visible light using capped ZnS nanoparticles, SolarEner.,86, 626-633 **(2012).**

[3] B. J. Liu, T. Torimoto, H. Yoneyama, Photocatalytic reduction of CO_2 using surface-modified CdS photocatalysts in organic solvents, J. Photochem. Photobiol. A: Chem., 113, 93–97 **(1998).**

[4] Y. Zhang, M.K. Ram, E. K. Stefanakos, D. Y. Goswami, Synthesis, Characterization and Applications of ZnO Nanowires, J. Nanomater. 2012 (2012). doi:10.1155/**2012**/624520.

[5] R. Ajay Rakkesh and S. Balakumar, Facile Synthesis of ZnO/TiO_2 Core-Shell Nanostructures and Their Photocatalytic Activities, J. Nanosci. Nanotechnol.13, 370 **(2013).**

[6] M.A. Behnajady, N. Modirshahla, R. Hamzavi, Kinetic study on photocatalytic degradation of C. I. Acid Yellow 23 by ZnO photocatalyst. J. Hazar.Mater.,B133, 226-232 **(2006).**

[7] C. Lizama, J. Freer, J. Baeza, H. Mansilla, Optimized photodegradation of Reactive Blue 19 on TiO_2 and ZnO suspensions, Catal. Tod., 76, 235–246 **(2002).**

[8] M. C. Yeber, J. Rodriguez, J.Freer, J. Baeza,N. Duran, H.Mansilla, Advanced oxidation of a pulp mill bleaching wastewater, Chemosph., 39, 1679–1688 **(1999).**

[9] A. A. Khodja,T. Sehili, J. Pilichowski, P. Boule, Photocatalytic Degradation of 2-phenylphenol on TiO_2 and ZnO in Aqueous Suspensions , J. Photochem. Photobiol. A: Chem., 141,231–239 **(2001).**

[10] M. A. Mahmood, S. Baruah, J. Dutta, Enhanced visible light photocatalysis by manganese doping or rapid crystallization with ZnO nanoparticles, Mater. Chem. and Physics, 130, 531–535 **(2011)**.

[11] X. L. Wang, C. Y. Luan, Q. Shao, A. Pruna, C. W. Leung, R. Lortz, J. A. Zapien, A. Ruotolo, Effect of the magnetic order on the room-temperature band-gap of Mn-doped ZnO Thin films, App. Phy. Lett. 102, 102112 **(2013).**

[12] F. Schoofs, T. Fix, A. M. H. R. Hakimi, S. S. Dhesi, G. V. Laan, S. A. Cavill, S. Langridge, J. L. M.Driscoll, M. G. Blamire, Strain dependent defects mediated ferromagnetism in Mn-doped and undoped ZnO thin films, J. App. Phy., 108, 053911 **(2010).**

[13] Y. Zheng, L. Zheng, Y. Zhan, X. Lin, Q. Zheng, K. Wei, Ag/ZnO hetrostructure nanocrystals: synthesis, characterization and photocatalysis, Inorgan. Chem., 46, 6980-6986 **(2007)**.

[14] Y. Kanai, Admittance Spectroscopy of Cu-Doped ZnO Crystals, Jpn. J. Appl. Phys., 30, 703-707 **(1991)**.

[15] R. Maithy and K.K.Chattopadhyay, Synthesis and optical characterization of ZnS and ZnS:Mn nanocrystalline thin films by chemical route, Nanotechn., 15 (7),812 **(2004).**

[16] J. I. Pankove, Optical process in semiconductors (Prentice-Hall, Engle- wood Cliffs, NJ, **(1971).**

[17] M. Sharma,S. Singh, O.P. Pandey, Excitation induced tunable emission in biocompatible chitosan capped ZnS nanophosphors, J. App.Phy.,107, 104319 **(2010).**

[18] G. Cherepanov, Point defect in solids. Fundamentals of Deformation and Fracture,

605-623 **(1984).**
[19] B. Halprin, M. Lax, Impurity-band tails in the high density limit.l. Minimum counting methods, Phy. Rev.,148 (2), 722-740 **(1966).**
[20] N. Tahir, S. T. Hussain, M. Usman,S.K.Husanain, A.Mumtaz, Effect of vanadium doping on structural, magnetic and optical properties of ZnO nanoparticles, App. Surf. Sci., 255 (20), 8506-8510 **(2009).**
[21] P. Chakraborty, G.Dutta, K.Ghatak, A simple theoretical analysis of the effective electron mass in heavily doped lll-V semiconductor in the presence of band-tails, Physica Script.,68,368-377 **(2003).**
[22] A. Fujishima, T. N.Rao and D. A. Tryk, Titanium dioxide photocatalysis, J. Photochem. andPhotobio. C:Photochem. Rev.,1, 1-21 **(2000).**
[23] V. Eskizeybek,F.Sari, H. Gulce.A. Gulce,A. Avci, Preperation of the new polyaniline/ZnO nanocomposite and its photocatalytic activity for degradation of methylene blue and malachite green dyes under UV and natural sun lights irradiations, App. Catal. B. Env., 119-120, 197-206 **(2012).**
[24] Y. Abdollahi, A. H. Abdullah, Z. Zainal, N. A. Yousof, Synthesis and Characterization of Manganese Doped ZnO Nanoparticles, IJBAS-IJENS, 11 (04), 44-50 **(2011).**
[2 5] R. Kitture, S. J. Koppikar, R. K. Ghanekar, S. N. Kale, Catalyst efficiency, photostability and reusability study of ZnO nanoparticles in visible light for dye degradation, J. Phy. and Chem. Sol., 72, 60-66**(2011).**
[26] J. Zhang,L. D. Sun, J. L. Yin, H. L. Su, C. S. Liao, C. H. Yan, Control of ZnO Morphology via a Simple Solution Route, Chem.Mater. 14,4172 **(2002).**
[27] C. L. Tsai, Y. C. Tseng,W. M. Cho, H. C. Chang, Y. H. Chen, C. H.Lin, Effects of ultraviolet treatment on the optical and structural properties of ZnO nanoparticles, Mater. Chem. and Phy., 130, 299-302 **(2011).**
[28] S. K. Mishra, R. K. Srivastava, S. G. Prakash, R.S. Yadav, A. C. Pandey, Photoluminescence and photoconductive characteristics of hydrothermally synthesized ZnO nanoparticles, Opto-Electron. Rev.,18, 467 **(2010).**
[29] C. F. Jin, X. Yuan,W. W.Ge, J. M. Hong,X. Q. Xin, Synthesis of ZnO nanorods by solid state reaction at room temperature, Nanotech., 14, 667**(2003).**
[30] K. Vanheusden, W. L. Warren, C. H. Seager, D. R. Tallant, J. A. Voigt, B. E. Gnade, Mechanisms behind green photoluminescence in ZnO phosphor powders, J. Appl. Phys., 79, 7983-7990 **(1996).**
[31] W. C. Zhang, X. L. Wu, H. T. Chen, J. Zhu, G. S. Huang, Excitation wavelength dependence of the visible photoluminescence from amorphous ZnO granular films, J. Appl. Phys. 103, 093718-093722 **(2008).**
[32] C. H. Hung, W. T. Whang, Effect of surface stabilization of nanoparticles on luminescent characteristics in ZnO/poly(hydroxyethyl methacrylate) nanohybrid films, J. Mater. Chem., 15, 267-274 **(2005).**
[33] H. Zeng, W. Cai, J. Hu, G. Duan, P. Liu, Y. Li, Violet photoluminescence from shell layer of Zn/ZnO core-shell nanoparticles induced by laser ablation, Appl. Phys. Lett., 88, 171910-171912 **(2006).**
[34] A. Singh, R. Kaur, O. P. Pandey, X. Wei, M. Sharma, Synthesis of fluorescent core-shell nanomaterials and strategies to generate white light, J. Appl. Phys., 118, 044305 **(2015)**.
[35] R. Viswanatha, S. Sapra, S. S. Gupta, B. Satpati, P. V. Satyam, B. N. Dev, D. D. Sarma, Synthesis and characterization of Mn-doped ZnO nanocrystals, J. Phys. Chem. B, 108 6303–6310 **(2004)**.

[36] Y.Yang,Y. Li, L. Zhu, H. He,L. Hu,J. Huang,F. Hu,B. He, Z. Ye, Shape control of colloidal Mn doped ZnO nanocrystals and their visible light photocatalytic properties, Nanoscale, 10461-10471 **(2013).**

[37] D. Gusain, S. N. Upadhyay, Y. S. Sharma, Adsorption of Orange G dye on nano zirconia: error analysis for achieving the best equilibrium and kinetic modeling, RSC Adv., 4, 18755-18762 **(2014).**

[38] P. Ji, J. Zhang, F. Chen, M. Anpo, Study of adsorption and degradation of acid orange 7 on the surface of CeO_2 under visible light irradiation, Appl. Catal. B: Environ., 85, 148-154 **(2009).**

[39] J. Z. Kong, A. D. Li, X. Y. Li, H. F. Zhai, W. Q. Zhang, Y. P. Gong, H. Li, D. Wu, Photo- degradation of methylene blue using Ta doped ZnO nanoparticle, J. Sol. State Chem., 183, 1359–1364 **(2010).**

[40] J. Zhao, T. Wu, K. Wu, K. Oikawa, H. Hidaka, N. Serpone, Photoasisted degradation of dye pollutants, 3. Degradation of the cationic dye rhodamine B in aqueous anionic surfactant/ TiO_2 dispersion under visible light irradiation: evidence for the need of substrate adsorption on TiO_2 particles, Environ. Sci. Technol., 32, 2394-2400 **(1998).**

[41] C. A. K. Gouvea, F. Wypych, S. G. Moraes, N. Duran, N. Nagata, P. P. Zamor, Semiconductor assisted photocatalytic degradation of reactive dyes in aqueous solution, Chemosph., 40, 433-440 **(2000).**

[42] R. D. Shannon, Revised effective ionic radii and systematic studies of interatomic distances in halides and chalcogenides, Acta Cryst., A32, 751–767 **(1976).**

[43] X. Peng, J. Xu, H. Zang, B. Wang, Structural and PL properties of Cu-doped ZnO films, J. Lumin., 128, 297-300 **(2008).**

[44] X. Y. Li, H. J. Lia, M. Yuan, Z. J. Wang, Z. Y. Zhou, R. B. Xu, Influence of oxygen partial pressure on electrical and optical properties of $Zn_{0.93}Mn_{0.07}O$ thin films, J. Alloys and Compd., 509, 3025-3031 **(2011)**.

[45] R. B. Bylsma, W. M. Becker, J. Kossut, U. Debska, D. Yoder-short, Dependance of energy gap on x and T in $Zn_{1-x}Mn_x$ Se: the role of exchange interaction, Phys. Rev. B, 33, 8207-15 **(1986).**

[46] J. Wang, L. Gao, Synthesis of uniform rod-like, multi-pod-like ZnO whiskers and their photoluminescence properties, J. Cryst. Grow., 262, 290-294 **(2004).**

[47] Y. W. Chen, Y. C. Liu, S. X. Lu, C. S. Xu, C. L. Shao, C. Wang, J. Y. Zhang, Y. M. Lu, D. Z. Shen, and X. W. Fan, Optical properties of ZnO and ZnO-In nanorods assembled by sol-gel method, J. Chem. Phys., 123, 134701 **(2005).**

[48] A. Ghosh, N.G. Despande, Y.G. Gudage, R.A. Joshi, A.A. Sagade, D.M. Phase, R. Sharma, Effect of annealing on structural and optical properties of zinc oxide thin film deposited by successive ionic layer adsorption and reaction technique, J. Alloys Compd., 469, 56-60 **(2009)**.

[49] K. Okamoto, Y. Yamamoto, H. Tanaka, M. Tanaka, A. Itaya, Heterogeneous Photocatalytic Decomposition of Phenol over TiO_2 powder, Bull. Chem. Soc. Jpn., 58, 2015-2022 **(1985).**

[50] A. Sclafani,, L., M. Palmisano, Schiavello, N_2 photoreduction and phenol and nitrophenol isomers photooxidation as example of heterogeneous photocatalytic reactions, Res. Chem. Intermed.,18, 211-226 **(1992).**

[51] P. Ji, J. Zhang, F. Chen, M. Anpo, Study of adsorption and degradation of acid orange 7 on the surface of CeO_2 under visible light irradiation, Appl. Catal. B: Env., 85, 148-154 **(2009).**

[52] M.A. Fox, M. T. Dulay, Heterogeneous Photocatalysis, Chem. Rev., 93, 341-357 **(1993).**

[53] S. K. Pardeshi, A. B. Patil, A simple route for photocatalytic degradation of phenol in aqueous zinc oxide suspension under solar energy, Solar Ener.,82, 700-705 **(2008).**

[54] U. G. Akpan, B. H. Hameed, Parameters affecting the photocatalytic degradation of dyes using TiO_2 – based photocatalysts: A review J. Hazard. Mater.,170 520-529 **(2009).**

CHAPTER 5

RESULTS AND DISCUSSION

Doped (Au and Ag) CeO_2 nanoparticles

Overview

The present chapter describes the study of doped CeO_2 (ceria) nanoparticles (NPs) synthesized by co-precipitation method. Various techniques viz. X-ray diffraction (XRD), transmission electron microscopy (TEM), energy dispersive spectroscopy (EDS), UV-Visible spectroscopy, photoluminescence (PL) emission and excitation spectroscopy has been employed to characterize as synthesized doped and capped NPs. Photocatalytic efficiency of synthesized NPs has been studied by evaluating the degradation of rhodamine B (RhB) dye under UV-Visible irradiations. Further the effect of pH has also been studied in detail. Here it is important to mention that the pH of NPs has been adjusted during synthesis only.

5.1 Introduction

As discussed in previous chapter, doping of Mn and Cu can enhance the photocatalytic efficiency of nanosized semiconductor photocatalyst. Except ZnO, CeO_2 has also been found to be efficient catalyst as it has some properties similar to TiO_2 such as wide band gap, high stability and non-toxicity [1]. It has high resistance to chemical and photo corrosion and has strong light absorption ability in far UV region. Also, the ability of CeO_2 to absorb and release of oxygen plays a critical role in overall performance of its catalytic activity. CeO_2 has large oxygen storage capacity depending on redox cycle of Ce^{4+}/Ce^{3+}, which further depends upon the type and concentration of oxygen vacancies in the lattice structure [2]. Quantum mechanically the most favorable defect structure in CeO_2 is Ce^{4+} - O_v – Ce^{3+} (O_v - oxygen vacancy) and Ce^{3+} formation shows red shift in band gap of CeO_2 nanomaterials [2]. Actually CeO_2 is a wide band gap semiconductor with optical indirect band gap of 3.2eV which strictly limits its application in ultraviolet (UV) region only [3]. In order to reduce the band gap of CeO_2 various metal or non-metal ions like Fe [4], Y [5], in [6], Sm [7], N [8] have been doped in CeO_2 lattice. All of these dopants have not shown the significant photodegradation of organic pollutants. Apart from these the loading of Au in CeO_2 has shown better catalytic efficiency [9]. Lei et al. [9] have shown that loading of 11.6 wt % Au/CeO_2 exhibit 1.3 times higher photoreactivity under UV light as compared to visible light. The catalytic activity of Au/ CeO_2 catalyst was mainly due to coexistence of active species Au^{3+} and Au^0 in Au loaded CeO_2 NPs. Therefore in order to further explore the photocatalytic efficiency of ceria NPs, we have doped it with silver (Ag) and gold (Au) metal ions and studied their photocatalytic activity under UV-Visible light irradiations. Also, doped ceria NPs has been synthesized at different pH to study the effect of pH along with doping.

5.2 Undoped and doped (Mn and Cu) CeO_2 nanoparticles

As discussed in chapter4 that Mn and Cu metal ion doped ZnO NPs has shown better photocatalytic efficiency, therefore optimal concentration of Mn and Cu ion has been doped in ceria lattice to evaluate their photocatalytic efficiency.

5.2.1 XRD studies

Figure 5.1 shows the typical XRD pattern for undoped and Mn(1.0%) and Cu(3.0%) doped CeO_2 NPs. All the peaks of as synthesized nanopowder in the 25-80º range of 2θ value are indexed to single crystalline with face-centered cubic (FCC) fluorite structure of pure CeO_2 (JCPDS 34-0394). Further no diffraction peaks corresponding to cerium oxide or dopant ion

related impurity has been detected. This confirms the successful doping of Mn and Cu into ceria. The average nanocrystallite size of undoped and doped ceria NPs estimated by Debye-Scherrer formula is in the range 7-12nm.

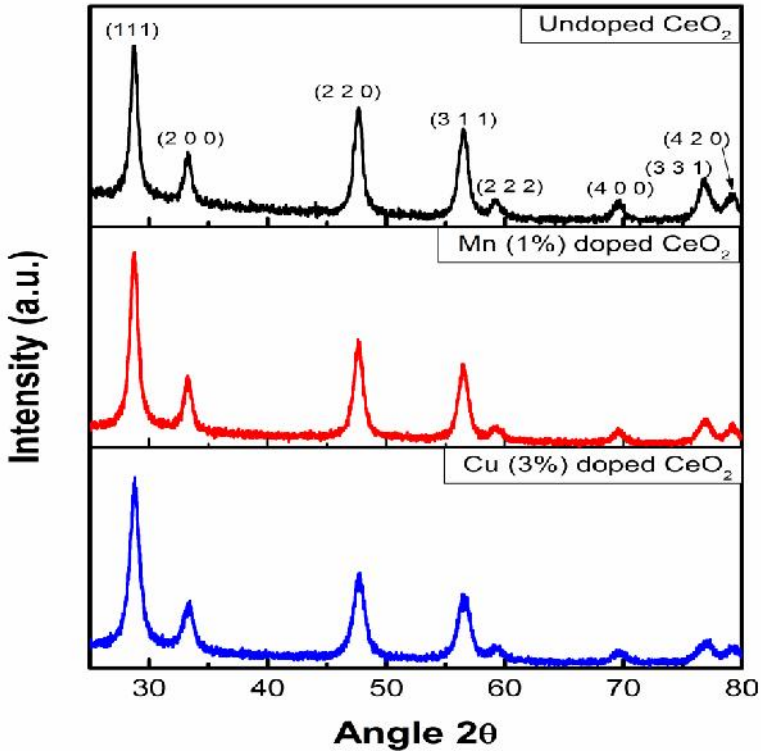

Figure 5.1: XRD pattern for undoped and doped CeO_2 NPs.

5.2.2 UV-Visible spectroscopy

Figure 5.2 reveals the UV-Visible absorption spectra of undoped and Mn(1.0%) and Cu(3.0%) doped CeO_2 NPs.

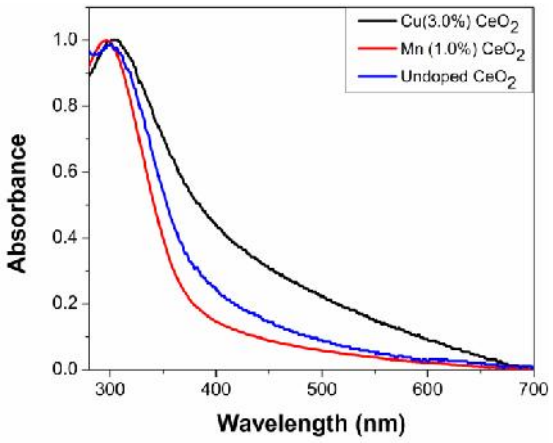

Figure 5.2: UV-Visible absorption spectra for undoped and doped CeO_2 NPs.

There is a strong absorption band from 300nm to 350nm in the spectra, which is attributed to charge transfer from O^{2-} in O 2p to Ce^{4+} in Ce 4f [10]. The band gap determines the portion of the solar spectrum that the photocatalyst absorbs.

5.2.3 Photocatalytic studies

The photocatalytic performance of as prepared undoped and doped samples has been evaluated by the degradation of Rhodamine B (RhB) dye under UV-Visible light radiations.

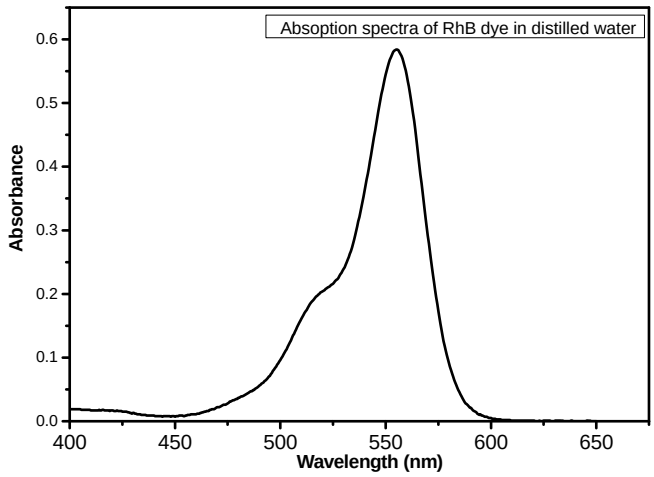

Figure 5.3: Calibration curve of RhB dye.

The photo-degradation process was evaluated by monitoring the change in concentration of RhB dye. In this study, without any adjustment, the pH of slurry (dye and photocatalyst solution) was at natural pH. The photocatalytic degradation of RhB dye in under UV-Vis. radiations with as synthesized

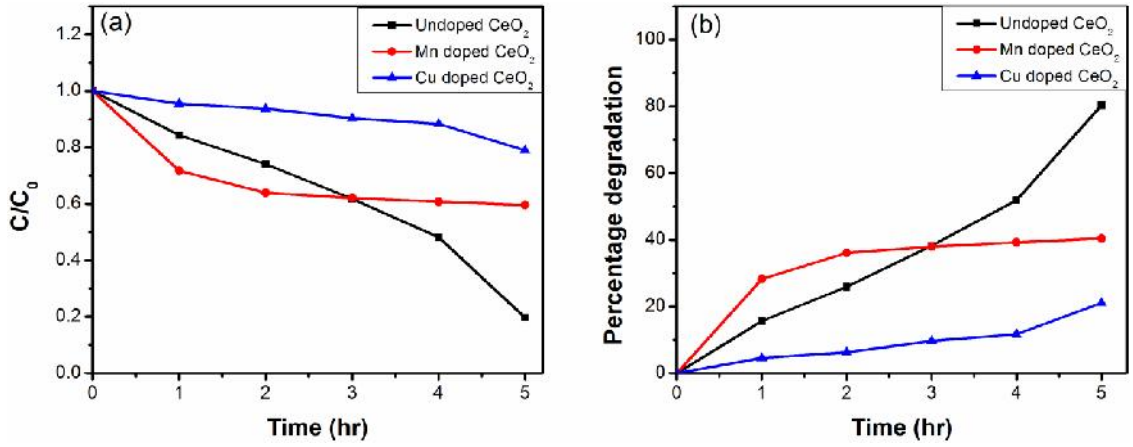

Figure 5.4: (a) Change in concentration and (b) Percentage degradation of RhB dye with undoped and Mn and Cu doped CeO_2 NPs.

undoped and doped ceria samples is shown in Figure 5.4(a), which shows the normalized concentration of RhB dye (C/C_0) as a function of light irradiations time. C_0 and C denotes initial concentration after adsorption-desorption equilibrium under dark conditions and the concentration of RhB at different irradiation times (t) respectively. The lower value of C/C_0 denotes the higher degradation of RhB dye. Figure 5.4(b) demonstrate that 79.2%, 40.1% and 21.6% of the dye has been degraded with undoped, Mn(1.0%) and Cu(3.0%) doped CeO_2 samples respectively under UV-Vis. light irradiations. The doped samples show lower photocatalytic activity than undoped sample. The oxygen vacancies play the dominant role in photocatalytic activity. However, the ionic radii of Mn^{2+}(81pm) and Cu^{2+} (91pm) is smaller than Ce^{3+} (115pm) and Ce^{4+} (101pm). Therefore the probability for generation of oxygen vacancies is reduced and CeO_2 doped with Mn and Cu doesn't give good photocatalytic results as compared to undoped CeO_2 NPs. Also, no shifting in XRD peaks has been observed which means no contraction or expension of the ceria lattice with doping has occurred. This confirms the reduction in oxygen vacancies with Mn or Cu doping. Oxygen vacancies act as the trapping centres for photoexcited electrons available in conduction band of CeO_2 and thus reduce the electron–holes recombination and results in faster photocatalytic degradation of organic pollutants. Therefore Mn and Cu doped CeO_2 NPs have shown smaller photodegradation of RhB dye as compared to undoped CeO_2 NPs.

Thus the above photocatalytic studies demonstrate that Mn and Cu metal ion doping has reduce the degradation efficiency of CeO_2 nanoparticles. In order to further enhance the photocatalytic degradation activity of ceria, we have doped silver (Ag) and gold (Au) metal ions in CeO_2 and evaluate their photocatalytic studies. These are discussed in next sections.

5.3 Ag doped CeO_2 nanoparticles

To evaluate the effect of Ag doping on morphological, optical and photocatalytic studies of CeO_2 lattice, we have synthesized silver doped ceria NPs at natural pH (7.5). Then Ag doped ceria NPs has been synthesized at pH-10.0 and 12.0 at optimal doping concentration. For simplification, the samples synthesized at pH-7.5 are denoted as undoped CeO_2 (CS0), 1 at% Ag-doped CeO_2 (CS1), 2 at% Ag-CeO_2 (CS2), 3 at% Ag-doped CeO_2 (CS3) and 2 at% Ag-doped CeO_2 synthesized at pH-10.0 and 12.0 are denoted as (CS210) and (CS212) respectively.

5.3.1 XRD studies

The X-ray diffraction (XRD) patterns of as synthesized undoped and Ag doped NPs (CS0, CS1, CS2, CS3, CS210, CS212) are depicted in Figure 5.5(a). All the peaks of as synthesized NPs in

the 20-80º range of 2θ value are indexed to single crystalline face-centered cubic (FCC) fluorite structure of pure CeO_2 (JCPDS 34-0394). Further no diffraction peaks corresponding to cerium oxide or Ag-related impurity has been detected. This confirms the successful doping of Ag into ceria (CeO_2) NPs. Samples with Ag doping show shift in the (111) peak towards higher 2θ values as compared to undoped sample as shown in Figure 5.5(b). Also with increase in Ag doping upto 2%, (111) peak has been observed to shift continuously. However, sample CS3 has shown smaller shift as compared to CS1 and CS2. Moreover, by increasing the Ag doping content, the calculated crystallite size and lattice parameter decreased slightly even though the ionic radius of Ag^{1+} is slightly larger than that of Ce^{3+} (0.129 nm and 0.115 nm, respectively). This reverse behavior may be due to an increase in oxygen vacancy concentration with Ag doping because the effective anionic radius in ceria lattice decreases with an increase in oxygen vacancies [11]. This further confirms the incorporation of Ag ions into ceria lattice. Recently similar type of behavior has been observed in Yttrium doped CeO_2 NPs [5]. The average nanocrystallite size of NPs has been estimated by Debye-Scherer formula. The calculated D

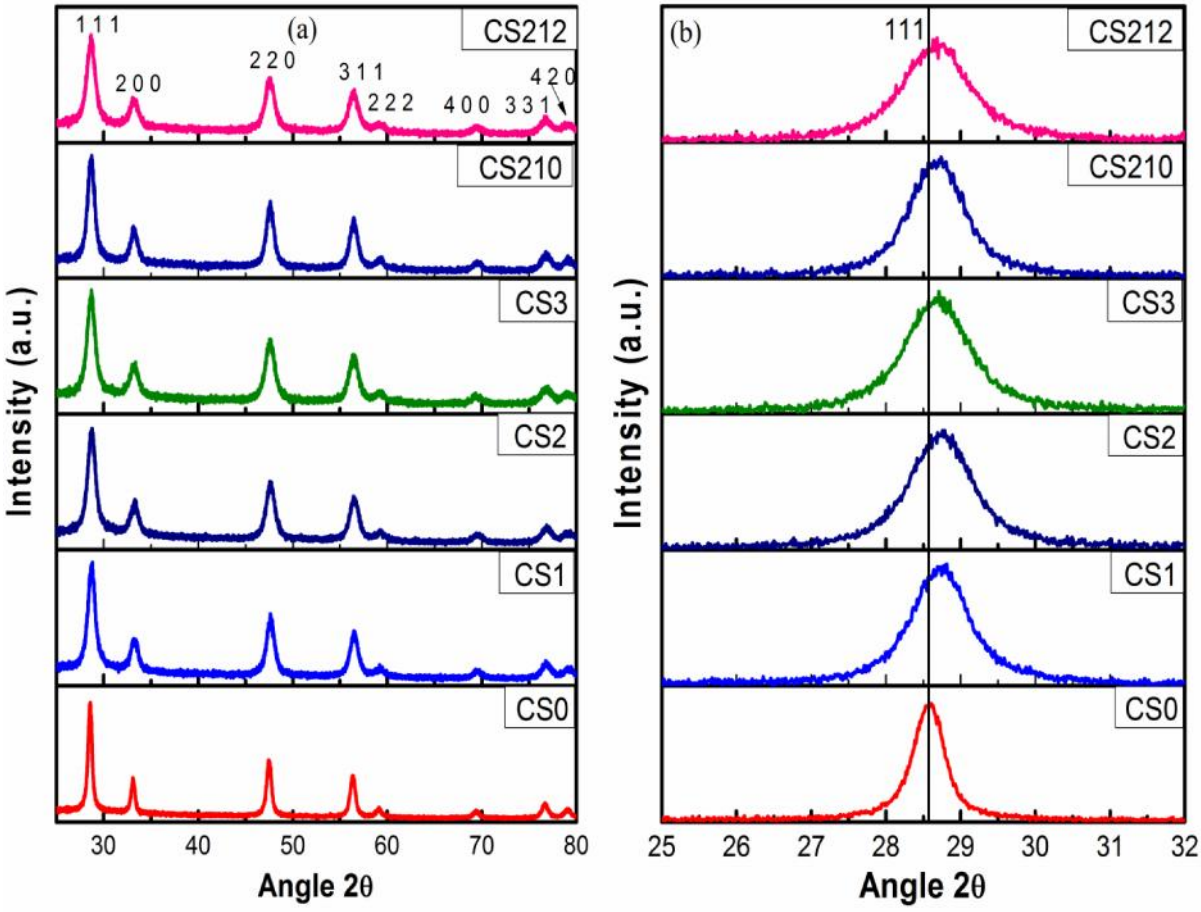

Figure 5.5: (a) XRD pattern and (b) Peak shift of CS0-CS212 NPs.

The calculated D values are in the range of 6.6-10.2 nm. Further the crystallite size of NPs are also estimated by Williamson-Hall plot (W-H plot) using equation

$$\beta \cos\theta/\lambda = K/D + 4\varepsilon \sin\theta/\lambda \quad \ldots\ldots(5.1)$$

The crystallite size is estimated from the y- intercept of the fit. The W-H plots are shown in Figure 5.6. The crystallite size so estimated has been presented in Table 5.1 and found to be very close to the crystallite size calculated from Debye-Scherer equation.

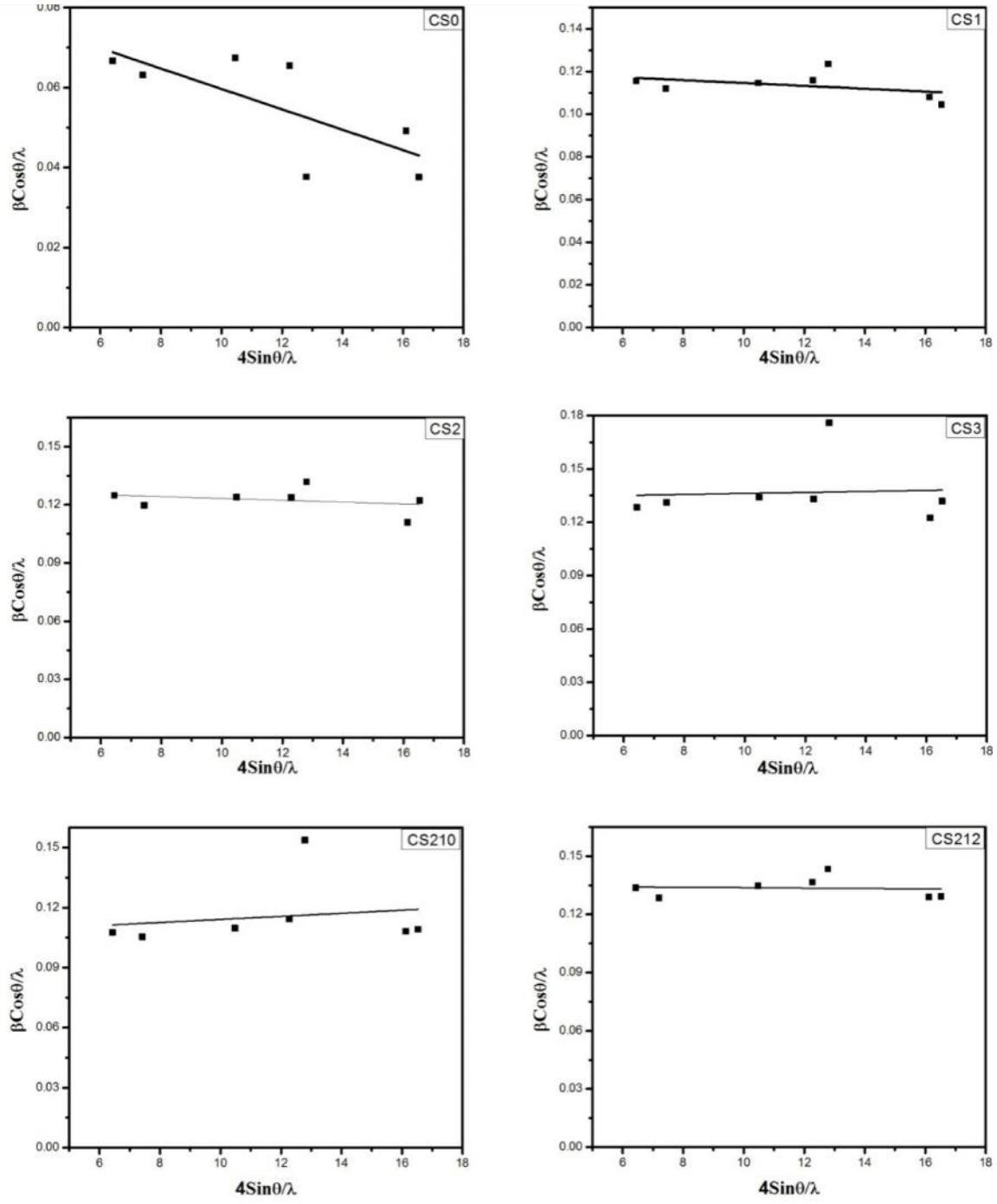

Figure 5.6: Williamson-hall plot for CS0-CS212 NPs.

Table 5.1: Lattice parameter, d-spacing and crystallite size of as synthesized samples

S. No	Sample Name	2θ	Lattice parameter (nm)	d-spacing (nm)	Crystallite size (nm)	
					Scherrer formula	W-H Plot
1	CS0	28.57	0.5306	0.3121	10.2	11.7
2	CS1	28.726	0.528	0.3104	7.6	7.4
3	CS2	28.735	0.527	0.3103	7.1	7.1
4	CS3	28.683	0.528	0.3109	6.6	6.1
5	CS210	28.682	0.528	0.3108	7.9	8.4
6	CS212	28.671	0.528	0.3109	6.7	6.6

5.3.2 TEM and EDS analysis

TEM has been utilized to determine the morphology of the as-prepared samples. Figure 5.7(a,b) presents the micrographs of CS0 and CS2 NPs respectively. It can be observed that the resulting NPs are uniform in shape and size, and the diameter of the NPs are in the range of 5-8 nm and 3-6 nm with narrow size distributions for CS0 and CS2 respectively. This is consistent with XRD and W-H plot results. Lattice fringes in the insets of Figure 5.7(a,b) are clearly visible with d-spacing of 0.312nm and 0.31nm for CS0 and CS2 respectively. These d-spacings are attributed to (111) planes of ceria (JCPDS 34-0394) which matches well with XRD results. Figure 5.8 shows energy dispersive spectroscopy (EDS) of as synthesized samples. It clearly demonstrates the presence of Ce and O in undoped and Ce, O and Ag in Ag doped samples respectively. Table 5.2 summarizes the elemental compositional data derived from Figure 5.8. This confirms the incorporation of Ag in ceria lattice.

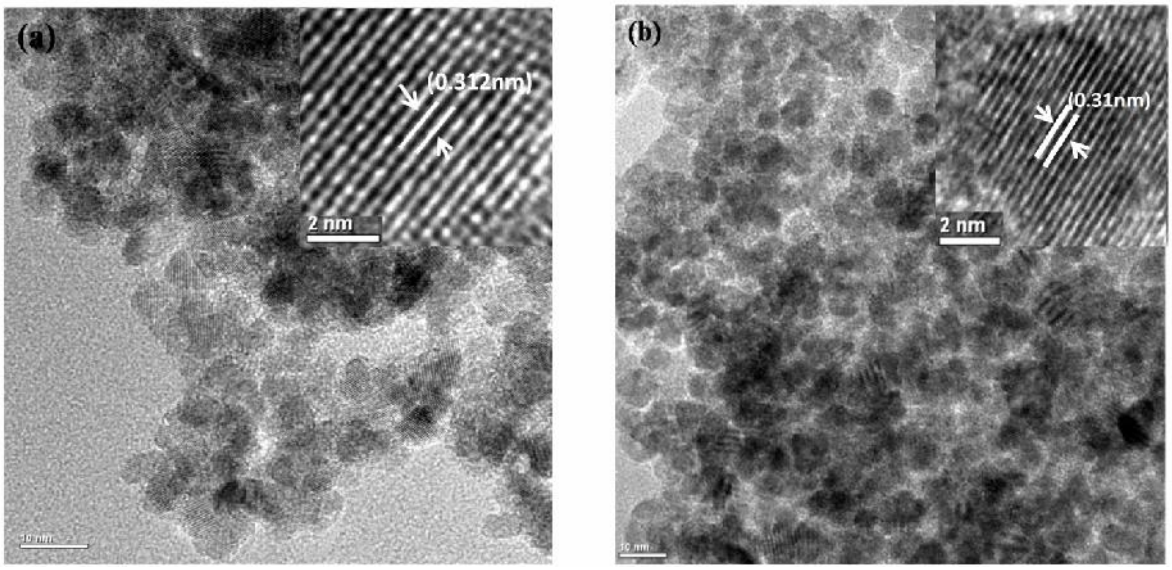

Figure 5.7: TEM images of (a) CS0 (b) CS2 NPs.

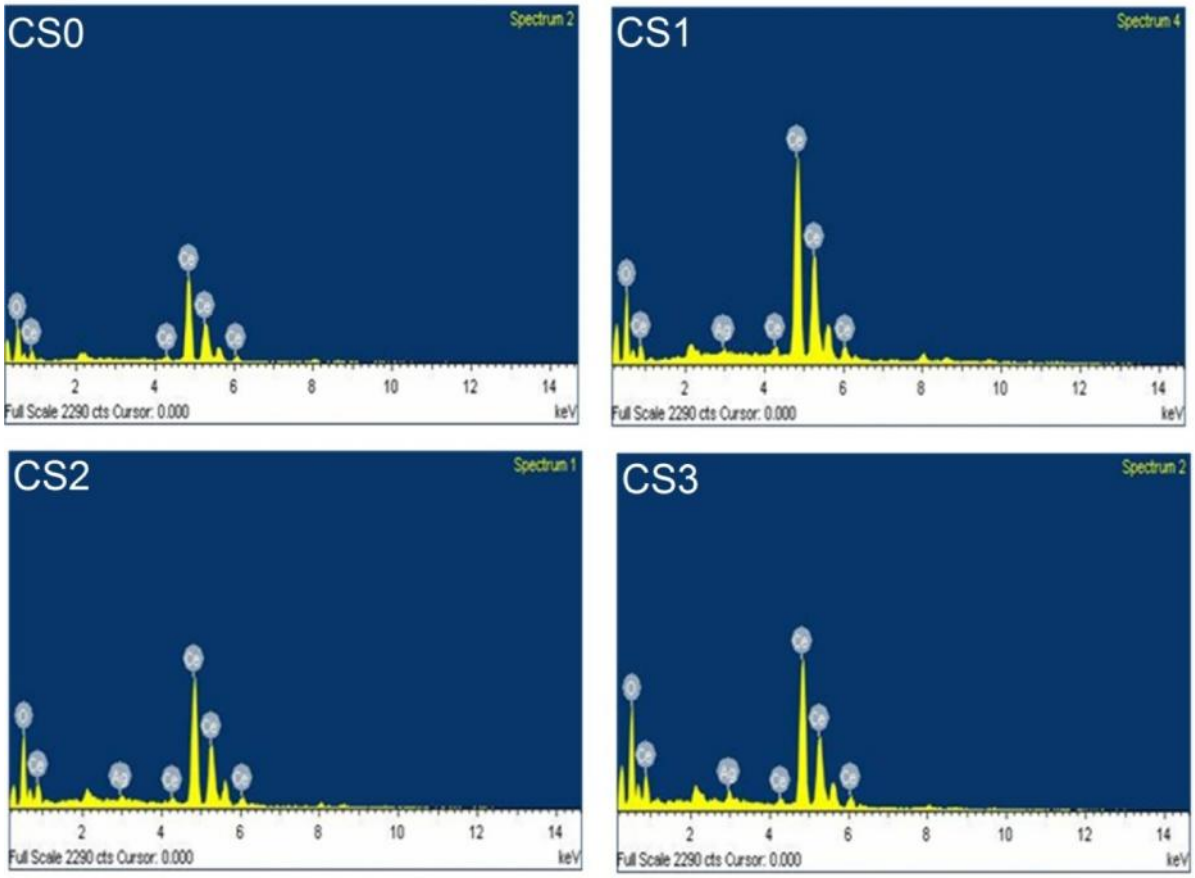

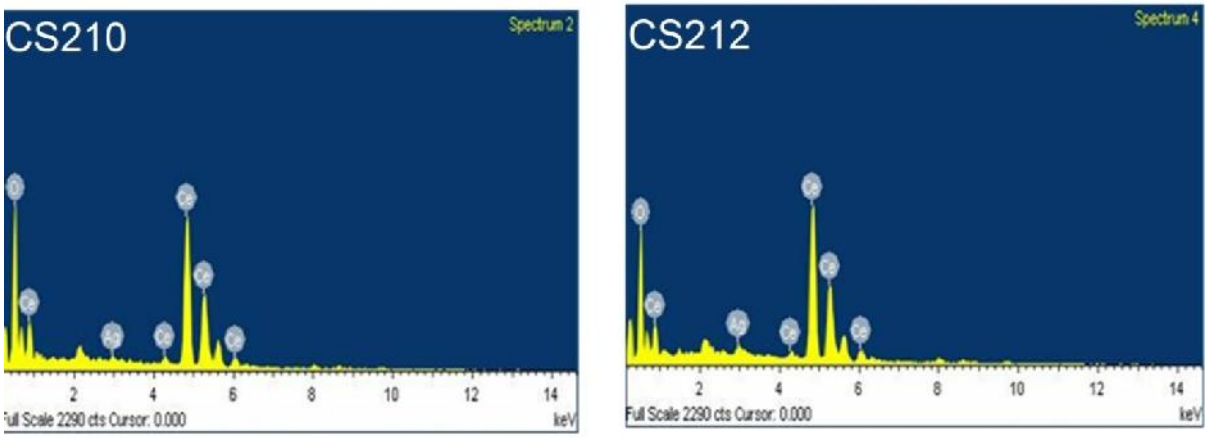

Figure 5.8: EDS of CS0-CS212 samples.

Table 5.2: Elemental composition of undoped and Ag doped CeO_2 NPs.

S. No.	Photocatalyst	Elements	Weight %	Atomic %
1	CS0	Ce	85.38	40
		O	14.62	60
2	CS1	Ag	0.67	0.41
		Ce	84.77	39.76
		O	14.57	59.84
3	CS2	Ag	2.11	1.29
		Ce	83.44	39.23
		O	14.45	59.48
4	CS3	Ag	3.53	2.16
		Ce	82.14	38.71
		O	14.33	59.14
5	CS210	Ag	2.07	1.26
		Ce	83.48	39.24
		O	14.45	59.5
6	CS212	Ag	2.10	1.28
		Ce	83.45	39.23
		O	14.45	59.49

5.3.3 UV-Visible spectroscopy

Figure 5.9(a,b) reveals the absorption spectra of as synthesized undoped and Ag doped CeO_2 NPs. There is a strong absorption band from 300nm to 350nm in the spectra, which is attributed to charge transfer from O^{2-} in O 2p to Ce^{4+} in Ce 4f [10]. The band gap determines the portion of the solar spectrum that the photocatalyst absorbs. The relationship between the optical absorption coefficient of an indirect band gap semiconductor and band gap energy follows the Tauc's relation as

$$(\alpha h\nu)^{1/2} = A(h\nu - E_g) \quad \ldots\ldots(5.2)$$

Where hν is the photon energy, α is the absorption coefficient and A is a constant. The band gap values has been determined by extrapolating the straight line portion of $(\alpha h\nu)^{1/2}$ versus hν graph.

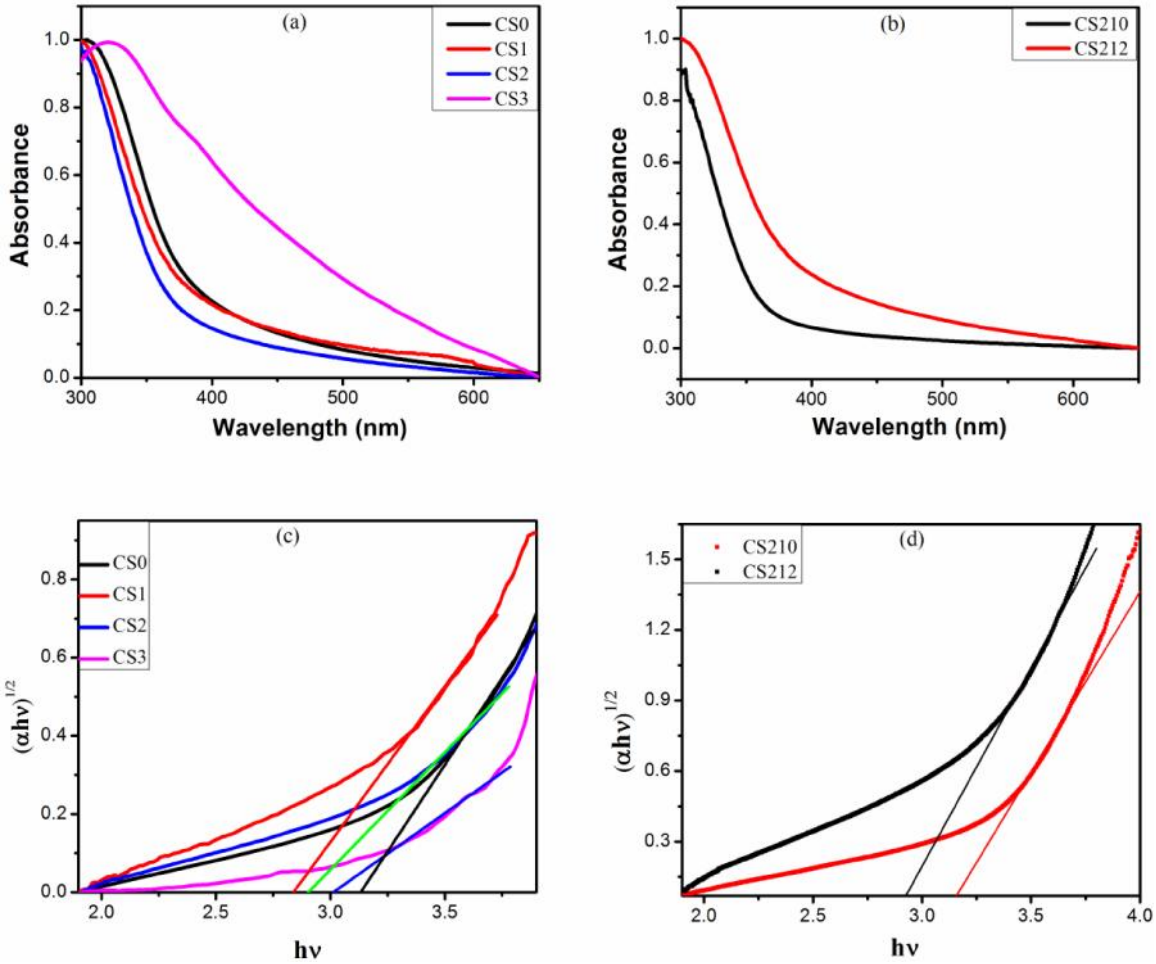

Figure 5.9: (a,b) UV-Visible absorption spectra and (c,d) Tauc's plot for CS0-CS3 NPs.

Figure 5.9(c,d) shows the graphs between $(\alpha h\nu)^{1/2}$ and hν for undoped and Ag doped samples synthesized at different doping concentration and at different pH values. Calculated band gap

(E_g) values has been found to be 3.12eV, 2.84eV, 2.90eV, 3.02eV, 3.13eV and 2.91eV for CS0, CS1, CS2, CS3 for CS210 and CS212 respectively which are smaller than the theoretical value of 3.2eV for bulk CeO_2. This is because at nanoscale size the existence of quantum confinement effect shifts the absorption spectra towards blue region, but simultaneously the decrease in particle size led to increase in Ce^{3+} ion concentration. But the blue shift of absorption edge in CeO_2 occurred with a decrease in Ce^{3+} content [12]. Therefore, the red shift in band gap for CeO_2 NPs is due to the transformation between Ce^{4+} to Ce^{3+}. Thus the band gap narrowing of as synthesized NPs is the integrated results of quantum confinement effect and transformation of two ionic states of cerium ion. This band gap narrowing is beneficial for photocatalytic process (discussed later).

5.3.4 XPS studies

The surface composition and oxidation state of the elements of as synthesized samples have been analyzed by XPS technique. The presence of Ce, O, C and Ce, O, C and Ag has been confirmed with XPS survey spectrum of undoped and Ag doped CeO_2 NPs respectively (Figure 5.10 (a, b)). Here Ce, O, C and Ag assigned to Ce3d, O1s, C1s and Ag3d orbitals respectively. The highly resolved XPS spectra of Ce3d with different chemical states of Ce ions for CS0 and CS2 samples are shown in Figure 5.10(c & d). The Ce 3d spectrum is composed of two multiplets (u and v) corresponding to spin-orbit split of 3d3/2 and 3d5/2. The Ce 3d core level spectrum consisting peaks corresponding to Ce^{3+} and Ce^{4+} states have been Gaussian fitted. The peaks labeled as v_o, v', u_o and u' imply the presence of Ce^{3+} states and peaks labeled as v, v'', v''', u, u'' and u''' reveal the presence of Ce^{4+} states. The relative amount of cerium in trivalent states and oxygen vacancies has been calculated using the following equations:

$$Ce^{3+} = \frac{Ce^{3+}}{Ce^{3+} + Ce^{4+}} = \text{area } (v_o, v', u_o, u') \text{ / total area} \quad \ldots\ldots(5.3)$$

$$O_{vac} = \frac{O_{sur}}{O_{sur} + O_{lat}} = \text{area } (O_{sur}) \text{ / total area} \quad \ldots\ldots(5.4)$$

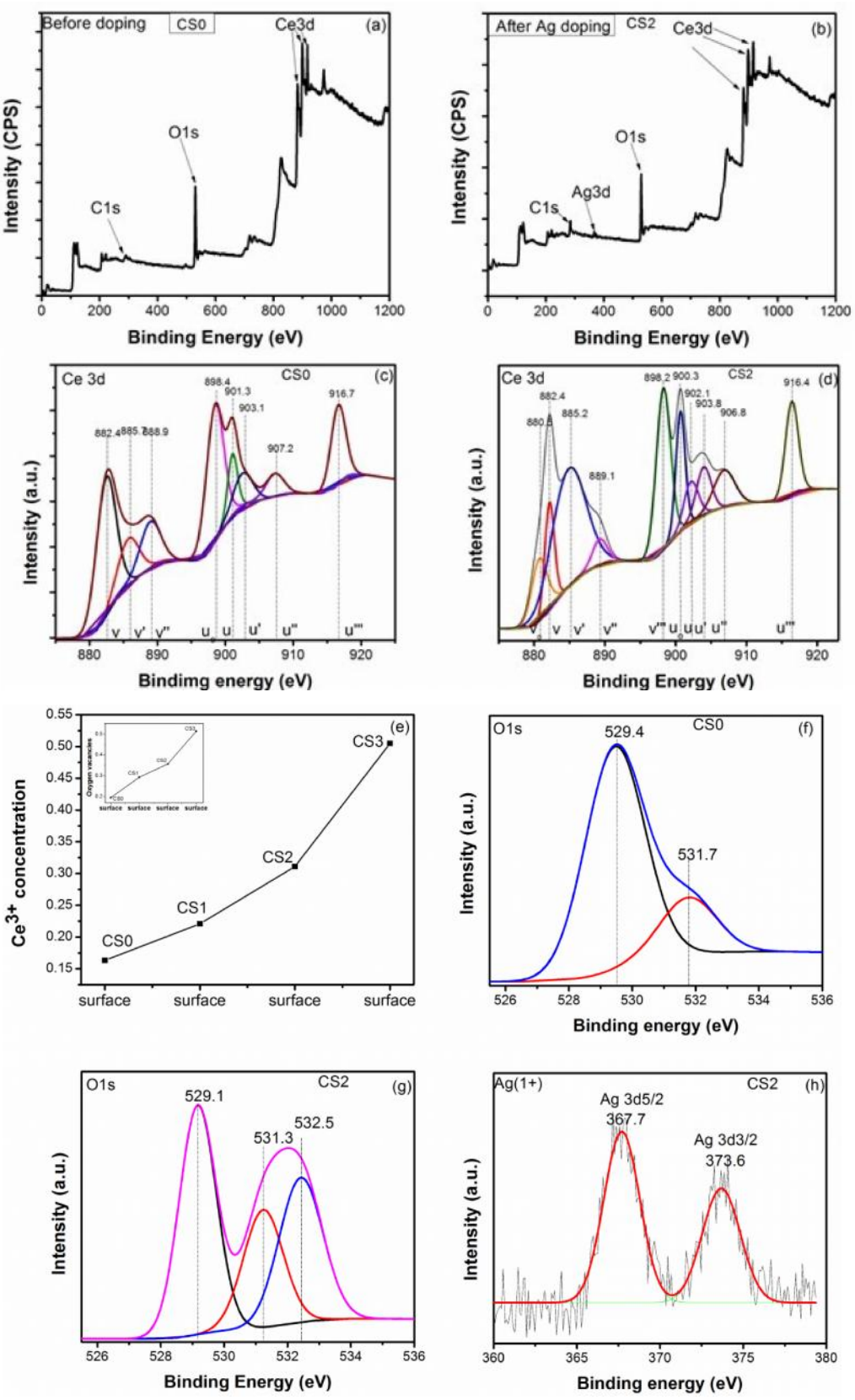

Figure 5.10: (a,b) survey before and after doping of ceria (c,d) Ce3d of CS0 and CS2 NPs (e) Ce^{3+} centration on the surface of CS0-CS3 (inset : concentration of oxygen vacancies of CS0-CS3) (f,g) O1s of CS0 and CS2 and (h) Ag(3d) spectrum in CS2 NPs.

Both the samples have been found to be nonstoichiometric, from the area under each peak, with 84% and 69% of the Ce3d photoemission due to Ce^{4+} and the remaining 16% and 31% due to Ce^{3+} state in CS0 and CS2 samples respectively. The results of oxidation state in all as synthesized samples have been summarized in Table 5.3. The increase in Ce^{3+} concentration from 16.3% to 50.5% on doping with silver (0-3%) is shown in Figure 5.10(e), which certainly justifies the charge compensation due to silver ion incorporation. The O1s electron core spectra for CS0 and CS2 are shown in Figure 5.10(f & g). The peak with binding energy of around 529eV is the major component and a shoulder around 531eV can be clearly seen in both the samples. The peak around 529eV is attributed to the lattice oxygen of Ce^{4+}- O^{2-} and the peak around 531eV is due to lattice oxygen of Ce^{3+}-O^{2-}. The third peak at 532.5eV in CS2 sample which is absent in CS0 sample, may be due to either defect oxides or surface hydroxyl like groups. Similar types of findings were also reported by Levasseur and co-workers [12] who assigned the peak between 532 to 533eV to ionized oxygen species that could allow compensation of deficiencies in the subsurface of metal oxide. Also inset of figure 5.10(e) shows

Table 5.3: Ce^{3+} concentration of various as synthesized undoped and doped samples.

S. No.	Sample	$Ce^{3+}/ [Ce^{3+} + Ce^{4+}]$%
1	CS0	16.3
2	CS1	22.1
3	CS2	31.1
4	CS3	50.5
5	CS210	35.6
6	CS212	42.4

that the oxygen vacancies increase with increase in silver doping. Similar findings were also reported by Younis and co-workers [6] in indium doped CeO_2 nanocrystals. Further, the concentration of Ce^{3+} is least for CS0 sample, almost double for CS2 sample and is around three times for CS212 sample as compared to CS0 sample respectively. This behavior confirm the generation of larger concentration of oxygen vacancies with silver doping. Thus it can be concluded that the silver doping promotes the formation of oxygen vacancies on the surface of as synthesized samples. Figure 5.10(h) demonstrate that the Ag 3d spectrum showing two peaks at 367.7 and 373.6eV, which can be assigned to Ag $3d^{3/2}$ orbitals and Ag $3d^{5/2}$ respectively

which correspond to Ag^{1+} doping in CeO_2 NPs [13]. These findings indicate that no metallic Ag^0 appears in Ag doped samples.

Further to strengthen the above mentioned arguments about the oxygen vacancies, the surface depth profiling XPS experiments have been conducted and the concentration of Ce^{3+} on the surface and at various depths below the surface has been calculated for CS0, CS2, CS210 and CS212 by Argon etching. The etching was varied from 0 to 10 and then 20 seconds.

The concentration of Ce^{3+} at various sample depths were extracted from XPS data and plotted in Figure 5.11. These finding clearly suggest that the concentrations of Ce^{3+} or oxygen vacancies are much higher on the surface as compared to inner part of the nanomaterials. Also the concentration of oxygen vacancies decreases with increase in etching time. This trend provides the evidence to the presence of oxygen vacancies on the surface of as synthesized samples.

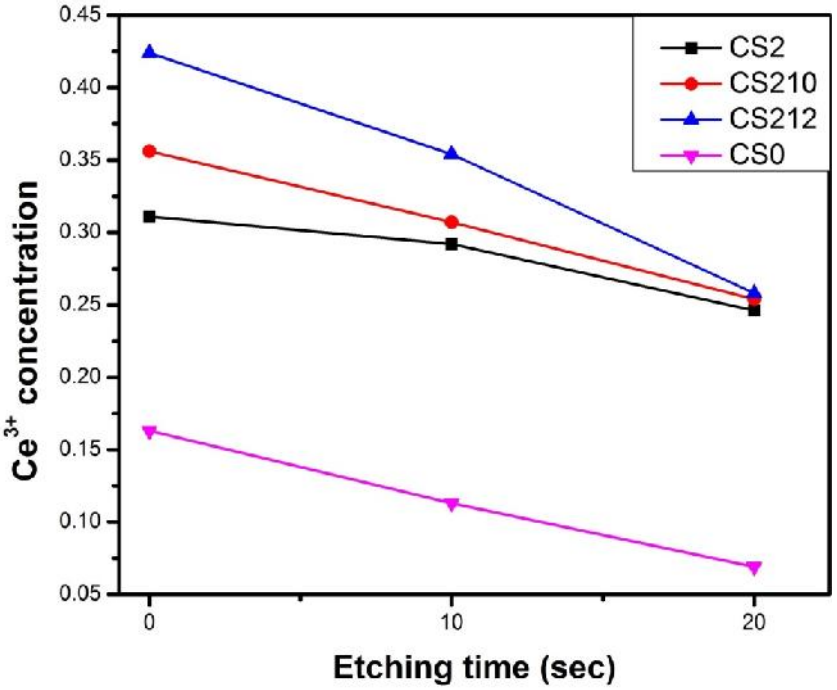

Figure 5.11: Variations in Ce^{3+} of undoped and Ag doped CeO_2 extracted from XPS data with respect to etching time by using Ar ion beam.

5.3.5 Photocatalytic studies

The photocatalytic performance of as prepared undoped and Ag doped samples has been evaluated by the degradation of Rhodamine B (RhB) dye under UV-Visible light radiations. The photo-degradation process was evaluated by monitoring the change in concentration of RhB dye. In this study, without any adjustment, the pH of slurry (dye and photocatalyst solution) was

at natural pH. The photocatalytic degradation of RhB dye in dark, under UV-Vis. radiations with as synthesized samples (CS0, CS1, CS2 and CS3) is shown in Figure 5.12(a), which shows the normalized concentration of RhB dye (C/C_0) as a function of light irradiations time. C_0 and C denotes initial concentration after adsorption-desorption equilibrium under dark conditions and the concentration of RhB at different irradiation times (t) respectively. The lower value of C/C_0 denotes the higher degradation of RhB dye. Figure 5.12(b) demonstrate that 4.9% and 29.68% of the dye has been degraded in dark and under UV-Vis. radiations without any photocatalyst and 79.2%, 95.1%, 99.8% and 98.0% of RhB dye has been degraded with CS0, CS1, CS2 and CS3 samples under UV-Vis. light irradiations. Thus the doped samples show higher photocatalytic activity than undoped and at other conditions. Also, in doped samples, CS2 sample has shown the maximum degradation efficiency than CS1and CS3.

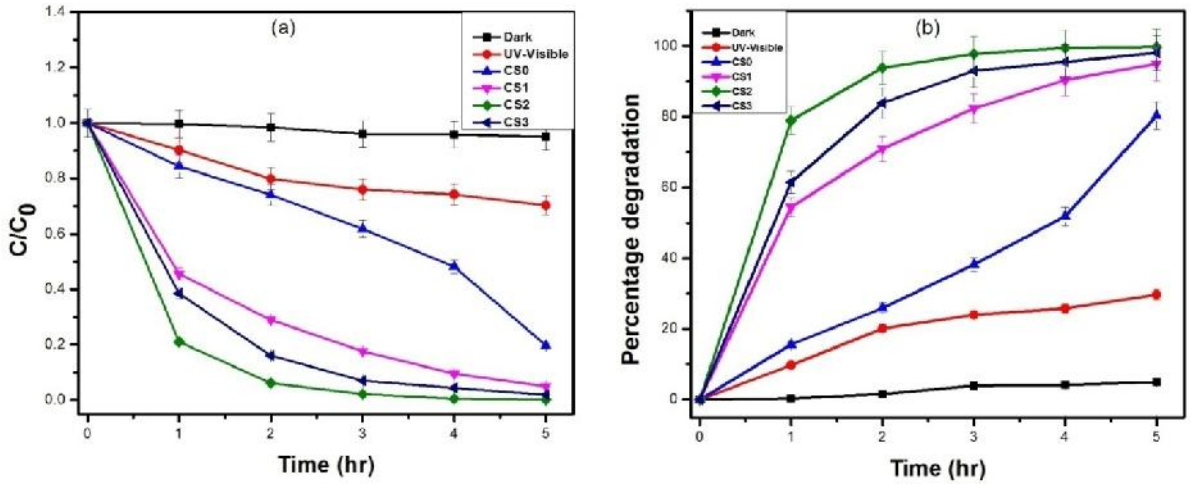

Figure 5.12: (a) Change in concentration and (b) percentage degradation of RhB under various conditions.

In other words, when the doping concentration in CeO_2 NPs increases up to 2% the degradation efficiency increases as compared to undoped CeO_2 NPs (CS0). But on further increasing the doping level of Ag to 3%, a decrease in photocatalytic activity is observed. This might be due to increase in oxygen vacancies in CS3 samples beyond the optimum level of oxygen vacancies. Table 5.3 (shown above) shows that the oxygen vacancies increase with increase in Ag doping. Oxygen vacancies are double and three times for CS2 and CS3 samples as compared to CS0 sample respectively. Further it is well known that the electron-hole pair separation is closely related to the availability of oxygen vacancies in the photocatalyst [6]. The doping of Ag generates or induces more oxygen vacancies (discussed above), so the probability of cations

lying closer to each other increases. Therefore the existing oxygen vacancies come together to form deep traps and as a result, small micro-domains may be generated due to the re-arrangement or ordering of oxygen vacancies and isolated cations in the lattice [7]. However, beyond the optimum level, the increased concentration of deep traps favors a fast electron-hole recombination rate which resulted in decrease in photocatalytic efficiency. Also the Ag content above the optimum level acts as a recombination centre and hence cause the reduction in photocatalytic efficiencies [13, 14]. Thus from the above discussions it is clear that 2.0% Ag doping in CeO_2 lattice is optimal which provides the optimum number of oxygen vacancies for highest photocatalytic activity.

Table5.4: Reaction rate constant of RhB dye with and without photocatalyst at different pH.

S. No.	Concentration of dye (mg/L)	Photocatalyst	pH of photocatalyst during synthesis	Rate constant (K)(per min)	R^2	Rate constant (K)(per min) (Fe doped Ceria)
1	10	No catalyst in dark	------	0.0002	0.9395	0.0004 [4]
2	10	UV-Visible radiations only	------	0.0012	0.9331	
3	10	CS0	7.5	0.0047	0.8373	0.0017 [4]
4	10	CS1	7.5	0.0096	0.9973	0.0025 [4]
5	10	CS2	7.5	0.0209	0.9969	0.0028 [4]
6	10	CS3	7.5	0.0128	0.9907	
7	10	CS210	10.0	0.0270	0.9591	
8	10	CS212	12.0	0.0300	0.9618	

Kinetic studies of the photocatalytic degradation of RhB dye under various conditions is shown in Figure 5.13 using an equation $-\ln (C/C_0) = kt$, which indicates that the degradation of RhB dye follows pseudo-first-order kinetic model. The rate of degradation of RhB dye in dark and under UV-Vis. light irradiations are very slow and are 0.0002 and 0.0012 min^{-1} respectively. CS0, CS1, CS2 and CS3 have shown relatively higher degradation rates such as 0.0047, 0.0096, 0.0209 and 0.0128 min^{-1} respectively. The degradation rate constants of RhB dye under various conditions have been summarized in Table 5.4. Here the photocatalytic degradation and hence degradation rate for CS2 is higher than those of undoped and doped samples. The degradation rate of CS2 is 4.5 and 2.2- fold higher than that of CS0 and CS1 respectively.

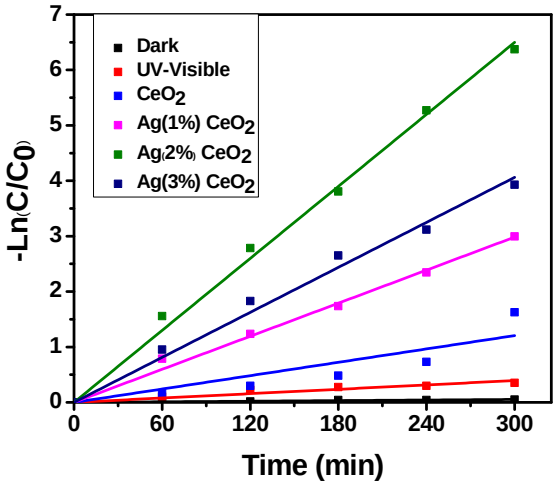

Figure 5.13: Kinetic studies of the photocatalytic degradation of RhB dye under various conditions.

5.3.5.1 Effect of pH

Since the pH of waste water from the textile industries have wide range and it is very difficult to adjust the pH of photocatalytic reaction at each time. Till date no photocatalyst has been reported which show commendable degradation of dye at all pH. Many groups have studied the effect of pH by varying the pH of dye solution with the addition of acids and bases [11, 15]. With this motivation, attempt has been made to optimize the pH of synthesized NPs during synthesis, so that maximum degradation of dye could be achieved under UV-Vis. light irradiations. As discussed above, CS2 sample has shown the maximum degradation of RhB dye, therefore this optimized silver doping has been selected for varying the pH during the synthesis from natural pH to 10.0 (CS210) and 12.0 (CS212). The photocatalytic degradation efficiencies of RhB dye using photocatalysts CS210 and CS212 under UV-Vis. light irradiations for 3h are shown in Figure 5.14(a). It demonstrates that these samples exhibited higher degree of degradation in smaller time. 99.3% and 99.6% of dye degradation has been achieved with as synthesized CS210 and CS212 samples respectively. Here it is important to mention that the pH of dye solution after the addition of photocatalyst was still at natural pH value. Therefore no change in pH of dye solution has taken place by addition of NPs synthesized at higher pH and thus the increase in degradation of RhB dye is mainly due to photocatalysts synthesized at higher pH. Inset of Figure 5.14(a) demonstrate the change in color of dye in the presence of CS212 sample after 3h of UV-Vis. irradiation.

Kinetic studies of photodegradation of RhB dye with NPs synthesized at higher pH have been shown in Figure 5.15, which shows that it follows pseudo-first order kinetic model. The

degradation rate for CS210 and CS212 are relatively higher than that of CS2. This means that the samples synthesized at higher pH value has shown faster degradation, this might be due to the presence of optimal level of oxygen vacancies. The point of zero charge (PZC) of ceria is 7.9 [16], therefore if the pH of the photocatalyst is greater than PZC of ceria, the surface of the photocatalyst becomes negatively charged. Hence, the anionic dyes have a greater affinity towards the catalyst. The sample synthesized at pH 10.0 and 12.0 have strong interaction towards the cationic dyes. The sample CS212 have stronger interaction towards the RhB dye as compared to CS210, attributed to higher synthesized pH value. Hence, greater RhB dye molecules were adsorbed on the surface of CS212 photocatalyst causing higher degradation efficiency in comparison to CS210. Furthermore, higher degradation efficiencies at higher pH is due to the presence of high concentration of adsorbed hydroxyl groups [17].

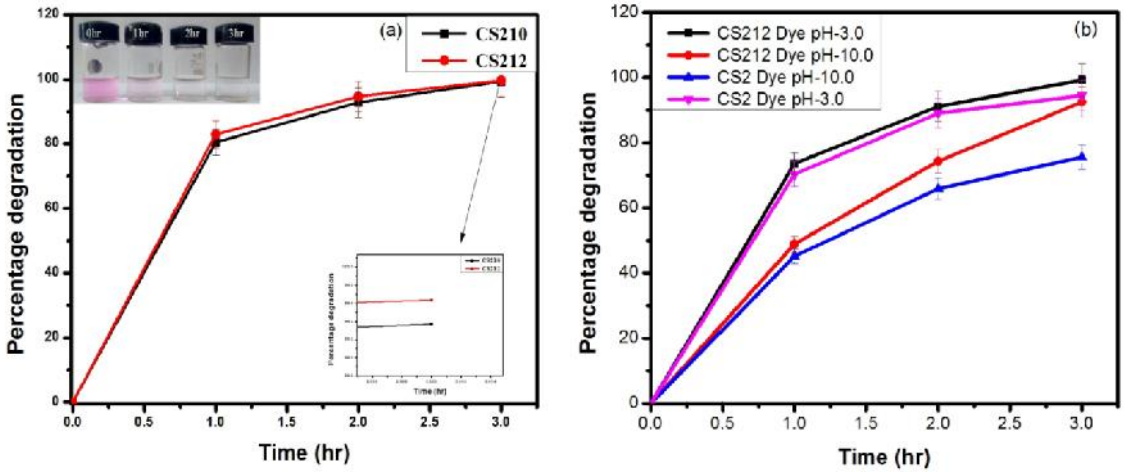

Figure 5.14: (a) Percentage degradation of RhB using CS210 and CS212 photocatalysts (inset: Change in color of RhB with CS212) and (b) percentage degradation using CS2 and CS212 photocatalysts with the variation of pH of dye solution.

In order to check, the photodegradation efficiency of CS212, the pH of RhB dye solution has been prepared at pH-3.0 (acidic medium) and 10.0 (basic medium) with the addition of HNO_3 and NaOH. These dye solutions at different pH were considered for studying the degradation behavior of as synthesized CS212 and CS2 samples. Figure 5.14(b) shows the percentage degradation of RhB dye solution at different pH value in the presence of CS2 and CS212 photocatalysts. It shows 99.3% and 92.4% RhB dye solution at pH- 3.0 and pH-10.0 respectively that has been degraded with CS212. However, 75.58% and 94.47% dye solution could be degraded with CS2 sample with pH-3.0 and pH-10.0 respectively. Thus CS212 has efficiently degraded the RhB dye in acidic, neutral and basic medium. The results confirm the

utility of these NPs in degradation of waste water effluents from various industries without studying their pH values.

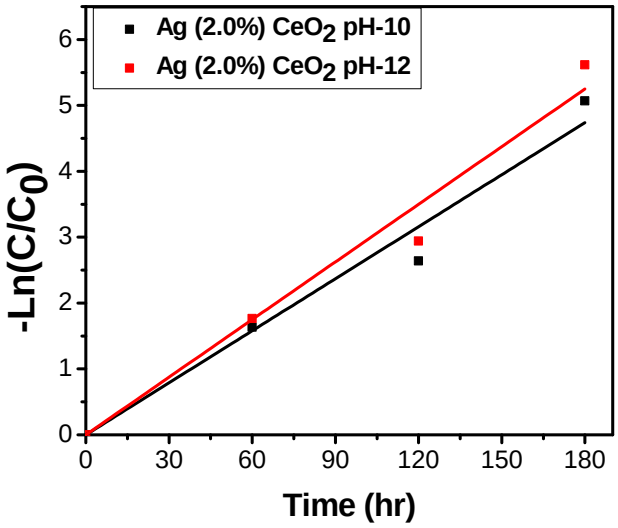

Figure 5.15: Kinetic studies of the photocatalytic degradation of RhB dye with CS210 and CS212 NPs.

5.3.5.2 Reusability studies

To determine the photocatalytic efficiency, the repetitive use of CS212 by the degradation of RhB dye for three cycles has been studied and is shown in Figure 5.16.

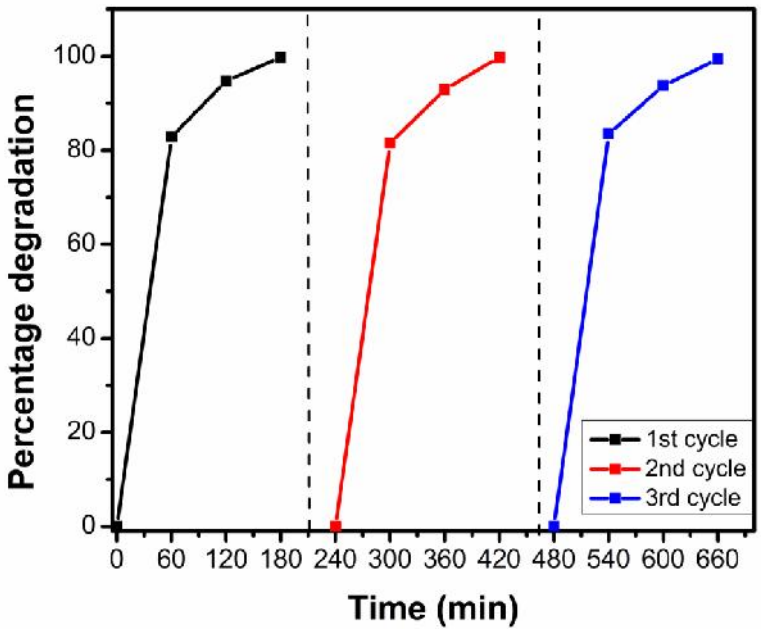

Figure 5.16: Cyclic runs of RhB degradation using CS212 photocatalyst.

It is clearly observed that the degradation efficiency of CS212 persisted without any self-degradation, thus the degradation efficiency of the photocatalyst remains unaltered even after three cycles of reuse.

5.3.6 Mechanism

To determine the probability of electron-hole recombination of the photocatalyst, the photoluminescence (PL) spectra of CeO_2 NPs has been recorded and shown in Figure 5.17. The PL spectrum shows broad band at 363-440 nm centered at 395 nm along with small emission peaks at 454nm and 484nm for all as synthesized undoped and doped samples. The appearance of broad blue emission band originates from the charge transitions from 4f band to the VB of CeO_2 and peaks positioned at 454 nm and 484 nm are associated with the defect levels localized between the O 2p and the Ce 4f bands. Also, Li et al. [18] reported that the broad emission band around 350-700 nm is responsible for Ce^{3+} ions and oxide defects in CeO_2. Since PL emission spectra originate from the recombination of excited electrons and holes, thus the higher PL intensity shows the higher recombination of excited electrons–hole pairs. The CS0 sample shows higher PL intensity as compared to CS1 and CS2 samples. This means on increasing the doping concentration of Ag from 1.0 to 2.0 at.% the recombination of excited electrons and holes reduces. However, further increasing the doping concentration from 2.0 to 3.0 at.% the recombination of electron-hole pairs increases. This is because the Ag content above the optimum level acts as a recombination center [13, 14].

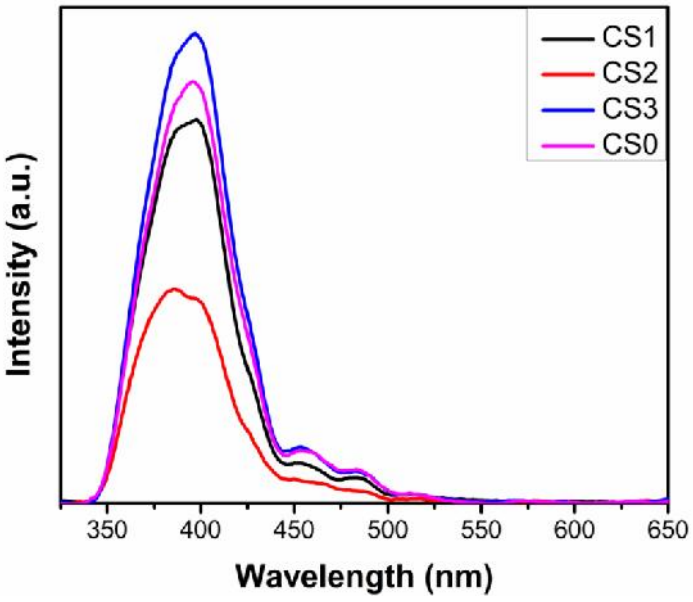

Figure 5.17: Photoluminescence emission spectra of CS0-CS3 samples.

The band gap energies as calculated from Tauc's relation were 3.12eV, 2.84eV, 2.90eV, 3.02eV for CS0, CS1, CS2 and CS3 respectively. Using these values, the valance band (VB) and conduction band (CB) potential can be calculated from the following relations as [4, 19]:

$E_{cb}(CeO_2) = \chi(CeO_2) - E^c - 0.5E_g\,(CeO_2)$ ……(5.5)

$E_{vb}(CeO_2) = E_g\,(CeO_2) - E_{cb}\,(CeO_2)$ ……(5.6)

Where χ is the absolute electro-negativity of the semiconductor (χ = 5.56eV for CeO_2), E^c is the scaling factor relating to hydrogen electrode scale (NHE) to the absolute vacuum scale (AVS) (4.5eV vs AVS for 0V vs NHE) and E_g is the bandgap energy of CeO_2 (3.12eV for CS0). The calculated VB and CB potentials are 2.63 and -0.49eV respectively.

Based on the above results, Figure 5.18 presents the general mechanism for the photodegradation of RhB dye with CS0 and CS212 samples under UV-Vis. irradiations. For CS0, when it is irradiated, electrons get excited from valance band (O_{2p}) to an empty conduction band (Ce^{4f}). The photo generated electrons localized on cerium ions are scavenged by oxygen molecules dissolved in water to yield superoxide radical anions and hydroxyl radicals which are highly oxidative species and are responsible for decomposition of RhB dye. However, in CS0 sample the recombination of electron-hole pair is higher than the modified ceria samples (confirmed from PL studies). Therefore, undoped sample shows smaller degradation and mineralization of RhB dye. Moreover, it has been found that the amount of Ag dopant and effect of pH during synthesis of ceria samples greatly influences the photocatalytic activity of as synthesized doped ceria NPs.

The observed photocatalytic activity of synthesized samples increases with increase in Ag doping concentrations up to 2.0 at%. Further, the activity decreases with increasing Ag content above 2.0 at%. This is because the small amount of Ag^{1+} act as an electron acceptor (from Ag^{1+} to Ag^0) and/or a hole donor (from Ag^{1+} to Ag^{2+}) to facilitate charge carrier localization and thus resulted in prolonged separation by trapping at energy levels close to conduction or valance band respectively [4, 6]. Also Ag^0 and Ag^{2+} are relatively unstable than Ag^{1+} and thus leads to the transfer of trapped charge carriers from Ag^0 or Ag^{2+} to the adsorbed O_2 or OH^- to regenerate Ag^{1+}. Thus the newly produced hydroxyl radical ($OH^{\cdot}$) and super oxide anion radical ($^{\cdot}O_2^-$) are highly oxidative and initiate the photocatalytic reactions. Thus doping of Ag^{1+} delays electron hole recombination and hence increasing the lifetime of charge carrier's separation which is useful in photocatalytic reactions. The doping of Ag^{1+} in ceria induces oxygen vacancies (confirmed from XPS), which may be another possible reason for enhancement in photocatalytic activity of CS2, CS210 and CS212 with respect to other samples. The adsorption of dye on the photocatalyst is the necessity for effective degradation of dye. As CS212 sample has been

synthesized at pH-12.0 and RhB dye is cationic in nature, so there is strong interaction between as synthesized CS212 NPs and dye molecules.

Figure 5.18: Schematic diagram of the degradation mechanism for RhB dye (red spheres) with CS0 and CS212 NPs under UV-Visible irradiations.

So the effective adsorption of RhB dye on CS212 NPs may result enhancement in photodegradation efficiency. Also, the doping of Ag can serve not only as a mediator of interfacial charge recombination but also as a recombination centre. In this study the optimal doping concentration of Ag is 2.0 at%. Above this concentration, Ag^{1+} become recombination centre and thus reduce the photocatalytic activity.

From above discussion it is clear that optimal Ag doping has increased the photocatalytic degradation efficiency in comparison to undoped samples. It has been reported earlier also that on changing the pH of dye solution, NPs tend to agglomerate at acidic conditions, thus results in decrease in available surface area for adsorption of dye and photon absorption [20, 21]. Here in present case we have varied the pH during the synthesis of Ag doped ceria NPs in order to avoid agglomeration of NPs which occurs during pH adjustment of dye solution. Spherical morphology, maximum adsorption of RhB dye, optimal Ag doping and generation of optimum level of oxygen vacancies are the main reasons for better photocatalytic activity of CS212 NPs.

5.4 Au doped CeO_2 nanoparticles

5.4.1 XRD studies

The X-ray diffraction (XRD) patterns of as synthesized undoped and Au doped NPs (CA0, CA1, CA2, CA3, CA4, CA410, CA412) are depicted in Figure 5.19. All the peaks of as synthesized NPs in the 20-80º range of 2θ value are indexed to single crystalline face-centered cubic (FCC) fluorite structure of pure CeO_2 (JCPDS 34-0394). Further no diffraction peaks corresponding to cerium oxide or Au-related impurity has been detected. This confirms the successful doping of Au into ceria (CeO_2) NPs.

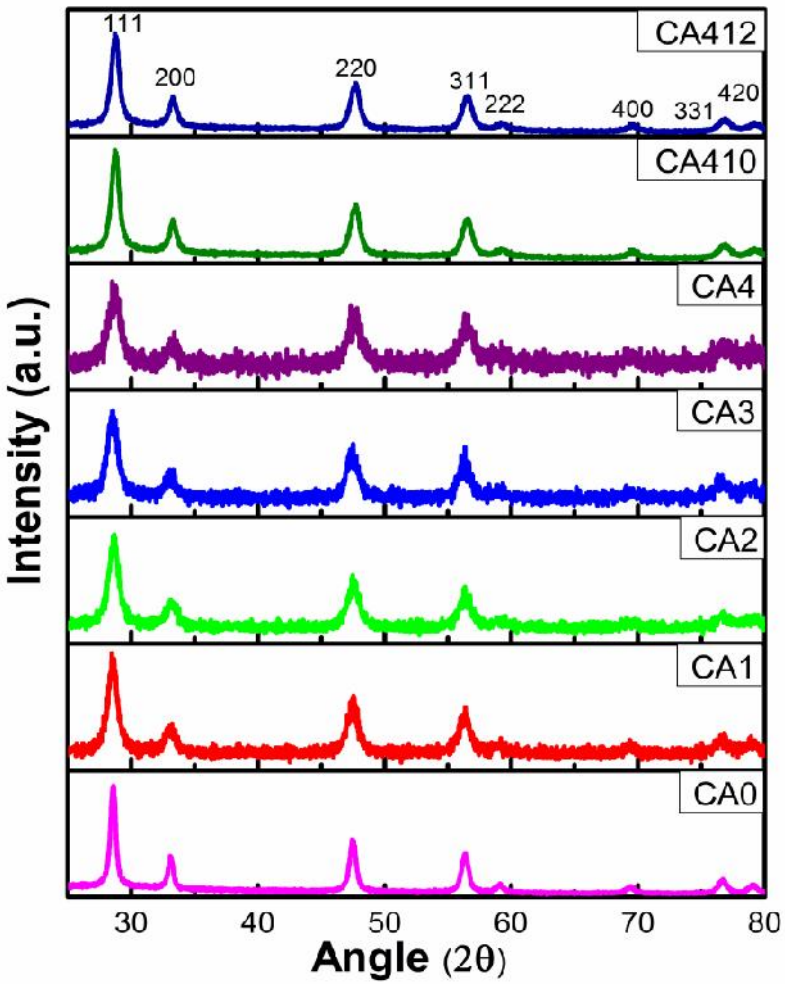

Figure 5.19: XRD pattern of CA0-CA412 NPs.

Samples with Au doping show shift in the (1 1 1) peak towards higher 2θ values as compared to undoped sample as shown in Figure 5.20. Sample CA4 has shown maximum shift as compared to CA1, CA2 and CA3. It can be observed that peak shifting further increases for the samples synthesized at higher pH value during synthesis. The shifting towards higher 2θ values shows

the contraction of the lattice. This might be attributed to smaller ionic radius of Au^{3+} than that of Ce^{3+} (0.099nm and 0.115nm, respectively). Also with doping in ceria the oxygen vacancies increases which also contribute for the contraction of the lattice [11]. This further confirms the incorporation of Au ions into ceria lattice. The average crystallite size has been calculated from Debye-Scherer formula and is found to be in 8.0 - 12.0nm range.

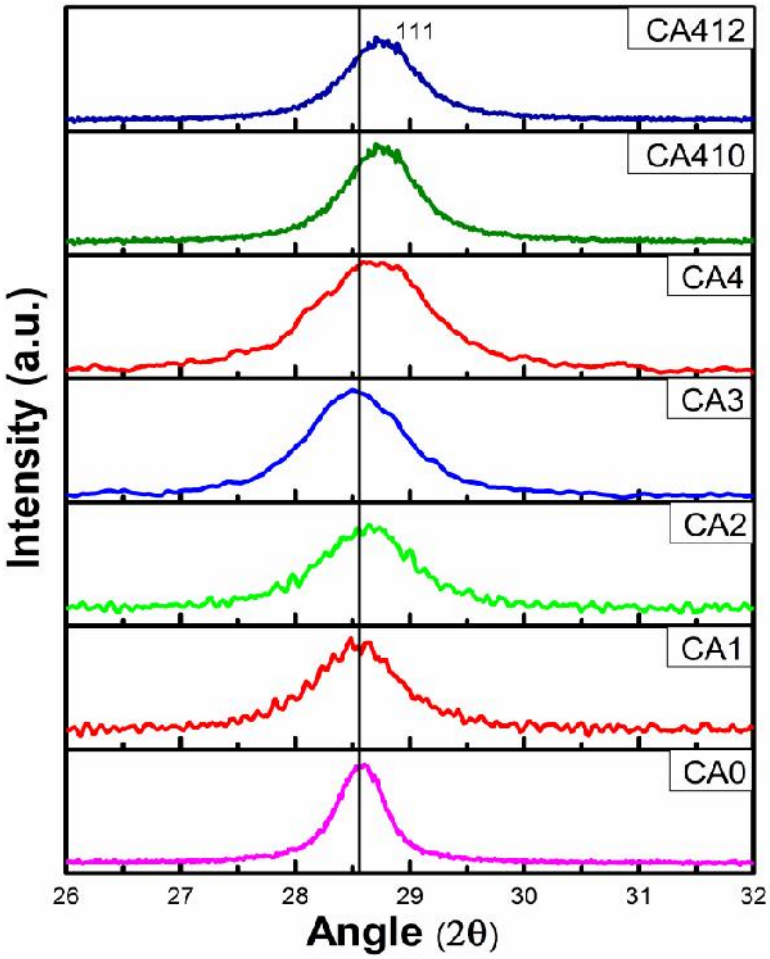

Figure 5.20: Peak shift of CA0-CA412 NPs.

5.4.2 TEM studies

TEM has been utilized to determine the morphology of the as-prepared samples. Figure 5.21(a,b) presents the micrographs of CA0 and CA4 NPs respectively. It can be observed that the resulting NPs are uniform in shape and size, and the diameter of the NPs are in the range of 5-8 nm and 7-12 nm with narrow size distributions for CA0 and CA4 respectively which are consistent with XRD results.

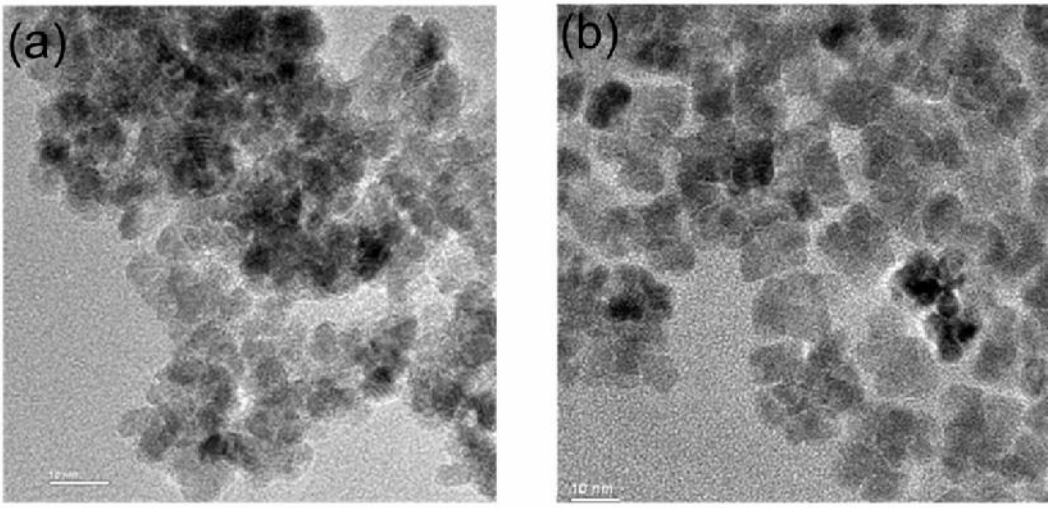

Figure 5.21: TEM images of (a) CA0 (b) CA4 NPs.

5.4.3 UV-Visible spectroscopy

Figure 5.22(a,b) reveals the absorption spectra of as synthesized undoped and Au doped CeO_2 NPs. There is a strong absorption band from 300nm to 350nm in the spectra, which is attributed to charge transfer from O^{2-} in O 2p to Ce^{4+} in Ce 4f [10]. CA4 sample shows better absorption of solar radiations as compared to other undoped and doped sample. This might be due better doping of Au. The band gap determines the portion of the solar spectrum that the photocatalyst absorbs. The relationship between the optical absorption coefficient of an indirect band gap semiconductor and band gap energy follows the Tauc's relation as

$$(\alpha h\nu)^{1/2} = A(h\nu - E_g) \qquad \ldots\ldots(5.7)$$

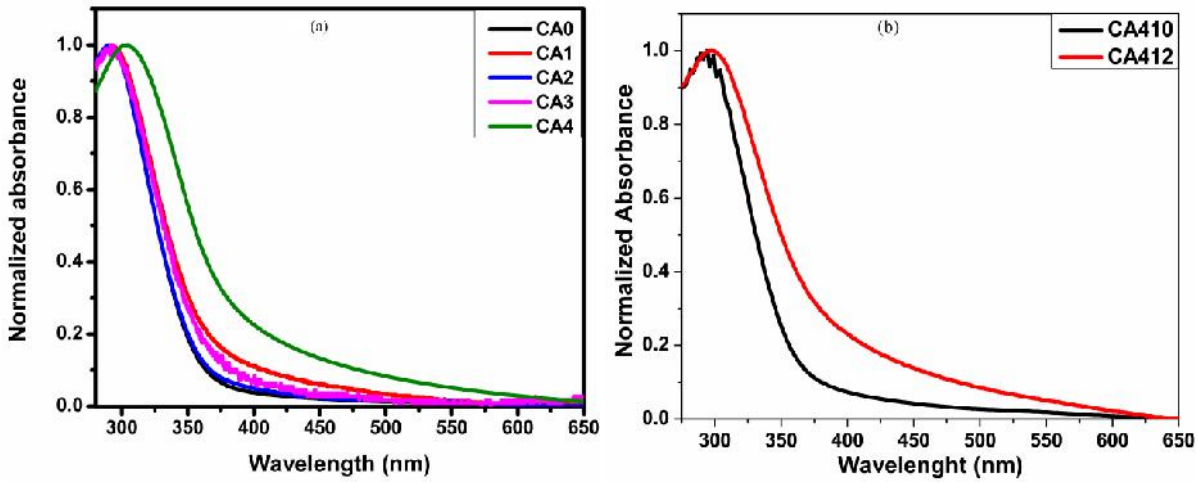

Figure 5.22: UV-Visible absorption spectra of (a) CA0-CA4 and (b) CA410 and CA412 NPs.

Where hν is the photon energy, α is the absorption coefficient and A is a constant. The band gap values has been determined by extrapolating the straight line portion of $(\alpha h\nu)^{1/2}$ versus hν graph. Figure 5.23(a-f) shows the graphs between $(\alpha h\nu)^{1/2}$ and hν for undoped and Au doped samples synthesized at different doping concentration and at different pH values. Calculated band gap (E_g) values has been found to be lying between 2.9-3.25eV. CA412 has smallest band gap value as compared to other undoped and Au doped samples synthesized at natural and higher pH values.

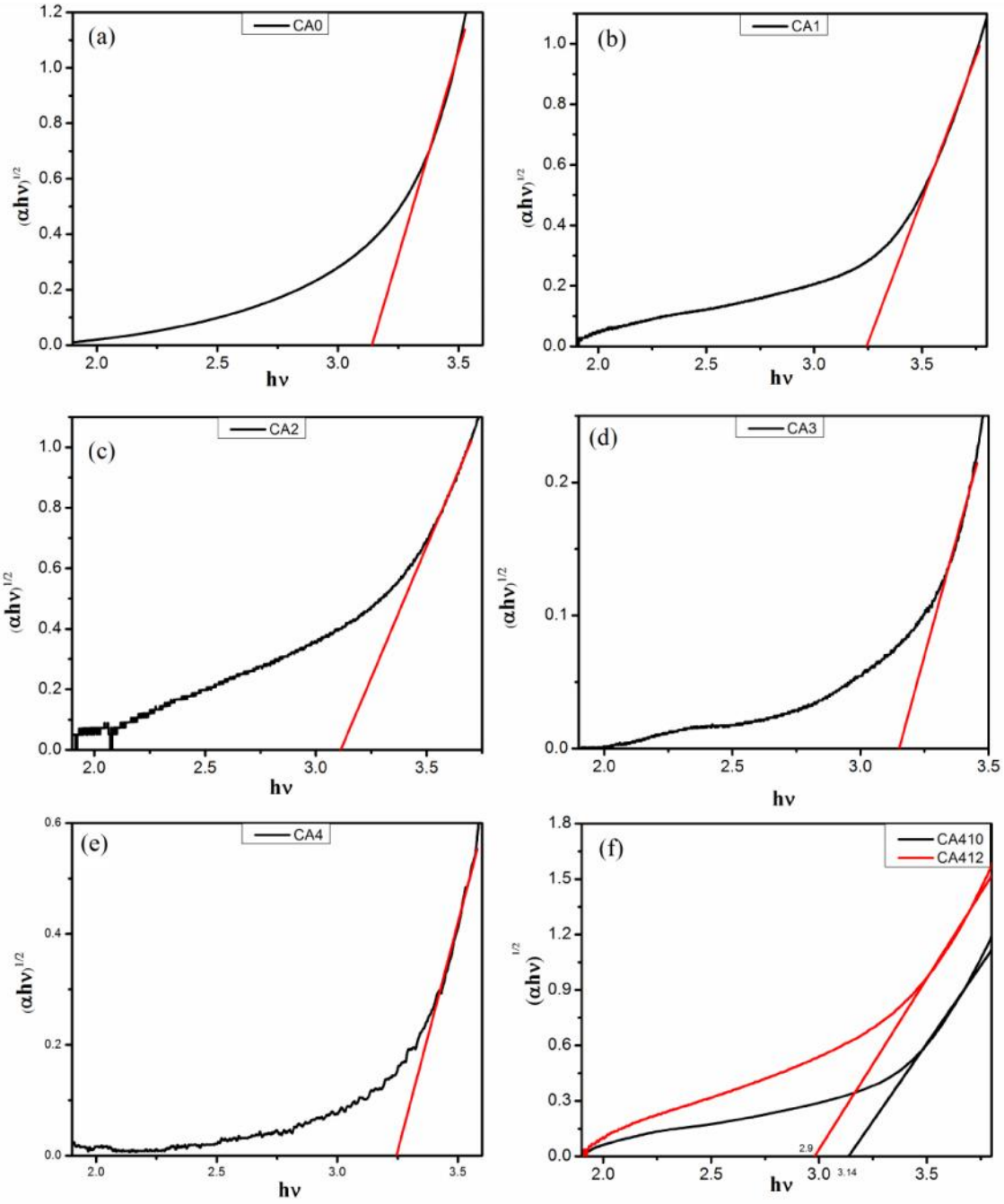

Figure 5.23: Tauc's plot for band gap determination of CA0-CA412 NPs.

5.4.4 Photocatalytic studies

The photocatalytic performance of as prepared undoped and Au doped samples has been evaluated by the degradation of Rhodamine B (RhB) dye under UV-Visible light radiations. The photo-degradation process was evaluated by monitoring the change in concentration of RhB dye. In this study, without any adjustment, the pH of slurry (dye and photocatalyst solution) was at natural pH. The percentage degradation of RhB dye in dark, under UV-Vis. radiations with as synthesized samples (CA0, CA1, CA2, CA3 and CA4) is shown in Figure 5.24. Figure demonstrate that 1.4% and 14.2% of the dye has been degraded in dark and under UV-Vis. radiations without any photocatalyst and 35.1%, 86.0%, 87.3%, 90.9% and 95.8% of RhB dye has been degraded with CA0, CA1, CA2, CA3 and CA4 samples under UV-Vis. light irradiations. Thus the doped samples show higher photocatalytic activity than undoped and at other conditions. Also, in doped samples, CS4 sample has shown the maximum degradation efficiency than other undoped and doped samples. This might be due better doping and more fractional absorption of solar radiations as discussed in above section.

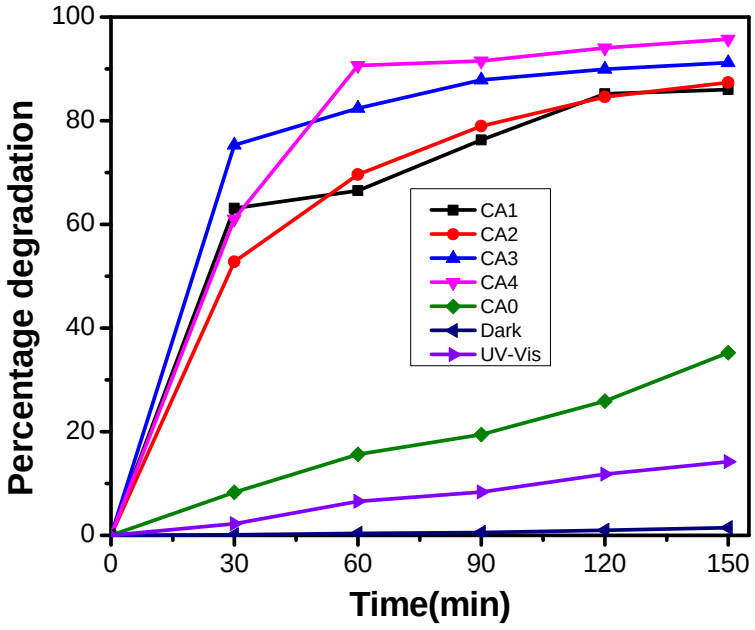

Figure 5.24: Percentage degradation of RhB under various conditions.

Kinetic studies of the photocatalytic degradation of RhB dye under various conditions is shown in Figure 5.25 using an equation $-\ln (C/C_0) = kt$, which indicates that the degradation of RhB dye follows pseudo-first-order kinetic model. The rate of degradation of RhB dye in dark and under UV-Vis. light irradiations are very slow and are 0.00004 and 0.00045 min^{-1} respectively. CA0, CA1, CA2, CA3 and CA4 have shown relatively higher degradation rates such as 0.00118,

0.00534, 0.00582, 0.0063 and 0.00879 min^{-1} respectively. The degradation rate constants of RhB dye under various conditions have been summarized in Table 5.5. Here the photocatalytic degradation and hence degradation rate for CA4 is higher than those of undoped and other doped samples.

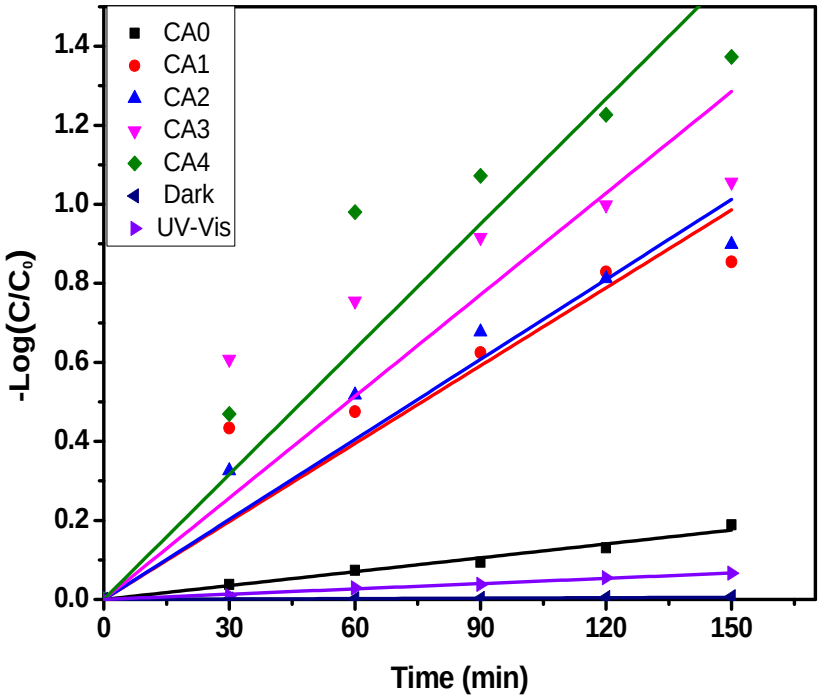

Figure 5.25: Kinetic studies of the photocatalytic degradation of RhB dye under various conditions.

Table 5.5: Reaction rate constant of RhB dye with and without photocatalyst at different pH.

S. No.	Concentration of dye (mg/L)	Photocatalyst	pH of photocatalyst during synthesis	Rate constant (K) (per min)	R^2
1	10	No catalyst in dark	------	0.00004	0.9924
2	10	UV-Visible radiations only	------	0.00045	0.9500
3	10	CA0	7.5	0.00118	0.9813
4	10	CA1	7.5	0.00534	0.9223
5	10	CA2	7.5	0.00582	0.9539
6	10	CA3	7.5	0.0063	0.9218
7	10	CA4	7.5	0.00879	0.9437
8	10	CA410	10.0	0.01353	0.9731
9	10	CA412	12.0	0.02276	0.9941

5.4.4.1 Effect of pH

Since the pH of waste water from the textile industries have wide range and it is very difficult to adjust the pH of photocatalytic reaction at each time. It has been reported earlier that on changing the pH of dye solution, NPs tend to agglomerate at acidic conditions, thus results in decrease in available surface area for adsorption of dye and photon absorption [20, 21]. With this motivation, attempt has been made to optimize the pH of synthesized NPs during synthesis, so that maximum degradation of dye could be achieved under UV-Vis. light irradiations. As discussed above, CA4 sample has shown the maximum degradation of RhB dye, therefore this optimized silver doping has been selected for varying the pH during the synthesis from natural pH to 10.0 (CA410) and 12.0 (CA412). The photocatalytic degradation efficiencies of RhB dye using photocatalysts CA410 and CA412 under UV-Vis. light irradiations for 2h are shown in Figure 5.26(a). It demonstrates that these samples exhibited higher degree of degradation in smaller time. 98.6 and 99.4% of dye degradation has been achieved with as synthesized CA410 and CA412 samples respectively. Here it is important to mention that the pH of dye solution after the addition of photocatalyst was still at natural pH value. Therefore no change in pH of dye solution has taken place by addition of NPs synthesized at higher pH and thus the increase in degradation of RhB dye is mainly due to photocatalysts synthesized at higher pH.

Kinetic studies of photodegradation of RhB dye with NPs synthesized at higher pH have been shown in Figure 5.26(b), which shows that it follows pseudo-first order kinetic model.

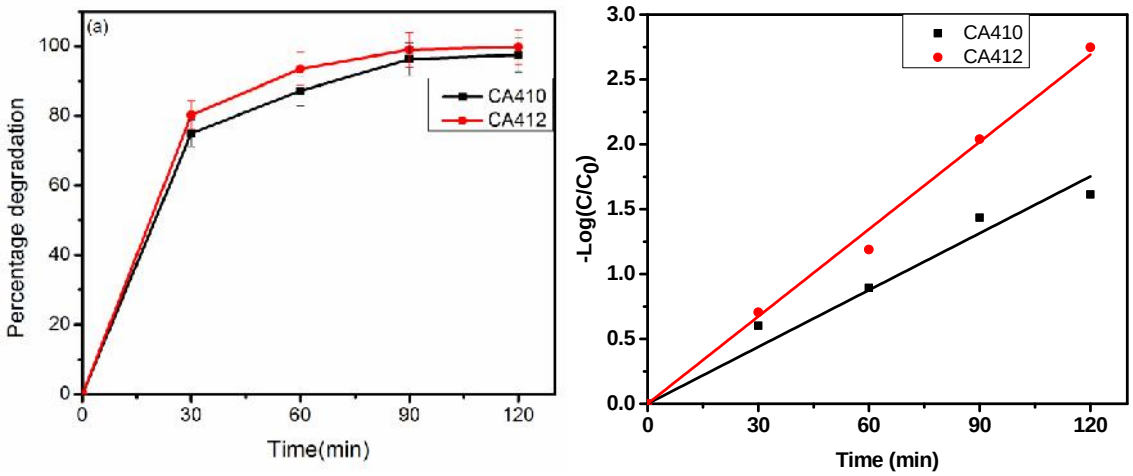

Figure 5.26: (a) Percentage degradation and (b) Kinetic studies of the photocatalytic degradation of RhB dye with CA410 and CA412 NPs.

The degradation rate for CA410 and CA412 are relatively higher than that of CA4 (Table 5.5). This means that the samples synthesized at higher pH value has shown faster degradation, this might be due to the presence of optimal level of oxygen vacancies. The point of zero charge (PZC) of ceria is 7.9 [16], therefore if the pH of the photocatalyst is greater than PZC of ceria, the surface of the photocatalyst becomes negatively charged. Hence, the anionic dyes have a greater affinity towards the catalyst. The sample synthesized at pH 10.0 and 12.0 have strong interaction towards the cationic dyes. The sample CS212 has stronger interaction towards the RhB dye as compared to CS210, attributed to higher synthesized pH value. Hence, greater RhB dye molecules were adsorbed on the surface of CA412 photocatalyst causing higher degradation efficiency in comparison to CA410. Furthermore, higher degradation efficiencies at higher pH is due to the presence of high concentration of adsorbed hydroxyl groups [17]. As discussed in XRD results CA4 sample synthesized at natural pH has shown maximum peak shift towards higher 2θ values. The shifting further increases for CA410 and CA412 samples. This shows the better doping of Au in ceria lattice. The contraction of lattice due to incorporation of smaller ionic radii ion (Au) as compared to host (Ce) also results in generation of oxygen vacancies which also plays a significant role in degradation of pollutants. When UV-Visible light radiations falls on Au doped ceria NPs, electrons get excited from VB to CB thus forms electron-hole pair. The resulted electrons are trapped by Au^{3+} to form Au^{2+} and thus promote the charge separation to some extent. As Au^{2+} state is unstable than Au^{3+} so it leads to the transfer of trapped charge carriers from Au^{2+} to the adsorbed O_2 or OH^- to regenerate Au^{3+}. Thus the newly produced hydroxyl radical ($OH^{\cdot}$) and super oxide anion radical ($^{\cdot}O_2^-$) are highly oxidative and initiate the photocatalytic reactions. The adsorption of dye on the photocatalyst is the necessity for effective degradation of dye. As CA41212 sample has been synthesized at pH-12.0 and RhB dye is cationic in nature, so there is strong interaction between as synthesized CA412 NPs and dye molecules. So the effective adsorption of RhB dye on CA412 NPs may result enhancement in photodegradation efficiency. Thus effect of pH and doping plays a significant role to enhance the photocatalytic activity of as synthesized doped ceria samples.

As synthesized Silver (Ag) and gold (Au) doped CeO_2 NPs has been used as photocatalysts for the degradation RhB dye. Ag doped CeO_2 NPs has degraded RhB dye to 99.8% in 5h at natural pH and almost 100% in 3h under UV-Visible light radiations. On the other side Au doped CeO_2 NPs at similar experimental conditions has degraded RhB dye to 95.8% in 2.5h at natural pH whereas almost 100% in just 2h at higher pH under the exposure of radiations. Thus, on comparing the results of two systems, it can be concluded that Au doped CeO_2 NPs has shown better photocatalytic efficiency as compared to Ag doped CeO_2 NPs. This might

be due to greater ionic radii of Au^{1+} (151pm) as compared Ag^{1+} (129pm) in CeO_2 lattice (Ce^{3+} (115pm) and Ce^{4+} (101pm)) resulting better generation of oxygen vacancies.

References

[1] P. Ji, J. Zhang, F. Chen, M. Anpo, Study of adsorption and degradation of acid orange 7 on the surface of CeO_2 under visible light irradiation. Applied Catalysis B: Environmental, 2009, **85**, 148-154.

[2] X. Liu, K. Zhou, L. Wang, B. Wang and Y. Li, Oxygen vacancy clusters promoting reducibility and activity of ceria nanorods, Journal of American Chemical Society, 2009, **131**, 3140-3141.

[3] P. J. Hay, R. L. Martin, J. Uddin, G. E. Scuseria, Theoretical study of CeO_2 and Ce_2O_3 using a screened hybrid density functional, Journal of Chemical Physics, 2006, **125**, 034712.

[4] D. Channei, B. Inceesungvorn, N. Wetchakun, S. Ukritnukun, A. Nattestad, J. Chen, S. Phanichphant, Photocatalytic Degradation of Methyl Orange by CeO_2 and Fe–doped CeO_2 Films under Visible Light Irradiation. Scientific Reports, 2014, **4**, 1-7.

[5] A. D. Liyanage, S. D. Perera, K. Tan, Y. Chabal, K. J. BalkusJr, Synthesis, characterization, and photocatalytic activity of Y- doped CeO_2 nanorods, ACS Catalysis, 2014, **4(2)**, 577-584.

[6] A. Younis, D. Chu, Y. Valentino and S. Li, Tuning of surface oxygen concentration of {111} surrounded ceria nanocrystals for enhanced photocatalytic studies. Nanoscale, 2016, **8**, 378-387.

[7] T. Mori, Y. Wang, J. Drennan, G. Auchterlonie, J. G. Li, T. Ikegami, Influence of particle morphology on nano-structural features and conducting property in Sm-doped CeO_2 sintered body, Solid State Ionics, 2004, **175**, 641-649.

[8] C. Mao, Y. Zhao, X. Qiu, J. Zhu, C. Burda, Synthesis, characterization and computational study of nitrogen-doped CeO_2 nanoparticles with visible-light activity, Physical Chemistry Chemical Physics, 2008, **10**, 5633-5638.

[9] W. Lei, T. Zhang, L. Gu, P. Liu, J. A. Rodriguez, G. Liu, M. Liu, Surface structure sensitivity of CeO_2 nanocrystals in photocatalysis and enhancing the reactivity with nanogold, ACS Catalysis, 2015, **5**, 4385-4393.

[10] M. J. Islam, D. A. Reddy, J. Choi, T. K. Kim, Surface oxygen vacancy assisted electron transfer and shuttling for enhanced photocatalytic activity of Z-scheme CeO2-AgI nanocomposite, RSC Advances, 2016, **6**, 19341-19350.

[11] S. B. Boskovic, D. R. Djurovic, S. P. Zec, B. Z. Motovic, M. Zinkevich, F. Aldinger, Doped and co- doped CeO_2: Preparation and properties, Ceramics International, 2008, **34**, 2001-2006.

[12] J. C. Dupin, D. Gonbeau, P. Vinatier and A. Levasseur, Systematic XPS Studies of Metal Oxides, Hydroxides and Peroxides, Physical Chemistry Chemical Physics, 2000, **2**, 1319-1324.

[13] X. Z. Li, F. B. Li, Study of Au/Au^{3+}-TiO_2 photocatalysts toward visible photooxidation for water and wastewater treatment, Environmental Science & Technology, 2001, **35**, 2381-2387.

[14] H. M. Sung-Suh, J. R. Choi, H. J. Hah, S. M. Koo, Y. C. Bae, Comparison of Ag deposition effects on the photocatalytic activity of nanopatriculate TiO_2 under visible and UV light irradiation, Journal of Photochemistry and Photobiology A: Chemistry, 2004, **163**, 37-44.

[15] H. R. Pouretedeal, A. Kadekhodaie, Synthetic CeO_2 NPs catalysis of methylene blue photodegradation: Kinetics and Mechanism, Chinese Journal of Catalysis, 2010, **31**, 1328-1334.

[16] M. Nabavi, O. Spalla, B. Cabane, Surface chemistry of nanometric ceria particles in aqueous dispersions, Journal of Colloid and Interface Science, 1993, **160**, 459-471.

[17] C.A.K. Gouvea, F. Wypych, S.G. Moraes, N. Duran, N. Nagata, P. P. Zamor, Semiconductor-assisted photocatalytic degradation of reactive dyes in aqueous solution. Chemosphere, 2000, **40**, 433–440.

[18] J. Li, O. Zalloum, T. Roschuk, C. Heng, J. Wojcik and P. Mascher, The formation of light emitting cerium silicates in cerium-doped silicon oxides, Applied Physics Letters, 2009, **94**, 011112.

[19] Y. Xu and M. A. A. Schoonen, The absolute energy positions of conduction and valance bands of selected semiconducting minerals, American Mineralogist, 2000, **85**, 543-556.

[20] W. Baran, A. Makowski, W. Wardas, The effect of UV radiation absorption of cationic and anionic dye solutions on their photocatalytic degradation in the presence of TiO_2, Dyes and Pigments, 2008, **76**, 226–230.

[21] U. G. Akpan, B. H. Hameed, Parameters affecting the photocatalytic degradation of dyes using TiO_2-based photocatalysts: a review. Journal of Hazardous Materials, 2009, **170**, 520–529.

CHAPTER 6

CONCLUSIONS AND FUTURE SCOPE

Overview

The present chapter summarizes the results obtained from various experiments discussed in previous chapters. Effect of morphology, capping agent, dopant and doping concentration, irradiation time and pH of the synthesized NPs (pH adjusted during synthesis) has been summarized. Results obtained from doped and capped ZnO NPs has been concluded. Further the conclusion drawn from the doped CeO_2 NPs have also been summarized. Based on the results obtained from the present work, some suggestions have been given at the end of the chapter to carry out more work in this field.

6.1 Conclusions

Undoped and doped ZnO nanoparticles (NPs) were synthesized by co-precipitation route under varying experimental conditions. The main objective behind this work was to synthesize photoactive material that could be used as a photocatalyst to remove harmful effluents from water sources and thus to safe human and aquatic life. As experimental conditions have dominant effect on structural and optical properties on photocatalysts so these were varied to obtain optimal parameters to synthesize highly photoactive photocatalysts.

Undoped and Mn (0.5%, 1.0%, 1.5% & 2%) doped with PVP (1%) capped ZnO NPs has been synthesized by co-precipitation method. XRD showed highly crystalline wurtzite structure with crystallite size of 18-30nm. From TEM micrographs particle size comes out to be almost 15-20nm and 22-25nm for Mn (1%) and Mn (2%) doped and PVP (1%) capped ZnO NPs respectively. PL and UV Visible spectroscopy has been done to see the influences of Mn doping on emission characteristics. Crystal violet dye has been successfully degraded using undoped and Mn doped ZnO NPs after 3.0h UV-Visible irradiation. Photocatalytic studies shows Mn (1%) doped and PVP (1%) capped ZnO NPs to be a better photocatalyst for degradation of crystal violet dye as compared to other photocatalysts when exposed to UV- Visible radiations for 1h only. Almost 100% dye has been degraded using Mn (1%) doped with PVP (1%) capped ZnO NPs after 3h of UV-Visible radiations. Kinetic studies show that photo degradation of CV follow a pseudo first-order kinetic law and reaction rate of Mn (1%) doped and PVP (1%) ZnO NPs is better as compared to others. Reusability studies showed that Mn (1%) doped and PVP (1%) capped ZnO NPs degrade CV dye at better rate. This shows that the synthesized catalyst has become a better catalyst after exposing it in UV-Visible radiations for 3h due to surface modification which leads to transition from hydrophobic state (low surface energy) to hydrophilic (high surface energy) state that is also supported by UV-Visible and Photoluminescence spectra of Mn (1%) doped and PVP (1%) capped ZnO NPs without and with 3h UV treatment.

Further, undoped and Mn doped and TG capped ZnO NPs were synthesized by co-precipitation route initially at pH-6.7. XRD pattern confirm the formation of doped ZnO samples without any secondary phase appearance. PLE spectra have shown large absorption in visible region as compared to undoped NPs. PL emission and excitation spectra showed that incorporation of Mn ions in NPs have decreased electron-hole recombination. Photocatalytic studies shows that Mn (1.0%) doped ZnO NPs synthesized at pH-6.7 exhibits better photocatalyst when exposed to UV-Visible light radiations for 1h only. Similarly Mn doped ZnO samples synthesized at

pH-8.0 and 10.0 have shown 95% and more than 98% degradation of CV dye under similar conditions. When pH of the as synthesized Mn (1.0%) doped ZnO samples were raised to 12.0, almost 100% CV dye has been degraded in 2.5h only. Further fast and quick CV dye degradation has been observed when only 1.0% of H_2O_2 is added during photocatalytic reaction. 100% CV dye has been degraded in 90mins with Mn (1.0%) doped ZnO NPs synthesized at pH-8.0 and 10.0 in the presence of H_2O_2. Mn (1.0%) doped ZnO NPs synthesized at pH-12.0 has shown highest degradation reaction rate of CV dye and has degraded 100% dye in 30mins in the presence of H_2O_2. To check the utility of highly efficient photocatalyst for anionic dyes also in industries, degradation of polyazo Sirius red F3B (SRF3B) industrial dye has been studied and 100% degradation has been achieved in 15mins under UV-Visible light radiations. This means doping, pH and presence of H_2O_2 all have shown significant contribution for quick degradation of dye. With this system industrial effluents of any pH can be degraded quickly and thus will help to save aquatic life.

As different dopant have different effects on photodegradation efficiency of host semiconductor materials. Therefore, TG (1.0%) capped undoped and Cu (1.0% - 5.0%) doped ZnO NPs were synthesized at pH-8.0 by co-precipitation route. XRD results confirm the formation of doped ZnO samples without any appearance of secondary phase. EDS studies shows the doping of Cu ions into the ZnO lattice. PLE spectra shows large absorption in visible region for Cu doped samples as compared to undoped NPs. PL emission spectra shows emission in visible region due to Cu ions by suppressing the emission in UV region appeared in undoped ZnO NPs. Cu doped ZnO NPs have exhibited higher degree of degradation as compared to other undoped samples at pH-8.0. Thus doping has enhanced the degradation by trapping electrons and holes and thus by reducing electron-hole recombination. Doping concentration of Cu has been optimized to be 3.0% showing smaller particle size, maximum PL emission intensity and red shifted band gap. Effect of changing pH on nucleation, morphology, related photo physical and photocatalytic properties has been successfully studied for Cu (3.0%) doped ZnO NPs synthesized at pH 8.0, 10.0 and 12.0. It has been found that Cu (3.0%) doped NPs synthesized at pH-8.0 and 10.0 degrades 78.7% and 96.5% of dye after 3.5h under exposure of UV-visible radiations and similar doped and capped sample prepared at pH-12.0 degrades 100% of same concentration of dye after 2.5h under similar UV-Visible radiations. Loading of catalyst shows that 3.0g/L of catalyst shows maximum photodegradation of CV dye. Similar type of results has been obtained when Cu (1.0-5.0%) doped and PVP (1.0%) capped ZnO NPs were synthesized and evaluated their photocatalytic efficiency. Again Cu (3.0%) was found to be optimal initially at natural pH and was further selected to study the

effect of pH (adjusted during synthesis) on photocatalytic efficiency of ZnO NPs. It was found that Cu (3.0%) doped ZnO NPs synthesized at pH-12 has degraded almost 100% dye in 150mins only which is 60 minutes early than the similar Cu doped ZnO NPs synthesized at natural pH. This means Cu doped with both TG and PVP capped samples has shown similar results indicting Cu (3.0%) doping is optimum for better photocatalytic activity.

Also as ceria has high oxygen storage capacity so has been selected to evaluate as a photocatalyst. Ag doped ceria NPs with different amount of doping has been synthesized by co-precipitation method. Increase of doping concentration has resulted in increase in the amount of oxygen vacancies. 2.0 at.% of Ag doping has shown the higher photocatalytic activity than other as synthesized lower level of doped and undoped NPs due to lower band gap and the presence of optimum level of oxygen vacancies. However, above the optimal level of doping concentration, Ag^{1+} become recombination center which increases the electron-hole pair recombination and results in decrease in photocatalytic degradation efficiencies. As the NPs agglomerates in acidic environment of dye solution, at optimized dopant concentration, Ag^{1+} doped ceria NPs has been synthesized at higher pH value. Thus the presence of Ag^{1+}/ Ag^{0} and Ag^{2+}/Ag^{1+} additional energy levels of Ag^{1+} in ceria NPs, presence of sufficient oxygen vacancies and proper maintenance of pH during synthesis of optimal doped ceria NPs have shown higher photodegradation efficiency of RhB dye in UV-Vis. irradiations. Further Au doped CeO_2 NPs has also been synthesized initially at natural pH. XRD results have shown no peak related to Au or any other impurity indicating that Au has been doped into ceria lattice. Further there is a (1 1 1) peak shifting towards higher 2θ value attributed to smaller ionic radii of Au^{3+} ion as compared to Ce. Also contraction in ceria lattice may be due to oxygen vacancies. Au (4.0%) doped ceria sample synthesized at natural pH have shown highest photocatalytic efficiency as compared to undoped and other doped ceria samples. This category of doping has been selected to synthesize at higher pH value during synthesis. Sample synthesized at pH-12 has shown remarkable photocatalytic efficiency. Within 120 minutes more than 99% RhB dye has been degraded with Au (0.4%) doped sample synthesized at pH-12.0. This means Ag and Au doped ceria samples synthesized at higher pH value can be used as a photocatalyst in various industries to reduce water pollution.

6.2 Future scope

Although extensive studies has been done to improve the photocatalytic efficiency of ZnO and CeO_2 NPs, still there are many possibilities of further investigations to enhance their photocatalytic properties. Some of the suggested possibilities are listed below:

- Effect of UV treatment at different time period can be studied on optical, morphological and photocatalytic properties of doped semiconductor photocatalysts.
- Effect of temperature on photocatalytic reactions can be studied to further explore the photocatalytic efficiencies of semiconductor photocatalysts.
- ZnO-CeO_2 nano-composites can be synthesized at different pH values to study their effect on optical and photocatalytic properties.
- For better charge transportation, semiconductor materials along with doping can be decorated on graphene so as to increase the movement of e-h pair towards the surface of synthesized NPs by retarding the e-h pair recombination and thus to increase the photocatalytic efficiency of semiconductor photocatalysts.
- Ceria based photocatalysts can play an important role is renewable energy production from solar energy, environment protection and remediation, so it is important to study its optical, morphological and photocatalytic properties in detail along with doping and co-doing.